Etude du comportement hygrothermique des matériaux biosourcés : effet du vieillissement sur leurs propriétés thermiques et hydriques

Achraf Charaka

To cite this version:

Achraf Charaka. Etude du comportement hygrothermique des matériaux biosourcés : effet du vieillissement sur leurs propriétés thermiques et hydriques. Matériaux. Université de La Rochelle, 2024. Français. NNT : 2024LAROS001 . tel-04748167

HAL Id: tel-04748167
https://theses.hal.science/tel-04748167v1

LA ROCHELLE UNIVERSITE

ED 618 *Euclide*

LABORATOIRE : LaSIE UMR - 7356 CNRS

THÈSE présentée par :

Achraf CHARAKA

soutenue le : **18 janvier 2024**
pour obtenir le grade de : **Docteur de La Rochelle université**
Discipline : **Génie Civil**

Étude du comportement hygrothermique des matériaux biosourcés : effet du vieillissement sur leurs propriétés thermiques et hydriques

JURY :

Delphine LACANETTE	Professeure, Université de Bordeaux, Rapporteur
Thibaut COLINART	Maître de Conférence HDR, Université de Bretagne Sud, Rapporteur
Geraldine CASAUX-GINESTET	Professeure, École Nationale Supérieure d'Architecture et de Paysage de Bordeaux, Examinatrice
Nathan MENDES	Professeur, Pontifical Catholic University of Parane in Brazil, Examinateur
Suelen GASPARIN	Chargée de Recherche CEREMA Nantes, Examinatrice
Marie DUQUESNE	Professeure, La Rochelle Université, Examinatrice
Julien BERGER	Chargé de Recherche CNRS, La Rochelle Université, Encadrant de thèse
Rafik BELARBI	Professeur, La Rochelle Université, Directeur de thèse

Remerciements

Ce travail de thèse doctoral a été réalisé au Laboratoire des Sciences de l'Ingénieur pour l'Environnement (LaSIE) de La Rochelle Université en France. Il n'aurait pas pu aboutir sans le soutien financier du projet CPER-FEDER Bâtiment durable Axis 2 MADUR et du laboratoire commun 4evLab, LaSIE, CNRS, EDF R&D. Je voudrais exprimer ma sincère reconnaissance envers les personnes qui ont joué un rôle essentiel dans la réalisation de cette thèse. Tout d'abord, j'adresse mes sincères remerciements à monsieur M. FAUGAS Xavier, directeur du LaSIE pour m'avoir accueilli au sein du laboratoire durant mes trois années de thèse.

Je tiens à remercier l'ensemble des membres du jury pour le temps précieux qu'elles/ils ont consacré à l'examen approfondi de cette thèse et pour leurs recommandations avisées qui contribueront à son amélioration continue :

Madame Delphine LACANETTE, Professeure à l'Université de Bordeaux, Rapporteur.
Monsieur Thibaut COLINART, Maître de Conférence HDR à l'Université de Bretagne Sud, Rapporteur.
Madame Geraldine CASAUX-GINESTET, Professeure à l'École Nationale Supérieure d'Architecture et de Paysage de Bordeaux (ENSAP), Examinatrice.
Monsieur Nathan MENDES, Professor at the Pontifical Catholic University of Parane in Brazil, Examinateur.
Madame Suelen GASPARIN, Chargée de Recherche à CEREMA Nantes, Examinatrice.
Madame Marie DUQUESNE, Professeure à la Rochelle Université, Examinatrice.

Je tiens à remercier du fond du cœur mon Directeur de thèse M. Rafik BELARBI Professeur des Universités, pour son dévouement, son expertise et sa patience tout au long de ce projet. Ses conseils avisés, son encadrement précieux et ses discussions stimulantes ont été la pierre angulaire de cette recherche. Sa disponibilité et ses orientations m'ont permis de repousser mes limites intellectuelles et méthodologiques, ce qui a grandement enrichi ce manuscrit.

Je souhaite également exprimer ma gratitude envers mon encadrant de thèse M. Julien BERGER Chargé de Recherche CNRS, pour sa contribution significative à ce travail. Ses conseils éclairés, ses suggestions pertinentes et son intérêt constant pour mes progrès ont été d'une valeur inestimable. Je suis vraiment reconnaissant pour son investissement dans ce travail.

Je tiens à adresser mes remerciements à l'ensemble de l'équipe du Laboratoire des Sciences de l'Ingénieur pour l'Environnement pour leur accueil, leur collaboration et les échanges fructueux qui ont enrichi mes réflexions tout au long de ces années de recherche. Leur expertise et leur amitié ont contribué de manière significative à l'aboutissement de cette thèse.

Je suis reconnaissant envers mes collègues de recherche Ferhat BENMAHIDDINE, Mohamed SAWADOGO, Rachid CHERIF, Anis BAHAR, Yara NASR et Bassel HABEEB pour leur soutien, leurs encouragements et les discussions stimulantes qui ont nourri ma réflexion et ont contribué à l'avancement de ce travail.

Je tiens à exprimer ma profonde reconnaissance envers ma famille pour son soutien indéfectible, ses encouragements constants et sa compréhension tout au long de cette aventure intellectuelle.

Enfin, je souhaite remercier toutes les personnes qui, de près ou de loin, ont contribué à cette recherche par leurs conseils, leur expertise ou leur soutien moral. Leur implication et leur contribution ont été des éléments essentiels dans la réalisation de cette thèse.

Résumé

Ce travail aborde la modélisation numérique et expérimentale des transferts de chaleur et d'humidité au sein des matériaux biosourcés. Il traite la problématique de l'évolution du comportement de ces derniers en fonction de leur vieillissement dans l'optique d'une meilleure fiabilité des simulations hygrothermiques des bâtiments. Grâce à une formulation adimensionnelle des équations de transferts couplés de chaleur et de masse, des nombres sans dimensions reliant les échelles caractéristiques des phénomènes physiques sont mis en évidence.

Cette formulation est utilisée pour établir une modélisation expérimentale à l'échelle du laboratoire pour étudier le vieillissement des matériaux, et notamment l'évolution de leurs propriétés en fonction des cycles de séchage et imbibition. Les lois de similitudes sont exploitées, en respectant les invariants caractérisés par des nombres adimensionnels, permettant ainsi de diminuer significativement la durée des essais. Ainsi si le phénomène de vieillissement a une échelle temporelle réelle de plusieurs années, la maquette expérimentale équivalente permet de réduire cette échelle à quelques dizaines de jours.

Dans un premier temps, deux expériences de validation des lois de similitude sont menées dans le cas de transferts de chaleur seuls et la deuxième, plus générale, dans le cas de transferts couplés de chaleur et masse au sein d'un matériau biosourcé. Pour chaque cas, deux maquettes expérimentales sont élaborées pour deux configurations : une dite de référence et une dite réduite, pour laquelle les échelles temporelles de transfert sont diminuées. Les deux configurations ont les mêmes nombres sans dimension et sont donc équivalentes d'un point de vue des similitudes. Les champs de température et de teneur en eau sont comparées pour les deux configurations au regard des incertitudes de mesures. Cette analyse par intervalle de confiance permet de valider les résultats obtenus et de fiabiliser ainsi l'approche des lois de similitudes pour les transferts de chaleur et de masse dans les matériaux poreux.

Dans un deuxième temps, cette méthodologie est appliqué pour développer un protocole de vieillissement d'un matériau biosourcé. Sur la base de données climatiques représentatives (température, précipitations, radiation solaire normale incidente) d'une zone géographique et des lois de similitudes de transfert, une maquette expérimentale réduite est générée. Cette maquette soumet le matériau à une alternance de cycle d'imbibition et de séchage sur une durée de 40 jours à défaut de 1 an pour la configuration réelle. Au cours de ce protocole accéléré de vieillissement, la porosité, la conductivité thermique, la perméabilité à la vapeur d'eau et le pH du matériau sont mesurées. Les observations expérimentales obtenues dévoilent une variation sensible de ces propriétés au cours du temps. L'exploitation de ces données a permis de proposer un modèle numérique du vieillissement de la porosité en fonction des charges thermiques et hydriques subies par le matériau.

Enfin, ce modèle a été inclus dans un modèle de transferts de chaleur et de masse à l'échelle d'une façade de bâtiment. Les simulations mettent en exergue que le vieillissement du matériau engendre une modification notable du bilan thermique et hydrique de la façade.

Abstract

This work addresses the numerical and experimental modeling of heat and moisture transfers within bio-based materials. It deals with the issue of aging of these materials, with a focus on improving the reliability of energy simulations in buildings. Through the dimensionless formulation of coupled heat and mass transfer equations, dimensionless numbers, which relate the characteristic scales of physical phenomena, are identified.

This formulation is used to propose an experimental modeling at the laboratory scale for the study of material aging. Particularly, the evolution of their properties is investigated based on drying and imbibition cycles. Similarity laws are applied, while meeting the hypotheses on dimensionless numbers, to reduce significantly the duration of experiments. Thus, if the aging process has a real time scale of several years, the equivalent experimental model reduces this scale to few weeks.

First, two experiments tests the application reliability of similarity laws in the case of heat transfer alone, and the second, more general, deals with coupled heat and mass transfers within a bio-based material. For each case, two experimental models are developed. These represent two configurations : one referred to as the reference and the second as the reduced configuration, in which transfer time scales are reduced. Both configurations have the same dimensionless numbers and are, therefore, equivalent in terms of similarity. For both configurations, temperature and moisture content fields are compared with regard to measurement uncertainties. Obtained results are validated through a confidence interval analysis. The latter reinforces the similarity laws approach for heat and mass transfers in porous materials.

In the second part, this methodology is applied to develop an aging model for a bio-based material. Based on representative climate data (temperature, precipitation, incident normal solar radiation) and transfer similarity laws , a reduced experimental model is generated. According to this experiment, the material is subjected to a succession of imbibition and drying cycles over a period of 40 days, instead of one year in the real-scale configuration. During the accelerated aging experiment, porosity, thermal conductivity, vapor permeability, and pH are measured. The experimental observations reveal a significant variation in these properties over time. The data are used to propose a physical model of aging. It describes the evolution of porosity due to the heat and moisture loads that undergoes a porous material.

Finally, the model of porosity is integrated into heat and mass transfer at the building wall scale. Simulations highlight that material aging causes a significant change in wall heat and moisture balance.

Introduction générale

L'étude de la performance énergétique et environnementale des bâtiments ambitionne d'optimiser l'efficacité des bâtiments, leur empreinte carbone et d'assurer un confort optimal aux occupants à moindre coût. Le contexte général de la transition énergétique est marqué par la prise de conscience croissante de l'impact environnemental lors de la conception des constructions neuves et la rénovation du parc ancien. En effet, le bâtiment est un secteur consommateur d'énergie à l'échelle mondiale [1, 2]. Il est aussi source des émissions de gaz à effet de serre et un facteur important du dérèglement climatique [3]. La réglementation nationale et les exigences internationales deviennent plus strictes et visent à réduire la facture énergétique et aussi à promouvoir l'exploitation des énergies renouvelables tout en veillant à atteindre la cible de la réduction de l'empreinte environnementale. D'un point de vue scientifique, les systèmes de chauffage et de climatisation des bâtiments sont dimensionnés sur la base des règles de calcul thermique. Les matériaux utilisés dans la construction des bâtiments jouent également un rôle important, car ils peuvent affecter le comportement hygrothermique les enveloppes de bâtiments et la qualité des environnements intérieurs. C'est, en effet, dans le cadre de cette problématique sociétale de transition énergétique et environnementale que s'inscrit ce travail. De nombreuses investigations ont été menées dans l'optique d'optimiser les performances énergétiques et environnementales des matériaux de construction [4]. Les recherches ont contribué à l'introduction de nouveaux types de matériaux. Il s'agit principalement de la formulation des écomatériaux innovants, des matériaux biosourcés [5] et géosourcés. Les écomatériaux sont conçus en employant des techniques de production plus durables et des matériaux recyclables réduisant ainsi à la fois, la part du ciment connue par un mauvais bilan carbone et aussi celle du sable qui est peu abondant. Les matériaux fabriqués à partir de ressources renouvelables d'origine biologique, telles que les plantes, les arbres, les animaux ou les déchets organiques, sont nommés matériaux bio-sourcés. Par exemple, les panneaux de construction, d'isolants, de cloisons, de revêtements de sol et de murs peuvent être fabriqués à partir des matériaux de construction recyclables tels que le bois, le bambou, le cuir et les fibres végétales. A vue des nombreux avantages, notamment ceux dédiés à la durabilité, la réduction des émissions de gaz à effet de serre et l'utilisation de déchets agricoles, les matériaux bio-sourcés représentent de nos jours une alternative viable par rapport aux matériaux conventionnels [6, 7, 8]. Les caractéristiques des matériaux bio-sourcés varient en fonction de leur composition chimique, leur structure et leur méthode de fabrication.

Quant aux normes, certaines encouragent le choix des matériaux biosourcés et valorisent leur utilisation dans le domaine de construction. En France, nous distinguons la norme NF EN 16516 et NF P01-010. La première s'intéresse aux émissions des composés organiques volatils des matériaux de construction, y compris ceux biosourcés. Pour la deuxième, elle porte sur les caractéristiques et les performances des isolants thermiques et acoustiques à base végétale. Mis à part de ces normes, les labels « Maison Passive » et « bâtiment bio-sourcé » recommandent l'intégration des matériaux à base de matières premières renouvelables dans les bâtiments passifs. Bien que ces normes appellent à l'intégration de ces matériaux, la promotion de ces derniers est freinée par la communauté scientifique du fait de la méconnaissance de leur comportement en fonction du temps et des sollicitations subies. En effet, de nombreuses investigations ont montré que les propriétés microscopiques d'un matériau biosourcé évoluent dans le temps [9, 10]. Pour un béton conventionnel, l'exposition à des variations de température et d'humidité, dans le domaine du bâtiment, n'affecte que légèrement sa microstructure. En parallèle, les mêmes sollicitations peuvent induire une variation significative des propriétés d'un matériau biosourcé. Ceci est due à la présence des fibres végétales, aux phénomènes de gonflement et de rétrécissement qui sont observés à l'échelle microscopique. Explicitement, une particule à base organique gonfle en absorbant de l'eau suite à des sollicitations d'humidité. Sinon, l'eau présent dans le matériau s'évapore sous la présence de chaleur, ce qui engendre un rétrécissement. Ces deux phénomènes inverses sont, entre autre, responsables de l'évolution temporelle de la structure poreuse d'un matériau biosourcé et donc de ses propriétés physiques. La communauté scientifique nomme cette évolution vieillissement. Ce phénomène a été investigué dans la littérature afin de comprendre ses mécanismes. Ainsi, l'étude du vieillissement est modélisée expérimentalement au laboratoire par l'intermédiaire des essais recourant à des cycles de température et d'humidité. La durée de ces cycles est généralement de quelques semaines voire des mois, ce qui montre l'aspect accéléré de ces essais. Par exemple, des cycles d'humidification, d'imbibition et de projections à l'eau sont appliqués pour représenter les sollicitations hydriques. En outre, des variations de température (séchage ou gel) et de rayonnement thermique sont considérées pour traduire les sollicitations de chaleur. Bien que des protocoles de vieillissement existants démontrent l'évolution de la microstructure des matériaux biosourcés. Néanmoins, ils peuvent manquer parfois de fiabilité vu le caractère lent du processus qui s'étend sur plusieurs années. De plus, ces protocoles se basent sur l'application des sollicitations climatiques défavorables. Ces dernières ne sont pas représentatives d'un climat normal où les conditions météorologiques varient dans le temps. Les normes ASTM G7 et ASTM G154 fournissent des recommandations générales sur l'exposition des matériaux aux environnements extérieurs. Ils sont utilisés par les laboratoires d'essais sur des sites de référence météorologiques extérieurs, pour tester des matériaux directement exposés à la lumière naturelle du soleil. Au final, il est difficile de décrire la configuration réelle qui correspond à un essai accéléré mené dans le laboratoire. Par conséquence, la variation des propriétés d'un matériau biosourcé, due à un protocole de vieillissement accéléré, peut être surestimée ou inversement.

La contribution de cette recherche répond à la problématique suivante : comment étudier le vieillissement naturel d'un matériau ? D'une part, nous proposons une méthodologie pour le développement d'un protocole de vieillissement basé sur des données météorologiques représentatives. Cependant, l'application expérimentale de cet essai est freinée par la longue durée qui caractérise ce phénomène. Pour y remédier, les lois de similitudes sont exploitées pour générer une maquette expérimentale qui représente le vieillissement à l'échelle du laboratoire. Ces lois reposent sur des invariants caractérisés par des nombres sans dimension. Ces invariants découlent de la formulation adimensionnelle des équations de transferts couplés de chaleur et de masse. Ils permettent de relier les échelles caractéristiques, notamment espace-temps, de ces phénomènes de transfert. En particulier, il est question de réduire la durée du protocole du vieillissement. La maquette expérimentale développée s'étend ainsi sur quelques dizaines de jours tout en restant fiable et représentatif du phénomène étudié. En guise d'application, l'effet du vieillissement dû au protocole proposé, est investigué sur le béton de chanvre en mesurant la variation de ses propriétés. Ce manuscrit sera décliné en cinq parties complémentaires.

Le premier chapitre est constitué d'un état de l'art qui résume les principaux travaux liés à cette thématique de recherche. Dans un premier lieu, il est convenu de définir le matériau poreux et ses caractéristiques intrinsèques. Cette étape est indispensable en raison de la nature poreuse du matériau biosourcé. Par ailleurs, la connaissance de la microstructure d'un matériau permet de déterminer ses propriétés thermiques et hydriques. Nous présentons, ainsi, les protocoles de mesures des principales propriétés qui sont abordées dans la littérature. Ensuite, nous nous décrivons la nature des matériaux biosourcés en étudiant quelques exemples. Leurs performances énergétiques et environnementales sont illustrées et discutées. Dans le secteur du bâtiment, les performances des différentes parois sont évaluées à partir de l'étude des transferts couplés de chaleur et d'humidité au sein des matériaux qui les composent. La réponse des enveloppes de bâtiments aux sollicitations climatiques (température, flux solaire, humidité relative, pluie ...) est quantifiée. Sur une longue durée, ces sollicitations impactent l'évolution de la microstructure des matériaux utilisés. Dans ce chapitre, les différents types du vieillissement sont présentés, y compris le vieillissement thermo-hydriques des matériaux de construction. Dans ce cadre, des exemples d'essais accélérés sont explicités. Finalement, nous clôturons l'état de l'art par la définition des lois de similitude et leurs domaines d'utilisation. En effet, leur emploi est déterminant pour la réduction de la durée des expériences à l'instar du processus de vieillissement. Cette partie distingue deux types de travaux. Certains valident expérimentalement les lois de similitude en travaillant sous des hypothèses bien définies. Les autres appliquent directement ces lois en proposant des maquettes simplifiées.

Lors du deuxième chapitre, il sera abordé la validation expérimentale des lois de similitude sur une configuration simple d'un transfert de chaleur par conduction unidirectionnelle. Cette partie reflète notre premier travail expérimental durant la thèse. La seconde constitue une généralisation de l'application des lois de similitude sur un cas complexe de transferts couplés de chaleur et d'humidité. Après le développement du modèle physique de transfert de chaleur et de la configuration de référence retenue, l'application des lois de similitude permet d'en déduire une configuration équivalente présentant une durée plus courte. Grâce à un suivi expérimental de l'évolution de la température, un calcul des incertitudes est entrepris afin de comparer les résultats des deux configurations et d'en conclure quant à la fiabilité de ces lois dans la prédiction du comportement thermique des matériaux en fonction de leur âge.

Dans le cadre du troisième chapitre, la validation expérimentale des lois de similitudes dans un cas plus généralisée sera effectuée. Contrairement à un phénomène de transfert de chaleur, cette partie aborde un modèle plus complexe qui fait intervenir des équations aux dérivées partielles fortement couplées. La généralisation des lois de similitude aux transferts couplés de chaleur et d'humidité est justifiée par la sensibilité d'un matériau biosourcé à la présence d'eau dans sa microstructure. Pour ce genre de matériaux, la sensibilité aux transferts de masse d'eau est plus remarquable contrairement aux matériaux de construction traditionnels. Les essais seront appliqués sur un béton de chanvre en se donnant une configuration de référence et une autre accéléré et équivalente. Les observations expérimentales et le calcul d'incertitudes sur le champ de température et d'humidité relative ont permis de justifier la méthodologie. Ce résultat est nécessaire pour aborder le phénomène du vieillissement.

Le quatrième chapitre porte sur l'étude du vieillissement du béton de chanvre. Grâce au développement d'une méthodologie, des données climatiques annuelles sont utilisées pour proposer un protocole de vieillissement, dit de référence. Cette méthodologie est élaborée sur la base d'un certain nombre d'hypothèses. Suite à la validation expérimentale des lois de similitude, celles-ci sont utilisées pour réduire la durée de ce protocole en proposant une maquette réalisable à l'échelle du laboratoire. Il sera, ensuite, abordée la campagne expérimentale. Cette dernière vise à évaluer la variation temporelle des propriétés du béton de chanvre due à l'application du protocole du vieillissement développé. Sur la base des observations, il sera conclu sur l'effet notable de ce phénomène sur la porosité en tant que propriété intrinsèque. Cette évolution de porosité sera accompagnée d'une variation significative de la conductivité thermique et de la perméabilité à la vapeur. Aussi, ces résultats expérimentaux seront comparés à des corrélations empiriques qui expriment les propriétés de transfert en fonction de la porosité.

Le cinquième et dernier chapitre est dédié à une investigation numérique. Il s'agit de développer un modèle phénoménologique de vieillissement des matériaux. Ce dernier décrit la variation de la porosité en fonction du temps en s'inspirant d'un modèle de croissance de populations. Dans ce cas, l'augmentation et la diminution de la porosité sont entraînées respectivement par l'exposition à des charges d'humidité et de chaleur. Dans le modèle de vieillissement, deux approches de définition des charges climatiques sont distinguées : une glissante et l'autre cumulée. En introduisant deux coefficients dans le modèle, une estimation de ces paramètres est menée dans l'optique d'obtenir les coefficients optimaux vis-à-vis des mesures de porosité. Cette investigation est réalisée en utilisant les mesures de porosité obtenues dans le chapitre précédent. Enfin, le vieillissement est pris en compte dans la simulation des transferts de chaleur et d'humidité. Moyennant une étude comparative, l'évaluation de l'impact du phénomène étudié sur la performance thermo-hydrique du béton de chanvre est entreprise. L'étude conclut sur la nécessité de considérer le vieillissement dans la prédiction du comportement thermo-hydrique des matériaux de construction. A l'échelle du bâtiment, l'intégration du modèle développé aiderait à mieux prédire la performance énergétique d'une construction lors de la phase de conception.

Chapitre 1

Introduction

Ce premier chapitre représente un état de l'art spécifique aux lignes directives de cette thèse. Il s'agit, principalement, de discuter des éléments de la littérature, portant sur les matériaux bio-sourcés et leur vieillissement hydrique et thermique. Ces matériaux sont des milieux hétérogènes à forte porosité. Dans cette optique, la première partie est consacrée à la définition du milieu poreux et de ses propriétés physiques. La connaissance de la microstructure d'un matériau poreux aide à mieux appréhender son comportement face aux sollicitations de chaleur et d'humidité. Afin d'y parvenir, la maîtrise du comportement d'un matériau passe par l'étape de caractérisation expérimentale des propriétés intrinsèques de ce dernier. Dans ce contexte, la deuxième partie du chapitre résume les procédures expérimentales utilisées pour la mesure des propriétés hydriques et thermiques d'un matériau. Nous exposons, aussi, lors de la troisième partie la notion du matériau biosourcé en illustrant, via des exemples, les résultats liés à leurs performances énergétiques et environnementales. Dans la quatrième partie, l'effet de l'âge (vieillissement) sur les propriétés des matériaux est abordé et ce pour différents domaines de recherche. Il sera évoqué les protocoles expérimentaux développés pour la modélisation de ce phénomène et nous nous intéressons, plus particulièrement, aux essais accélérés de vieillissement sous sollicitations hydriques et thermiques proposés dans la littérature. En effet, entreprendre des essais accélérés est justifié par le caractère très lent du vieillissement naturel qui peut s'étaler sur des décennies. Cette considération constitue un verrous scientifique qui freine le développement d'un protocole de vieillissement représentatif et l'existence de données fiables quant à la durabilité des matériaux et des structures. La cinquième partie met en exergue l'utilisation des lois des similitudes et ce pour des domaines d'applications variés. Grâce à ces lois, il est possible d'établir des équivalences entre des configurations ayant des échelles caractéristiques équivalentes. Sous certaines conditions, l'échelle spatiale et temporelle d'une configuration peuvent être réduites. De plus, suivant des domaines d'applications, la fiabilité de l'application de ces lois est discutée en faisant appel à quelques résultats issus de la littérature.

1 Milieu poreux

L'état bibliographique débute avec les concepts liés au milieu poreux. Ceux-ci se résument à la définition du milieu, quelques approches théoriques pour le modéliser ainsi que ses propriétés intrinsèques.

1.1 Définition

Un milieu poreux est une partie de l'espace occupée par une matière hétérogène ou multiphasique comme le montre la Figure 1.1. Au moins une des phases composant ce milieu n'est pas solide. Elle peut être gazeuse et/ou liquide. La phase solide est appelée matrice solide. L'espace compris dans un milieu poreux et ne faisant pas partie de la matrice solide est appelé espace vide (ou espace poral). Dans un milieu poreux, certains pores sont interconnectés. L'espace poreux interconnecté est souvent dénommé espace poreux effectif. Dans le cadre d'un écoulement à travers un milieu poreux, les pores non interconnectés peuvent être considérés comme une partie de la matrice solide. De plus, certaines régions de l'espace interconnecté peuvent être sans effet vis-à-vis de l'écoulement d'un fluide. Ainsi, des pores peuvent être fermés, à savoir des canaux qui ne présentent qu'une seule connexion avec l'espace poreux interconnecté, empêchant ainsi tout écoulement à travers ces pores.

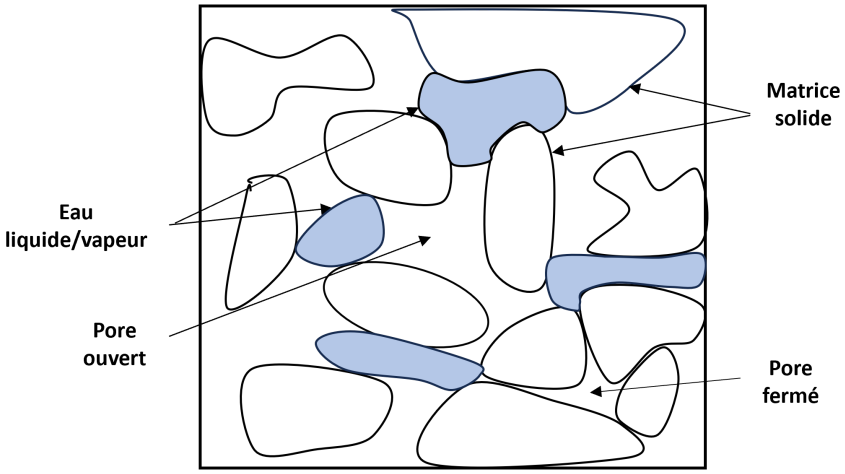

Figure 1.1 – Illustration du milieu poreux.

Il n'existe pas une classification unique des milieux poreux. Toutefois, nous distinguons la famille des milieux artificiels et l'autre des milieux naturels. Les milieux artificiels sont conçus par l'homme à l'échelle macroscopique, autrement dit, ils n'existent pas dans la nature. A titre d'exemple, les membranes poreuses sont utilisées dans les systèmes de filtration d'eau pour éliminer les impuretés et les particules. Les tissus imperméables respirants sont conçus avec des pores microscopiques qui permettent à la vapeur d'eau de s'échapper tout en empêchant l'eau liquide de pénétrer. Aussi, l'apparition récente des imprimantes 3D permet de concevoir différentes formes de microstructure en utilisant de la matière synthétique. Plus loin, la nature est à l'origine de l'existence des milieux poreux biologiques et géologiques. Parmi les différents exemples inspirés de la biologie (os, tissus, membranes, anas et fibres), nous citons les réseaux de pétioles et ceux capillaires [11]. Par ailleurs, la formation des milieux géologiques passe par des processus complexes. Ce type de milieux est abordé parce qu'il apporte un aperçu de la terminologie géologique. Voici quelques exemples de milieux géologiques : le sable, le grès, le calcaire et la craie, etc. Les milieux poreux de nature géologique présentent deux types d'hétérogénéité géométrique [12]. Premièrement, une porosité qui varie dans l'espace et deuxièmement l'existence de discontinuités sous la forme de fissures. Pour les matériaux de construction, les éléments utilisés pour les formulation sont majoritairement des dérivés naturels.

1.2 Les propriétés intrinsèques

L'identification des propriétés intrinsèques est utile pour décrire entièrement la microstructure d'un milieu poreux. Ces propriétés ne dépendent que de la géométrie de la structure poreuse. Cette section aborde la surface spécifique, la connectivité, la tortuosité, la porosité et la perméabilité intrinsèque. En complément, le milieu poreux est décrit en introduisant deux propriétés intrinsèques supplémentaires de nature statistique, à savoir la distribution de tailles des pores et de particules.

1.2.1 Porosité et volume élémentaire représentatif

La porosité est un paramètre essentiel pour évaluer la durabilité des matériaux et pour caractériser leur structure interne. Elle représente la proportion des espaces vides capables de contenir un fluide par rapport au volume total du matériau. La structure poreuse, qui se compose de pores et de canaux de petite taille, peut être classée en différentes catégories. Par exemple, nous utilisons les termes "porosité résiduelle" ou "porosité fermée" pour décrire la partie du système poreux qui renferme des pores isolés, ne communiquant pas avec le reste de l'espace poreux ni avec l'extérieur.

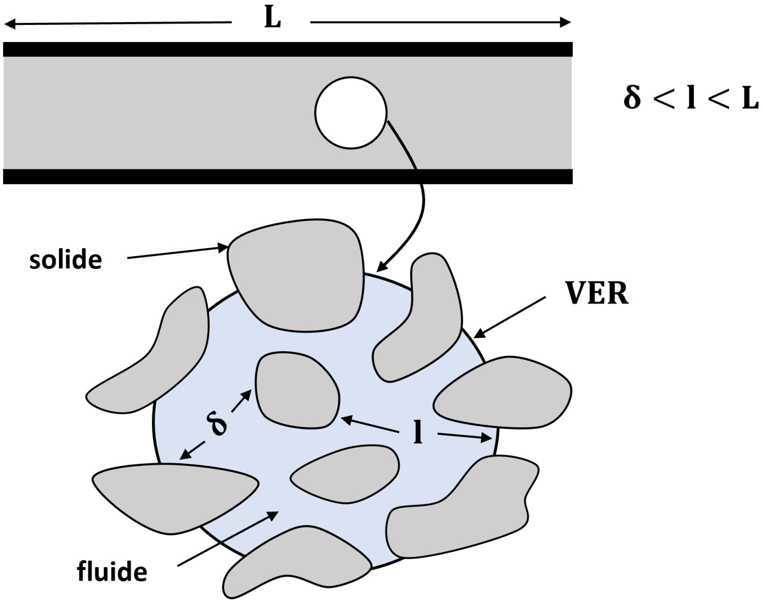

Figure 1.2 – Illustration de la porosité ouverte et des dimensions du volume élémentaire représentatif.

Cette forme de porosité n'a pas d'incidence sur les écoulements de fluides, mais elle peut influencer la résistance mécanique du matériau en créant des zones de contraintes. En outre, la "porosité effective" ou "porosité ouverte", notée $n\,[-]$ se rapporte aux pores qui sont interconnectés et permettent le passage de substances à travers le matériau. D'un point de vue macroscopique, Elle est définie par :

$$n = \frac{V_v}{V}\,, \tag{1.1}$$

où $V_v\,[\mathsf{m}^3]$ désigne le volume des pores ouverts. Cette définition est valable pour des volumes apparents supérieurs au volume élémentaire représentatif (VER) (voir Figure 1.2). Celui-ci est défini à travers l'évolution de la porosité en fonction du volume du matériau. Il représente le volume minimal à partir duquel la porosité ne varie plus. Il réduit la complexité des structures poreuses en les ramenant à une échelle représentative du caractère macroscopique du matériau. Par exemple, la porosité des roches sédimentaires est mesurée moyennant l'utilisation d'un volume cubique de quelques centimètres de côtés. Pour les matériaux composites de construction, le VER dépend de la nature des fibres et de la matrice. Son ordre de grandeur est situé sur une échelle de quelques centimètres cubes [13].

1.2.2 Surface spécifique

La surface spécifique $A\,[\mathsf{m}^{-1}]$ d'un milieu est définie comme la surface d'interface moyenne par unité de volume :

$$A = \frac{S}{V}\,, \tag{1.2}$$

où $S\,[\mathsf{m}^2]$ est la surface d'interface solide/fluide à l'intérieur du volume apparent du matériau $V\,[\mathsf{m}^3]$ (voir Figure 1.3). Il existe plusieurs méthodes de mesure de cette propriété [14]. Voici une brève description de certaines de ces méthodes.

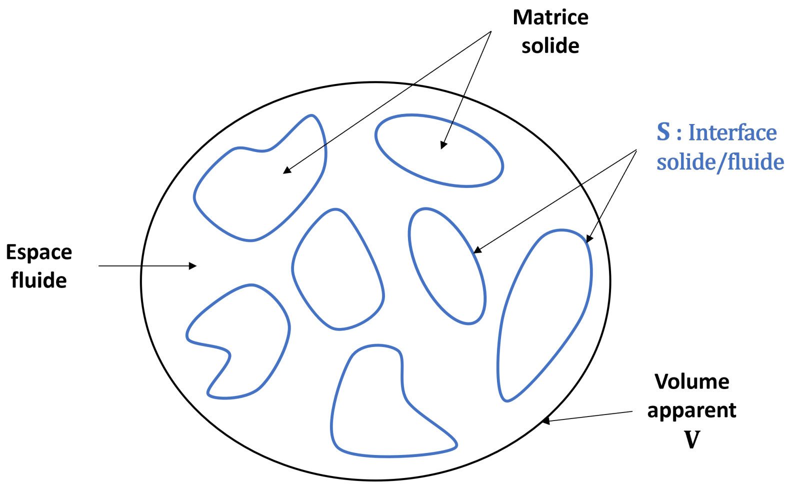

Figure 1.3 – Schéma descriptif en 2D de la surface spécifique d'un milieu poreux.

Une première approche repose sur l'adsorption de la phase gazeuse par la surface solide de la matrice. La surface est déterminée en mesurant la quantité de gaz adsorbée, en supposant que le gaz recouvre intégralement la surface sous forme d'une couche monomoléculaire. Une deuxième méthode est basée sur la chaleur d'humidification. Elle consiste à calculer la surface à partir de la chaleur humide générée lorsque le milieu est immergé dans un liquide [15]. Plus loin, une autre méthode basée sur l'écoulement des fluides a été développée par *Kozeny* et modifiée par la suite. Cette méthode établit une relation entre la perméabilité d'un milieu et sa surface spécifique. En l'utilisant, il est possible de déduire la surface spécifique en mesurant la perméabilité. D'après [16], *Brooks* et *Purcell* (1952) ont comparé la surface spécifique obtenue à partir de l'équation de *Kozeny* avec d'autres méthodes.

1.2.3 Connectivité

C'est un paramètre qui mesure le degré de connexion entre les pores. Sur cette base, les réseaux poreux ouverts et fermés sont distingués. La connectivité peut être adoptée davantage pour identifier les chemins traversés dans une structure poreuse lors d'un écoulement de fluide. Dans la littérature, Dallien et *al.* [17] définissent cette propriété comme le plus grand nombre de branches du réseau qui peuvent être coupées sans créer des parties indépendantes.

1.2.4 Tortuosité

La tortuosité T_H a été introduite pour la première fois par *Carman* (1937) pour désigner une direction particulière associée à un écoulement macroscopique donné. Elle a été précisément définie comme le carré du rapport entre la distance moyenne effective L_e et la distance la plus courte L mesurée le long de cette direction particulière :

$$T_H = \left(\frac{L_e}{L}\right)^2 . \tag{1.3}$$

Dans le contexte de la perméabilité des milieux poreux, la tortuosité mesure la déviation ou la courbure du chemin que doit emprunter un fluide pour se déplacer à travers les pores d'un matériau (voir Figure 1.4). Plus la tortuosité est élevée, plus le chemin est complexe, ce qui peut entraîner une résistance accrue à l'écoulement du fluide. La tortuosité est un paramètre important pour décrire la perméabilité des matériaux poreux.

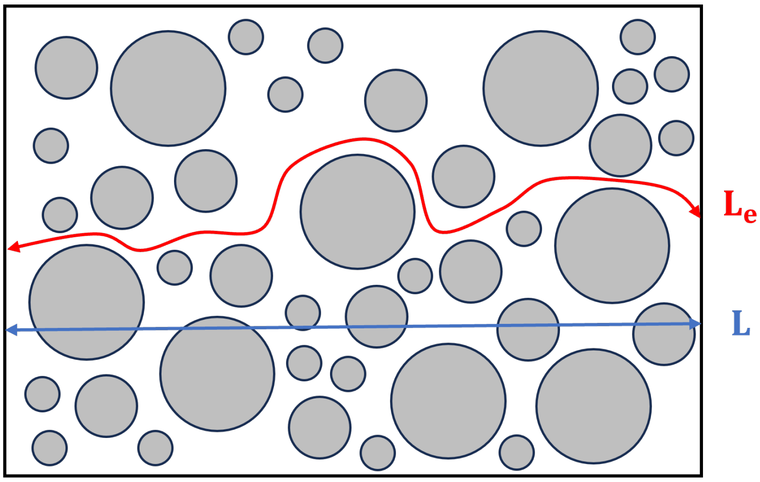

Figure 1.4 – Tortuosité d'un réseau poreux.

1.2.5 Perméabilité intrinsèque

$k\,[\mathsf{m}^2]$ est dite perméabilité (ou perméabilité intrinsèque) de la matrice poreuse. Elle dépend uniquement des propriétés géométriques du milieu poreux. Diverses formules sont décrites dans la littérature, liant la perméabilité aux différentes propriétés de la matrice. Certaines de ces formules sont purement empiriques, comme par exemple la formule (1.4) illustrée par la Figure 1.5 où k en cm^2 est fonction du diamètre moyen (ou effectif) des grains en µm.

$$k = 0.617 \times 10^{-11}\, d^2\,. \tag{1.4}$$

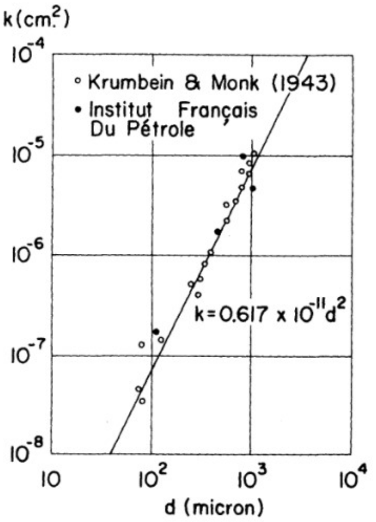

FIGURE 1.5 – La variation de la perméabilité intrinsèque en fonction du diamètre des grains du sable [18].

Un autre exemple est la formule de *Fair et Hatch* (1933) [19] développée sur la base de données dimensionnelles et vérifiée par l'expérience. Elle est donnée par l'équation suivante :

$$k = \frac{1}{m}\left[\frac{(1-n)^2}{n^3}\left(\frac{\alpha}{100}\sum\frac{P}{d_m}\right)^2\right]^{-1}, \tag{1.5}$$

où $m\,[-]$ est un facteur de tassement, estimé expérimentalement à environ 5, $\alpha\,[-]$ est un facteur relatif à la géométrie des grains du sable, variant de 6 pour les grains sphériques à 7.7 pour les grains anguleux. $P\,[-]$ est le pourcentage de sable retenu entre les tamis adjacents et $d_m\,[\mathsf{m}]$ est la moyenne géométrique des calibres des tamis adjacents. D'autres formules sont obtenues à partir de la dérivation de la loi de *Darcy*. Les plus connues sont l'équation de *Kozeny* (1.6) et celle de *Kozeny-Carman* [20] (1.7).

$$k = c_0\,\frac{n^3}{A^2}\,, \tag{1.6}$$

$$k = \frac{1}{5\,A_s^2}\,\frac{n^3}{(1-n)^2}\,. \tag{1.7}$$

A et $A_s\,[\mathsf{m}^{-1}]$ sont les surfaces spécifiques en considérant respectivement le volume apparent du milieu poreux et celui de la matrice solide. En plus, l'équation (1.6) introduit un coefficient empirique $c_0\,[-]$, c'est une formule semi-empirique. Dans ce cas, ce coefficient est déterminé via l'expérience et dépend de la géométrie du réseau poreux ouvert. Par exemple, $c_0 = 0.5$ pour un cercle, $c_0 = 0.562$ pour un carré, $c_0 = 0.597$ pour un triangle équilatéral. Les différentes formules citées ont la forme générale suivante :

$$k = f_1\,(\,s\,)\,f_2\,(\,n\,)\,d^2\,, \tag{1.8}$$

où s est un paramètre adimensionnel qui reflète la forme des grains (ou des pores), $f_1\,[-]$ est ainsi nommé facteur de forme, $f_2\,[-]$ est appelé facteur de porosité et $d\,[\mathsf{m}]$ est le diamètre effectif des grains. Selon l'étude considérée, le choix du diamètre d est relatif où la grandeur d_{10} peut être adoptée. Si la perméabilité dépend de l'espace, le milieu poreux est dit hétérogène. Par ailleurs, le milieu est considéré anisotrope si la perméabilité dépend de la direction d'écoulement. Dans certaines conditions, la perméabilité est susceptible de varier dans le temps. Cette modification est généralement induite par des charges externes qui engendrent des contraintes internes, modifiant la structure de la matrice poreuse. Il est important de noter que les formules analytiques de la perméabilité intrinsèque sont établies en fixant des hypothèses sur la géométrie du milieu poreux. Par exemple, l'équation (1.6) est obtenue en considérant le milieu un bloc géométrique régulier. Particulièrement, le bloc de sphères est un modèle empirique pour la représentation d'un réseau poreux et est donné pour $c_0 = 0.5$. Ce modèle a été initialement abordé pour étudier les écoulements de fluides dans les milieux poreux [21, 22]. La Figure 1.6 illustre l'exemple d'un regroupement de sphères.

Finalement, la connaissance des propriétés intrinsèques d'un matériau poreux ainsi que sa composition permettent d'évaluer ses propriétés thermiques et hydriques. En particulier, la porosité sera utilisé pour définir des corrélations avec les propriétés du transfert de chaleur et d'humidité lors du cinquième chapitre. Dans cette perspective, la prochaine section définit les propriétés liées à ces modes de transfert. En général, ces propriétés dépendent de la microstructure, la température et la teneur en eau. En outre, les méthodes courantes de mesure de chaque propriété sont décrites.

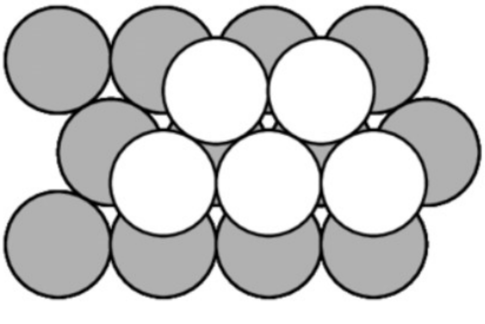

FIGURE 1.6 – Modélisation du milieu poreux sous forme de bloc de sphères [23].

2 Caractéristiques thermiques et hydriques

2.1 Conductivité thermique

La conductivité thermique est une quantité introduite dès 1822 via la loi de *Fourier*. Elle traduit la capacité d'un matériau à conduire la chaleur. La conductivité thermique, exprimée en $W.m^{-1}.K^{-1}$, est le flux de chaleur à travers une unité de surface d'un matériau homogène ayant une épaisseur de 1 m, induit par une différence de température de 1 K entre ses deux surfaces. Pour la mesure, nous distinguons les méthodes suivantes.

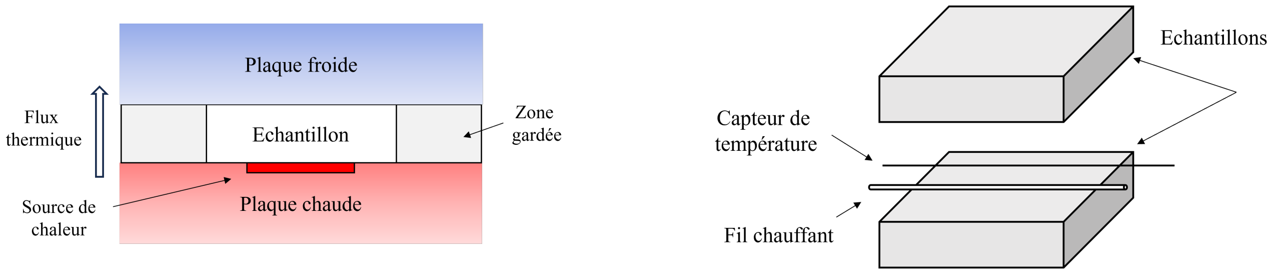

(a) Plaque chaude gardée.

(b) Fil chauffant.

FIGURE 1.7 – Illustration de deux protocoles expérimentaux pour la mesure de conductivité thermique.

L'essai de la plaque chaude gardée [24] est basé sur l'utilisation d'un échantillon et une puissance thermique grâce à un plan chaud. Les pertes de chaleur sont minimisées grâce à la présence d'une zone de garde comme illustré par la Figure 1.7a. Cet essai est réalisé en conformité avec la norme *ISO 8302 : 1901 − NF EN 12667*. La méthode du fil chaud [25] peut également être utilisée pour mesurer la conductivité thermique d'un matériau. Conformément à la norme *EN ISO 8894 − 1*, cette méthode est basée sur le principe de la puissance électrique dissipée par un fil chauffé (Figure 1.7b) et sa relation avec la conductivité thermique. Par ailleurs, la méthode du "*Hot Disk*" (disque chaud) en est de même une technique de mesure. Elle est basée sur le principe de la méthode du fil chaud, mais utilise un disque chauffant plutôt qu'un fil pour générer un flux de chaleur à travers l'échantillon. Elle est basée sur la norme *ISO 22007 − 2*. Finalement, cette propriété dépend de l'état thermique et hydrique du matériau.

2.2 Chaleur spécifique

La chaleur spécifique est une propriété importante dans de nombreux domaines de la science et de l'ingénierie, notamment pour la conception de systèmes de chauffage et de refroidissement, le calcul des besoins énergétiques. En transfert de chaleur, la chaleur spécifique d'un matériau, exprimée en $J.kg^{-1}.K^{-1}$, est la capacité d'un matériau à stocker ou restituer la chaleur. La valeur de la chaleur spécifique dépend du type de matériau considéré, de sa composition chimique et de sa structure moléculaire. La méthode de la calorimétrie différentielle à balayage (DSC) [26] est une technique qui mesure les différences de chaleur absorbée ou libérée par un matériau lorsqu'il est soumis à un chauffage ou un refroidissement contrôlé. Cette propriété est déterminée en mesurant la différence de chaleur entre l'échantillon et une référence. Cette méthode est conforme à la norme *ISO 11357 − 4*. Une seconde technique appelée analyse thermogravimétrique (ATG), mesure les changements de masse d'un matériau lorsqu'il est soumis à un chauffage ou un refroidissement contrôlé. En utilisant cette méthode, la chaleur spécifique peut être évaluée en quantifiant la perte ou le gain de masse en fonction de la température. Finalement, la chaleur spécifique est mesurée avec une bonne précision via le calorimètre Calvet [27, 28]. Ce dispositif réalise une analyse 3D grâce à un réseau de thermocouples entourant entièrement l'échantillon. Il est particulièrement utile pour étudier les changements de phase tels que la fusion, la solidification, la vaporisation et la condensation.

2.3 Perméabilité à la vapeur d'eau

La perméabilité à la vapeur d'eau d'un matériau, exprimée en s, caractérise la capacité d'un matériau à laisser passer la vapeur d'eau. Sa mesure est basée sur la quantité de vapeur qui traverse le matériau par unité de surface, d'épaisseur et de temps sous un gradient de 1 Pa de pression de vapeur.

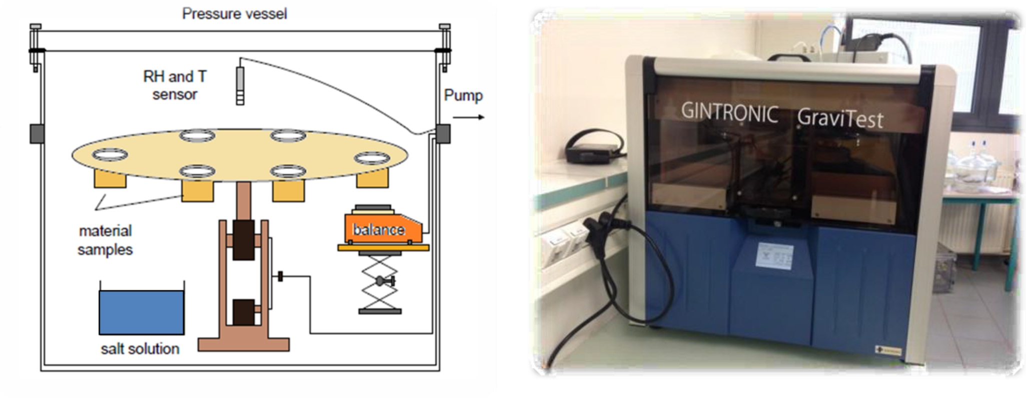

Figure 1.8 – Descriptif de la méthode automatisée de la coupelle moyennant le recours au dispositif Gintronic Gravitest [28].

La perméabilité à la vapeur d'eau dépend des propriétés intrinsèques du matériau, telles que sa structure moléculaire, sa porosité et sa densité. Elle peut également être influencée par des facteurs tels que la température et l'humidité relative. La méthode de la coupelle gravimétrique [29], est l'une des méthodes couramment utilisées pour mesurer la perméabilité à la vapeur d'eau d'un matériau. Cette méthode est basée sur l'utilisation de solutions salines (Figure 1.8) afin de contrôler l'humidité relative d'un côté du matériau. La mesure de cette propriété est obtenue grâce au suivi de masse de l'échantillon jusqu'à l'atteinte de l'équilibre. Il est important de noter que la méthode de la coupelle fournit une mesure de la perméabilité à la vapeur d'eau suivant une seule direction de transfert. De plus, cette méthode doit être réalisée conformément à des normes spécifiques, à savoir *NF EN ISO 12572* ou encore *ISO 1663*.

2.4 Isotherme d'adsorption et de désorption

Un isotherme d'adsorption ou de désorption représente la variation de la teneur en eau du matériau en fonction de l'humidité relative de l'air ambiant à température constante. Nous parlons d'adsorption si le matériau est initialement sec (humidification) et désorption s'il est saturé (déshumidification). Les deux courbes présentent généralement des différences en raison de l'irréversibilité du processus, ce phénomène est l'hystérésis. Quant à la démarche expérimentale, les méthodes volumétrique et gravimétrique sont adoptées. Pour la méthode gravimétrique, deux types d'essais sont considérés. Le premier fait intervenir de l'air à l'état statique [30] alors que le deuxième considère un débit constant d'air. Dans le premier cas, une éprouvette préalablement séchée et pesée est exposée à une ambiance constante de température et d'humidité relative afin de mesurer sa variation de masse jusqu'à atteindre un état d'équilibre. Ce processus est répété en augmentant progressivement l'humidité relative (adsorption) ou en la diminuant (désorption).

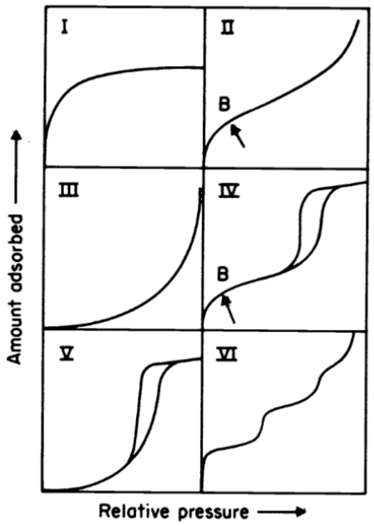

Figure 1.9 – La classification des isothermes d'adsorption [Sing et al. 1985]

A l'issue de ce processus, les courbes d'adsorption-désorption sont obtenues moyennant les données expérimentales de la teneur en eau du matériau en fonction de l'humidité relative extérieure. Pour réaliser cet essai, des solutions salines ou une enceinte climatique contrôlée en termes de température et d'humidité relative sont employés. La méthode gravimétrique suit la norme *NF EN ISO standard 12572*. Des dispositifs expérimentaux comme le DVS (dynamic vapor sorption) et le VSA (vapor sorption analyser) sont basés sur cette méthode avec un processus automatisé. L'essai dynamique consiste à exposer le matériau à un courant d'air constant en température et humidité relative. De même, l'équilibre est atteint quand la masse du matériau ne varie plus. Cet essai est plus rapide, ne dure que quelques heures mais demeure imprécis. Mis à part de l'approche gravimétrique, la méthode volumétrique vise à mesurer le volume de vapeur d'eau adsorbé ou restitué par l'échantillon. Ce dernier est positionné dans une ambiance contrôlée où une quantité de vapeur est injecté. L'évaluation du volume de vapeur passe par l'utilisation de la loi des gaz parfaits et le suivi de variation de pression de l'ambiance jusqu'à l'équilibre. Cette méthode requiert moins de temps d'essai en raison des faibles dimensions d'échantillons et des débits dynamiques de vapeur d'eau. Le BELSORP Aqua3 représente un dispositif qui évalue les phases adsorption-désorption en recourant à la méthode volumétrique.

2.5 Valeur tampon d'humidité (MBV)

La valeur tampon d'humidité (MBV) est un indicateur utilisé pour caractériser la capacité de régulation d'humidité des matériaux de construction. Elle est définie par la variation de la masse d'eau par rapport à une unité de surface et d'humidité relative. Son unité est

$\mathsf{g.m^{-2}.\%^{-1}}$. Le pouvoir tampon d'un matériau représente sa capacité à absorber ou à libérer l'humidité. Il renseigne sur le degré de modération du matériau vis-à-vis des variations d'humidité à l'intérieur d'un bâtiment. Un bon régulateur d'humidité absorbe l'excès d'humidité de l'air ambiant lorsque celui-ci est trop chargé, et libère cette humidité lorsque l'air est trop sec. Pour ce test, aucune norme n'existe encore, cependant le projet NORDTEST [31] propose un protocole d'essai normalisé et suggère la classification résumée dans le tableau 1.1.

TABLE 1.1 – Classes des valeurs tampons d'humidité

Classe MBV	Valeur minimale	Valeur maximale
Negligible	0	0.2
Limited	0.2	0.5
Moderate	0.5	1
Good	1	2
Excellent	2	–

Grâce à cette partie, les propriétés du transfert thermo-hydrique sont présentées. De plus, les méthodes de caractérisation les plus répandues ont été décrites en introduisant quelques dispositifs de mesure. Durant cette thèse, certains équipements seront employés pour l'évaluation des propriétés de transfert, notamment la conductivité thermique et la perméabilité à la vapeur. Les mesures effectuées seront dans le cadre d'une investigation expérimentale portant sur le vieillissement du béton de chanvre. Ce matériau est biosourcé et constituera notre choix d'application en raison de la sensibilité de sa microstructure vis-à-vis des sollicitations climatiques extérieurs. A ce propos, la prochaine partie définit ce type de matériaux. Également, leurs avantages sont discutés vis-à-vis du contexte actuel. Au final, les caractéristiques de ces matériaux sont mis en évidence via quelques résultats sur différentes sources végétales.

3 Les matériaux biosourcés

3.1 Définition

Un matériau de construction est dit biosourcé quand il intègre de la matière végétale ou animale. La matière végétale est d'origine biologique [32, 33]. Elle est issue en grande partie de ressources renouvelables et utilise principalement des dérivés d'agriculture. Contrairement aux matériaux traditionnels d'isolation (laine de verre, laine de roche ...), les matériaux biosourcés se caractérisent par un comportement hygroscopique, réunissant une perméabilité élevée à la vapeur d'eau et un bon indicateur MBV [34, 35].

3.2 Contexte actuel

Les matériaux biosourcés sont renouvelables, répandus sur la planète sous diverses formes, facilement accessibles, adaptés aux besoins d'utilisation, poreux et recyclables. Ces caractéristiques ont favorisé la croissance récente de la bio-économie, qui implique l'utilisation de ces matériaux [36]. A présent, les matériaux biosourcés sont employés dans nombreuses applications de construction, en tant qu'élément porteur, enduit ou isolant [37, 38]. Selon la formulation utilisée, la structure de ces matériaux peut varier [39, 40]. De plus, les fibres végétales peuvent être ajoutées à des liants et utilisées dans la construction de manière à garantir des caractéristiques particulières thermiques, hydriques ou structurelles. Le comportement du béton à base de fibres végétales est principalement gouverné par la quantité de fibres constituant le matériau. A cet égard, il a été démontré que l'augmentation de cette teneur augmente la porosité, le pouvoir tampon d'humidité et la teneur maximale en eau absorbée. En revanche, la densité, la conductivité thermique et la résistance à la compression sont réduites [41, 42]. Mis à part des propriétés thermiques et hydriques, Il est aussi important de garantir un environnement intérieur confortable. Les matériaux de construction affectent l'environnement intérieur [43]. En effet, les propriétés physiques des surfaces intérieures de parois contribuent en partie à la qualité de l'air intérieur. Par exemple, le bois absorbe et relâche l'humidité, modulant ainsi les variations quotidiennes d'humidité et de température.

3.3 Exemples de matériaux biosourcés

3.3.1 Bois

Le bois est utilisé comme matériau de construction à travers le monde depuis des milliers d'années. Les propriétés chimiques du bois sont complexes par nature, cependant, ses caractéristiques [44] sont exploitées pour construire une variété de structures. Les propriétés thermiques et hydriques du bois sont évalués à l'échelle macroscopique. À ce titre, les résultats de mesure de la conductivité thermique, la diffusivité de la vapeur et les isothermes de sorption sont présentés [45] pour trois types de matériaux à base de bois. Le premier est un panneau isolant en fibres de bois, dont la densité a été évaluée à $150\,\mathsf{kg.m^{-3}}$. En outre, deux panneaux d'épaisseur différente sont testés. Le deuxième matériau est constitué de panneaux de lamelles orientées (OSB). Ils sont composés de coupeaux de bois et assemblés avec la résine. Avec une densité de $600\,\mathsf{kg.m^{-3}}$, ce matériau a été également examiné selon deux épaisseurs différentes. Le troisième matériau est constitué du bois massif (NRW), ces propriétés sont déterminées suivant le plan longitudinal et tangentiel. La mesure des isothermes d'adsorption et de désorption confirment la forme des courbes liée au bois [46]. Les valeurs élevées de la teneur en eau mettent en évidence le caractère hygroscopique des matériaux à base de bois par rapport au béton [47].

En ce qui concerne la conductivité thermique, les valeurs obtenues représentent des moyennes sur 5 essais. À l'état sec, la fibre de bois présente la conductivité thermique la plus faible, soit environ $45\,\mathsf{mW.m^{-1}.K^{-1}}$, suivie du bois massif avec $80\,\mathsf{mW.m^{-1}.K^{-1}}$ et de l'OSB avec $95\,\mathsf{mW.m^{-1}.K^{-1}}$. D'après la littérature, ces valeurs sont bien inférieures à celles d'autres matériaux de construction tels que $0.5\,\mathsf{W.m^{-1}.K^{-1}}$ pour les briques et $1.75\,\mathsf{W.m^{-1}.K^{-1}}$ pour le béton [48]. Par ailleurs, la conductivité thermique augmente avec la température et la teneur en eau des matériaux étudiés. Une variation linéaire a été constatée en fonction de la température, contrairement à la variation en fonction de la teneur en eau. Enfin, l'étude expose les résultats relatifs aux valeurs de la résistance à la diffusion et l'épaisseur de la couche d'air équivalente. Parmi les matériaux étudiés, la fibre de bois est la plus perméable à la vapeur d'eau avec une valeur maximale de $8.3\,10^{-11}\,\mathsf{s}$. Par ailleurs, la perméabilité à la vapeur d'eau est plus élevée pour l'essai de la coupelle humide et est proportionnelle à la teneur en eau du matériau.

3.3.2 Paille

La paille est obtenue en plaçant la récolte dans un procédé qui élimine les grains et la balle. Sa structure consiste en des tubes résistants. La cellulose, la lignine et la silice confèrent à la paille une grande résistance à la flexion et à la traction. Les pailles de riz, d'orge et de blé (Figure 1.10a) sont souvent des restes de matériaux et peuvent donc être exploitées en tant qu'isolant pour produire différents matériaux. Ceci est dû à une structure interne creuse caractérisée par une faible densité et une bonne performance thermique [49, 50]. En outre, la transformation des olives engendre plusieurs coproduits. Il s'agit d'un mélange de particules ligneuses, de petites branches et de feuilles. Ces résidus sont abondants et renouvelables. Dans le cadre d'une investigation [51], les propriétés thermiques, hydriques et acoustiques de panneaux, à base de liant de silicate de sodium et contenant des fibres de paille et d'olive, ont été étudiées. Ainsi, la valeur de le porosité mesurée est de 0.9 et 0.85 respectivement pour les matériaux à base de paille et d'olives. Quant aux propriétés hydriques, le facteur de résistance à la diffusion de la vapeur d'eau a été mesuré. Les observations expérimentales ont révélé que le matériau à base de paille est plus perméable à la vapeur avec un coefficient de résistance de 2.59 contre 5.35 pour les composites de fibres d'olive. Les isothermes d'adsorption ont également été analysés. Selon les recommandations de l'IUPAC, "International Union of Pure and Applied Chemistry", ces formes sont regroupées suivant six catégories comme indiqué dans la figure 1.9 et celle du matériau correspond à l'isotherme de type 2. En outre, les valeurs expérimentales ont été ajustées en utilisant le modèle GAB [52]. En comparant les deux matériaux, la paille absorbe plus d'eau que les fibres d'olives, en particulier dans la zone capillaire.


(a) (b)

FIGURE 1.10 – Illustration des fibres de paille de blé (a) et des anas de chanvre (b).

Par ailleurs, les composites étudiés sont qualifiés d'excellents régulateurs d'humidité par rapport aux mesures du tampon d'humidité. Toutefois, le matériau à base de paille fournit une valeur plus élevée d'environ 5.05. Parallèlement, la performance thermique a été évaluée en effectuant des tests de conductivité thermique. Des valeurs similaires ont été obtenues pour les deux matériaux, avec une valeur légèrement inférieure pour la paille. Cela peut être lié à la valeur élevée de 0.9 de la porosité apparente de ce composite. Enfin, l'étude s'achève avec la détermination des propriétés acoustiques. Les mesures de résistivité acoustique ont donné les valeurs de 9.5 et 18 $\mathsf{kPa.s.m}^{-2}$ respectivement pour les matériaux à base de paille et d'olive. D'autres caractéristiques ont montré que ces matériaux pourraient servir, en particulier pour des couches plus épaisses, à remplacer avantageusement les matériaux d'absorption acoustiques traditionnels.

3.3.3 Chanvre

Le chanvre a une longue histoire en tant que plante et une variété utilisée dans un nombre d'industries. L'utilisation du chanvre comme matériau de construction a été progressivement étendue de l'Europe vers d'autres continents. En outre, l'application de ce matériau naturel ne cesse d'augmenter dans les nouvelles constructions. De nombreuses études ont porté sur l'utilisation de la chènevotte (Figure 1.10b) dans la production de composites, principalement le béton de chanvre [53, 54]. Outre l'utilisation de la chaux, d'autres produits pourraient être une alternative de liant. A ce propos, [55] se concentre sur le développement de composites bio-sourcés résistants à l'eau avec des performances hydriques et thermiques améliorées pour des applications de construction. Les composites ont été élaborés à partir d'une matrice à base d'amidon ou de silice, tandis que des anas de chanvre ont été utilisés comme agrégats. Trois types de composites ont été obtenus. Le premier utilise un procédé assez simple impliquant le mélange d'anas de chanvre avec un liant à base de silice. Les composites C_2 et C_3 utilisent un liant à base d'amidon qui durci à l'aide d'une presse thermique. En revanche, un traitement hydrophobe a été appliqué à la chènevotte dans le deuxième composite. Premièrement, la perméabilité à la vapeur a été obtenue pour les méthodes de la coupelle humide et sèche en utilisant une solution saline et des billes de silice. Les résultats ont révélé que les composites C_1 et C_2 étaient les plus perméables au cours des tests de coupelle sèche et humide, respectivement. Par ailleurs, les variations d'humidité dans les espaces intérieurs d'un bâtiment sont en partie dues à la capacité des matériaux à stocker ou restituer l'humidité. À cet égard, cette caractéristique a été mesurée en confrontant les composites aux paliers d'humidité relative 33 % et 75 %, comme le propose le projet NORDTEST. Selon la classification relative aux valeurs des tampons hydriques, les matériaux ont montré une excellente capacité, étant donné que les valeurs obtenues sont supérieures à 2.

En outre, l'absorption d'eau a été évaluée d'après la norme EN 1609-2013. Le composite C_2, ayant subi un traitement hydrophobe, représentait le matériau le moins absorbant. Les propriétés thermiques ont également été analysées à l'aide d'un système de mesure dynamique (fluxmétrique). La valeur de la conductivité thermique est comprise entre 0.051 et 0.058 $\mathsf{W.m^{-1}.K^{-1}}$ tandis que la capacité thermique spécifique entre 760 et 1050 $\mathsf{J.kg^{-1}.K^{-1}}$. Enfin, le comportement mécanique des composites a été analysé à l'aide d'expériences de résistance à la compression. En général, les matériaux ont de bonnes performances mécaniques. Ils ont atteint une contrainte de compression comprise entre 0.49 et 1.05 MPa. La rupture n'a pas été atteinte même à 60 % de déformation. Ceci pourrait être lié à une bonne adhérence entre les agrégats et les liants.

4 Vieillissement

D'après la section précédente, les matériaux biosourcés présentent des avantages qui se résument à une bonne isolation thermique, une excellente régulation d'humidité et un faible impact environnemental. Cependant, ils sont fortement sensibles aux variations de température et d'humidité. Ceci entraîne l'évolution de la microstructure du matériau biosourcé. Connu sous le terme de vieillissement, ce phénomène se traduit par la variation des différentes propriétés, notamment celles liée au transfert de chaleur et d'humidité. Dans un premier lieu, cette section résume les différents types du vieillissement qui sont fréquemment abordés dans la littérature. Ensuite, nous repérons les principaux protocoles expérimentaux qui sont développés pour étudier ce phénomène. Pour différents matériaux, les résultats rapportés montrent que les effets du vieillissement sont notables et spécifiques au type d'essai proposé. L'impact de chaque protocole de vieillissement est mis en évidence en illustrant l'évolution des propriétés du matériau. Entre autres, nous nous intéressons à la variation des propriétés du transfert de chaleur et d'humidité due au vieillissement thermo-hydrique.

4.1 Définition

Le vieillissement est un phénomène de détérioration qui se produit naturellement au fil du temps. En biologie, le vieillissement est défini par les changements physiologiques progressifs d'un organisme qui conduisent au recul des fonctions biologiques et de la capacité d'adaptation au stress métabolique. Dans le domaine de la construction, le vieillissement d'un matériau se traduit par l'évolution des propriétés intrinsèques en fonction du temps. Ces changements peuvent engendrer des fissures, création de nouveaux pores, le gonflement et le rétrécissement des pores existants. Le vieillissement est induit par une longue exposition d'un matériau à des sollicitations climatiques. Au laboratoire, des essais accélérés sont effectués pour mesurer l'évolution de la microstructure et les propriétés intrinsèques des matériaux sous des conditions climatiques extrêmes. Ces essais consistent en des cycles successifs de sollicitations thermiques et hydriques. La température et les radiations ultraviolets sont adoptés pour modéliser les sollicitations thermiques induisant un séchage des matériaux. Pour les sollicitations hydriques, des cycles d'humidification et d'imbibition sont considérés. La littérature fait état de différents types de vieillissement.

Premièrement, nous distinguons l'effet du rayonnement. Dans ce cadre, les tests les plus courants étudient le processus de vieillissement des matériaux lors de leur exposition aux radiations ultraviolets en quantités contrôlées. Ces essais sont également réalisés pour évaluer les effets des rayonnements ionisants tels que les rayons X et gamma. Un vieillissement peut être entraîné par des variations de température. Cela consiste à placer les matériaux dans des chambres climatiques pour des températures constantes ou variables. S'ensuit les essais d'humidité qui mesurent l'action corrosive de l'eau en tenant compte de facteurs pertinents tels que l'humidité relative de l'air et sa salinité. Plus loin, des gaz polluants peuvent être à l'origine du vieillissement d'un matériau. Il existe des essais qui analysent l'effet des gaz présents dans l'environnement, y compris ceux générés par la pollution dans les villes. Nous distinguons l'ozone, le dichlore et d'autres gaz corrosifs tels que le sulfure d'hydrogène, le dioxyde de soufre ou le dioxyde d'azote. Finalement, la présence des ions corrosifs dans les milieux marins peut infliger des dégâts. Pour investiguer ces détériorations, les essais consistent à placer les échantillons dans une solution chargée d'ions agressifs. Ils sont responsables de la corrosion des matériaux incorporant des armatures ferreuses.

D'après la littérature, l'étude du vieillissement, moyennant ces essais accélérés, révèle le degré de résistance d'un matériau. Ainsi, ceci peut contribuer à la prédiction de ses indicateurs de durabilité et ses performances énergétiques dans le temps. La section suivante sera dédiée à un état de l'art du vieillissement. Elle met en évidence l'effet de certains essais sur des matériaux de construction. L'analyse des travaux précédents montre que le vieillissement est considérablement investigué en considérant les essais suivants. Les premiers consistent en des variations de température, les deuxièmes reposent sur l'utilisation des gaz polluants et les derniers combinent des sollicitations de chaleur (température et/ou rayonnement ultraviolet) et d'humidité (eau sous la forme vapeur et/ou liquide). Ce choix est justifié par rapport à la grande quantité des travaux qui s'intéressent à l'étude de ces types de vieillissement.

4.2 Effets de la variation de température

Des changements microscopiques peuvent se produire dans les matériaux lorsque ces derniers sont exposés à des cycles de variation de température [56]. L'intensité du cycle et le temps d'exposition peuvent affecter la vitesse d'évolution de la microstructure. Dans ce sens, les matériaux se dégradent lorsqu'ils sont exposés à des températures élevées pendant une longue période. La littérature fait état de l'existence de différents cycles thermiques. Ces derniers diffèrent en termes d'intensité et de durée. Dans cette optique, les résultats de deux travaux de recherche sont proposés. D'après [57], les auteurs déterminent l'effet du vieillissement, tel que défini dans la norme européenne EN 14066, sur quatre types de granites de construction. Le protocole de vieillissement consiste en 42 cycles thermiques où les températures appliquées varient entre 20 et 105 °C. Un cycle consiste à exposer des échantillons à 105 °C pendant 18 h et ensuite les refroidir à 20 °C pendant 6 h. L'effet des cycles est mis en évidence sur les propriétés physiques et celles liées à la surface des pierres de construction sélectionnées. Les observations ont révélé que la densité apparente et la porosité sont affectées. Cependant, les variations de densité sont négligeables. Quant à la porosité, les valeurs initiales se situaient entre 0.71 % et 1.72 %. Cette quantité a peu varié pour chaque matériau, à l'exception du CO dont la porosité est passée de 0.71 % à 4.2 %. Par ailleurs, la vitesse de propagation des ultrasons a été mesurée pour les trois directions de l'espace. A cet égard, les valeurs moyennes sont retenues pour la comparaison. L'exposition aux cycles de température induisait une baisse de vitesse dans les quatre matériaux. Ceci est la conséquence de l'augmentation de porosité. En outre, la résistance mécanique a été mesurée à travers le module dynamique de Young. Elle diminue après 42 cycles avec un écart maximum de 13 %. À l'échelle microscopique, la distribution du diamètre des pores a été analysée en effectuant des tests de porosimétrie par intrusion de mercure. Les cycles accélérés n'affectent pas seulement la porosité, la microstructure est également modifiée. Enfin, des micro-fissures sont créées suite à la variation de température. Ceux-ci contribuent en partie à l'augmentation de la porosité ouverte des matériaux. La densité des fissures linéaires a été étudiée au moyen d'une fractographie. Les échantillons ZA ont marqué la fin de l'essai avec le plus grand nombre de microfissures où la valeur de densité linéaire des fissures a atteint 2.5.

Par ailleurs, l'effet du vieillissement thermique sur le béton à haute performance (HPC) a été évalué en analysant les propriétés mécaniques et l'absorption capillaire de l'eau tout en tenant compte des changements micro-structuraux [58]. Dans la formulation, un sable de rivière est utilisé comme agrégat fin et deux agrégats grossiers différents sont considérés avec les propriétés de mélange 40 % et 60 %. Ainsi, deux types de béton, désignés HPC40 et HPC60, ont été obtenus. Après la période de durcissement, les échantillons ont subi une série de cycles thermiques. A cet égard, ils sont laissés à la même température pendant 5 heures, puis refroidis dans une chambre climatique pendant 1 heure afin d'atteindre 20 °C. Ce cycle est répété 135 fois. Des mesures de la résistance à la compression, la résistance à la traction et le module d'élasticité ont été effectuées. Une diminution globale des propriétés mécaniques est constatée. Ceci peut être lié à la fragilisation de la microstructure suite aux chocs thermiques. En outre, l'influence des cycles thermiques sur le transport d'eau au sein des matériaux est caractérisée via des expériences d'absorption capillaire [59]. Une augmentation de teneur en eau commence après 480 min d'immersion et est plus significative en fonction du nombre des cycles thermiques. En outre, la variation de la teneur en eau du HPC60 est pratiquement deux fois plus grande que celle du HPC40. D'après les résultats, le comportement mécanique et hydrique du béton HPC60 change majoritairement, et est la conséquence d'une détérioration plus aiguë. Ce résultat est confirmé suite à la comparaison des observations microscopiques des deux types de béton. La longueur, la largeur et la quantité de microfissures dans le HPC60 sont plus marquantes. L'existence des fissures induit une diminution plus importante de la résistance mécanique. Ceci améliorent également la cinétique d'absorption et augmentent la quantité d'eau absorbée. La rigidité supérieure du béton HPC60 induit une dégradation plus significative face aux sollicitations thermiques imposées.

4.3 Gaz polluants

Les principaux polluants qui altèrent les matériaux sont le dioxyde de soufre, les sulfates, les oxydes d'azote, les nitrates, les chlorures, le dioxyde de carbone et l'ozone. Les matériaux les plus sensibles aux polluants sont les matériaux de construction calciques et les autres armés. Les dégradations comprennent une perte de masse, une modification de la porosité, une décoloration, une fragilisation et une variation des propriétés optiques de la surface. En cas d'atmosphères pollués, les dégâts subis par les matériaux peuvent être associés à des dépôts secs ou humides de contaminants, ou à des dissolutions lors des précipitations. Parmi les matériaux endommagés, nous retrouvons la pierre, le béton et le bois. Un nombre important de contributions portent sur les mécanismes d'attaque des pierres par des polluants [60, 61]. Concernant le béton, il a été confirmé, selon [62], que le dioxyde de carbone est le principal gaz atmosphérique responsable de l'endommagement du béton. De plus, un léger effet est attribué au dioxyde de soufre et aux oxydes d'azote. Néanmoins, les auteurs de l'étude [63] ont suggéré que de fortes concentrations de dioxyde de soufre, d'oxydes d'azote et de chlorure d'hydrogène pourraient accélérer les dégâts. Étant donné que les concentrations atmosphériques de CO_2 sont beaucoup plus élevées que celles de SO_2, la carbonatation est la principale forme de détérioration du béton. Hormis la dégradation biologique, les principaux facteurs du déclin atmosphérique du bois sont les rayons ultraviolets, l'humidité et l'ozone. L'acidité peut conduire au phénomène d'hydrolyse du constituant cellulosique ou à des augmentations mineures des taux d'altération. Par ailleurs, le dioxyde de soufre et les oxydes d'azote peuvent entraîner l'oxydation et la rupture de la structure de la cellulose [64]. Cela qui peut entraîner une perte de performances mécaniques.

Afin de mettre en évidence les effets des gaz polluants, nous exposons les résultats d'une étude récente [65]. Elle examine la dégradation due au climat acide des pierres de construction naturelles et artificielles. L'objectif est l'évaluation des effets de composés azotés et soufrés sur quatre pierres différents. Les deux premières, la pierre de Courville (Cv) et celle Bajocienne (Bj), sont fortement employées dans la construction et ont été extraites à l'état frais pour cette étude. Les deux dernières, la pierre de Savonnières (Sv) et la pierre reconstituée (Rs), sont dédiées aux bâtiments patrimoniaux et utilisées pour la réhabilitation. Ces quatre types de pierre ont été soumises à deux conditions climatiques différentes. Dans chaque cas, les échantillons sont exposés aux gaz produits par une solution acide et volatile mélangée. Une première solution chimique, notée (S>N), assure un rapport gazeux SO_2/NO_x de 4, tandis que la seconde (S<N),

garantit un rapport gazeux de 1/3. Ces quantités ont été fixées sur la base de mesures climatiques. Les valeurs 4 et 1/3 font référence respectivement au ratios SO_2/NO_x entre le passé et le présent. En outre, ces tests ont été réalisé pendant 28 jours. Pour évaluer l'effet du vieillissement, des mesures de masse, de porosité ouverte et de distribution de taille de pores ont été effectuées. Après l'essai, la masse augmente dans les deux cas. En particulier, le gain a été plus important pendant le premier test avec entre 0.6 et 1.2 % d'augmentation. Dans le deuxième cas, la masse augmente moins nettement avec 0.4 % représentant la valeur la plus élevée. Cette augmentation est due à la précipitation du gypse. Étant un produit d'une réaction comportant le sulfure, la présence de plus de gypse dans le premier cas est logique. Ensuite, il a été noté que la porosité ouverte varie davantage pendant le deuxième test. L'augmentation absolue la plus élevée était 5 %, tandis que la diminution la plus forte 1.5 %. De plus, la distribution de taille des pores est évaluée en fonction du matériau et de la solution utilisée. Les différences sont plus remarquables pour (Bj) et (Sv). Pour ces pierres, un comportement similaire est observé pour des rayons de pores inférieurs à 1 µm et le contraire pour d'autres intervalles de rayons. Au final, les dépôts gazeux peuvent affecter considérablement les matériaux de construction. En addition, le rapport SO_4^{2-}/NO_x des solutions chimiques est un facteur déterminant des altérations lors d'essais de vieillissement. Une quantité plus élevée de sulfures induit une dégradation plus sévère.

4.4 Vieillissement thermique et hydrique des matériaux biosourcés

Durant l'exposition à une alternance de sollicitations d'humidité (humidification ou imbibition) et de chaleur (température ou radiation ultraviolet), les matériaux biosourcés peuvent subir des changements conséquents. Plusieurs causes peuvent être à l'origine de cette évolution. En considérant un climat chaud, les hautes températures peuvent générer des microfissures. Ces dernières apparaissent suite à la fragilisation de la liaison qui associe le liant aux particules végétales. Un deuxième facteur serait l'augmentation de porosité. En effet, des pores supplémentaires se créent sous l'effet d'humidité [66]. Aussi, la coalescence des pores voisins peut être à l'origine d'une augmentation de porosité. La présence d'eau peut également induire le gonflement des particules végétales [67]. Ceci peut affecter la microstructure du matériau biosourcé. Par ailleurs, une haute température favorise le rétrécissement des particules végétales. Le retrait d'eau, initialement présent dans ces fibres, en est la cause. Tout ces phénomènes sont à l'origine de l'évolution de la microstructure. Dans la littérature, nous retrouvons des travaux qui montrent l'effet du vieillissement en s'appuyant sur des mesures de propriétés ou des observations. Pour cela, des essais de vieillissement sont proposés. Ils réunissent à la fois des cycles de variation de température et d'humidité. Certains sont moins agressifs que d'autres. Néanmoins, ces tests sont tous accélérés (quelques jours ou semaines). Dans cette partie, nous exposons quelques résultats montrant l'effet du vieillissement hydrique et thermique sur des matériaux biosourcés.

D'après [68], l'objectif est d'évaluer la durabilité des composites de polyéthylène à base de fibres naturelles. Ce matériau peut être destiné à des applications de toiture extérieure moyennant le recours à des protocoles de vieillissement accéléré. A cet effet, des échantillons ont été testés en mesurant les changements dans les propriétés de flexion dus à l'altération accélérée dans le temps. En termes de matériaux, quatre ont été formulés à base de polyéthylène, dont deux à base de fibres naturelles. Le premier contient 50 % de fibres de bois et le second 50 %

de fibres de Kénaf. L'essai de vieillissement consiste à exposer une face d'un échantillon à 102 minutes des rayons UV, suivies de 18 minutes de pulvérisation à l'eau. Pendant ce temps, les deux faces sont soumises à des niveaux élevés d'humidité. La durée totale du protocole est fixée à 4000 h. Sur la base de prélèvements effectués toutes les 500 h, les modules d'élasticité et de rupture ont été déterminés avant et pendant les cycles climatiques. Les résultats ont montré que le module de flexion du polyéthylène à base de fibres naturelles diminuait après 4000 h d'exposition. La perte d'élasticité la plus importante a été enregistrée pour les composites à base de Kénaf avec une diminution relative de 62 %. Pour les composites à base de bois, la valeur finale ne représentait que 45 % de la valeur initiale. Quant à la résistance à la flexion, elle a également baissé au cours des cycles. Ces pertes sont liées notamment à la dépolymérisation de la lignine et de l'hémicellulose sous l'effet des rayons UV et de la présence d'eau liquide. Dans ce cas, les contraintes appliquées ne pourront être transmises correctement entre la matrice solide et la matière végétale. En outre, la profondeur de la dégradation a été estimée visuellement à l'aide d'un microscope afin de quantifier le degré de détérioration des surfaces exposées. Il a été constaté qu'elle augmente progressivement. Les valeurs moyennes de 0.5 et 0.4 mm sont atteintes respectivement pour les composites à base de Kénaf et de bois. Malgré les changements du comportement mécanique de ces composites, ce type de matériaux restent généralement plus performants que ceux sans additions végétales [69, 70].

Par ailleurs, l'évolution des propriétés de deux bétons de chanvre a été étudiée sur 2 ans de contraintes climatiques d'après [71]. Le premier matériau est à base de chaux, que nous désignons par FL-HC. Le second est fabriqué à partir d'un ciment naturel noté NC-HC. Ils ont été soumis à deux essais climatiques différents. Le premier lot d'échantillons a été stocké dans un environnement statique dans une pièce climatisée à 20 °C et 50 % d'humidité relative. Ce premier test sert de référence. Le deuxième lot d'échantillons a été soumis à des cycles d'humidification et de séchage où la température est maintenue à 30 °C. Dans ce protocole expérimental, un cycle dure une semaine, avec 5 jours à 98 % d'humidité relative suivis de 2 jours à 40 %. Par ailleurs, la variation de la conductivité thermique, la résistance à la compression, la porosité et la tortuosité ont été évaluées. Les résultats ont montré que le test de référence de deux ans n'a pas d'effets significatifs sur les propriétés des matériaux. Quant à la conductivité thermique, sa variation a été mesurée pour les deux essais et les deux matériaux. Une augmentation relative de 19 % a été observée pour le FL-HC et de 7 % pour les échantillons à base de ciment. Ces changements se sont accentués respectivement après 6 et 18 mois pour le FL-HC et le NC-HC. Quant à l'isotherme d'adsorption, la capacité d'adsorption d'eau a augmenté après 18 mois d'essai lorsque l'humidité relative dépasse 20 %. Dans ce cas, le vieillissement a augmenté la capacité du béton de chanvre à absorber la vapeur d'eau. Pour ce qui est du comportement mécanique, son évolution a été déterminée grâce à des mesures de la résistance à la compression. Au vu des valeurs obtenues et de leurs dispersions, le béton de chanvre demeure inerte face aux cycles d'humidification et de séchage. Pour décrire la microstructure, l'étude a examiné en outre la porosité et la tortuosité au moyen de mesures acoustiques. Les résultats ont révélé que la porosité n'est pas affectée pour les échantillons stockés à des conditions climatiques normales et statiques. Au contraire, la hausse de la porosité après 2 ans de cycles d'humidification et de séchage est comprise entre 0.03 et 0.04. En ce qui concerne la tortuosité, la variation a été aléatoire pour FL-HC. Pour le second matériau, la tortuosité a augmenté tout au long des cycles. D'après l'étude, la variation des propriétés est liée à l'altération des propriétés chimiques dont l'hydratation, la carbonatation et l'attaque des fibres végétales par les micro-organismes.

Également, le gonflement et le rétrécissement des fibres en font une cause également.

Une autre étude [72] aborde le vieillissement accéléré et ses effets sur les propriétés du béton de chanvre. Le vieillissement consistait en une succession de cycles d'immersion dans l'eau et de séchage. Les échantillons de béton de chanvre sont composés de chaux et d'anas de chanvre. Quant au protocole accéléré, il a été réalisé au laboratoire en soumettant les échantillons à 48 h d'immersion totale dans l'eau, puis un séchage de 72 h à 50 °C. Ceci a donné lieu à un cycle qui a été répété sur une période de 40 jours. Bien que le test proposé semble plus agressif que les conditions extérieures normales, celui-ci renseigne sur le comportement de ce matériau à l'état dégradé. Pour la comparaison, des échantillons de référence ont été conservés dans une chambre climatique sous des conditions atmosphériques normales. Il est essentiel d'assurer les mêmes états hydriques et thermiques entre les échantillons frais et les échantillons vieillis [73]. Une caractérisation est réalisée sur les propriétés suivantes : porosité, conductivité thermique, perméabilité à la vapeur d'eau, capacité tampon d'humidité, résistance à la compression et le pH. De plus, l'évolution de la microstructure est donnée à travers des observations au microscope avant et après l'essai. Des fissures se sont créées à l'interface liant-anas après 40 jours. Ceci peut être lié à la sensibilité des anas à l'humidité. Dans ce cas, des mécanismes de gonflement et de rétrécissement se produisent suite à la variation de la teneur en eau liquide. De plus, la fragilisation des liaisons liant/anas est due à la température élevée pendant les périodes de séchage.

Par ailleurs, l'évolution de la microstructure a été quantifiée en étudiant la porosité. Cette dernière a augmenté de 71.51 % à 73.4 % ce qui est en accord avec la microstructure observée. Les résultats de porosité peuvent constituer la base justifiant la variation des autres propriétés. Concernant la conductivité thermique, la valeur de 100.94 $\mathrm{mW.m^{-1}.K^{-1}}$ a été mesurée à l'état de référence, pour ensuite diminuer à 94.25 $\mathrm{mW.m^{-1}.K^{-1}}$. En effet, la création de pores supplémentaires entraîne plus de présence d'air à l'intérieur du matériau. Or, l'air étant l'élément le plus isolant, il baisse la valeur de la conductivité thermique du matériau. Aussi, le vieillissement des anas de chanvre a induit une dégradation de la capacité de fixation et de restitution d'humidité. À ce propos, la valeur tampon d'humidité a légèrement diminué. Néanmoins, les deux valeurs obtenues montrent que le béton de chanvre assure une excellente régulation hydrique, même à l'état altéré. Parallèlement, la perméabilité à la vapeur d'eau a subi une augmentation sous l'effet des cycles de vieillissement. Sa valeur est passée de 2.85×10^{-11} à 3.94×10^{-11} s. Ce résultat est également lié à la variation de porosité. Quant au comportement mécanique du béton de chanvre, il a considérablement diminué en raison de la fragilisation de la structure et de la présence de fissures. La résistance à la compression passe, en effet, de 0.94 à 0.46 MPa. Contrairement à cette dégradation, d'autres recherches [74, 75] ont montré que le béton de chanvre est plus durable vis-à-vis des protocoles de séchage et d'humidification à la vapeur d'eau. Enfin, les cycles d'immersion-séchage n'affectent pas le pH du béton de chanvre. Ses valeurs sont restées aux alentours de 11, ce qui ne favorise pas la croissance fongique.

Les propriétés d'un matériau à l'état sain et après vieillissement peuvent être exploitées pour prédire son comportement thermique et hydrique en tenant compte de ces deux configurations. D'après les propos de cette recherche [76], l'effet du vieillissement a été investigué sur le béton de chanvre à différentes échelles. En particulier, l'étude a mis en évidence l'effet de la prise en compte du vieillissement sur le comportement du matériau à l'échelle de la paroi. Les cycles de vieillissement ont été plus sévères en ajoutant un jour de gel à −18 °C entre l'immersion et le séchage. Pour la prédiction, un modèle de transfert de chaleur et d'humidité a été utilisé. En addition, des mesures de la densité apparente, la conductivité thermique, la chaleur spécifique et la perméabilité à la vapeur d'eau ont été réalisées avant et après l'essai.

TABLE 1.2 – Les propriétés à l'état de référence et après vieillissement du béton de chanvre [76].

Propriété	Référence	Vieilli
$\rho_s\,[\mathsf{kg.m^{-3}}]$	484.46	480.27
$\lambda\,[\mathsf{mW.m^{-1}.K^{-1}}]$	100.73	89.42
$C_p\,[\mathsf{J.kg^{-1}.K^{-1}}]$	872.34	902.6
$\delta_p\,[\mathsf{s}]$	2.85×10^{-11}	3.95×10^{-11}

Le Tableau 1.2 rapporte les valeurs obtenues. D'après les prédictions numériques, le vieillissement impacte le comportement hygrothermique du béton de chanvre à l'échelle du matériau et de la paroi. Les écarts ont atteint un maximum absolu de 18 % en termes d'humidité relative et 1 °C de température. En outre, les flux thermiques intérieurs, y compris les charges sensibles et latentes, ainsi que le flux de conduction ont été évalués. Les résultats ont mis en évidence des valeurs plus faibles du flux sensible en comparant le comportement du matériau vieilli à celui du matériau neuf. L'opposé a été constaté en considérant le flux latent. Ces résultats sont cohérents avec les mesures de la conductivité thermique et la perméabilité à la vapeur. Globalement, la charge de conduction est plus petite pour le cas du matériau vieilli, entraînant ainsi une amélioration de l'efficacité thermique. Compte tenu de l'agressivité de l'essai proposé, il convient de noter que ce dernier ne reflète que le cas de dégradation extrême après plusieurs années d'utilisation dans des climats durs.

4.5 Synthèse et problématique

L'analyse bibliographique des investigations du vieillissement a révélé la considération d'approches expérimentales pour aborder ce phénomène. Cette approche est indépendante du type de vieillissement étudié. Pour le vieillissement thermique et hydrique, les travaux cités proposent des protocoles expérimentaux accélérés pour évaluer l'impact de ce phénomène. Le Tableau 1.3 résume ces essais dans le cas des matériaux biosourcés. La description de tels essais montre qu'ils se basent sur des conditions extérieurs extrêmes. Ces dernières ne représentent le climat que dans les cas les plus défavorables. Ainsi, cela justifie l'aspect agressif des protocoles développés. En outre, aucun travail n'établit un lien entre ces essais accélérés et un cas d'étude réel. Une configuration réelle, qui serait représentative du protocole expérimental, reste inconnue. Pour ces raisons, notre travail de recherche propose une solution pour lever ces verrous scientifiques. Grâce au développement d'une méthodologie, nous proposons un protocole expérimental représentatif d'un phénomène de vieillissement long et naturel. En raison de la longue durée du protocole, une maquette réduite est générée en laboratoire. Cette maquette expérimentale est équivalente au protocole développé et est obtenue grâce à l'application des lois de similitude.

Table 1.3 – Récapitulatif des essais de vieillissement menés sur des matériaux de construction.

Vieillissement	Référence	Matériau	Durée de l'essai	Sollicitations	Cycles
variations de température	[56]	Polymère renforcé de fibres de verre	25 jours	refroidissement chauffage	20 min à $-10\,°C$ 20 min à $20\,°C$
variations de température	[57]	roche de granite	42 jours	chauffage refroidissement	18 h à $105\,°C$ 6 h à $20\,°C$
variations de température	[58]	béton à haute performance	34 jours	chauffage refroidissement	5 h à $65\,°C$ 1 h à $20\,°C$
polluants	[65]	pierre de calcaire	28 jours 32 jours	pulvérisation pulvérisation	SO_2/NO_x $H_2SO_4 + HNO_3$
thermique hydrique	[68]	fiber-filled polyethylene	4000 h	séchage imbibition	102 min rayons UV 18 min
thermique hydrique	[71]	hemp concrete	2 ans	humidification séchage	5 j à 98 % HR et $30\,°C$ 2 j à 40 % HR et $30\,°C$
thermique hydrique	[72]	hemp concrete	40 jours	imbibition séchage	2 jours 3 j à $50\,°C$
thermique hydrique	[74]	hemp concrete	20 jours 5 jours	séchage imbibition séchage gel	3 h à 30 % HR et $70\,°C$ 1 h à $20\,°C$ 8 h à 30 % HR et $50\,°C$ 16 h à $-20\,°C$
thermique hydrique	[75]	hemp concrete	75 jours	humidification séchage	4 j à 90 % HR et $30\,°C$ 4 j à 40 % HR et $30\,°C$
thermique hydrique	[76]	hemp concrete	42 jours	imbibition gel séchage	2 j 1 j à $-18\,°C$ 3 j à $50\,°C$

5 Les lois de similitude

Les lois de similitude servent à définir des équivalences entre des configurations physiques ayant des échelles caractéristiques différentes. Les similitudes sont fondées sur des invariances caractérisées par des nombres caractéristiques sans dimension. En l'occurrence, des systèmes physiques, avec des échelles spatiales et temporelles différentes, peuvent être jugés similaires. Nous verrons que ces lois sont utilisables, notamment, pour réduire la durée des longs phénomènes physiques. Dans ce qui suit, une définition des lois de similitude est donnée. Ensuite, nous testons la fiabilité de leur application expérimentale dans différents domaines. Une analyse exhaustive des résultats est proposée.

5.1 Définition

La théorie des similitudes repose sur des lois qui peuvent garantir des équivalences entre des systèmes physiques, présentant des échelles caractéristiques différentes. Ces dernières peuvent changer d'une configuration à une autre tout en veillant à assurer les mêmes invariances. En se donnant un phénomène physique, la définition des similitudes est basée sur la formulation adimensionnelle des équations qui définissent ce phénomène. En fixant une grandeur caractéristique pour chaque variable, le système est transformé du domaine physique au domaine adimensionnel. Ceci simplifie le problème en réduisant le nombre de ses paramètres comme le démontre le théorème de *Buckingham* [77]. D'après ce dernier, la formulation obtenue fait intervenir des nombres sans dimension qui sont exprimés via les grandeurs caractéristiques définies. Des nombres comme *Reynolds* [78], *Peclet*, *Fourier* et *Biot* en font partie. Dans cette perspective, une similitude est assurée si ces nombres demeurent invariants en passant d'une configuration à une autre.

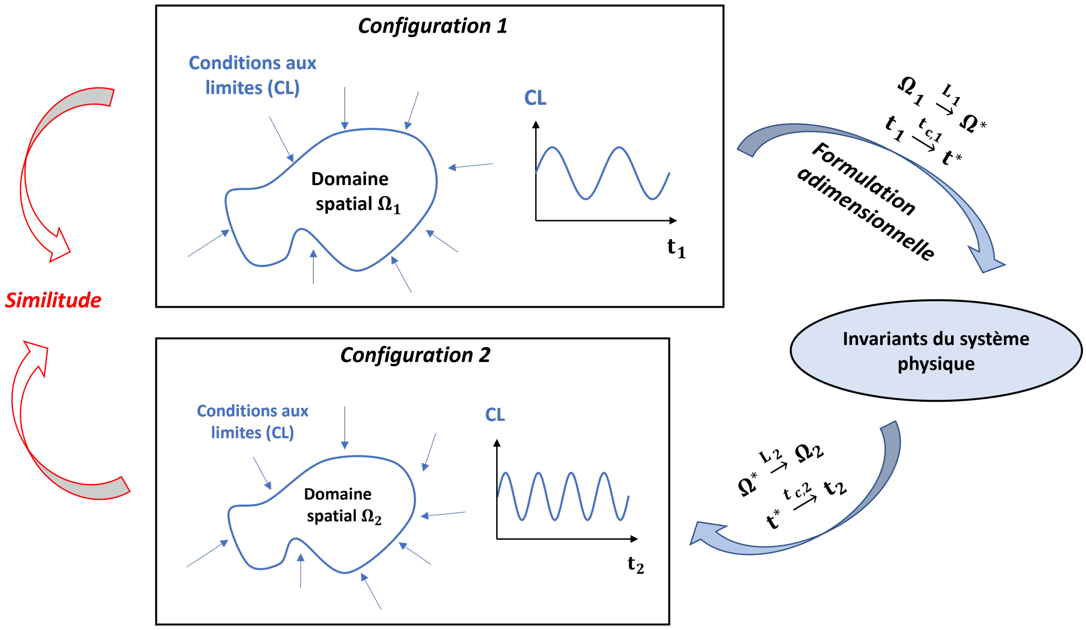

FIGURE 1.11 – Principe des lois de similitude.

La Figure 1.11 décrit le principe des similitudes entre deux configurations 1 et 2. Initialement, la configuration 1 est bien définie à travers un domaine d'étude spatial Ω_1 et une durée d'expérience t_1. Ensuite, la formulation adimensionnelle du domaine physique requiert la définition des échelles caractéristiques de la configuration 1, notamment une longueur L_1 et une durée $t_{c,1}$. La migration vers la domaine adimensionnel permet d'obtenir les nombres sans dimension liés au phénomène étudié. Sur cette base, une configuration 2 équivalente est obtenue. Les échelles caractéristiques liées à cette dernière, dont L_2 et $t_{c,2}$, doivent vérifier les lois des invariants. D'après certaines études, les lois de similitudes peuvent réduire la complexité des phénomènes physiques en proposant des modèles simplifiés. Ces derniers sont généralement plus faciles à aborder et peuvent prédire, avec une précision acceptable, les résultats de la configuration de référence.

5.2 Applications

Selon le but d'application, les lois de similitudes peuvent être utilisés de trois manières différentes. Il s'agit des similitudes cinétiques, géométriques et dynamiques. Grâce au premier type, nous visons à établir une équivalence entre des configurations en fixant la durée du phénomène étudié. Ces configurations se distinguent par l'échelle spatiale ou le type du matériau utilisé. Les similitudes sont dites géométriques si les configurations équivalentes définissent des échelles spatiales identiques. Dans ce cas, ces lois visent à établir les durées équivalentes en considérant des matériaux différents. Dans le troisième cas, seul le matériau est le même entre les configurations. Principalement, les similitudes dynamiques sont appliqués pour réduire la durée des longs phénomènes physiques. Dans le reste de cette partie, les études appliquant ces lois sont présentées en identifiant le type de similitude utilisé.

5.2.1 La vibration des structures

La vibration des structures est un champ qui s'intéresse à la réponse vibratoire des structures face aux chargements mécaniques. Dans ce cadre, les lois de similitude ont été déduits et leur précision a été évalué [79, 80]. Un exemple [81] établit les lois de similitude cinétiques vis-à-vis de la réponse vibratoire des plaques minces rectangulaires. Au préalable, Ces lois ont été vérifiées grâce à des simulations numériques et s'avèrent exactes pour des couples de modèles et de prototypes, qui respectent les invariants de similitude. Dans ce cas, un modèle en aluminium a été comparé à un prototype en acier inoxydable. Pour six ratios longueur/largeur différents, deux approches ont été menées afin d'évaluer les fréquences propres d'un prototype en acier inoxydable. La première consiste à calculer théoriquement cette quantité à l'aide des équations régissant la vibration des plaques minces rectangulaires isotropes. La seconde approche s'appuie sur la fréquence théorique du modèle en aluminium et sur les lois de similitude pour déduire la fréquence du prototype en acier. Les résultats ont révélé que ces lois sont applicables à un couple de modèles et de prototypes ayant le même rapport longueur/largeur en dépit de l'utilisation de matériaux différents. Afin de confirmer la justesse de ces lois pour une application réelle, des expériences de vibration ont été réalisées sur plusieurs échantillons afin de déterminer leurs trois premières fréquences propres. Ces échantillons étaient composés de deux types d'aluminium A et B, d'un acier de construction et d'un acier inoxydable. La méthodologie a consisté à mesurer la fréquence propre des échantillons liés aux modèles et prototypes. Ensuite, les fréquences du modèle ont été introduites dans les lois de similitude afin d'obtenir celle des prototypes. Ensuite, ces dernières ont été comparées aux fréquences mesurées des prototypes. Durant l'investigation expérimentale, l'effet de la taille et du type de matériau ont été étudiés séparément sur les résultats de similitude.

Table 1.4 – Écarts relatifs entre la fréquence propre mesurée et celle obtenue via les lois de similitude pour des échantillons avec différentes dimensions [81].

Longueur/largeur	Modèle [mm^2]	Prototype [mm^2]	Mode 1 [%]	Mode 2 [%]	Mode 3 [%]
1	200 × 200	300 × 300	−7.47	2.61	0.77
	250 × 250	200 × 200	−0.79	−5.59	−4.79
	300 × 300	250 × 250	8.93	3.23	4.23
1.5	300 × 200	450 × 300	−1.29	−2.42	0.27
	375 × 250	300 × 200	6.31	6.05	1.33
	450 × 300	375 × 250	−4.7	−3.36	−1.58
2	400 × 200	600 × 300	−1.54	−3.34	−2.29
	500 × 250	400 × 200	3.64	5.87	1.24
	600 × 300	500 × 250	−2.01	−2.29	1.09

Table 1.5 – Écarts relatifs entre la fréquence propre mesurée et celle obtenue via les lois de similitude pour des matériaux différents [81].

Modèle	Prototype	Taille [mm^2]	Mode 1 [%]	Mode 2 [%]	Mode 3 [%]
Al-A	Al-B	300 × 200	10.47	−2.39	9.59
		375 × 250	14.15	3.53	7.11
	Acier	300 × 200	2.86	9.71	4.06
		375 × 250	5.71	−3.17	−7.84
	Acier inoxydable	300 × 200	2.28	6.98	9.13
		375 × 250	14.66	1.15	−1.53
Al-B	Acier	300 × 200	−6.89	12.39	−5.05
		375 × 250	−7.4	−6.47	−13.95
	Acier inoxydable	300 × 200	−7.42	9.59	−0.42
		375 × 250	0.45	−2.3	−8.06
Acier	Acier inoxydable	300 × 200	−0.57	−2.49	4.87
		375 × 250	8.47	4.46	6.84

Afin d'étudier l'effet de la taille, un modèle en aluminium et des prototypes de différentes tailles ont été considérés. Sur 27 comparaisons, l'écart relatif moyen obtenu est de 3.3 % d'après les valeurs dans le Tableau 1.4. Malgré les écarts faibles, le modèle et les prototypes ne sont pas entièrement similaires. Selon les auteurs, le degré de non-planéité était probablement différent entre les échantillons. Par ailleurs, les fréquences propres des prototypes ont été prédites en recourant à des échantillons modèles de différents matériaux. D'après le Tableau 1.5, les similitudes permettent de prédire avec une marge d'incertitude la fréquence propre du prototype. Sur la base de 36 comparaisons, seules 5 paires présentent un écart supérieur à 10 %. Selon Singhatanadgid *et al.* [81], l'incertitude expérimentale qui découle de l'imperfection des conditions aux limites et des échantillons serait probablement à l'origine des écarts constatés.

5.2.2 Résistance des matériaux

Ce domaine étudie le comportement des matériaux vis-à-vis des contraintes mécaniques [82, 83]. Dans ce contexte, les similitudes cinétiques ont été utilisées pour étudier les performances des structures offshore telles que les conduites d'extraction. Ces structures font partie du système utilisé pour acheminer le pétrole jusqu'à la surface d'eau. Les collecteurs sous-marins sont exposés à un environnement corrosif qui entraîne une dégradation de leurs surfaces internes et externes. Cette dégradation peut se manifester par une perte d'épaisseur de la paroi et une détérioration de la fonctionnalité au fil du temps. Dans ce contexte, Chan *et al.* [84] ont analysé les performances d'une conduite en acier réparée avec un polymère composite à base de fibres et soumise à des chargements mécaniques. Le comportement du système charge-déformation a été modélisé et résolu par la méthode des éléments finis. L'avantage des lois de similitude a été la validation de ce modèle en proposant un prototype expérimental à échelle réduite. Ce dernier peut reproduire le comportement mécanique des conduites tout en économisant le temps nécessaire à la préparation des matériaux et le coût élevé des ressources. Lors des simulations et expériences, trois états de conduite ont été pris en compte : non corrodées, corrodées et réparées avec des fibres de carbone de différentes orientations.

Table 1.6 – L'erreur quadratique moyenne (RMSE) et l'écart relatif maximum entre les résultats numériques et les mesures [84].

État d'acier	Écart relatif maximal [%]	RMSE [-]
Normal	4.44	0.0035
Corrodé	15.95	0.025
Réparé 0°	25.47	0.023
Réparé 30°	10.83	0.012
Réparé 60°	5.61	0.0018
Réparé 90°	7.58	0.0091

Concernant la partie expérimentale, des tuyaux en acier doux ont été sélectionnés pour concevoir la conduite. Quant à la modélisation numérique, le même matériau a été considéré dans le cadre d'une configuration réelle. Les résultats sont obtenus en termes de loi de comportement mécanique entre celle mesurée et l'autre calculée. Pour les échantillons réparés, les différentes orientations correspondent aux angles qui font les fibres de carbone avec l'axe de la barre d'acier. L'écart relatif maximum et l'erreur quadratique moyenne sont résumés dans le Tableau 1.6. Les valeurs d'écart les plus marquantes sont 15.95 % et 25.47 %. D'après les auteurs, la première est liée à l'erreur systématique lors de la conception expérimentale de la corrosion. Quant à la seconde valeur, elle a été justifiée par rapport à l'hypothèse d'une liaison parfaite entre les fibres et le tube d'acier. En effet, le modèle numérique a été basé sur cette hypothèse et a surestimé la résistance des fibres.

5.2.3 Aérodynamique

le domaine aéronautique et aérospatial ont également tiré profit de ces lois [85, 86]. Principalement, des prototypes réduits d'avion sont développés pendant la phase de conception. Le but est la vérification de la résistance et la stabilité des modèles réels à l'écoulement d'air pendant les vols. Pour y parvenir, les équations de *Navier-Stokes* [87] sont décrits pour établir des équivalences. En addition, la phase d'atterrissage est examinée en menant des tests sur des prototypes. Selon [88], la dynamique d'atterrissage des engins spatiaux a été analysée dans le cadre de la mission d'exploration de l'une des deux lunes de Mars [89].

À cet égard, l'étude a été basée sur les similitudes cinétiques afin d'établir une corrélation entre le vaisseau et un modèle réduit. Pour ce fait, trois configurations expérimentales équivalentes ont été comparées. Une configuration réduite consiste à représenter l'impact du pied du vaisseau spatial par un test de chute d'un support cylindrique. En outre, l'étude a considéré le sable siliceux pour modéliser la partie du sol de la lune recouvrant la roche-mère (régolithe). Il a été supposé que les deux avaient la même densité. Cela a permis de simplifier en partie les relations d'équivalence. Les trois essais ont été définis, chacun via une longueur caractéristique. Il faut noter que les trois configurations sont équivalentes à celle du vaisseau spatial réel. La hauteur d'enfoncement adimensionnelle a été considérée pour la comparaison des configurations. En supposant que le régolithe/sable joue le rôle du ressort au moment d'atterrissage, la hauteur d'enfoncement varie suivant la vitesse de l'engin spatial. Pour une même vitesse, les configurations étaient généralement en bon accord.

5.2.4 Transfert de chaleur et d'humidité

Ces transferts couplés représentent les phénomènes qui ont lieu au cours du vieillissement thermique et hydrique. Les différents types de sollicitations induisant ce vieillissement sont cités dans la Section 4.4. Certains modèles de transfert de chaleur et d'humidité [90, 91, 92] ont été utilisé pour établir les lois de similitude. Dans ce cas, des équivalences peuvent être définies à base des nombres adimensionnels suivants : *Fourier*, *Biot* et *Lewis* [93]. En analysant les travaux de la littérature, les lois de similitudes sont rarement utilisées [94, 95]. En effet, la fiabilité de l'application expérimentale de ces lois n'est pas vérifiée.

Matsumoto *et al.* [96] ont appliqué ces lois sur les phénomènes de transfert. Grâce à cette investigation, une méthode expérimentale est développée, elle est basée sur un modèle réduit de mur de bâtiment et sur l'application des lois de similitude dynamiques. Celles-ci ont été fondées sur la base des équations qui régissent le transfert unidimensionnel de chaleur et d'humidité à travers les milieux poreux. Le modèle réduit a été conçu avec les mêmes matériaux que le mur réel du bâtiment. En outre, les conditions aux limites sont les mêmes que celles du mur réel. Enfin, la valeur 0.2 a été choisie comme facteur de réduction spatiale. Ainsi, la taille réelle du mur est 5 fois plus petite dans le modèle réduit. Sur la base des lois de similitude, il en a découlé que le facteur de réduction temporelle est 0.04. Ainsi, les variations annuelles d'humidité et de température dans le mur réel peuvent être simulées par le modèle réduit avec une durée 25 fois plus courte (environ deux semaines). Quant aux matériaux utilisés, le contreplaqué, la laine de verre et le béton léger ont été utilisés pour construire le mur. La température et l'humidité relative ont été maintenues à des constantes du côté intérieur. Quant aux conditions extérieures, la variation de la température a été basée sur des données climatiques annuelles. Contrairement à la température, l'humidité relative extérieure n'a pas été contrôlée. À des fins de comparaison, le comportement du modèle à échelle réelle a été évalué numériquement. Entre-temps, les mesures ont été converties à l'échelle réelle du mur et de temps en utilisant les similitudes. La distribution de la température dans le mur a été obtenue pour des résultats numériques et des mesures à six moments différents. Les prédictions numériques concordent bien avec les mesures. De plus, malgré l'humidité élevée de l'air ambiant, les valeurs numériques et expérimentales de l'humidité sont relativement en accordance tout en notant quelques écarts. Ces derniers sont plus significatifs que ceux concernant la température. Il sont dus à la difficulté de maintenir expérimentalement des coefficients convectifs extérieurs et intérieurs qui respectent les lois des invariants. En effet, le protocole expérimental utilisé n'a pas permis de contrôler ces grandeurs.

Conclusion

Dans le cadre de cet état de l'art, il a été reporté des éléments bibliographiques liés aux matériaux biosourcés et au vieillissement. Par ailleurs, le milieu poreux a été initialement défini et ses caractéristiques ont été explicitées. Cette description est indispensable en raison de la nature poreuse du matériau biosourcé. De plus, un grand intérêt est porté au vieillissement thermique et hydrique des matériaux de construction. Sur cette base, la majorité des auteurs modélisent ce type de vieillissement en proposant des essais au laboratoire. Ces derniers consistent en des cycles récurrents de chaleur et d'humidité.

L'analyse de ces essais a permis de soulever un premier verrous scientifique. En effet, le développement des protocoles de vieillissement est basé sur des conditions climatiques extrêmes. Sous cette hypothèse, l'essai est agressif et représente ainsi moins le phénomène naturel. Par ailleurs, nous remarquons que ces protocoles sont accélérés et ne durent que quelques dizaine de jours. En réalité, la durée du vieillissement naturel est beaucoup plus importante. Par conséquent, il est difficile de définir les échelles spatio-temporelles de la configuration qui correspond à un essai accéléré. Dans ces travaux, une méthodologie pour le développement d'un protocole expérimental répondra à la première problématique. Grâce à ce protocole, le vieillissement, comme phénomène long et naturel, est mieux représenté. Cependant, l'essai proposé n'est pas réalisable à l'échelle du laboratoire à cause de sa longue durée. Comme montré dans la littérature, les lois de similitudes peuvent être utilisées pour réduire l'échelle temporelle des longs phénomènes. Ainsi, le deuxième objectif sera de vérifier l'application de ces lois. La fiabilité de leur application expérimentale est testée sur deux expériences. La première porte sur le transfert de chaleur seul et la deuxième, plus généralisée, traite des transferts couplés de chaleur et de masse d'eau. Après leur vérification, ces lois seront appliquées pour générer et étudier une maquette expérimentale réduite et équivalente du protocole développé. Grâce à ce test accéléré, nous étudions l'effet du vieillissement sur les propriétés du transfert du béton de chanvre. Il est évalué en mesurant la variation des propriétés durant l'essai réalisé. Sur l'appui des mesures de porosité, nous développons un modèle phénoménologique qui décrit le vieillissement d'un matériau en fonction des charges d'imbibition et de séchage. Dans le cadre de cet objectif, il s'agit aussi d'intégrer le modèle dans les transferts de chaleur et de masse au sein des matériaux de construction. Cette étape permet d'évaluer l'impact du vieillissement sur l'efficacité énergétique à l'échelle des parois de bâtiment.

Chapitre 2

Experimental assessment of the similarity law for a heat conduction problem

Abstract

Similarities are mathematical laws, which are based on the dimensionless formulation of the governing equation of a physical phenomenon. Consequently, a set of characteristic dimensionless numbers is obtained. Similarities aim, via these numbers, to find equivalences between particular configurations. This approach is widely adopted, especially in fluid and aerodynamic problems. In the building context, the phenomena of heat and mass transfer in porous media occur with slow kinetics. Thus, similarities can be employed to reduce the duration of experimental campaigns to characterize material properties. These laws were investigated here in the case of a heat transfer problem through an experimental campaign. Two equivalent configurations were submitted to a heat stress. Temperatures inside materials were measured and compared to assess the validity of thermal similarity. A complete evaluation of uncertainty propagation was then carried out. Uncertainties related to the sensor position, its response time, the omission of mass transfer, the sensor systematic accuracy, the random measurement aspect, the one-dimensional transfer hypothesis and the boundary condition modeling were evaluated. The comparison of both configurations was carried out based on the confidence interval of both measurements. The results showed a good agreement between the reference and reduced experiment. On the basis of these findings, similarities were experimentally verified within a margin of discrepancy that was justified. Thus, they can be adopted in heat transfer experiments in order to identify equivalent configurations that are easier to conduct.

Highlights

1. Similarity laws are investigated in the framework of a heat transfer problem through an experimental campaign.
2. Two equivalent configurations undergo the same heat stress, and temperatures at equivalent positions are compared.
3. The reliability of results is supported with a rigorous uncertainty evaluation.
4. Results highlight a good agreement between the reference and reduced experiment.

Keywords

Heat transfer, similarity analysis, porous material, experimental benchmarking, uncertainty quantification.

1 Introduction

In the building sector, energy consumption has increased continuously in the recent years, depleting natural resources and in turn increasing greenhouse gas emissions [97]. One option for addressing this is to focus on the envelope and building materials, reducing their environmental footprint and better controlling sensible and latent heat flows. Recently, new types of materials have been proposed in building sector. On the one hand, there are bio-based materials, which are generally based on the use of concrete with the partial substitution of a plant substance. They are good insulators and moisture regulators [72]. Studies conducted on this type of material have shown that it is a suitable alternative in terms of energy efficiency [41]. On the other hand, agricultural and industrial waste can also be used to form composite concretes. It has also been shown [98] that the manufacture of recycled concrete reduces CO_2 emissions by 58% compared to the production of clinker.

All such materials are porous media, composed of a solid matrix, a water liquid phase and a humid air phase. They have complex and heterogeneous micro-structures [99, 100]. With the presence of temperature and humidity variations induced by climatic conditions and building use, coupled heat and mass transfer phenomena [101] occur through the material. To accurately model these phenomena through porous building walls, it is necessary to determine the material properties of heat and mass transfer. In other words, experimental campaigns are required to characterize the materials. However, some procedures require a long period. For example, determining the adsorption and desorption curves of concrete can last several months. The classical method lies on the use of saturated saline solutions. A study of the adsorption curve [102] showed that it takes approximately five months for different concrete samples. Indeed, the water mass equilibrium at each relative humidity level is reached slowly. The `ProUmid` device is used in laboratories world-wide to determine the adsorption curve and examine the moisture adsorption behavior of materials. This dynamic vapor adsorption device employs the gravimetric method, assessing the mass variation of samples until it reaches a mass equilibrium. The test duration can range from three to six months, depending mainly on the micro-structure of a material and its porosity. The long duration of these kinds of tests is primarily due to the kinetics of heat and mass transfer phenomena. Indeed, water transport is slow [103]. The Fourier number Fo $[-]$ is the parameter that describes the kinetics of transfer. Take for example a hemp concrete sample whose thickness is $L = 20\,\mathsf{cm}$. Considering that it undergoes a moisture stress during $t_0 = 10\,\mathsf{d}$ while remaining in the hygroscopic mode, the hemp concrete mass diffusivity is estimated at $D_0 = 1.06\,10^{-8}\,[\mathsf{m}^2.\mathsf{s}^{-1}]$ where $T = 20\,^{\circ}\mathsf{C}$. Thus, the typical experience duration is deduced $\tau = 43.6\,\mathsf{d}$. To overcome this problem, the similarity law can be employed to reduce the duration of experiments. By definition, similarities are mathematical laws which aim to find equivalences among several configurations. This method consists of the dimensionless formulation of the governing equations [104]. As a result, dimensionless characteristic numbers are obtained which are used to obtain equivalences.

The literature shows that similarity laws have been adopted in various scientific fields [105, 106, 107]. In acoustics, for example, it has been demonstrated that the sound analysis of two equivalent centrifugal fans was similar [108]. Another study [109] focused on the evaluation of the temperature of enclosed turbulent flames for different lengths. Analysis of the experimental results has shown that the behavior of temperatures, measured by means of an optical pyrometer, satisfies a similarity law. Similarities were also used in a study of structures [110] exposed to impacts with low and high velocity projectiles. It presented an experimental verification of these laws, using three different scales, three different materials and two loading cases. In addition, fluid dynamics constitutes a major field highlighting the use of these techniques [111, 112, 113]. In [114], an analysis was performed to study the fluid flow and heat transfer characteristics of the steady laminar natural convection boundary layer flow over a semi-infinite horizontal flat plate. This plate was subjected to a variable wall temperature. Similarity laws were used to identify the parameters governing the dynamic and thermal wall-fluid interaction. Within the same scientific field, other studies were carried out in order to evaluate the impact of certain physical parameters on the flow of particular fluids [115, 116, 117]. In this case, temperature, pressure gradient, velocity and shear stress were investigated by means of preliminary similarity analysis. For example, a study was conducted on a steady incompressible Williamson fluid flow [118]. Using appropriate similarity transformations, the authors converted a set of partial differential equations based on flow situations into a system of non-linear coupled ordinary differential equations. Thereby, the impact of some parameters, namely the one related to the Williamson fluid, was observed on some problem variables.

In the field of heat and mass transfer in buildings, these laws are applied for different purposes. A method for calculating the solution of the transfer equations has been described in [119]. A dimensionless formulation was suggested as an intermediate step. In addition, the advantages of using a dimensionless analysis by scaling the governing equations of heat and mass transfer were explored in [94]. It also permitted the definition of heat and mass kinetics, geometric and dynamic similarities among different physical materials. The dimensionless analysis of a heat and mass transfer model has also been addressed in [104]. The authors adopted this approach to estimate the mechanisms governing these transfers for a medium density fiberboard. This was achieved by assessing the magnitude of the dimensionless numbers of the model and their response surface. An experimental method using a small-scale model for the building wall and similarity laws based on the governing equations of simultaneous heat and moisture transfer through porous media was presented in [96]. Converted values from the small-scale model were compared with the numerical results of the reference configuration, this comparison showed a good agreement. Apart from the application of such laws, it is worth noting that most studies used them to obtain equivalent theoretical configurations. Nevertheless, this approach requires an experimental campaign to compare the results between equivalent cases and evaluate the noticed discrepancies.

In general, it is easy to express theoretically the laws of similarity related to a physical problem, particularly the one concerning heat transfer in porous materials. In addition, these laws are based on several assumptions that can be modeled mathematically. As an example, the boundary conditions and the variation laws of material properties constitute two important hypotheses. Experimentally, it would not always be evident to respect entirely the defined assumptions. For example, a material property is supposed constant at the macroscopic scale. In reality, it varies in space following the micro-structure and pores distribution. Thus, two samples issued from a material do not have necessarily the same properties. In this context, it would be judicious to evaluate how far the experimental similarities are validated. Errors, that would arise from assumptions, can be discussed by means of a study of uncertainty. Many researches have proposed methodologies to compute uncertainties following two main approaches : probabilistic and deterministic. In the deterministic approach, uncertainty is defined as a scalar. In this case, the calculation is less costly but less accurate. On the other hand, uncertainty is evaluated more accurately in the probabilistic approach. However, this requires more data and computation time. For example, the authors in [120] focused on the analysis of experimental uncertainties related to the convective transfer coefficient h_c. They relied on random uncertainty in the measurements of air and wall temperatures. Through a differential calculation, they were able to express and evaluate the ratio of the relative uncertainty of h to the relative uncertainties of the measured temperatures. The viewpoint of the study is purely deterministic, and shows that the expressions obtained are in good agreement with the ones simulated via the Monte Carlo method. Based on their results, the ratio can be used as a continuous function to minimize the uncertainty on h_c for similar configurations. A second study [121] introduced a non-probabilistic interval process model to the characterization of time-varying parameter uncertainties. Two numerical methods referred to as the *Monte Carlo method under interval process model* and the *sensitivity analysis method under interval process model* were adopted simultaneously to predict the uncertain temperature. Furthermore, this method involved the use of a finite differences scheme for the estimation of temperature derivatives according to model parameters. Other authors have adopted the probabilistic approach. In [122], the work was based on a random aspect governing the input parameters of the model. Indeed, propagation of uncertainty through the physical model was investigated by solving two specific simple stochastic problems using the Non-Intrusive Spectral Projection method. The uncertain parameters were described by either a Gaussian or a Log-Normal probability distribution function. For each of the problems, the stochastic and the deterministic mean solutions were compared and the resulting confidence intervals were obtained. Similarly, a random aspect was taken into account in [123] to generate multiple model inputs. Moreover, a random collocation method and a modified random collocation method were advanced, based on spectral analysis theory. In both methods, the truncated high-order polynomial series were adopted to approximate temperature responses with respect to random parameters. The accuracy of the two methods was then tested using a traditional Monte Carlo simulation and two numerical examples.

In this work, we carry out an experimental assessment of similarity laws on a unidirectional heat transfer problem. Mass transfers will be neglected in this study. Indeed, the coupling of the two phenomena is less easy to control than a pure heat transfer model. The study provides also a detailed calculation of the uncertainties related to the hypothesis of the experimental tests and the accuracy of the used equipment. The uncertainty evaluation is essential to discuss the validity of heat transfer similarities. The study of uncertainties is of great importance. The numerical or experimental result is not conclusive and needs to be completed by using the associated confidence interval. This justifies the result and is obtained due to the study of uncertainties. The paper is structured as follows. The next section defines the governing equations, the dimensionless formulation of the problem and the similarity law. Section 3 introduces the experimental facility to assess the heat transfer similarity. Section 4 contains a complete evaluation of the measurement uncertainty. Section 5 presents the results and discusses the validity of the similarity for two configurations. Section 6 concludes and suggests future works.

2 Methodology

2.1 Governing equations

First, the study case consists in defining the equation that describes the heat transfer in homogeneous media (superior in size that the representative elemental volume) [124], [125] with high porosity. In this work, the mathematical model considers temperature T [K] as a driving potential. It is based on the general heat equation, first developed by Joseph Fourier (1822). The problem is written as follows :

$$\rho\, c_q \frac{\partial T}{\partial t} = \nabla \cdot \Bigl(k_q \, \nabla T \Bigr) . \tag{2.1}$$

In Eq. (2.1), three coefficients have been introduced. k_q [W.m^{-1}.K^{-1}] is the heat transfer coefficient and ρ [kg.m^{-3}] the material density. In addition, c_q [J.kg^{-1}.K^{-1}] is the heat storage coefficient. We define both material density and heat transfer coefficient as follows :

$$\rho = (1 - n)\, \rho_s + n\, S_w\, \rho_w + n\, S_a\, \rho_a . \tag{2.2}$$

$$k_q = n\, k_{qw} + (1 - n)\, k_{qs} . \tag{2.3}$$

Equation (2.2) expresses the density of a porous material according to the three phases solid, liquid and air [126], where n represents the porosity of the material, and ρ_s, ρ_w and ρ_a the density of solid phase, water and air respectively. S_w and S_a represent the degree of saturation in liquid water and the gas phase. Moreover, the work of LAGARDE (1965) [18] expresses the heat transfer coefficient in Eq. (2.3) in terms of the porosity in a saturated porous media, where k_{qw} is the liquid water thermal conductivity and k_{qs} that of the solid matrix.

We present **Hypothesis 1**, which considers a one-dimensional transfer along the x-axis [127]. This is possible by insulating the facets parallel to the transfer direction. In these areas, thermal flux is negligible. Moreover, we neglect water mass transfers in our case. The impact of these on heat transfer is assumed therefore not considered. This will be the **Hypothesis 2** of our study [128]. For $x \in \Omega_x$ and $t \in \Omega_t$ where x is the first space coordinate, t the instant of the experiment. Eq. (2.1) can be simply reduced to :

$$\rho\, c_q \frac{\partial T}{\partial t} = \frac{\partial}{\partial x} \Bigl(k_q \frac{\partial T}{\partial x} \Bigr) . \tag{2.4}$$

$\Omega_x = [0, L]$ is the space domain where x varies and $\Omega_t = [0, t_{\text{ref}}]$ the trial time interval. L and t_{ref} are the sample length and experiment duration respectively. At the initial state, the temperature is known :

$$T = T_0(x) \qquad \forall x \in \Omega_x . \tag{2.5}$$

where T_0 is a given function of space. At the material/air interface, the Robin condition is generally applied, where air temperature is known. In the case of a high ambient homogenization and a large air flow, we define the **Hypothesis 3**. It assumes that temperature at the interface is very close to that of air. Thus, we present the Dirichlet condition [129] :

$$T = T^{\infty}(t) , \qquad x = 0 , \, t \in \Omega_t . \tag{2.6}$$

The temperature T^{∞} at the interface is a time function that represents the varying climatic stress. The other side of the material is insulated, meaning that the thermal flow is negligible, thus :

$$\frac{\partial T}{\partial x} = 0 , \qquad x = L , \, t \in \Omega_t . \tag{2.7}$$

Furthermore, the assumption of a local thermal equilibrium is made, given the slow kinetics of the transfer and the predominance of diffusion effects compared to convection through the porous matrix [130]. Thus, the hypotheses of the model can be summarized as follows :

Hypothesis 1 *The heat transfer is one-dimensional.* ■

Hypothesis 2 *Mass transfer and latent effects are negligible.* ■

Hypothesis 3 *The boundary conditions are assumed to be of the* Dirichlet *type.* ■

Hypothesis 4 *The local thermal equilibrium is assumed.* ■

Next section is devoted to the study of the dimensionless heat transfer case. This step is important before discussing the notion of similarities. Indeed, the dimensionless formulation is an intermediate procedure which aims to define similarities, or equivalent configurations.

2.2 Dimensionless problem

The dimensionless formulation of an equation consists in describing its variables as constants corresponding to a particular case. This latter is defined by the researcher, and can represent the initial instant of an experiment. Dimensionless studies have been discussed in previous research [131]. More precisely, it has been applied to heat and mass transfer equations according to [94], [104] and [119]. The first step is to transform the spatial and temporal field into :

$$t^{\star} = \frac{t}{t_{\text{ref}}} , \qquad x^{\star} = \frac{x}{L} . \tag{2.8}$$

Equation (2.8) introduces the dimensionless first space coordinate $x^{\star}$ and experiment instant $t^{\star}$. In parallel, temperature follows the same reasoning, and the reference value of this quantity can represent that of the material at its initial state :

$$u = \frac{T}{T_0} . \tag{2.9}$$

u represents the dimensionless temperature. On the other hand, the heat transfer k_q and thermal storage c_q coefficients change under the same formulation :

$$k_q^\star = \frac{k_q}{k_q^{\text{ref}}}\,, \qquad \rho^\star = \frac{\rho}{\rho^{\text{ref}}}\,, \quad c_q^\star = \frac{c_q}{c_q^{\text{ref}}}\,. \tag{2.10}$$

Likewise, k_q^{ref}, c_q^{ref} and ρ^{ref} are the material heat transfer, heat storage coefficients and density respectively at $t = 0$. The substitution of the dimensionless quantity u and the coefficients $k_q^\star$, $c_q^\star$ and $\rho^\star$ in Eq. (2.4) enables us to obtain the new equality :

$$\rho^\star\, c_q^\star\, \frac{\partial u}{\partial t^\star} = \mathrm{Fo}_q\, \frac{\partial}{\partial x^\star}\left(k_q^\star\, \frac{\partial u}{\partial x^\star}\right). \tag{2.11}$$

Thus we observe the dimensionless Fourier number Fo appearing, and its expression is given as follows :

$$\mathrm{Fo}_q = \frac{k_q^{\text{ref}}\, t_{\text{ref}}}{\rho^{\text{ref}}\, c_q^{\text{ref}}\, L^2}\,. \tag{2.12}$$

Finally, the new boundary conditions for heat transfer are written as follows :

$$u = u^\infty(t^\star) \quad at \quad x^\star = 0\,, \qquad \frac{\partial u}{\partial x^\star} = 0 \quad at \quad x^\star = 1\,. \tag{2.13}$$

Where, u^∞ designates the dimensionless air temperature. Thus, the dimensionless formulation has built a new closed system, independent of time and space fields. It relies only on the number Fo_q. This transformation was introduced to ensure a transition to the laws of similarity. Indeed, equivalences would have to be determined using a basic configuration. Then, the transformation shown in this section, is used to operate on this configuration.

2.3 Similarity law

In practice, the laws of similarity are applied to a reference case. Their usefulness consists in obtaining configurations equivalent to our reference case [132]. They can minimize some difficulties related to the real case. In the context of heat transfer, we can use these laws to change the material while maintaining similarity of results [108] and [133].

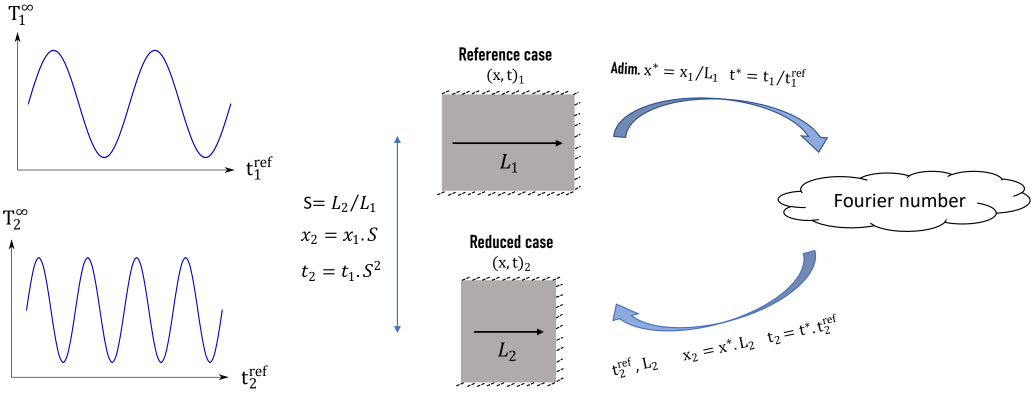

FIGURE 2.1 – The mapping of two equivalent configurations

The dimensions of the sample can also be changed. Since the transfer phenomena have a slow kinetic, the goal of the study is to reduce the duration of an experiment, while working on the same material. In heat transfer, kinetic describes the rate of heat diffusion within a material. In the building physics field, the Fourier number describes fully this notion. Fig. 2.1 highlights the process that defines these laws. The Fourier number is the unique parameter in the dimensionless equation. By means of this characteristic number, a similarity can be established between the reference case where $x \in \Omega_x^1$, $t \in \Omega_t^1$ and the equivalent case such that $x \in \Omega_x^2$, $t \in \Omega_t^2$. With :

$$\Omega_x^i = \Big\{ x \in \mathbb{R}^+ ,\, 0 \leq x \leq L_i \Big\} = \Big[0 \,,\, L_i \Big] , \tag{2.14a}$$

$$\Omega_t^i = \Big\{ t \in \mathbb{R}^+ ,\, 0 \leq t \leq t_i^{ref} \Big\} = \Big[0 \,,\, t_i^{ref} \Big] , \qquad \forall i \in \Big\{ 1 \,,\, 2 \Big\} . \tag{2.14b}$$

where i refers to the number of the experiment configuration. Two different configurations 1 and 2 are said to be equivalent or similar if they verify the following equality :

$$\mathrm{Fo}_q^1 = \mathrm{Fo}_q^2 \,. \tag{2.15}$$

As a reminder, both experiments have been carried out on two samples, made of the same material. Moreover, we assume that these samples have the same porosity and initially the same hydric state. This means : $k_{q\,1}^{\mathrm{ref}} = k_{q\,2}^{\mathrm{ref}}$, $c_{q\,1}^{\mathrm{ref}} = c_{q\,2}^{\mathrm{ref}}$ and $\rho_1^{\mathrm{ref}} = \rho_2^{\mathrm{ref}}$. Thus, Eq. (2.15) is simplified to :

$$\frac{t_2^{\mathrm{ref}}}{t_1^{\mathrm{ref}}} = \left(\frac{L_2}{L_1} \right)^2 . \tag{2.16}$$

We defined the proportionality factor between the two configurations by :

$$\Sigma = \frac{L_2}{L_1} \,. \tag{2.17}$$

Σ designates the ratio between two characteristic lengths L_1 and L_2. These represent the dimensions according to which, the heat transfer occurs in both configurations. Mathematically, we carry out a mapping, based on the dimensionless numbers, from a first configuration to a second by applying the proportionality factor Σ.

$$\Omega_x^1 \times \Omega_t^1 \longrightarrow \Omega_x^2 \times \Omega_t^2 \tag{2.18a}$$

$$\Big(x_1 \,,\, t_1 \Big) \longmapsto \Big(x_2 = x_1 \cdot \Sigma \,,\, t_2 = t_1 \cdot \Sigma^2 \Big) \tag{2.18b}$$

The next section will define the adopted experimental protocol. First, we define the material studied and its manufacturing phase. This is followed by a description of the equipment and the sensors used. Finally, the experimental configurations are highlighted, allowing us to verify the validity of the hypotheses.

3 Materials and experimental facility

We chose hemp concrete for the similar tests. It is a bio-based composite material made of hemp and lime (Fig. 2.2). The material was manufactured using the following products : Biofibat, a calibrated hemp aggregate with a density of $\rho = 110\,[\mathsf{kg.m^{-3}}]$ and $k_q = 0.05\,[\mathsf{W.m^{-1}.K^{-1}}]$

and a moisture content of less than 15%, and Tradical^{R} PF 70, a class FL A 3.5 formulated lime in accordance with the NF EN 459 standard where $\rho = 620\,[\mathsf{kg.m^{-3}}]$ and $k_q = 0.096\,[\mathsf{W.m^{-1}.K^{-1}}]$. The hemp concrete formulation was based on the proportions, defined by the French standard, which are 16% hemp, 34% lime and 50% water. Moreover, the homogenization of the mixture was ensured using a mixer for approximately three minutes. We let the mixture cure for 10 days in molds of $15 \times 15 \times 15\,\mathsf{cm}^3$. The molds were also treated with an agent to facilitate the release of samples. The experimental characterization of hemp concrete thermal properties under this formulation [41], provides the following results $k_q = 100.23\,[\mathsf{mW.m^{-1}.K^{-1}}]$, $c_q = 5.52\,10^5\,[\mathsf{J.m^{-3}.K^{-1}}]$ and $\rho = 480\,[\mathsf{kg.m^{-3}}]$.

FIGURE 2.2 – Lime and hemp used in the process

In addition, we used a climatic chamber brand Climats (Fig. 2.3a) which can generate stress scenarios such as a variation in temperature and relative humidity. We mainly used it to simulate thermal stress in our study, with a humidity set at 85%. An Almemo (Ahlborn) acquisition unit and series FHA 646 R Ahlborn sensors were used. The Ahlborn FHA 646 R is a cylindrical sensor with a 5 mm diameter, and can be used within a range from −30 to 100 °C and from 5 to 95% relative humidity. These sensors are calibrated at 23 °C, 35% and 80% relative humidity. The factory calibration certificate indicates an accuracy of 0.3 K in temperature and ±3% in relative humidity. The response time of the sensor is around 10 s estimated at 1 m/s air velocity. The samples manufactured and the equipment described were used for the three tests. Two tests verify the limitations of Hypotheses 1 and 3 and the third is devoted to the validation of thermal similarity.

3.1 The one-dimensional transfer

The sample is a $10 \times 10 \times 10\,\mathsf{cm}^3$ cube, initially preconditioned at 85 % relative humidity and 25 °C in the climatic chamber, as shown in Fig. 2.3a. The material was isolated from four sides using a 3 cm layer of industrial polystyrene with a thermal conductivity of $k_q = 0.035\,[\mathsf{W.m^{-1}.K^{-1}}]$, to limit the flux perpendicular to the chosen direction of transfer. In fact, the measured thermal conductivity of hemp concrete is almost three times higher than that of the insulation used. Hemp concrete is still three times less efficient than the current insulators used, namely rock or glass wool where $k_q \in [\,0.03\,,\,0.04\,]\,[\mathsf{mW.m^{-1}.K^{-1}}]$. In order to maintain a good bond between the concrete and the insulation, we attached two layers of an aluminum adhesive ribbon to the assembly (Fig. 2.3b).

(a) (b)

FIGURE 2.3 – The climatic chamber (a) and the tested sample (b)

TABLE 2.1 – Sensor position coordinates

	x [cm]	y [cm]
χ_1	2.5	2.5
χ_2	2.5	5
χ_3	2.5	7.5
χ_4	7.5	2.5
χ_5	7.5	7.5

Six sensors were used with a diameter of 5 mm and a height of 5 to 7 cm, we positioned five within the sample at a height of 5 cm, the corresponding coordinates were given in Table 2.1. The sensors formed two rows, the first at a depth of 2.5 cm (three sensors) and the second at 7.5 cm (two sensors) as shown in Fig. 2.4. We used the last one to read the value of T and ϕ of the ambient air. We consider making an error during the positioning of sensors. The error is of the same magnitude as the sensor diameter and will be useful for the calculation of uncertainties. This first experiment aims to evaluate the thermal flux along the y-axis. The hypothesis is validated as long as this flux is negligible.

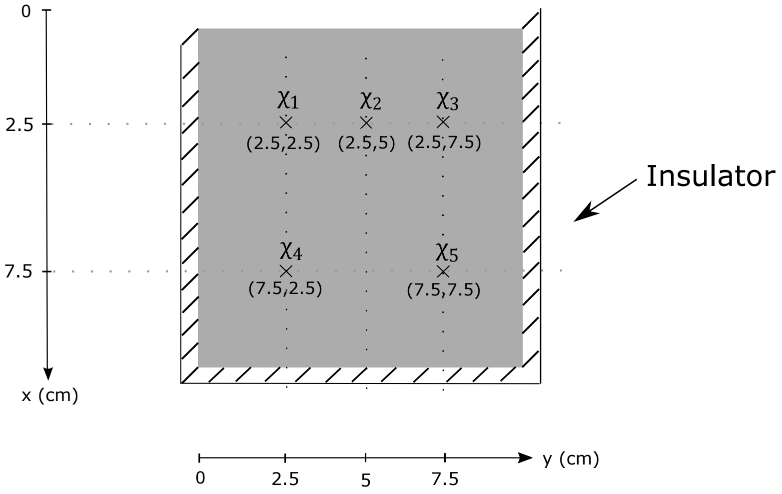

FIGURE 2.4 – Sensor positions in the sample

3.2 The Dirichlet approximation

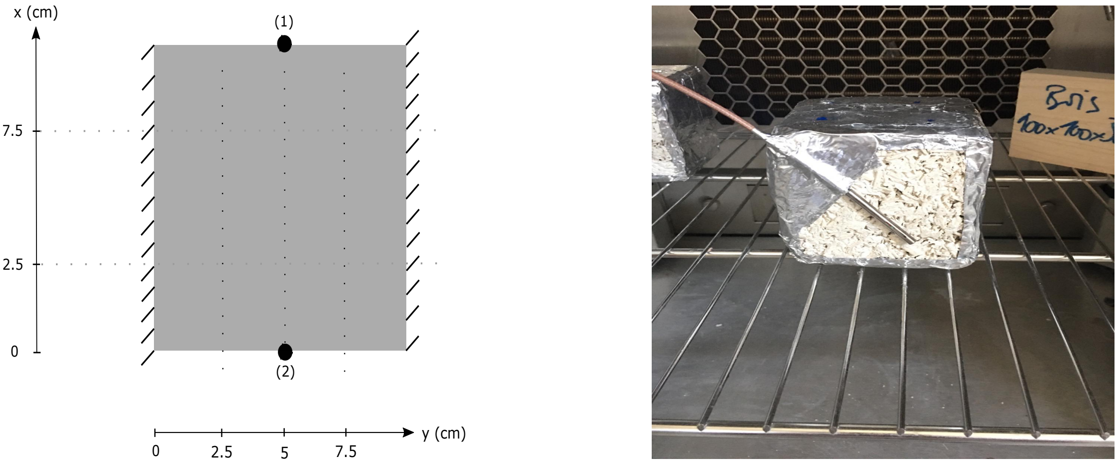

(a)

(b)

FIGURE 2.5 – Sensors positions in the sample

The same sample used for **Hypothesis 1** was adopted for the next test. Fig. 2.5 represents the experimental protocol to verify the assumption made about the Dirichlet boundary condition. The configuration was exactly the same, with four sensors this time. The first two measured air temperature and the last ones were fixed on the surface of the material and measured its temperature. The sensors on the surface were not isolated, based on the assumption that there were no radiation effects in the chamber. They were embedded within the sample surface and fixed using an adhesive ribbon. This enabled an almost perfect sensor-surface adherence. The integrated fan in the climate chamber operated at a constant and nominal flow rate. The material was placed inside the chamber in such a way as to allow the surface $x = 10\,\mathrm{cm}$ to be perpendicular to the ventilation direction. The purpose of this second test was to measure the temperature variation at the surfaces $x = 0\,\mathrm{cm}$ and $x = 10\,\mathrm{cm}$. It was then compared to the ambient air temperature.

3.3 Experimental thermal similarities

Previously, we explained the procedure for the verification and validation of the predefined hypotheses. This step is necessary in order to control relatively the conditions of both configurations obtained via the similarity laws. This section consists in the presentation of the two tests that aim to verify these laws experimentally. Both test samples were from the same formulation of hemp concrete. After the curing period, both samples were stored at 25 °C and 85% relative humidity. Therefore, we consider a reference configuration where samples are cubic and have the size of the molds. Using the laws of similarity, we want to reduce the duration of the test that represents the reference configuration. A reduction calls for the application of a proportionality factor lower than 1, we chose $0 < \Sigma < 1$. Thus, a sample having a thickness L_1 was taken, then a second one was selected, and sliced to reduce its thickness to L_2 such that $L_2 = \Sigma\, L_1$ (Fig. 2.6). Next, the materials were similarly preconditioned in temperature and relative humidity. Subsequently, they underwent a thermal stress according to two well-defined scenarios. These scenarios must have the same amplitudes and verify the following equality : $t_2^{\text{ref}} = \Sigma^2\, t_1^{\text{ref}}$.

FIGURE 2.6 – Samples for the similarity experiment

4 Uncertainty propagation in the measurements

Experimental measurements are sensitive to errors of various kinds. Some of them may be due to the experimenter's lack of expertise. They can also be affected by the systematic accuracy of an equipment. It is therefore necessary to include the confidence interval in a study. In this regard, we introduce the notion of uncertainties [134]. For similarity tests, we define the total uncertainty as :

$$\sigma_{Tot}^2 = \sigma_x^2 + \sigma_t^2 + \sigma_\phi^2 + \sigma_{\mathsf{Sys}}^2 + \sigma_{\mathsf{Rdm}}^2 + \sigma_{\mathsf{Dlt}}^2 + \sigma_{\mathsf{1D}}^2 + \sigma_{\mathsf{Sensor}}^2 \,. \tag{2.19}$$

The assessment of the global uncertainty σ_{Tot} is based on the evaluation of the different contributions. They are explained starting with σ_x, which is the uncertainty associated with the sensor location regarding the desired measurement position :

$$\sigma_x(\,t\,) = \frac{\partial T}{\partial x}\,\delta_x\,. \tag{2.20}$$

The temperature derivative is thus evaluated at the same position. This is possible by computing the model in Eq. (2.4) using the implicit Euler method and central finite-differences. δ_x represents the average error made and estimated by the experimenter when positioning the sensor. σ_x is a time function because temperature and its derivative are.

The reaction time of a sensor can also be a source of uncertainty. A sensor that requires 1 minute to measure a change in temperature is less accurate than one that takes only 10 seconds to respond. σ_t is the uncertainty regarding the response time. It displays the time derivative of temperature.

$$\sigma_t(\,t\,) = \frac{\partial T}{\partial t}\,\delta_t\,. \tag{2.21}$$

This derivative is evaluated at the measurement position and throughout the test. It was calculated using the same model as for σ_x. The response time is given by the term δ_t.

After introducing the vapor pressure and temperature model, we simplified both equations, considering the small impact of relative humidity on temperature. This implies the omission of the term $\nabla\,P_v$ in heat and mass transfer equations [93, 135]. In order to estimate the uncertainty due to the decoupling of temperature and vapor pressure, we evaluate the parameter σ_ϕ.

$$\sigma_\phi(\,t\,) = \frac{\partial T}{\partial \phi}\,\delta_\phi = \frac{\partial T}{\partial t}\left(\frac{\partial \phi}{\partial t}\right)^{-1}\delta_\phi\,. \tag{2.22}$$

Its estimation would be based on the solution of coupled heat and mass transfer equations [92, 136, 137]. The initial condition is the one reached by the material after the preconditioning phase. Moreover, the boundary conditions used are the measured temperature and relative humidity at the surface of the material throughout the experiment. The term δ_ϕ is the difference between the relative humidity at an instant t and the one at the initial state of the sensor position.

The sensor as a conceived system is an uncertain device in terms of measurement, and represents a systematic uncertainty. Indeed, the manufacturer performs calibration tests on the sensor to define its margin of error. Thus, this uncertainty is indicated within the product record. It is constant and requires no calculation, we denote it σ_{Sys}.

The random experimental uncertainty is also proposed and defined. It is obtained by the principle of repeatability. A sample undergoing the same experiment several times, can lead to different results. In this case, the values obtained approximate a mean value which is the one generally retained by the experimenter. Let N be the number of tests carried out, T the measured temperature and $\bar{T}$ the average value of the measurements, the random uncertainty σ_{Rdm} is estimated as follows :

$$\sigma_{\mathsf{rdm}} = \frac{1}{\sqrt{N}}\sqrt{\frac{1}{N-1}\sum_{i=1}^{N}(\,T_i - \bar{T}\,)^2}\,, \qquad \bar{T} = \frac{1}{N}\sum_{i=1}^{N} T_i\,. \tag{2.23}$$

Furthermore, we estimate the errors resulting from the Dirichlet approximation discussed in Section 3.2. This is performed through a sensitivity analysis regarding the surface temperature. The uncertainty related to this hypothesis is determined by the following expression :

$$\sigma_{\mathsf{Dlt}}(\,t\,) = \frac{\partial T}{\partial T_s}\,\delta_{T_s}\,, \tag{2.24}$$

where T_s is the temperature at the surface of the material and δ_{T_s} is the difference between both air and surface temperatures at an instant t, discussed previously in Eq. (2.44). The temperature derivative can be calculated numerically. For this, we performed a differentiation of Eq. (2.4) according to the variable T_s :

$$\frac{\partial}{\partial T_s}\left(\rho\,c_q\,\frac{\partial T}{\partial t}\right) = \frac{\partial}{\partial T_s}\left(\frac{\partial}{\partial x}\left(k_q\,\frac{\partial T}{\partial x}\right)\right). \tag{2.25}$$

Since temperature is twice derivable and its derivatives are continuous, we can invert the order of the derivation (Schwartz theorem). The thermal properties are assumed constant. A new variable θ is introduced and defined by $\theta = \dfrac{\partial T}{\partial T_s}$, so θ verifies the following equation :

$$\rho\,c_q\,\frac{\partial \theta}{\partial t} = \frac{\partial}{\partial x}\left(k_q\,\frac{\partial \theta}{\partial x}\right). \tag{2.26}$$

The equations expressing the boundary conditions of our problem are also derived according to the surface temperature and become :

$$\theta = 1\,, \quad x = 0\,,\, t\,\in\,\Omega_{\,t}\,, \qquad \frac{\partial \theta}{\partial x} = 0\,, \quad x = L\,,\, t\,\in\,\Omega_{\,t}\,. \tag{2.27}$$

Finally, at the initial state we obtain :

$$\theta = 0 \quad at \quad t = 0\,. \tag{2.28}$$

Equations (2.26), (2.27) and (2.28) constitute a closed mathematical system that we solve numerically via the implicit Euler method as well. Thus, the variable $\theta\,[-]$ is evaluated at all test instants and that enables to compute σ_{Dlt}.

On the other hand, the uncertainty related to **Hypothesis 1** σ_{1D} (one-dimensional transfer) is estimated by means of the test carried out to validate it. Theoretically, the exact evaluation of σ_{1D} is given by the following formula [134] :

$$\sigma_{\,\mathsf{1D}} = \lim_{N \to +\infty}\left(\frac{1}{N\,(\,N-1\,)}\sum_{i=1}^{N}(\,T_i - \bar{T}\,)^{\,2}\right)^{0.5}. \tag{2.29}$$

where :

$$\bar{T} = \lim_{N \to +\infty}\frac{1}{N}\sum_{i=1}^{N} T_i\,. \tag{2.30}$$

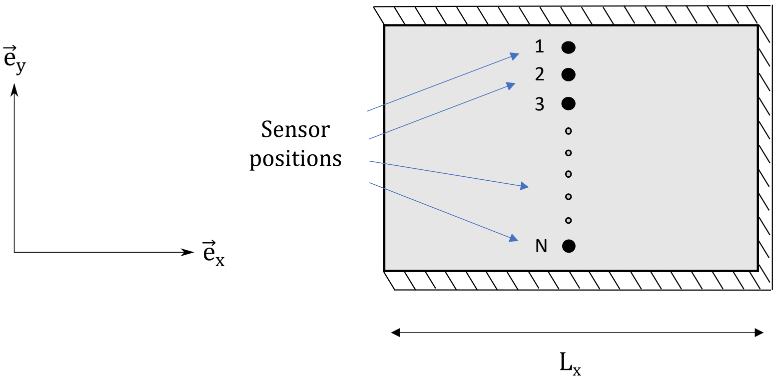

FIGURE 2.7 – Sensor positions for the evaluation of the one dimensional transfer hypothesis

N represents the number of sensors placed inside the material along the y-axis while fixing the x coordinate (Fig. 2.7). According to Eq. (2.29), the uncertainty is exact if the positions number is infinite. However, given experimental constraints, it is quite difficult to achieve this condition. Indeed, the material dimension along the y-axis, which is $y_{max} = 10\,\mathsf{cm}$, does not allow the placement of more than five sensors having a $5\,\mathsf{mm}$ diameter. Furthermore, we restricted ourselves to three to avoid interactions between sensors and perturbation of heat transfer. We used temperature measurements at the three positions χ_1, χ_2 and χ_3 (Fig. 2.4). Furthermore, the formula in (2.29) is adopted, which is normally used for the evaluation of random uncertainty, and applied to these three positions according to Eq. (2.32). $\bar{T}$ designates the arithmetic mean of the three measured temperatures.

$$\bar{T} = \frac{1}{3}\sum_{i=1}^{N=3} T_i \,. \tag{2.31}$$

$$\sigma_{\mathsf{1D}} = \frac{1}{\sqrt{3}}\sqrt{\frac{1}{2}\sum_{i=1}^{N=3}\left(T_i - \bar{T}\right)^2} \,. \tag{2.32}$$

Then, the last sub-uncertainty denoted σ_{Sensor}, is defined and introduced it in Eq. (2.19). σ_{Sensor} considers the error related to the sensor rate of adherence on the sample surface. The sensor set-up shown in Fig. 2.5, measures an area weighted mean temperature as opposite to the surface area. This is due to the fact that the sensor is not protected against the surrounding air, it adheres to the surface on the one hand and is exposed to air on the other. Uncertainty σ_{Sensor} is defined according to the following expression :

$$\sigma_{\mathsf{Sensor}}\left(t\right) = \frac{\partial T}{\partial T_{\mathsf{Sensor}}}\,\delta_{\mathsf{Sensor}} \,. \tag{2.33}$$

Equation (2.33) contains two time-dependent terms. The first represents the temperature partial derivative according to the mean temperature T_{Sensor} which is that recorded by the surface sensor. This derivative is assessed in the same way as in Eq. (2.24). The sensitivity analysis remains the same in this instance, while considering that the surface temperature is not that given by the sensor. The second term is the error between the true surface temperature T_s and that measured by the sensor T_{Sensor}. It is denoted δ_{Sensor} [°C] and its expression is given below :

$$\delta_{\mathsf{Sensor}}\left(t\right) = \left| T_{\mathsf{Sensor}} - T_s \right| \,. \tag{2.34}$$

The goal is to evaluate the error δ_{Sensor}, and for this purpose we express the temperature measured by the sensor as the weighted mean of air and the real surface temperature denoted T^{∞} and T_s respectively. Mathematically, the sensor temperature is given in Eq. (2.35) :

$$T_{\mathsf{Sensor}}\,(\,t\,) = \frac{T_s\,S_s + T^{\infty}\,S^{\infty}}{S_{Tot}}\,. \tag{2.35}$$

Where S_s, S^{∞} and S_{Tot} $[\mathsf{m}^2]$ represent sensor surfaces in adherence to the sample surface, exposed to the ambient air and the entire surface of the sensor (Fig. 2.8). These terms verify the following equality :

$$S_{Tot} = S_s + S^{\infty}\,. \tag{2.36}$$

Thus, we deduce the sample surface temperature :

$$T_s = \frac{S_{Tot}}{S_s}\left(T_{\mathsf{Sensor}} - \frac{S^{\infty}}{S_{Tot}}\,T^{\infty}\right). \tag{2.37}$$

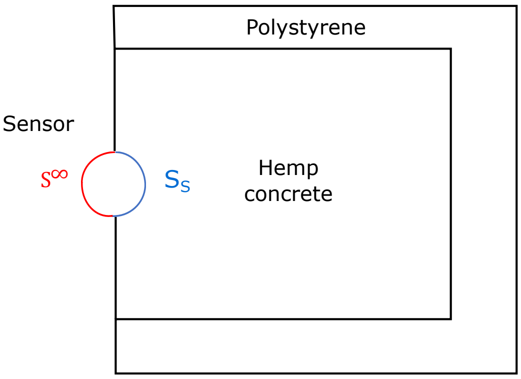

FIGURE 2.8 – The set-up adopted for the temperature sensor on the sample surface. The sensor has been increased for the illustration.

T_{Sensor} and T^{∞} are determined experimentally using the two sensors shown in Fig. 2.5. In addition, the area terms in Eq. (2.35) are set respecting the conditions of the Hypothesis 2 experiment. Finally, this information enables us to deduce the error time variation δ_{Sensor} and thus the uncertainty σ_{Sensor} at the desired position χ.

5 Results and discussion

5.1 Validation of the one-dimensional transfer (Hypothesis 1)

After the preconditioning phase, the sample was exposed to a temperature sinusoidal stress, with an amplitude of 14°C and a mean value of 25°C, where the period $\Gamma = 24\,\mathsf{h}$. The relative humidity was maintained at ϕ_0 (Fig. 2.9). The aim is to determine the quantities or expressions in order to assess the Hypothesis 1. We consider the heat transfer coefficient constant. Thus, in order to obtain a similar expression to that in Eq. (2.4), we need to ensure that :

$$\frac{\partial^2 T}{\partial y^2} \leqslant \epsilon\,, \quad \forall t \in \Omega_t\,. \tag{2.38}$$

Where y is the second space coordinate and ϵ represents a constant close to zero. This derivative can be approximated by a centered numerical scheme of second order. The approximation, at $x = x_2$, is given by the following relation, where $\Delta\, y = y\,(\chi_2) - y\,(\chi_1)$:

$$\frac{\partial^2 T}{\partial y^2} \simeq \frac{T\,(\chi_1) - 2\,T(\chi_2) + T\,(\chi_3)}{\Delta\, y^2} + o\,(\,\Delta\, y^2\,). \tag{2.39}$$

Therefore, during an experimental test, the measurements recorded on the nodes 1, 2 and 3 are used to verify the following equality :

$$T\,(\chi_1) - 2\,T\,(\chi_2) + T\,(\chi_3) = 0\,. \tag{2.40}$$

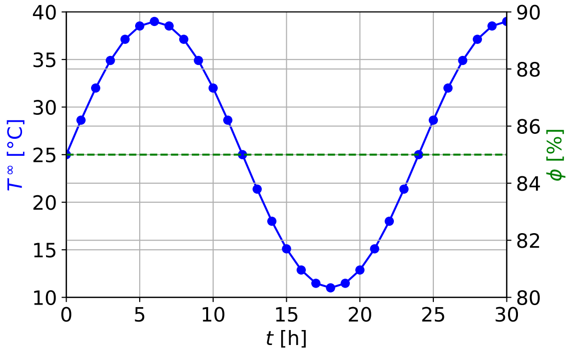

FIGURE 2.9 – boundary conditions set by the climatic chamber

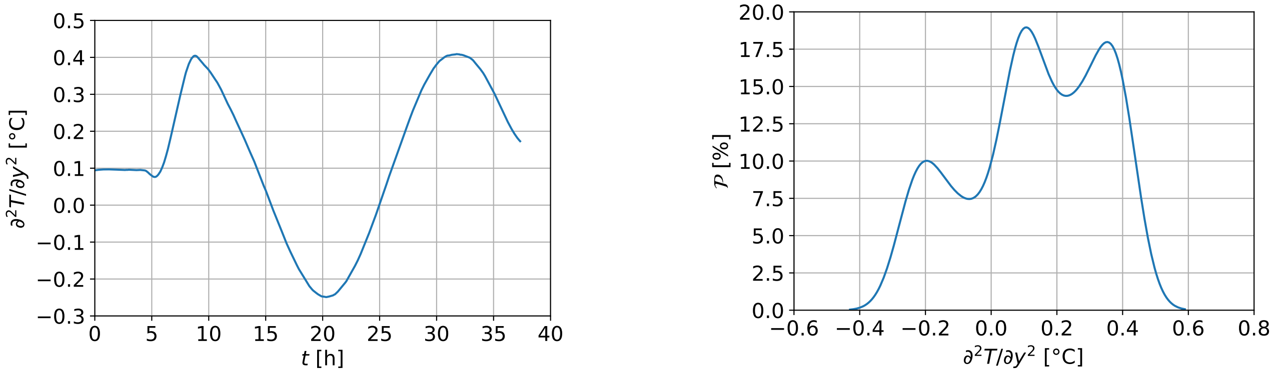

(a) (b)

FIGURE 2.10 – Temperature second derivative (a) and its value distribution (b)

By means of the quantity introduced in Eq. (2.40), it is possible to evaluate the order of magnitude of the second temperature derivative along the y axis, at each instant. Figs. 2.10a and 2.10b illustrate the variation of this quantity, as well as the distribution of its values. This distribution is evaluated using the calculation of the probability density $\mathcal{P}$ associated with the temperature second derivative along y. The probability density $\mathcal{P}$ is a function of a continuous random variable, whose integral across an interval gives the probability that the value of the variable lies within the same interval. In this work, we adopt the Kernel distribution as a probability density function. The quantity evaluated is about 0.1 °C during the preconditioning phase. During the stress period, it varies in a sinusoidal shape between 0.1 and 0.4°C (Fig. 2.10a). Figure 2.10b shows that propagation of the values is almost uniform. Indeed, the probability density varies from 10 to 20% over a large range of values. Thus, it is deduced that the hypothesis can be confirmed with a maximum error of $\epsilon = 0.4$ °C.

It is also possible to argue in terms of flow. The direction x is favored in transfer over the others if $\dfrac{\partial T}{\partial x} \gg \dfrac{\partial T}{\partial y}$ and $\dfrac{\partial T}{\partial x} \gg \dfrac{\partial T}{\partial z}$. With the sensors we dispose of, it is possible for example to compare the thermal flux φ_x and φ_y along the x and y axis respectively. Using a first order upward scheme at node 4, we can write :

$$\varphi_y = \left| -k_q \frac{\partial T}{\partial y} \right| \simeq \left| -k_q \frac{T_5 - T_4}{y_5 - y_4} \right|, \qquad \varphi_x = \left| -k_q \frac{\partial T}{\partial x} \right| \simeq \left| -k_q \frac{T_1 - T_4}{x_1 - x_4} \right|, \tag{2.41}$$

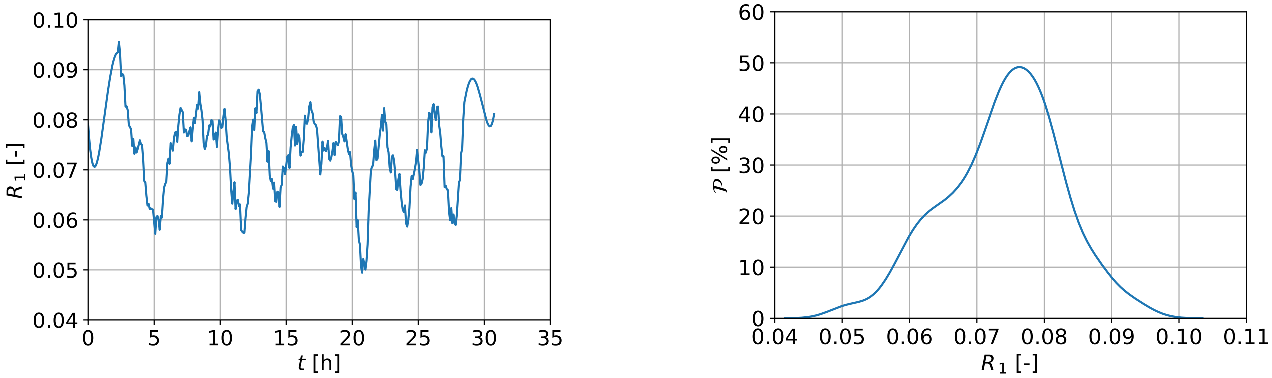

(a) (b)

FIGURE 2.11 – The heat flow along the y axis related to the one along the x axis (a) and the ratio values distribution (b).

given that $\Delta x = x_1 - x_4 = y_5 - y_4 = \Delta y$. We can define the ratio R_1, which represents the quotient of the two introduced fluxes. R_1 is calculated as follows :

$$R_1 = \frac{\varphi_y}{\varphi_x} \,. \tag{2.42}$$

R_1 compares the order of magnitude of the studied fluxes. It is evaluated during the same experiment, and its variation is shown in Fig. 2.11a. The values can be as low as 0.05 and up to 0.09. This means that the flux along the y axis is 10 to 20 times smaller than the one along x. This is mainly due to the fact that the x-axis direction is privileged when insulating the surrounding faces. This aspect can be reinforced by increasing the length and increasing the thermal insulation. Fig. 2.11b shows the distribution of the ratio values. It is around 0.075 for a probability of 50%. In addition, a complementary investigation was developed to evaluate the error due to the one-dimensional transfer design. A comparative numerical study was performed between the proposed one-dimensional case and the experimental case. On the one hand, the experimental case reproduces the realistic conditions in the climate chamber as shown on the left in Fig. 2.12a.

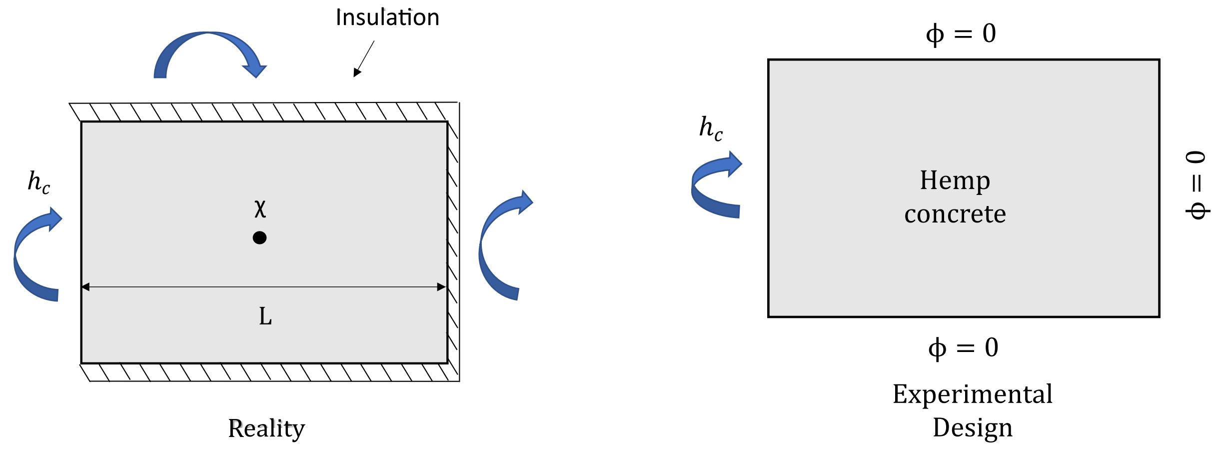

(a) (b)

FIGURE 2.12 – (a) Realistic model of the experiment in two dimensions, (b) lumped approach in one dimension

Figure 2.12b represents the lumped approach modeled in one-dimension as considered in our work. In this case, a 4 cm polystyrene thickness and a convective coefficient $h_c = 5\,[\mathsf{W.m^{-2}.K^{-1}}]$ are considered. On the other hand, the ideal case consists of considering perfectly adiabatic walls where the heat flux equals 0; see Fig. 2.12b. Numerical computations of the temperature for both cases were carried out using `COMSOL` software. Indeed, the method used in the experimental design (Eq. (2.41)) is an approximation employing the following meshes $\Delta x = \Delta y = 5\,\mathsf{cm}$.

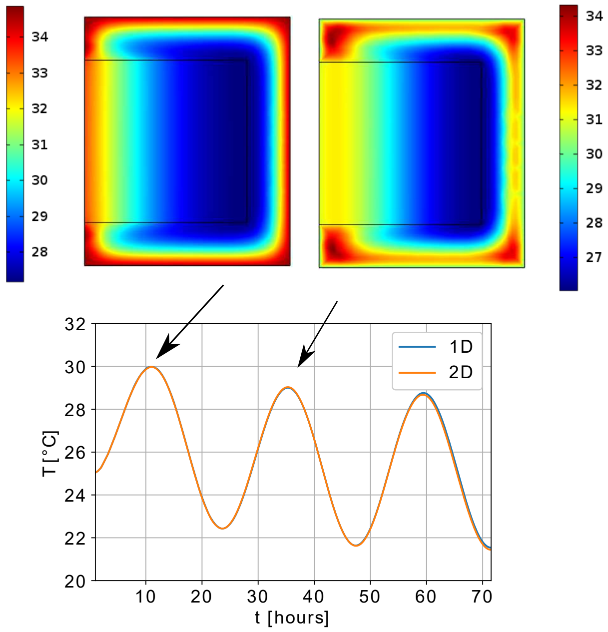

FIGURE 2.13 – Temporal temperature evolution at the middle of the sample between the $1D$ and $2D$ heat transfer approach

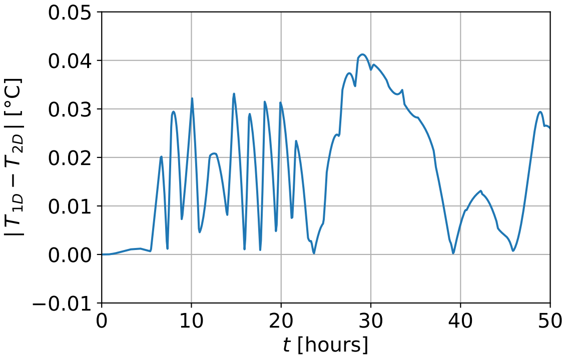

FIGURE 2.14 – Temperature error evaluation at the middle of the sample between the two approaches.

Thus, to overcome this issue we performed a numerical simulation using smaller meshes $\Delta x = \Delta y = 10^{-3}\,\mathsf{cm}$. Both materials were modeled considering $4\,\mathsf{cm}$ and $10\,\mathsf{cm}$ thickness for polystyrene and hemp concrete respectively. The Robin type was considered for boundary conditions where $h_c = 17\,\mathsf{W.m^{-2}.K^{-1}}$ as a conventional value and T^{∞} was provided by the ambient air sensor.

Fig. 2.13 presents the variation of temperature at the middle of the sample for both approaches. As shown in Fig. 2.13, the temperature variation when adopting the experimental design is close to that of the theoretical 1D model. In addition, errors are noticeable, for example at the instants $t = 10,\ 35,\ 58\,\mathsf{h}$. The overall error variation at the middle of the sample is given in Fig. 2.14. The error is small and ranges from 0 to $0.04\,°\mathsf{C}$. A second investigation consisted in the numerical evaluation of R_1 at the same position used for measurements. Its time variation, using a logarithmic scale, is illustrated in Fig. 2.15.

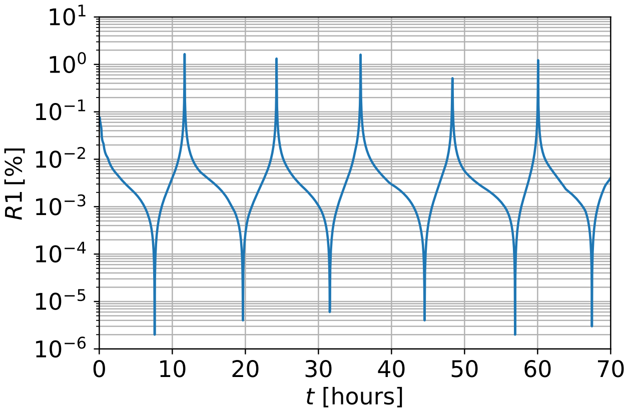

FIGURE 2.15 – Variation of the heat flux ratio R_1

Notice that R_1 is smaller than the one assessed experimentally. It is almost zero during long time sequences. In addition, there are some instants where the ratio reaches maximum values of about $1.1\,\%$. The choice of a mesh size equal to $10^{-3}\,\mathsf{cm}$ along the x and y axis was sufficient to obtain a numerical solution with a suitable accuracy. This was deduced by performing a study of sensitivity according to the mesh size. In this framework, two additional simulations, where

$\Delta x = \Delta y = 10^{-5}\,\mathsf{cm}$ and $\Delta x = \Delta y = 10^{-7}\,\mathsf{cm}$, were performed while maintaining the same time step. The study revealed that the variation of the ratio R_1 is almost the same for smaller mesh sizes. In terms of deviation, a maximum value of 10^{-8} was reached when comparing the three variations. Thus, choosing smaller mesh sizes did not have a significant influence on the magnitude of this numerical result. Another study was performed to analyze the heat map of our configuration following two instants. Both heat maps are illustrated in Fig. 2.13. It is worth noting that the isothermal lines obtained are perpendicular to the direction along x in hemp concrete. If we focus on the insulation material, the isothermal lines have no longer this characteristic. This means that heat transfer in hemp concrete tends to be one-dimensional. Moreover, it is possible to confirm this by studying flux streamlines. Fig. 2.16 plots these at the same instants. Notice that heat flux is mostly along the x direction in the studied material.

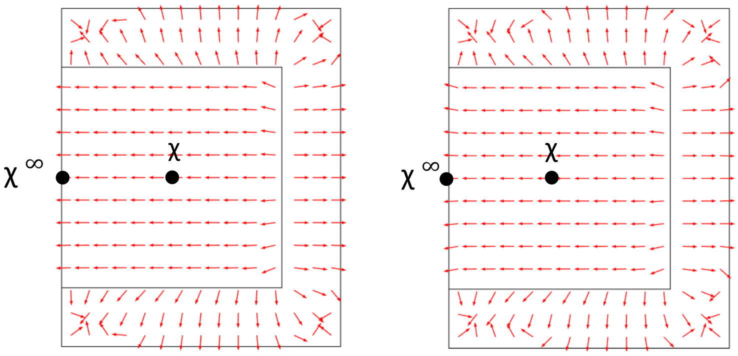

FIGURE 2.16 – Streamlines representing the heat flow direction within the hemp concrete and the insulator at two different instants (a) $t = 10\,h$ and (b) $t = 35\,h$

5.2 Validation of the Dirichlet approximation (Hypothesis 2)

In a realistic case, the boundary condition of a material in contact with a fluid is defined as follows :

$$-\frac{\partial T}{\partial x} = \frac{h_c}{k_q}\left(T^{\infty} - T\right), \qquad x = 0\,. \tag{2.43}$$

This is the Robin boundary condition, where T^{∞} [K] is the ambient temperature and h_c [W/(m^2.K)] the surface heat transfer coefficient. Notice that, if h_c is large or the thermal conductivity is small, we face a situation where thermal flux is large. Thus, the equality (2.43) is possible as long as we verify that $T \simeq T^{\infty}$ at the material surface, which corresponds to the Dirichlet condition. The two considered hypotheses for the convective thermal coefficient and thermal conductivity can be approached experimentally. A material with high insulating potential can be chosen. Moreover, the coefficient depends on the nature of the fluid flow and the surface imposed to the impact. In particular, it depends on the flow velocity according to the Nusselt number. Hemp concrete has a good insulating potential which is characteristic of hemp concrete. In addition, we studied the condition regarding the thermal coefficient h_c. Based on the position of the sensors in the configuration (Fig. 2.5), the goal is to verify the following expression :

$$\left|\,T\,(x = 0, t) - T^{\infty}\,\right| \leqslant \epsilon\,, \quad \forall t \,\in\, \Omega_{\,t}\,. \tag{2.44}$$

A preconditioning phase not being necessary, we used the same stress adopted for the validation of the first hypothesis and shown in Fig. 2.9. The variation of both temperatures is shown in

Fig. 2.17. We observe that the variation is almost the same as shown in Figs. 2.18a and 2.18b. Indeed, the comparison over two different time ranges highlights the quasi-superposition of both curves.

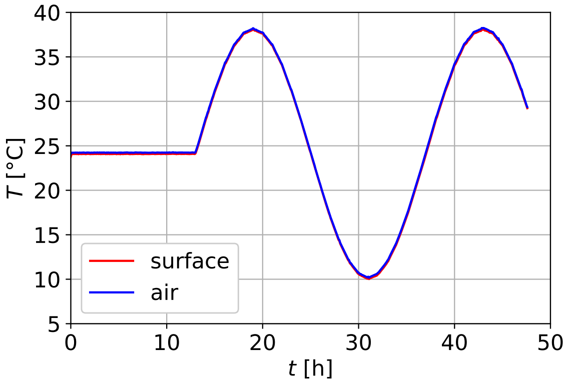

Figure 2.17 – Variation of air and material surface temperatures during the preconditioning and the stress phases

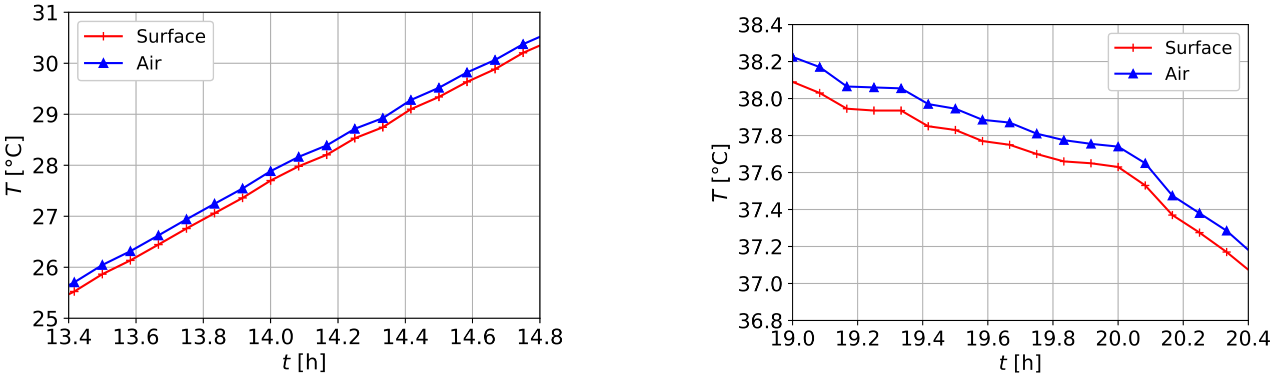

(a) (b)

Figure 2.18 – Air and material surface temperatures at two different experiment sequences

In addition, it was possible to evaluate the discrepancy throughout the experiment as well as its corresponding distribution (probability density). It ranges from 0.075 to 0.225 °C (Fig. 2.19a). It was also demonstrated that it is centered around 0.15 °C as shown in Fig. 2.19b. Under similar conditions and with regard to these results, Hypothesis 2 is validated, with an uncertainty on surface temperature reaching 0.225 °C. Thus, $\delta_{T_s} = 0.225$ °C.

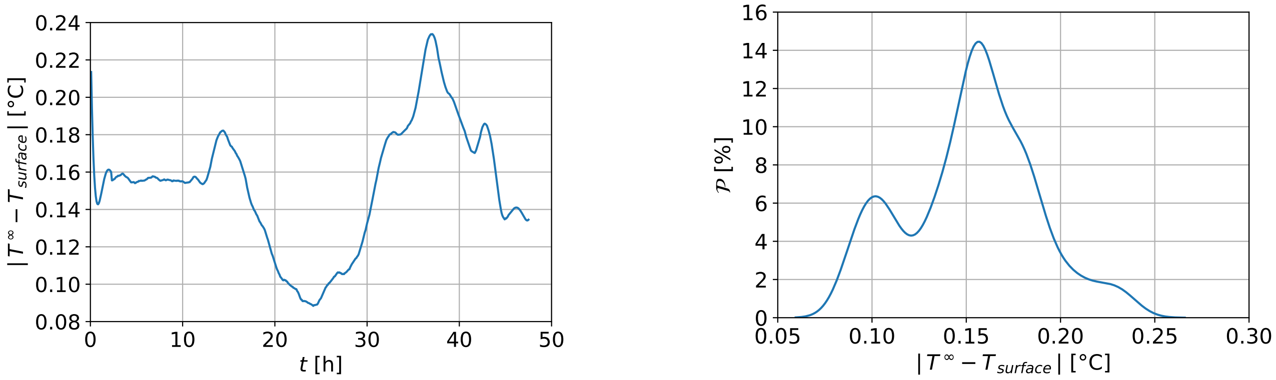

(a)

(b)

FIGURE 2.19 – The calculated discrepancy between the measured air and material surface temperatures (a) discrepancy distribution throughout the experiment

5.3 Assessment of thermal similarity

5.3.1 Definition of the case

Calculation of the uncertainties is necessary in combination with the results of experimental work. It helps defining the acceptable margin of uncertainty on a measured quantity. After having introduced the seven sub-uncertainties, they are evaluated for both configurations. The reference configuration is given using a $L_1 = 15\,\text{cm}$ thick material. This sample is exposed to the same stress, that is presented in Fig. 2.9, where the experiment horizon is $t_1^{\text{ref}} = 72\,\text{h}$ and the time period $\Gamma_1 = 24\,\text{h}$.

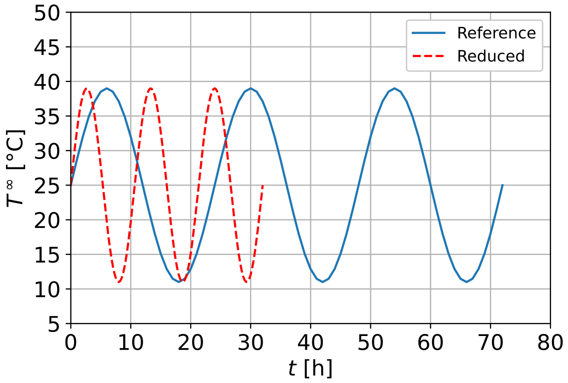

FIGURE 2.20 – The equivalent boundary conditions

The equivalent configuration was based on a smaller sample with a thickness of $L_2 = 10\,\text{cm}$. Thus, the factor of proportionality is $\Sigma = \dfrac{2}{3}$. By means of the expression in Eq. (2.15), a reduced experiment duration was obtained where $t_2^{\text{ref}} = 32\,\text{h}$ and $\Gamma_2 = 10.66\,\text{h}$. The evaluation of uncertainties was limited to the middle values of both samples $x_1 = 7.5\,\text{cm}$ and its equivalent $x_2 = 5\,\text{cm}$. The boundary conditions defining the two configurations are illustrated in Fig. 2.20.

5.3.2 Evaluation of measurement uncertainties

We recall that the systematic uncertainty is $0.3\,^{\circ}\mathsf{C}$ according to the manufacturer documentation. Its thermal response time is about $\delta_t = 10\,\mathsf{s}$. The sensor position uncertainty is approximately the diameter of the sensor, corresponding to $\delta_x = 5\,\mathsf{mm}$. It is worth noting that the uncertainties σ_x, σ_t, σ_{DIt}, σ_{Sensor} and σ_ϕ are determined numerically. The first four are computed by solving Eq. (2.4) and using the implicit Euler scheme. The space and time meshes are given for both configurations : $\Delta x_1 = 1.5\;10^{-2}\,[\mathsf{cm}]$, $\Delta t_1 = 8.3\;10^{-2}\,[\mathsf{h}]$, $\Delta x_2 = 10^{-2}\,[\mathsf{cm}]$ and $\Delta t_2 = 3.6\;10^{-2}\,[\mathsf{h}]$. Furthermore, σ_ϕ is calculated using a coupled heat and mass transfer model [93]. This model was computed with the finite element solver COMSOL Multiphysics. The hemp concrete properties are issued from [72]. The random uncertainty is calculated by running three times the experiment for each configuration, therefore $N = 3$. Whereas, σ_{1D} is evaluated based on the experimental results for the sample shown in Fig. 2.4. Its thickness corresponds to the one of the reduced configuration sample. Thus, the results during t_2 are adopted for the reduced configuration. In the reference case, we consider that the results in terms of σ_{1D} are equivalent. Finally, the experimental configuration to evaluate the hypothesis 2 (Fig. 2.8) corresponds to a surface $S_s = 0.1\,S_{Tot}$. This means that the surface of the sensor, adhering to the sample, represents $10\,\%$ of its total surface. The processing of experimental and numerical data, as well as the plotting of curves is done using the programming language PYTHON.

Figure 2.21 highlights the time propagation of uncertainties related to the reference case at the middle of the sample. In order to compare, note that σ_x and σ_ϕ are of a significant order of magnitude. They attain values ranging from 0.2 to $0.6\,^{\circ}\mathsf{C}$. Whereas σ_{DIt} varies in the shape of an exponential increasing from 0 to $0.2\,^{\circ}\mathsf{C}$. In parallel, σ_{1D} varies in a quasi-sinusoidal shape and reaches peaks of about $0.1\,^{\circ}\mathsf{C}$. These instants correspond to the attainment of maximum air temperatures. Conversely, this uncertainty is small (less than $0.01\,^{\circ}\mathsf{C}$) during the air-cooling phase. On the other hand, the uncertainties related to the thermal response of the sensor and the random aspect of the test are negligible. Regarding σ_{Sensor}, the evolution is quite the same between both configurations. Furthermore, each curve is almost periodic due to temperature stress periodicity. The uncertainty is quite zero at the beginning of the experiments and reaches a maximum value of $0.18\,^{\circ}\mathsf{C}$.

We conclude that the total uncertainty of the reference case is oscillatory, almost periodic and varies between 0.4 and $0.8\,^{\circ}\mathsf{C}$. The reduced configuration is also approached in terms of uncertainties. As seen in Fig. 2.21, the order of magnitude of the calculated uncertainties remains the same. Nevertheless, there is a big difference between the reference and reduced configuration. σ_x, σ_ϕ and σ_{Rdm} are as important as we decrease the dimensions of the sample. Indeed, these uncertainties vary with the thickness of the sample. They are small for thick materials, and large for a-thin ones. In this case, it is due to the magnitude of relative humidity and temperature gradients. It varies differently around the equivalent positions x_1 and x_2. They are more important in the reduced case. σ_t, σ_{DIt} and σ_{Sensor} remain unchanged. Moreover, these do not depend on the factor of proportionality Σ, so increasing or decreasing the thickness of the sample does not influence these two uncertainties. Finally, the entire uncertainty is considerably greater than in the reference case. It reaches a maximum of $1.25\,^{\circ}\mathsf{C}$. Figs. 2.24a and 2.24b enable to visualize at two different time sequences the accumulated sub-uncertainty bands. Note that the magnitude of the entire uncertainty is not negligible. Consequently, it is necessary to carry out a calculation highlighting the propagation of uncertainties for the experimental results.

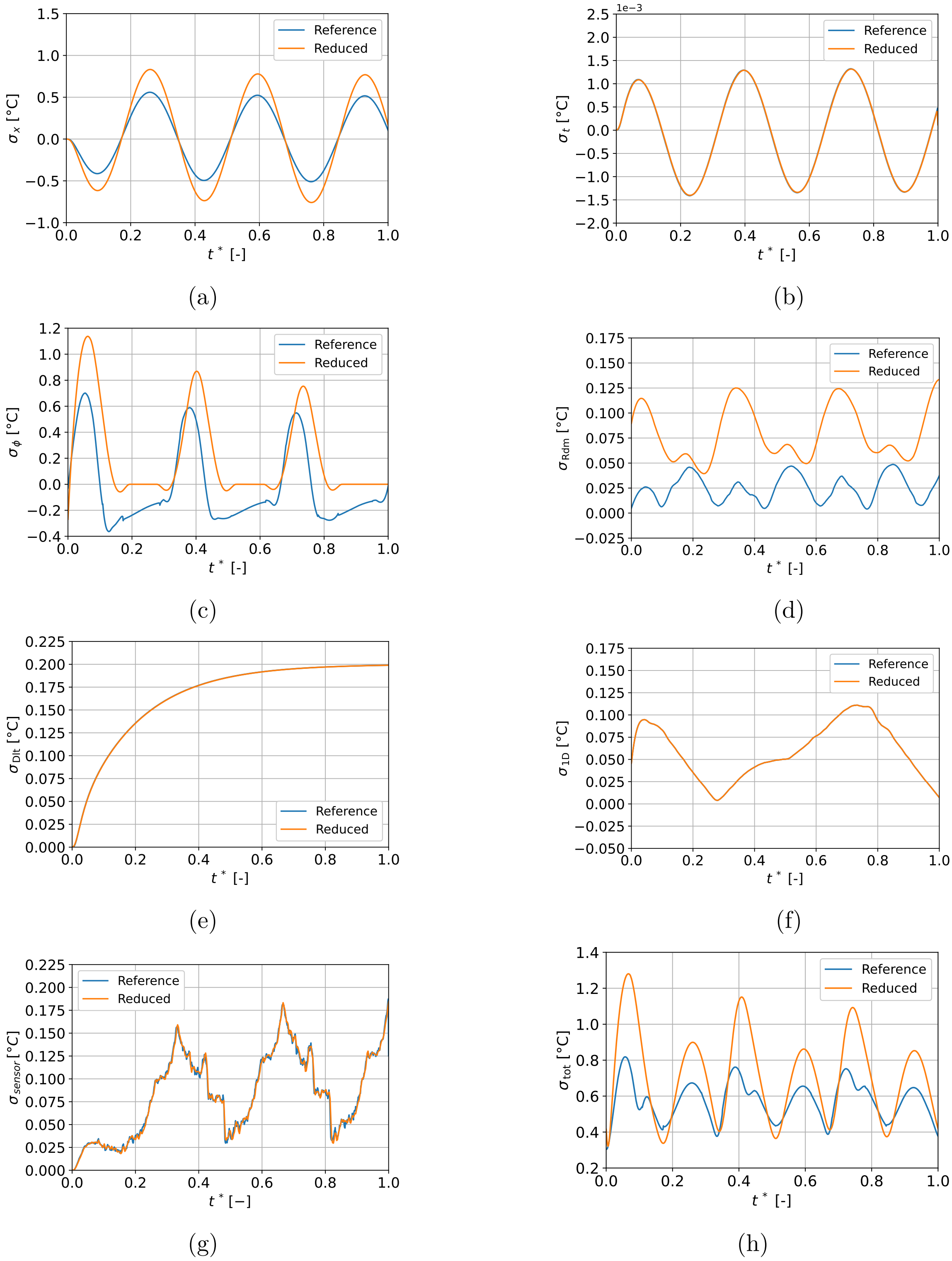

FIGURE 2.21 – Time variation of the uncertainties related to both reduced and reference configurations. Uncertainty due to (a) the sensor position, (b) its response time, (c) the mass transfer neglect, (d) the random aspect, (e) Hypothesis 2 and (f) Hypothesis1, (g) the sensor adherence rate to the sample surface. (h) Deduction of the entire uncertainty.

5.3.3 Discussion of validity of the thermal similarity

The parameters related to both tests and the boundary conditions (Fig. 2.20) were well defined in the previous section. The validity of the thermal similarity between the experimental results will be carried out on x_1 and x_2. The time variation in temperature at x_1 and x_2 in the dimensionless domain is shown in Fig. 2.22. We have approximately a good agreement between the similar cases and note that both curves have the same shape.

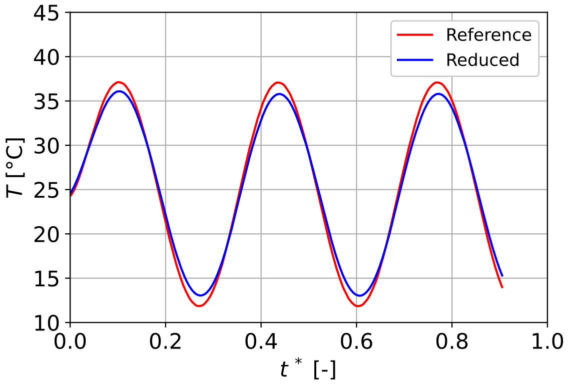

FIGURE 2.22 – Variation in temperature at $x^\star = 0.5\,[-]$ in the equivalent configurations.

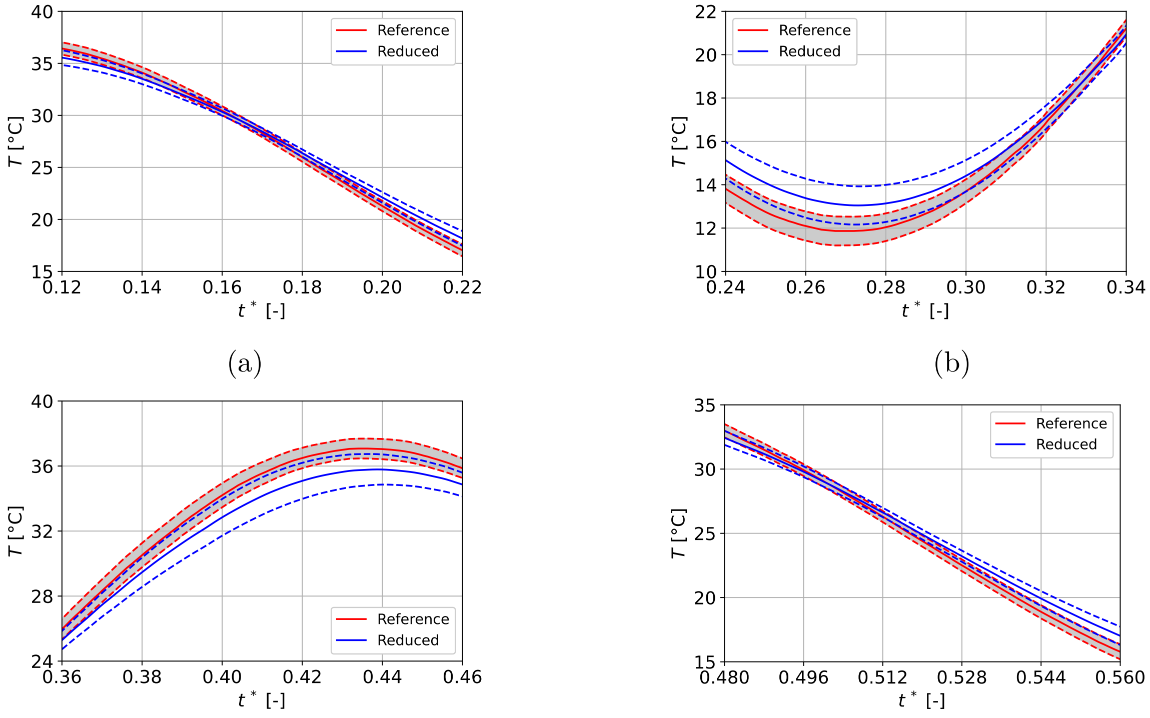

(a) (b)

(c) (d)

FIGURE 2.23 – Time variation in temperature at $x^\star = 0.5\,[-]$ during four different sequences. The dashed lines represent the entire uncertainties that correspond to each configuration.

Nevertheless, there are instants where the discrepancy increases relatively. These moments correspond to the minimum or maximum air temperature. This difference in magnitude could be interpreted in several ways. The water content in the samples may not be the same. Indeed, the thermal conductivity increases with water content. In our case, the reference sample would be more humid, as it reaches greater limits than the one representing the reduced case. The micro-structure and the pore distribution may also be the source of these discrepancies. A more porous material has lower thermal conductivity due to the presence of air. In order to include the calculated uncertainties in the experimental measurements, we focused more on sequences with a large discrepancy. This is illustrated in Fig. 2.23. It compares some experimental results while embedding the related entire uncertainties. The measurements are represented in a straight line. Moreover, the interval delimited by the dotted lines represents the range of the calculated entire uncertainty. During four different sequences, the uncertainty intervals for each configuration match within areas of different magnitudes.

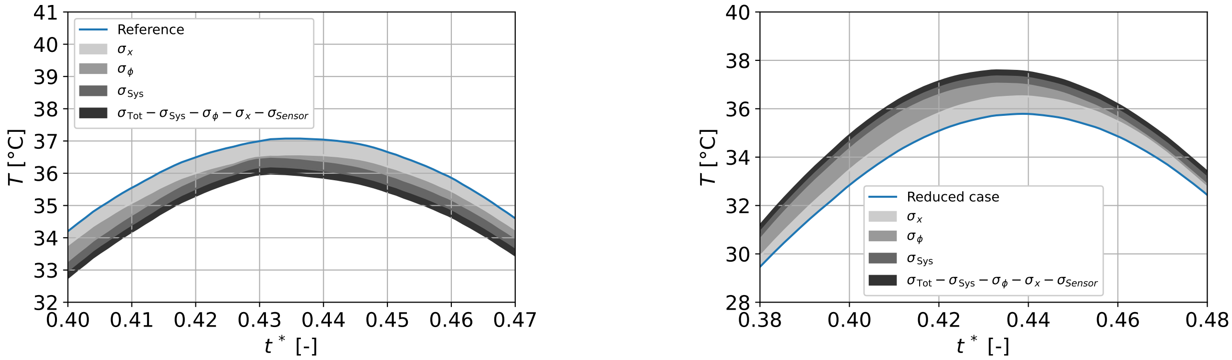

(a) (b)

FIGURE 2.24 – Temperature variation at two given time sequences for the reference case (a), and the reduced one (b) with the corresponding confidence intervals : sensor position σ_x, mass transfer influence σ_ϕ, sensor calibration σ_{Sys} and the remaining uncertainties $\sigma_t + \sigma_{\mathrm{Rdm}} + \sigma_{\mathrm{Dlt}} + \sigma_{\mathrm{1D}} + \sigma_{\mathrm{Sensor}}$.

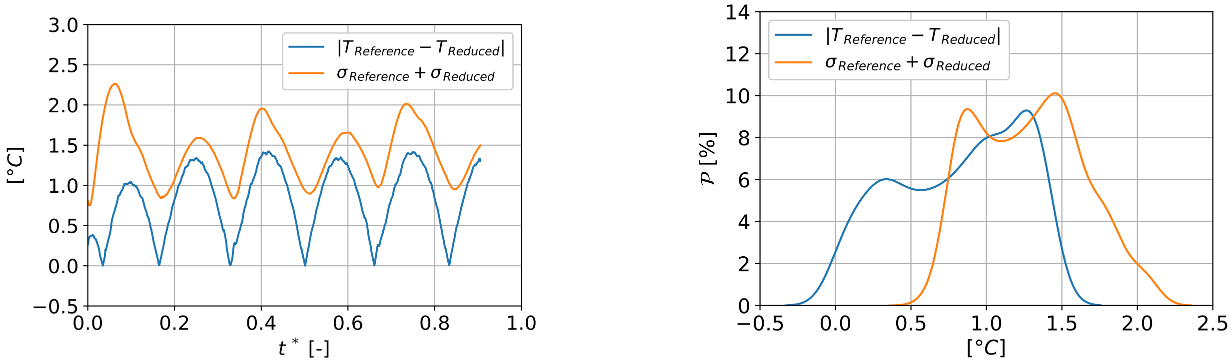

(a) (b)

FIGURE 2.25 – Temperature discrepancy and entire uncertainty between the configurations and the corresponding distributions

Regarding both experiments, the discrepancy reaches a maximum of about 1.5 °C as shown in Fig. 2.25a. On the other hand, the probability density shows a certain uniformity in the discrepancy distribution (Fig. 2.25b). The value 1.5 °C is largely justified by means of the calculated uncertainties $\sigma_{\mathsf{Tot}\,1}$ and $\sigma_{\mathsf{Tot}\,2}$. Indeed, $\sigma_{\mathsf{Tot}\,1} + \sigma_{\mathsf{Tot}\,2}$ is plotted with the discrepancy in the same Figure. Notice that the sum of both entire uncertainties is above the observed discrepancy most of the time. It ranges from 0.6 to 2 °C with an average of about 1.5 °C. (Fig. 2.25b).

5.4 Discussion and further remarks

In order to carry out a similarity experiment, it is essential to control the conditions of equivalent configurations. The experimental results confirm the similarity law within a given margin of error (Fig. 2.22). Indeed, discrepancies during some sequences were observed. These instants correspond to large temperature gradients. Discrepancies result mainly from certain experimental imperfections. In this study, the use of similarity laws was limited to a one-dimensional heat transfer case using a thermal insulator. In a more general case, similarities could also be applied to a three-dimensional case. As an example, a non-insulated cubic sample exposed to a thermal stress, can be the basis of a similarity study. Indeed, the governing equations and the dimensionless formulation are written this time according to three space dimensions L_x, L_y and L_z. As a result, the FOURIER number concept is extended. Thus, similarities between two different configurations are written according to Eq. (2.45) :

$$\mathrm{Fo}_x^1 = \mathrm{Fo}_x^2 \,, \quad \mathrm{Fo}_y^1 = \mathrm{Fo}_y^2 \,, \quad \mathrm{Fo}_z^1 = \mathrm{Fo}_z^2 \,. \tag{2.45}$$

where :

$$\mathrm{Fo}_{\mathrm{x}} = \frac{k_q^{ref}\, t_{ref}}{c_q^{ref}\, L_x^2} \,, \quad \mathrm{Fo}_{\mathrm{y}} = \frac{k_q^{ref}\, t_{ref}}{c_q^{ref}\, L_y^2} \,, \quad \mathrm{Fo}_{\mathrm{z}} = \frac{k_q^{ref}\, t_{ref}}{c_q^{ref}\, L_z^2} \,. \tag{2.46}$$

In addition, these laws can be applied to other types of boundary condition. In this study, the type Dirichlet was adopted to represent the conditions at the surface where $x = 0$. Dirichlet is the simplest type to model since temperature is assumed known at the surface. As for the Neumann type, an incident heat flux $\varphi\,[\mathsf{W.m}^{-2}]$ is considered. In this case, similarities involve, apart from FOURIER, a second dimensionless number, defined via Eq. (2.47) :

$$\frac{\varphi^{ref}\, L}{k_q^{ref}\, T^{ref}} \,. \tag{2.47}$$

Regarding the ROBIN type, it represents the most realistic boundary condition. It involves two following parameters : air temperature and a surface heat exchange coefficient h_c. Similarities can also be applied in this case. If we ensure the same variation of air temperature in both configurations, then these laws can be expressed through Eq. (2.48) :

$$\mathrm{Fo}_q^1 = \mathrm{Fo}_q^2 \,, \quad \mathrm{Bi}_q^1 = \mathrm{Bi}_q^2 \,. \tag{2.48}$$

The BIOT number Bi involves h_c according to the following expression :

$$\mathrm{Bi}_q = \frac{h_c\, L}{k_q^{ref}} \,. \tag{2.49}$$

In this case, if we assume the use of the same material in similarity tests, thus resulting in $k_{q\,1}^{ref} = k_{q\,2}^{ref}$, we obtain the following result :

$$h_c^1 = h_c^2\, \Sigma \,, \quad \textit{where} \quad \Sigma = \frac{L_2}{L_1}. \tag{2.50}$$

Clearly, imposing a factor of proportionality such that $\Sigma \neq 1$ means that the experiments must be represented by two different thermal coefficients h_c^1 and h_c^2. In this respect, the knowledge of this coefficient requires a complete characterization of the employed climate chamber, which leads to additional challenges. Indeed, the characterization depends on certain parameters such as the chamber size, air thermal properties as well as the flow velocity. Given that the chamber nor the fluid were changed, a variation of this coefficient could be caused only by an air velocity variation. It is therefore necessary to establish a law expressing h_c according to air velocity. Through this, it would be possible to fix the desired coefficient h_c by varying the flow velocity, which represents another challenge. Finally, this method would require a major investigation for cases considering a realistic boundary condition such as ROBIN.

Furthermore, there are uncertainties that can not be reduced. These are the ones related to the precision and response time of used equipment (sensors, measuring devices). There is also the random uncertainty which is due to the space variability of a material. In addition, the positioning of sensors induces also an unavoidable uncertainty that is proportional to the diameter of the sensor. On the other hand, other uncertainty sources can be controlled. In our case, they are the ones resulting from the three hypotheses initially set out. It was noticed that the effect of mass transfer on temperature is not quite negligible, and this was confirmed via the assessment of the uncertainty related to this hypothesis. The computation of this uncertainty was performed by means of Comsol Multiphysics. It is a numerical simulation software based on the finite element method. This software allows to simulate many physics and engineering applications, and especially coupled phenomena or multi-physics simulation. The last mentioned uncertainty was the predominant of the problem with values approaching 1 °C. Therefore, it would be important to define similarities taking into account the coupling of heat and mass transfer phenomena. This also requires a good control of the material initial moisture state and moisture boundary conditions.

Due to the heterogeneity of the material, it was not that easy to overcome fully the uncertainty due to the one-dimensional transfer hypothesis. The heat flux is slightly smaller in the directions with more pores. Moreover, the presence of air decreases the thermal conductivity in these areas. Another important factor is the order of magnitude of the involved thermal conductivity. Indeed, the magnitude of this property is very similar between hemp concrete and polystyrene with the following values 0.100 and 0.032 $\mathsf{W.m^{-1}.K^{-1}}$. On the other hand, the uncertainty related to this hypothesis can be reduced by improving the insulation of the material. This uncertainty will persist unless one of the two following possibilities is verified experimentally. The thermal conductivity of the insulator equals zero. The second possibility requires the use of an insulator with an infinite thickness. With only 4 cm, the one-dimensional transfer hypothesis was acceptable. The validation of the latter was based on a study which compared the real experimental approach and the lumped one representing a perfect one-dimensional case. In the above-mentioned investigations, analysis of temperature profiles was performed as well as the observed discrepancies. Heat maps and flux streamlines in experimental approach were discussed.

Moreover, it would be more appropriate to choose the right type of boundary conditions to better control similarity tests. Indeed, we emphasize that only air temperature is controlled in contrast to the one of the surface. Thus, we would not have necessarily a similarity in terms of surface temperatures, which is something that must be ensured. In order to control this temperature, suitable heating plates could be used, which adhere to the surface of the material. However, it would not be possible to vary it according to a variable time scenario. On the other hand, we ensure its perfect control. It would also be possible to use the Robin condition to control better climate scenario similarities, by varying the convective coefficient h_c in both configurations. This would be possible through the use of a climate chamber controlling not only air temperature and relative humidity, but also the flow rate of fans and thus the airflow velocity. Afterwards, similarity was established based on an additional assumption. It was assumed that the two samples used for tests have the same porosity. In reality, it was shown that hemp concrete has a porosity of about 72% [41]. Nevertheless, there is a margin of uncertainty related to this value. The latter can be estimated through reproducibility, which consists in evaluating the porosity of several samples issued from a same material. As a result, both samples have porosity around the mentioned value but slightly different. In this case, the heat transfer coefficient and density, which are directly correlated to porosity, are not exactly the same. Thus, it would have been possible to include this additional source of uncertainty in this study, by carrying out an analysis of sensitivity regarding these two coefficients.

Lastly, when analyzing the literature, it was important to find studies where the validity of similarities had been investigated experimentally on a similar problem. A relevant study, that combined experimental (reduced configuration) and numerical approaches (real configuration), assessed the accuracy of these laws on a heat and mass transfer problem [96]. The real system corresponded to a multi-layer wall which was exposed to the climate stress of Tokyo during two years. Subsequently, this configuration was reduced by proposing 0.2 as factor of proportionality. The analysis of temperature results showed that both configurations led almost to equivalent variations. In this regard, results were satisfying with a maximum deviation of 1 °C. This discrepancy could be due to an uncertainty on both convective and radiation coefficients in the reduced configuration. In terms of comparison, there are some reasons that would not allow to confront correctly the results of this reference to those of our article. Differently from the heat equation, the model in [96] considers moreover the coupling with mass transfer, and water activity was the driving potential. Furthermore, the boundary conditions are not the same, i.e. the Robin type was adopted while considering convective and radiation effects. Finally, the nature of the materials constituted a third factor. Indeed, a composite material, highly heterogeneous and with high porosity was used in our study. Meanwhile, the mentioned research employed ordinary materials with medium porosity. In addition, it is worth noting that the heterogeneity of a material and its pore distribution can impact significantly the results of two similar configurations. In other words, the larger is the space variability of macroscopic properties, less identical are the material samples that are selected to carry out a similarity experiment.

6 Conclusion

The conclusions of the work are the following :

1. Certain experimental protocols, related to transfer phenomena, entail a long period. These tests can last several months [102]. In order to address this problem and reduce the du-

ration of experimental campaigns, the laws of similarity were used for a heat conduction problem. It enabled the reduction of a reference configuration by means of a reduced version. This study aimed to assess the validity of these laws through an experimental analysis. Based on similarities, an equivalent configuration was obtained verifying the factor of proportionality Σ. The duration of this configuration was therefore reduced by Σ^2. The one-dimensional transfer was ensured in both cases through the use of thermal insulation on the surrounding faces. Subsequently, the two configurations underwent similar thermal stress where both duration are proportional according to Σ^2.

2. During both experiments, the aim was to measure and compare the temperature in equivalent positions. In order to discuss the validity of similarity, a complete evaluation of uncertainties was carried out. Uncertainties on sensor position, sensor response time, mass transfer effect, the systematic accuracy, the random aspect, the one dimensional transfer hypothesis, the modeling of a boundary condition and the one related to the adherence rate of a sensor were evaluated. The measurements in both configurations showed an acceptable agreement. The calculated discrepancy between equivalent fields of temperature reached 1.5 °C as a maximum value. It was often observed at instants corresponding to high air temperature gradients.

3. In terms of uncertainties, the analysis showed that σ_x and σ_ϕ are the most preponderant ones. It was also demonstrated that the entire uncertainty is greater in the reduced configuration compared to the one in the reference. Finally, the time variation of both tests induced non negligible discrepancies which were justified by means of entire uncertainties. Indeed, the sum of the latter for both configurations is much greater than the measured discrepancy.

4. The validity of thermal similarities is relatively confirmed as long as the hypotheses of the model are well controlled. Furthermore, these laws could also be extended to the coupled heat and mass transfer model and be verified for both temperature and relative humidity fields. In this regard, an important assumption concerns the material properties. It is assumed that thermal conductivity and heat capacity do not change in both configurations. This assumption is acceptable for heat transfer properties but requires further investigation for coupled heat and mass transfer, particularly for building materials with complex micro-structures such as hemp concrete. For this reason, the extension of similarity for coupled heat and mass transfer in porous building material should be demonstrated.

Acknowledgements

The Region and the European Union support the project <CPER-FEDER Bâtiment durable Axis 2 MADUR Project : High-performance building materials with low environmental impact, sustainable and resilient> within the framework of the « Operational Program FEDER/FSE 2015-2020 and Energy saving certificate program of the Ministry of Ecological and Solidarity Transition "SmartReno support" 2019-2021.

Chapitre 3

Experimental assessment of the similarity law for a one-dimensional coupled heat and water vapor diffusion in hemp concrete

Abstract

Similarity law is a mathematical mapping that aims to set up equivalences between different configurations regarding the involved physical parameters, space dimensions and the duration of the configuration. These equivalences are defined by means of the dimensionless formulation of the physical model that describes a phenomenon. This concept is widely adopted in some scientific fields, notably in computational fluid dynamics. In heat and water vapor diffusion, similarities are applicable theoretically on configurations distinct in terms of material, space dimensions, duration or even imposed stress magnitude. It is worth noting that these are slow kinetic phenomena. In this regard, this study aims to verify similarities experimentally while using hemp concrete and reducing the duration of a reference experiment. Before performing measurements, two main limitations are fixed. First, by means of an experimental design, heat and moisture transfer are assumed one-dimensional. In addition, Dirichlet boundary conditions are considered at the surface that is exposed to ambient air. Mainly, temperature and relative humidity are measured at the quarter and middle of the material in order to compare the two similar configurations. Afterwards, an uncertainty study is carried out in order to discuss and justify the observed discrepancies. Following a deterministic approach, this investigation considers five sub-uncertainties which are related to : the calibration of used sensors, their positions, time of response, randomness of an experiment and the boundary condition modeling. Results show a good agreement between the reference and reduced configurations. Indeed, the discrepancies between both are entirely within the calculated confidence intervals.

Highlights

1. Similarity laws are verified in the framework of a one-dimensional heat and water vapor diffusion problem through an experimental campaign.
2. Two configurations of hemp concrete samples, equivalent in terms of similarity laws, are exposed to thermal and hydric stress.
3. Temperature and relative humidity at equivalent positions in both samples are measured and compared.
4. A detailed uncertainty investigation is proposed to discuss the reliability of the observed discrepancies.
5. The comparison of discrepancies and entire uncertainties show a good agreement between the reference and reduced configurations.

Keywords

Heat conduction and water vapor diffusion, similarity analysis, porous material, experimental bench-marking, uncertainty quantification.

1 Introduction

Worldwide, the building sector is responsible for a consumption of 44 % of global energy. A significant part of building losses is due to the behavior of the envelope. Therefore, a decrease in the energy consumption of a building relies partially on the understanding of interactions between building outdoor walls and external environment, specifically for recently introduced bio-based materials. Explicitly, studies on thermal and water vapor diffusion through construction materials, highlight the necessity of considering the thermal and hydric response of a building in regard to variable climate stress. These phenomena are highly coupled and governed by second order differential equations which are derived from heat and water amount conservation formula [93]. Moreover, these diffusion are complex phenomena that occur slowly, especially the one of water vapor. The slow kinetic is related to the nature of moisture diffusion which is a transport phenomenon, where water can migrate only trough open pore networks in liquid and vapor forms. The tortuosity of a material, which is a property defining the complexity of its micro-structure, influences as well water transport. In this respect, a bio-based material is known by a high heterogeneity and micro-structure complexity as a composite media. Based on the latter, it is important noting that the long kinetic of heat and water vapor diffusion represents a serious experimental issue, which should be faced.

The hygrothermal behavior of construction materials is widely investigated using approaches based on experimental designs and numerical simulations. Some of the references cited in the literature review carried in [138] can be mentioned specifically. According to [139], the study provides data-sets for validating one-dimensional heat and moisture diffusion models step by step, gradually increasing the complexity of a multi-layer wall with hygroscopic components and using variable climate stress. Furthermore, the influence of sorption curves dependence on temperature is investigated on the hygrothermal behavior of hemp concrete [140]. Another study [141] highlights the experimental characterization of moisture, heat, physical and mechanical properties of a recycled expanded polystyrene mortar. The experimental characterization is conducted also on a cement paste in order to evaluate the insulator adding impact. Afterwards, numerical results are compared to a 85-day experiment in[30]. Generally, these works involve experiments which aim either to confront numerical models of heat and water vapor diffusion or to propose a data set serving as bench-marking. However, these studies analyze the diffusion phenomena during short periods. A more meaningful and challenging approach would be to perform long-term experiments (years) to discuss further the hygrothermal behavior of porous materials.

One of the solutions would be the use of similarities. It aims to set an equivalence between two or more distinct configurations. This mapping relies on the scaling of the model that is used for a theoretical prediction of a studied phenomenon. Afterwards, the equivalence is defined based on a set of dimensionless numbers, each describes generally an aspect that is associated to the phenomenon. For example, a study [142] analyzes the use of dimensionless numbers, such as the Buningham and plastic ones, in the context of viscoplastic materials. According to the latter, some number sets are preferable to others in order to explore the solution space. Generally, similarity is helpful in diverse scientific fields [143] such as structure resistance, computational fluid dynamics, acoustics, aerodynamics, ocean engineering [144] and mechanics. In fluid dynamics for example, the purpose is mainly to compare several fluid flows thanks to a set of dimensionless numbers. The authors in [145, 146] established a similarity theory for heat transfer at super-critical pressures in order to find similar phenomenological behaviors while considering different fluids. In addition, a scale analysis was carried out to develop relationships among physical and geometrical parameters for two types of coil cavity receivers [147]. Herein, the effects of scaling on the performance of a solar receiver is addressed in order to discuss the possibility of extending small designs to large-scale models. Moreover a study, from a different scientific field, proposes a method to relate models and prototype made with different materials, while considering small thickness distortions [148]. This approach is useful to evaluate the behavior of a plate structure against impulsive loading. In addition, similarity is applied to study the acoustic radiation of flat orthotropic flexural panels [80]. The paper assesses the validity of similarity on rectangular panels radiating sound in a semi-infinite light fluid medium. As for aero and hydrodynamics, large structures such as aircraft or wind turbines are pre-studied on a small scale [149, 150] and then designed using similarities. Subsequently, a similarity law of flow rate for ventilated hot-gas super cavity flows is found and described in [151]. The originality lied on water phase changes, whose effects were evaluated on similarity and the modeling scheme. Following another study [152], similarity is investigated on external flow field and internal heat transfer. Particularly, the law is verified by proposing a real aircraft and its scaled models. The results showed a good agreement between the scaled model and the real aircraft. Moreover, a dynamic similarity theory is introduced into a gear transmission system [153]. Particularly, the scale model is designed for the dynamic response. Thereafter, it is validated by free and forced vibration response. Authors in [154] carried simulations and a similarity model test to investigate the failure mechanism of a rock mass around the mined-out area above the high way tunnel. A law is revealed which could be significant for guiding similar engineering constructions.

In addition, heat and moisture diffusion through construction porous materials is a field where, to our best knowledge, a few works used similarity laws. In this respect, an annual moisture variation in a building wall is studied under a mild climate, employing a small-scale model and similarity [96]. In this investigation, an experimental design is proposed, using a wall small-scale model and similarity laws which are based on heat and moisture diffusion equations. Similarity is used to confront numerical results (standard configuration) to those of an experiment, which is an equivalent small-scale model. Lastly, the experimental validity of similarity is assessed for a heat conduction problem according to [155]. The study highlights the reliability of these laws on two similar experiments. For this purpose, temperatures inside materials are measured and confronted. First experiment (reference) lasts 72 h and the second (reduced) endures only 32 h. Based on the good agreement of measurements, the utility of such laws to reduce the duration of long heat diffusion experiments is evidenced. Focusing always on heat and moisture diffusion investigations, a study [94] deals with similarity to assess these phenomena while considering 49 types of material. Similarity was obtained if the dimensionless numbers related to the problem were equal from one configuration to another. Therefore, all cited studies showed that similarities might have a significant role when addressing an experimental work to reduce its duration. Besides, it is important to underline that similarity is validated in the literature only for heat diffusion within porous construction materials.

The present work ensures a continuity of [155], and consists in extending the validity of similarity to a more general case. It proposes an experimental methodology that verifies the validity of similarity of a one-dimensional heat and moisture diffusion phenomena within porous building materials. In particular, the paper aims to verify the reliability of this law in maintaining the same results, between two configurations different in duration. The comparison is performed using measurements at similar positions and time instants. Resulting experimental discrepancies are quantified and discussed, based on the assessment of uncertainties. This step is meaningful since it is unknown whether a discrepancy is within the confidence range. Mostly, an experimental similarity is reliable within a margin of error which can be interpreted by identifying the main constraints, hypotheses, and calculating the corresponding uncertainties.

The structure of this work is defined as follows. Section 2 proposes the physical model which is adopted to study heat and moisture diffusion in a porous material. In addition, it describes the dimensionless formulation of the problem, which will help defining the similarity laws. Afterwards, Section 3 presents the experimental facility that is used to assess the validity of an important assumption (Dirichlet condition modeling) as well as the reliability of similarity. Subsequently, Section 4 defines a detailed methodology to assess the propagation of uncertainty during a heat and moisture diffusion experiment. Thereafter, Section 5 highlights the results related to Dirichlet condition modeling assumption, both experiment uncertainty and the comparison of measurements in the standard and the reduced configuration. This section discusses additionally the experimental validity of similarity. Finally, a conclusion is given in Section 6 which suggests future investigations to improve the reliability of these laws.

2 Methodology

2.1 Assumptions of the study

Before defining the mathematical model that represents the coupled phenomena of heat and moisture diffusion, this section outlines the fixed assumptions for the remaining parts of this work. The assumptions are the following :

- Heat and moisture diffusion are one-dimensional.
- Heat and moisture boundary conditions at the surface are modeled according to Dirichlet type.
- Material intrinsic properties do not depend on temperature.
- The micro structure of the material are considered equals (from an averaged point of view) between two similar configurations. Thus, properties and their variation laws are considered the same for the two similar configurations.
- The phenomenon of hysteresis is neglected and the variation of water content according to relative humidity is based on the averaged isotherm sorption curve.
- Systematic uncertainty is constant and assumed independent of the location and the instant of a measurement.
- The assessment of random uncertainties is approximated by using $N = 3$ samples in each configuration.

First and second assumptions have major importance in regards to the validation of similarity laws, so they will be discussed in the results.

2.2 Mathematical model

This part is dedicated to the definition of the equations that govern the coupled heat and moisture diffusion in porous media [156, 157]. The problem considered in this study follows a macroscopic approach based on the representative element volume [158]. In this respect, phenomena at the microscopic scale are averaged [159, 160] and convection is neglected due to low velocity fields in the pores of building materials and the size of these pores. Temperature $T\,[\mathsf{°C}]$ and vapor pressure $P_v\,[\mathsf{Pa}]$ are the driving potentials of this model. These two variables are strongly coupled and thus impact each other. The problem is written for a one-direction diffusion according to the Equations (3.1) and (3.2) :

$$C_m\,\rho\,\frac{\partial P_v}{\partial t} = \frac{\partial}{\partial x}\Big(\,(\,k_l + k_v\,)\,\frac{\partial P_v}{\partial x} + k_T\,\frac{\partial T}{\partial x}\,\Big) + \beta\,\frac{\partial T}{\partial t}\,, \tag{3.1}$$

$$C_p\,\rho\,\frac{\partial T}{\partial t} = \frac{\partial}{\partial x}\Big(\,(\,\lambda + h_l\,k_T\,)\,\frac{\partial T}{\partial x} + \alpha\,\frac{\partial P_v}{\partial x}\,\Big)\,, \tag{3.2}$$

where $\rho\,[\mathsf{kg.m^{-3}}]$ designates the material density and is expressed as follows :

$$\rho = (1-n)\,\rho_s + n\,S_l\,\rho_l\,. \tag{3.3}$$

Where $n\,[-]$ is the porosity of the material, $\rho_s\,[\mathsf{kg.m^{-3}}]$ density of solid matrix, $S_l\,[-]$ the degree of saturation in water, $\rho_l\,[\mathsf{kg.m^{-3}}]$ water density. $C_p\,[\mathsf{J.kg^{-1}.K^{-1}}]$ is the global heat capacity. It is the combination of the specific heat of the material in the dry state $C_{ps}\,[\mathsf{J.kg^{-1}.K^{-1}}]$ and that of water in the pores of the medium $C_{pl}\,[\mathsf{J.kg^{-1}.K^{-1}}]$. It is expressed as follows :

$$C_p = \frac{(\,1-n\,)\,\rho_s\,C_{ps} + S_l\,n\,\rho_l\,C_{pl}}{(\,1-n\,)\,\rho_s + S_l\,n\,\rho_l}\,. \tag{3.4}$$

Furthermore, $C_m\,[\mathsf{Pa^{-1}}]$ represents the moisture storage capacity and is obtained via the isotherm adsorption and desorption curves. These curves illustrate the variation of water content

$w\,[-]$ according to relative humidity $\phi\,[-]$ within the material and at a constant temperature [161]. Let assume that the variation of water content, according to relative humidity within the material, is determined at a constant temperature. On the other hand, it is also assumed that the sorption curve is obtained by averaging those of adsorption and desorption. The isotherm curve during the wetting and the drying of a porous material is not the same, this is due to the hysteresis phenomenon. The physical modification of the material, caused by water outflow, is responsible for this phenomenon. It is usually induced by the non-uniformity of pores geometry. In order to simplify the problem, this phenomenon will be neglected in the study assumption 5. Thus, the moisture storage capacity is defined as follows :

$$C_m\,(\,P_v\,,\,T\,) = \frac{1}{P_{sat}\,(\,T\,)}\,\frac{\partial w}{\partial \phi}\,. \tag{3.5}$$

Where P_{sat} [Pa] represent the saturation pressure and is given by Antoine's law as follows :

$$P_{sat}\,(\,T\,) = P_{sat}^{\circ}\,\left(\frac{T - T_c}{T_d}\right)^{p}\,, \qquad T \geq T_c\,, \tag{3.6}$$

given that $P_{sat}^{\circ} = 997.3\,\mathsf{Pa}$, $T_c = 159.5\,\mathsf{K}$, $T_d = 120.6\,\mathsf{K}$ and $p = 8.275$. Afterwards, k_v [s] is water vapor permeability. It describes the transport of the water vapor form due to a vapor pressure gradient. This coefficient generally depends on water content and temperature. In this case, it is assumed constant. In addition, Equation (3.1) introduces three other coefficients k_l [s], k_T [kg.m^{-1}.s^{-1}.K^{-1}] and β [kg.m^{-3}.K^{-1}]. According to the model, they are defined as follows :

$$k_l\,(\,P_v\,,\,T\,) = \kappa_l\,\frac{R\,T\,\rho_l}{M\,P_v}\,. \tag{3.7}$$

$$k_T\,(\,P_v\,,\,T\,) = \frac{k_l\,R\,\rho_l}{M}\,\Big(T\,\frac{\partial\,\ln\,\phi}{\partial T} + \ln\,\phi\Big)\,. \tag{3.8}$$

$$\beta\,(\,P_v\,,\,T\,) = \rho_s\,C_m\,\frac{P_v}{P_{sat}}\,\frac{\partial P_{sat}}{\partial T}\,. \tag{3.9}$$

Where κ_l [s] is the liquid conductivity. R [J.mol^{-1}.K^{-1}] is the ideal gas constant and the molar mass is given as M [kg.mol^{-1}]. k_T represent the moisture transport coefficient due to a temperature gradient. Furthermore, heat diffusion is primarily governed by the the material conduction that is defined by the coefficient λ [W.m^{-1}.K^{-1}]. It generally depends on temperature and water content. However, this coefficient varies slightly with temperature. Therefore, only water content is considered in its expression, which is given below :

$$\lambda = n\,\lambda_l\,S_l + (1 - n)\,\lambda_s\,. \tag{3.10}$$

Where λ_s [W.m^{-1}.K^{-1}] and λ_l [W.m^{-1}.K^{-1}] represent the material thermal conductivity at its dry state and the one of water. Note that Equation (3.10) underlines that the thermal conductivity of a porous material depends only on the saturation degree in water or water content in other words. It is worth noting that certain properties depend on temperature such as λ, k_v, k_l. However, unlike water content, these properties vary slowly according to temperature. In addition, the range of temperature variation is reduced in building physics, which is not the case in other scientific fields where temperature reaches higher thresholds. Hence, it is further considered that intrinsic properties do not vary according to temperature , which corresponds to the assumption 3. Moreover, h_l [J.kg^{-1}] is the water mass enthalpy. Notice that heat diffusion is also impacted by the presence of water within the open porous network. This fact is quantified by $\alpha\,[\mathsf{W.m^{-1}.Pa^{-1}}]$ which is a heat diffusion coefficient due to a vapor pressure gradient. Its expression is given as follows :

$$\alpha\,(\,P_v\,,\,T\,) = h_l\,(\,k_l + k_v\,) + L_v\,k_v\,.$$

α indicates the heat fraction transmitted as latent energy due to water vapor [162, 163]. This is evidenced via the water vapor permeability k_v and the latent heat of vaporization L_v.

The upcoming study is carried out based on two hypotheses. On the one hand, the diffusion is considered one-dimensional along the x-axis for example. This is the first model assumption. It is possible to approximate the uni-directional flux condition. This is achieved by imposing a high thermal or moisture resistance along other diffusion directions. Materials with low thermal conductivity or water vapor permeability help limiting heat and moisture diffusion. Moreover, this assumption can also be approximated by considering the material a semi-infinite medium. For the rest of this study, it is chosen to use an insulating material and another one with a high water vapor sealing in order to ensure this first assumption. Space and time domains are defined by $\Omega_x = [\,0\,,\,L\,]$ and $\Omega_t = [\,0\,,\,t_f\,]$ respectively. L represents the material dimension along the diffusion direction. We introduce $\lambda_{ef}\,[\mathsf{W.m^{-1}.K^{-1}}]$ the effective thermal conductivity and $k_m\,[\mathsf{s}]$ the material total mass permeability. These two coefficients are expressed as follows :

$$k_m = k_v + k_l\,. \tag{3.11}$$

$$\lambda_{ef} = \lambda + h_l\,k_T\,. \tag{3.12}$$

Initially, temperature and vapor pressure fields are known in the material. They are positive functions defined in the spatial domain $\Omega_x = [\,0\,,\,L\,]$. In our case, material initial vapor pressure and temperature are assumed constant. The initial condition is written as follows :

$$\forall x \in [\,0\,,\,L\,]\,, \qquad P_v\,(\,x\,,\,0\,) = P_{v\,0}\,, \quad T\,(\,x\,,\,0\,) = T_0\,. \tag{3.13}$$

Where $P_{v\,0}$ and T_0 are the material vapor pressure and temperature at the initial instant respectively. It is important to remind that these last two quantities will represent the characteristic quantities related to temperature and vapor pressure, in the dimensionless formulation part. Regarding the boundary conditions, they can be constant or vary in time. In the case of this study, the face corresponding to $x = 0$ is exposed to time-dependent heat and moisture stress. Hereafter, we consider that temperature and relative humidity at this surface are identical to those of ambient air T^{∞}, ϕ^{∞}. This is the Dirichlet-type boundary condition, which will be the second assumption. At the exposed surface, temperature and vapor pressure are stated as follows :

$$\forall t \in [\,0\,,\,t_f\,]\,,\, x = 0 \qquad P_v\,(\,t\,) = P_v^{\infty}\,(\,t\,)\,, \quad T\,(t) = T^{\infty}\,(\,t\,)\,. \tag{3.14}$$

Furthermore, admit that the material is perfectly insulated Figure 3.1 and sealed against moisture on its last five faces. Thus, heat and water vapor diffusion are negligible on the other side of the material. This allows to write :

$$\forall t \in [\,0\,,\,t_f\,]\,,\, x = L \qquad \frac{\partial P_v}{\partial x}\,(\,t\,) = 0\,, \quad \frac{\partial T}{\partial x}\,(\,t\,) = 0\,. \tag{3.15}$$

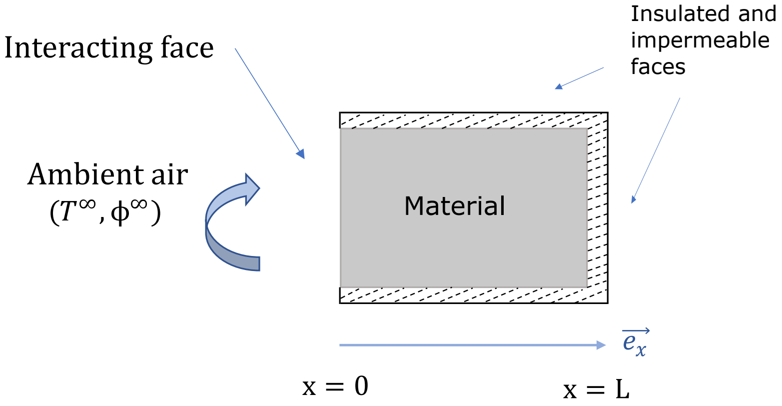

FIGURE 3.1 – The boundary conditions assumed in the model

In the next section, the dimensionless formulation of the problem is addressed. The aim is to obtain dimensionless equations that are independent of a given configuration. This operation is essential to obtain dimensionless numbers. These latter will be the basis for the definition of the similarity laws required for the formulated problem.

2.3 Dimensionless formulation

The dimensionless formulation of an equation [94, 104] requires first the definition of certain characteristic values. Afterwards, each problem variable will be reported to one of these values. For this purpose, we choose the following constants as the characteristic space and time values, L the material thickness and t_f experiment duration. Therefore, the first two dimensionless variables are deduced :

$$x^{\star} = \frac{x}{L}, \qquad t^{\star} = \frac{t}{t_f}. \tag{3.16}$$

In parallel, characteristic vapor pressure and temperature are the ones of the material at the initial state $P_{v\,0}$ and T_0. Likewise, we obtain :

$$u = \frac{P_v}{P_{v\,0}}, \qquad v = \frac{T}{T_0}. \tag{3.17}$$

Finally, all characteristic material properties are also the ones evaluated at $T = T_0$ and $P_v = P_{v\,0}$. Their dimensionless formulation is given as follows :

$$\rho_s^{\star} = \frac{\rho_s}{\rho_{s\,0}}, \quad C_m^{\star} = \frac{C_m}{C_{m\,0}}, \qquad k_m^{\star} = \frac{k_m}{k_{m\,0}}, \qquad k_T^{\star} = \frac{k_T}{k_{T\,0}}, \tag{3.18a}$$

$$\beta^{\star} = \frac{\beta}{\beta_0}, \qquad C_p^{\star} = \frac{C_p}{C_{p\,0}}, \qquad \lambda^{\star} = \frac{\lambda_{ef}}{\lambda_{ef\,0}}, \qquad \alpha^{\star} = \frac{\alpha}{\alpha_0}. \tag{3.18b}$$

Taking into account the scaling made on the variables of the problem, the dimensionless formulation of the equations (3.1) and (3.2) is given :

$$C_m^{\star}\,\rho_s^{\star}\,\frac{\partial u}{\partial t^{\star}} = \mathrm{Fo}_m\,\frac{\partial}{\partial x^{\star}}\left(k_m^{\star}\,\frac{\partial u}{\partial x^{\star}}\right) + \mathrm{Fo}_m\,\delta\,\frac{\partial}{\partial x^{\star}}\left(k_T^{\star}\,\frac{\partial v}{\partial x^{\star}}\right) + \eta\,\beta^{\star}\,\frac{\partial v}{\partial t^{\star}}, \tag{3.19}$$

$$C_p^{\star}\,\rho_s^{\star}\,\frac{\partial v}{\partial t^{\star}} = \mathrm{Fo}_q\,\frac{\partial}{\partial x^{\star}}\left(\lambda^{\star}\,\frac{\partial v}{\partial x^{\star}}\right) + \mathrm{Fo}_q\,\gamma\,\frac{\partial}{\partial x^{\star}}\left(\alpha^{\star}\,\frac{\partial u}{\partial x^{\star}}\right). \tag{3.20}$$

The dimensionless equations introduce constant and characteristic numbers [164]. First, Fourier numbers that are related to the kinetics of heat and moisture diffusion. Their expressions are given as follows :

$$\mathrm{Fo}_{m} = \frac{k_{m0}\, t_{f}}{\rho_{s0}\, C_{m0}\, L^{2}}\,, \qquad \mathrm{Fo}_{q} = \frac{\lambda_{ef0}\, t_{f}}{\rho_{s0}\, C_{p0}\, L^{2}}\,.$$

Fourier numbers represent the part of heat or moisture flux that is transmitted through the material compared to the stored heat or moisture. Differently, it is the ratio of the diffusive transport to the rate of storage. Moreover, three other characteristic numbers appear in equations (3.19) and (3.20). By definition, they describe the effect of heat or moisture diffusion on each other.

$$\delta = \frac{k_{T0}\, T_{0}}{k_{m0}\, P_{v0}}\,, \qquad \gamma = \frac{\alpha_{0}\, P_{v0}}{\lambda_{ef0}\, T_{0}}\,, \qquad \eta = \frac{T_{0}\, \beta_{0}}{P_{v0}\, C_{m0}\, \rho_{s0}}\,.$$

According to Equation (3.19), notice that the influence of heat on moisture diffusion is described by δ. If $\delta < 1$, the impact of heat on moisture diffusion is minor compared to the moisture flux driven by vapor pressure. In parallel, when $\gamma < 1$, the impact of moisture on heat diffusion is minor compared to the heat driven by temperature. Finally, the number η is a coupling parameter for the dynamics of heat over moisture diffusion. The dimensionless formulation is applied also on the defined initial and boundary conditions. u and v are initially defined as follows :

$$\forall x^{\star} \in [\,0\,,\,1\,]\,, \qquad u\,(\,x^{\star}\,,\,0\,) = 1\,, \quad v\,(\,x^{\star}\,,\,0\,) = 1\,.$$

In addition, the new boundary conditions are given as follows :

$$\forall t^{\star} \in [\,0\,,\,1\,]\,,\; x^{\star} = L \qquad \frac{\partial u}{\partial x^{\star}} = 0\,, \quad \frac{\partial v}{\partial x^{\star}} = 0\,.$$

$$\forall t^{\star} \in [\,0\,,\,1\,]\,,\; x^{\star} = 0 \qquad u = u^{\infty}\,, \quad v = v^{\infty}\,.$$

After formulating the whole problem into a dimensionless form, we reach a configuration, where the quantities u and v do not depend anymore on the parameters of the physical model. Only the characteristic numbers are used to evaluate the variation of these fields. Consequently, the concept of similarity laws is introduced. The following section will thus consist in defining these laws and presenting their applications in fields of applied physics.

2.4 Similarity laws on heat and moisture diffusion

In order to apply these laws, two different configurations indexed by 1 and 2 are introduced. The first configuration is defined by the space domain $\Omega_{x}^{1} = [\,0\,,\,L_{1}\,]$ and time domain $\Omega_{t}^{1} = [\,0\,,\,t_{f1}\,]$. The same for the second one where $\Omega_{x}^{2} = [\,0\,,\,L_{2}\,]$ and $\Omega_{t}^{2} = [\,0\,,\,t_{f2}\,]$. Where L_{1} and L_{2} represent the thicknesses of the material in configuration 1 and 2 respectively. Likewise for t_{f} which represents the duration of an experiment. Based on the latter, two configurations are stated similar if the dimensionless formulation of the problem is identical in both cases. This implies that the dimensionless numbers are equal in both configurations. Thus, it is deduced from Eqs. (3.19) and (3.20) the following :

$$\mathrm{Fo}_{m1} = \mathrm{Fo}_{m2}\,, \qquad \mathrm{Fo}_{q1} = \mathrm{Fo}_{q2}\,, \tag{3.21a}$$

$$\delta_{1} = \delta_{2}\,, \qquad \gamma_{1} = \gamma_{2}\,, \qquad \eta_{1} = \eta_{2}\,. \tag{3.21b}$$

In our study, the cases consist of two samples representing the same material and initially conditioned at the same temperature and vapor pressure. This implies that :

$$T_{0\,1} = T_{0\,2}\,, \qquad P_{v\,0\,1} = P_{v\,0\,2}\,.$$

Not changing the material from one configuration to another helps setting the assumption 4. Thus, notice that the equality on numbers δ, γ et η in Equation 3.21b is guaranteed . Moreover, the equivalence on heat and moisture Fourier numbers enables to obtain :

$$\frac{t_{f\,1}}{L_1^2} = \frac{t_{f\,2}}{L_2^2}\,. \tag{3.22}$$

Recalling that the properties $\rho_{s\,0}$, $k_{m\,0}$, $C_{m\,0}$, λ_0 and $C_{p\,0}$ are considered equal in both configurations.

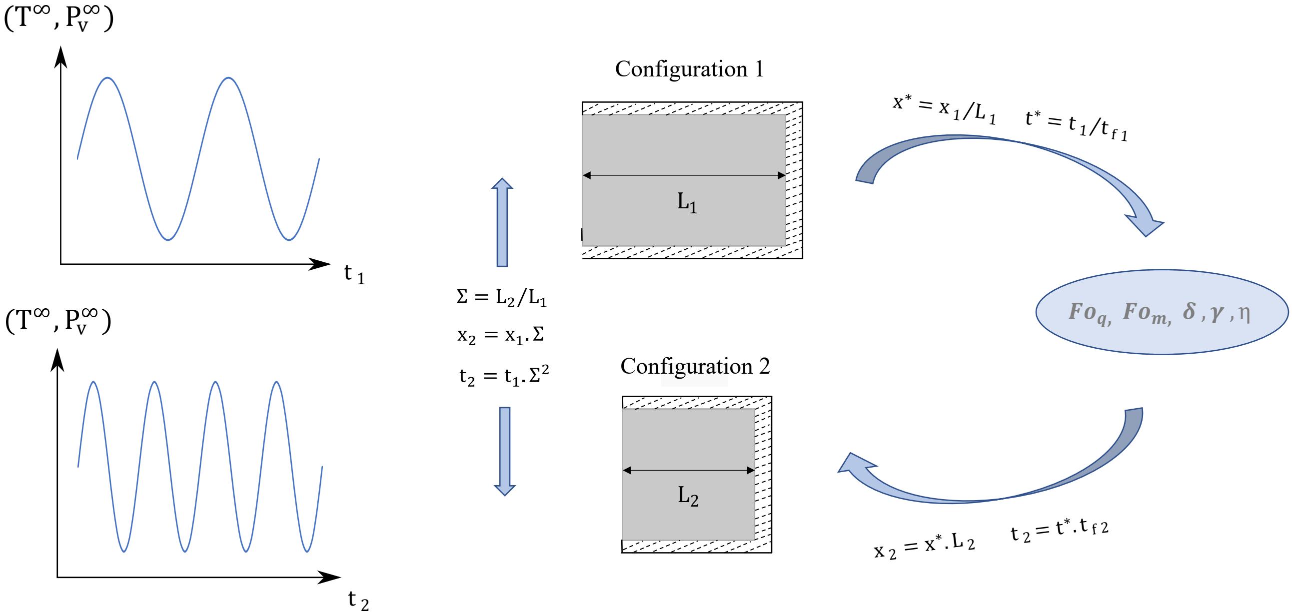

FIGURE 3.2 – The mapping between two configurations 1 and 2.

Remark that similarities create space-time equivalences between configurations. In this regard, the similarity proportionality factor Σ is defined which is a length ratio and defined as follows :

$$\Sigma = \frac{L_2}{L_1}\,. \tag{3.23}$$

When $\Sigma < 1$, *i.e.* $L_2 < L_1$, the space dimension of the reference configuration is reduced. This possibility constitutes our choice in order to overcome the slow kinetics of heat and moisture diffusion. Therefore, our objective would be to deal with a long experimental configuration called reference while working on a reduced design. Given that the duration of the long and short experiments are t_1 and t_2 respectively, an equivalence is set between these experiments if they verify :

$$t_{f\,2} = t_{f\,1}\,\Sigma^2\,. \tag{3.24}$$

In reality, assumption 3 is true only if the micro-structure of a sample remains unchanged going from the reference configuration to the reduced model. Ideally, the properties and their laws of variation are identical if it is assumed that the reduced configuration represents a sample that is identical to the one in the reference configuration in terms of porosity, tortuosity and pore size distribution. Note that the time scale of the reduced configuration is modified by two orders compared to the space scale. From a mathematical perspective, a mapping is carried Figure 3.2 linking the reference configuration to the equivalent one by means of the proportionality factor (3.23). This mapping is ensured through the obtained dimensionless numbers. Thus, it is formulated in the following way :

$$\Omega_x^1 \times \Omega_t^1 \longmapsto \Omega_x^2 \times \Omega_t^2 \,,$$
$$\Big(x_1 \,,\, t_1 \Big) \longmapsto \Big(x_2 = x_1 \cdot \Sigma \,,\, t_2 = t_1 \cdot \Sigma^2 \Big) \,.$$

2.5 Experimental assessment of the validity of similarity law

After defining the equivalent configurations 1 and 2, the experimental validation of the similarity laws is carried out by comparing temperature and relative humidity in both configurations. Indeed, the equivalence in temperature and vapor pressure induces that of relative humidity. This comparison can be carried according to the physical domain. In this case, for $x_1 \in \Omega_x^1$, $x_2 \in \Omega_x^2$, $t_1 \in \Omega_t^1$ and $t_2 \in \Omega_t^2$ such that $x_2 = x_1 \Sigma$ and $t_2 = t_1 \Sigma^2$, the following affirmations must be verified :

$$T(x_1, t_1) = T(x_2, t_2) \quad , \quad \phi(x_1, t_1) = \phi(x_2, t_2) \,. \tag{3.25}$$

Where ϕ represents the relative humidity that is defined according to Eq. (3.26) :

$$\phi = \frac{P_v}{P_{sat}} \,. \tag{3.26}$$

To validate the laws of similarity on this problem, discrepancies and total uncertainties should be estimated and compared. In this regard, the results related to the reference and reduced configurations are in agreement if :

$$\Big| \epsilon_T(\chi_i, t) \Big| \leq \sigma_T(\chi_i, t) + \sigma_T(\chi_i \Sigma, t\Sigma^2) \,, \tag{3.27a}$$
$$\Big| \epsilon_\phi(\chi_i, t) \Big| \leq \sigma_\phi(\chi_i, t) + \sigma_\phi(\chi_i \Sigma, t\Sigma^2) \,. \tag{3.27b}$$

Where $\chi_i \in [0, L_i]$ is a position within the material in the reference configuration considering that $i \in \{1, 2\}$ and $t \in [0, t_{fi}]$ are the instants during this same configuration. According to Eqs. (3.27a) and (3.27b), It should be ensured that the discrepancy one a given field (ϵ_ϕ or ϵ_T) as expressed in Equations (3.28a) and (3.28b), between two similar positions and at equivalent instants, is smaller in absolute value than the sum of the total uncertainties (σ_T, σ_ϕ). In the following section, the manufacturing phase of the material is evidenced. It is resumed to the formulation of samples, the used molds and the necessary curing period. Subsequently, the necessary devices and equipment are exposed. Finally, the samples which represent the reference and reduced configurations will also be announced.

$$\epsilon_T(\chi_i, t) = T(\chi_i, t) - T(\chi_i \Sigma, t\Sigma^2) \,, \tag{3.28a}$$
$$\epsilon_\phi(\chi_i, t) = \phi(\chi_i, t) - \phi(\chi_i \Sigma, t\Sigma^2) \tag{3.28b}$$

3 Experimental investigation

3.1 Material

FIGURE 3.3 – Formulation of the $15 \times 15 \times 15\,\text{cm}^3$ samples.

The tests, presented in this work, are performed on hemp concrete samples. It is a bio-based material with the substitution of hemp plant fibers [165]. All samples are derived from the same formulation. The manufacture of this material was described thanks to the standardization according to NF EN 459, NFP $15-314$ and NF EN $197-1$. It imposes the following mass fractions : 16% of hemp, 34% of cement and 50% of water. The hemp is issued from the Biofibat product. It is an aggregate made up exclusively of cellulose fibers, calibrated and dust-free, resulting from the defibration of hemp straw. The product technical description shows the following values : $\rho = 110\,\text{kg.m}^{-3}$, $\lambda = 0.05\,\text{W.m}^{-1}.\text{K}^{-1}$. These properties were evaluated at 15% moisture content. Tradical$^{\text{R}}$ PF70 is a formulated lime of class FL A 3.5, valid according to the NF 459 standard. This lime is designed to produce mortars for natural stone, hollow or full bricks, as well as traditional plasters. According to the manufacturer, the lime is characterized at the dry state as follows : $\rho_s = 620\,\text{kg.m}^{-3}$, $\lambda_s = 0.2\,\text{W.m}^{-1}.\text{K}^{-1}$.

In an industrial container, the correct proportions of water and lime are mixed for three minutes via a double speed mixer. A good hydration is ensured by the sufficient appearance of water bubbles. Then, hemp is added to the container and mixed for another 2 minutes. Afterwards, the obtained mixture is filled into $15 \times 15 \times 15\,\text{cm}^3$ molds. These are treated with a specific oil in order to facilitate the releasing. After ten days of hydration, the samples are obtained and stored in ambient air conditions for three months. The experimental characterization of heat and moisture properties of hemp concrete provided the following results at the dry state : $\lambda_s = 100.23\,\text{mW.m}^{-1}.\text{K}^{-1}$, $C_{ps} = 1150\,\text{J.kg}^{-1}.\text{K}^{-1}$, $\rho_s = 480\,\text{kg.m}^3$, $k_v = 2.8\,10^{-11}\,\text{s}$ and $k_l = 7.4\,10^{-13}\,\text{s}$.

$$\omega = \frac{m\,K\,\phi}{1 + K\,\phi}\,\frac{1 - k\,(1-w)}{1 - k\,\phi}\,. \tag{3.29}$$

For the determination of the average sorption curve of hemp concrete, the experimental results in [41] are used. The data are obtained for the same formulation of hemp concrete, at $T = 25\,°\text{C}$ and for different relative humidity values. Subsequently, the experimental curve was fitted using the Generalised D'arcy and Watt model (GDW) for the sorption curves which is given according to Eq. (3.29). Based on the performed fitting, the parameters of this model are estimated as : $m = 0.068$, $K = 2.722$, $k = 0.964$ and $w = 0.187$.

3.2 Experimental equipment

FIGURE 3.4 – The climatic chamber used in tests.

After the hydration of the samples, they are put under different experimental tests. It consists mainly in generating realistic climate conditions to apply on samples. This task was carried out thanks to a climatic chamber of CTS mark illustrated in the Figure 3.4. It is a cell having the dimensions $0.9 \times 1 \times 1.6\,\mathsf{m}^3$, ensuring a use range from -70 to $180\,^\circ\mathsf{C}$ in temperature and 10 to 98% in relative humidity. During the material exposure, temperature and relative humidity are measured at different locations using capacity humidity sensors. These are manufactured by Ahlborn, and have a diameter of $5\,\mathsf{mm}$ (Figure 3.5a). The operating ranges for temperature and relative humidity are -30 to $100\,^\circ\mathsf{C}$ and 5 to 98% respectively. Furthermore, based on the factory calibration certificate, the systematic accuracy of these sensors are given as $\sigma_{T,Sys} = 0.3\,^\circ\mathsf{C}$ and $\sigma_{\phi,Sys} = 4\%$ for temperature and relative humidity respectively. These values are obtained at a nominal temperature of $25\,^\circ\mathsf{C}$. During experiments, assume that the systematic accuracy do not depend on either measurement position or instant according to assumption 6. Indeed, the sensors are calibrated in relative humidity for values lower than 90% and at a temperature of $25\,^\circ\mathsf{C}$. Thus, 4% uncertainty in relative humidity is assumed. In temperature, three systematic uncertainties are provided for three different ranges of variation. The chosen uncertainty in temperature is given for a range from 0 to $70\,^\circ\mathsf{C}$. Based on these data, the considered systematic uncertainties are fully justified for temperature and relative humidity variations in this study. The response time of the sensor is around $10\,\mathsf{s}$ for a maximum of $1\,\mathsf{m.s}^{-1}$ air flow velocity. The display and recording of data each is ensured $5\,\mathsf{min}$ by the use of an acquisition unit and a memory card of Almemo brand shown in Figure 3.5b. The choice to record results on a minute-scale can be justified. The link can be made with the kinetics of heat and moisture diffusion. It was agreed that the recording should be on this scale because of a compromise between both transfer natures. Indeed, heat transfer is a purely diffusive phenomenon and is relatively faster than moisture transfer. The latter, requiring available open pore networks, represents a transport phenomenon. A recording on an hour-scale, for example, would be suitable to measure only relative humidity. However, since sensors measure simultaneously temperature and relative humidity, it is rather decided to take into account first the quick variation in temperature. Consequently, the interval between each measurement is set shorter, on a minute-scale.

(a) Ahlborn sensors

(b) Display screen

The described equipment will initially be used to test the hypotheses in Section 2.2. Assumption 1 will not be assessed in this study. Indeed, it is assumed verified on the basis of the work in [155], where it was dealt with a heat diffusion investigation. In the latter, a hemp concrete sample, insulated and sealed in the same way as in the two configurations, was exposed to variable heat stress. The one-dimensional transfer assumption was assessed following two different approaches. A first experimental investigation was carried out where the flux along the x-axis (transfer direction) is compared to the one along the y-axis. These fluxes are calculated using finite differences with a centered scheme and sensors around the chosen position where $\Delta x = \Delta y = 5\,\mathsf{cm}$. It was shown that the flux along y represents 5 to 9% of the one along the privileged direction. In the same work, a second approach consisted in investigating numerically the same fluxes by simulating the thermal behavior of hemp concrete. This time, the resolution method was based on finite elements where $\Delta x = \Delta y = 10^{-3}\,\mathsf{cm}$. Results showed that the flux along y does not exceed 1% of the one along x. Note that both approaches confirm the validity of this assumption within a certain error. The latter is more important in the experimental investigation because of the large mesh size. This could not be refined due to constraints related to the experimental design. The following part will be dedicated to the description of the experimental procedure aiming to evaluate the Assumption 2.

3.3 Experimental procedure to evaluate the assumption 2 on the Dirichlet condition modeling

In assumption 2, it is assumed that air temperature and vapor pressure are the ones at the exposed material surface. However, this statement defines Dirichlet boundary conditions. Indeed, the latter requires in this case the knowledge of temperature and vapor pressure at the surface of the material. In reality, a heat and moisture resistance exist and which define the interaction between a material and air. In this case, these interactions at the interface are defined thanks to the condition of Robin, whose dimensionless formulation induces the Biot number. Its expression for both heat and moisture diffusion is given as follows :

$$\mathrm{Bi}_{\mathrm{q}} = \frac{h_c\, L}{\lambda}\,, \qquad \mathrm{Bi}_{\mathrm{m}} = \frac{h_m\, L}{k_m}\,. \tag{3.30}$$

Where $h_c\,[\mathsf{W.m^{-2}.K^{-1}}]$ and $h_m\,[\mathsf{kg.m^{-2}.s^{-1}.Pa^{-1}}]$ are the surface heat and moisture diffusion coefficients respectively. In this field, Biot numbers designate the ratio of heat or moisture diffusion resistance at the surface and inside the material. When $\mathrm{Bi}_{q,m} > 1$, the diffusion inside the material is slower than the heat or moisture reaching the exposed surface. According to the preceding, the second assumption is more justified if the Biot number is large. This implies a great surface diffusion coefficient. Moreover, most empirical laws, expressing this coefficient, link it directly to air velocity [166, 167]. Thus, it follows that assumption 2 is more reliable if tests are performed using high air flow velocity ranges. Concerning this test, the first step is selecting a sample which is $L = 10\,\mathsf{cm}$ thick and exposing it to the conditions presented in the mathematical model in Section 2.2. Note that the sample undergoes a preliminary preconditioning step where air temperature and relative humidity are set at $T = 23\,^{\circ}\mathsf{C}$ and $\phi = 50\,\%$ respectively. Additionally, it is necessary to ensure that heat and moisture diffusion are one-dimensional. In order to validate this condition, we use a $5\,\mathsf{cm}$ thick layer of synthetic thermal insulator made of polyethylene. For a good moisture sealing, an additional layer of a low-permeability aluminum band is employed. In addition, the surface defined by the equation $x = L$ is insulated in the same way. Indeed, heat and moisture flux must be negligible at $x = L$.

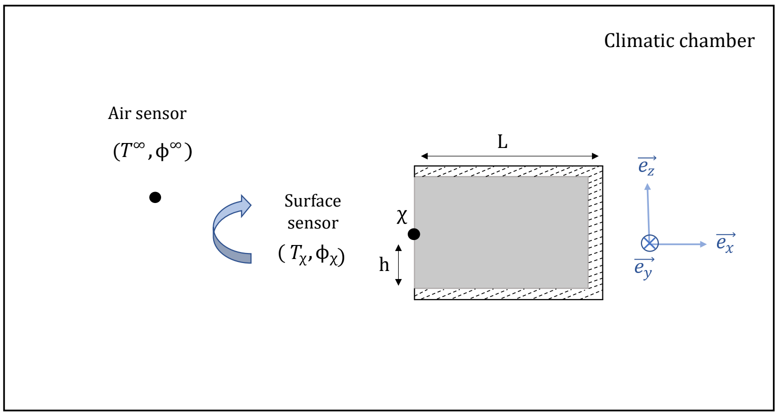

FIGURE 3.6 – Illustration of the experimental configuration to assess the validity of assumption 2 (Dirichlet boundary condition).

The second step consists in using two Ahlborn sensors as shown in Figure 3.6. The first one is positioned on the node $\chi\,(\,x = 0\,,\, y = l\,,\, z = h\,)$ where $l = h = 5\,\mathsf{cm}$. It can be fixed using an adhesive ribbon, while the second is suspended inside the climatic chamber. Afterwards, the sample is put in the cell while creating the climatic stress scenario.

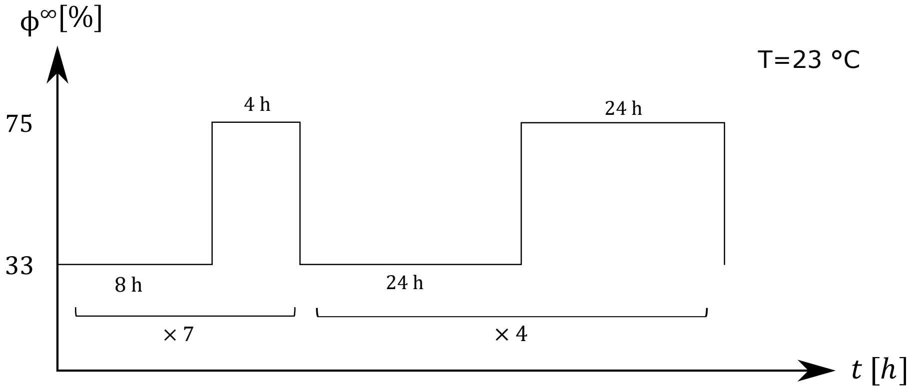

FIGURE 3.7 – Hydric stress considered for the verification test of the assumption 2.

Throughout the experiment, the same temperature during the preconditioning is maintained. Moreover, air relative humidity varies between two values 33 % and 75 % as shown in Figure 3.7. According to the latter, the presence of two phases is observed, a drying at 33 % then humidification at 75 %. Additionally, the experiment duration is split into two parts. During the first one, the sample undergoes 7 cycles. Each cycle consists of setting 33 % relative humidity for 8 hours, then 75 % for 4 hours. As for the second part, it is longer and consists of only 4 cycles. These latter include drying during 24 hours and humidification considering the same duration. The goal is to follow the variation in temperature as well as the relative humidity of both sensor positions. Thus, errors ε_{T_s} and ε_{ϕ_s} are deduced with regard to the assumption 2.

$$\varepsilon_{T_s}(t) = \Big| T(\chi, t) - T^{\infty}(t) \Big|, \qquad \varepsilon_{\phi_s}(t) = \Big| \phi(\chi, t) - \phi^{\infty}(t) \Big|. \tag{3.31}$$

The evaluation of both errors is essential to discuss the limits of this assumption. In this context, both errors are compared in terms of magnitude. In particular, these data are necessary for the evaluation of the uncertainties [168] related to this assumption. After describing the experimental procedure, the next part defines the tests which aim to verify, under the defined hypotheses, the law of similarities.

3.4 Experimental procedure to assess the heat and mass similarity

Three months after the material formulation, two samples are selected to assess the validity of similarity. The goal is to create two equivalent configurations in regard to these laws. The configurations 1 and 2 are denoted reference and reduced, respectively. In this case, $\Sigma < 1$ ($L_{ref} > L_{red}$), which means a reduction of time and space scales of the reference configuration. For this purpose, a one sample is sliced to ensure the desired thickness. Then, both samples undergo the same preconditioning phase for 15 days under a temperature of 23 °C and a relative humidity of 50%. Afterwards, both samples are insulated and sealed as explained in Section 3.3. In each configuration, two sensors are placed at two different sample depths. In order to compare the experimental results between both configurations, the positions chosen must verify the following condition :

$$\chi_{red} = \chi_{ref}\,\Sigma\,.$$

Regarding the boundary conditions, a dynamic stress scenario is considered for the reference configuration with a duration t_{ref}. In this case, similarity imposes the adoption of the same scenario in terms of magnitude, but reduced in duration. In particular, the duration of the reduced test must satisfy this equality :

$$t_{red} = \Sigma^2 \, t_{ref} \, .$$

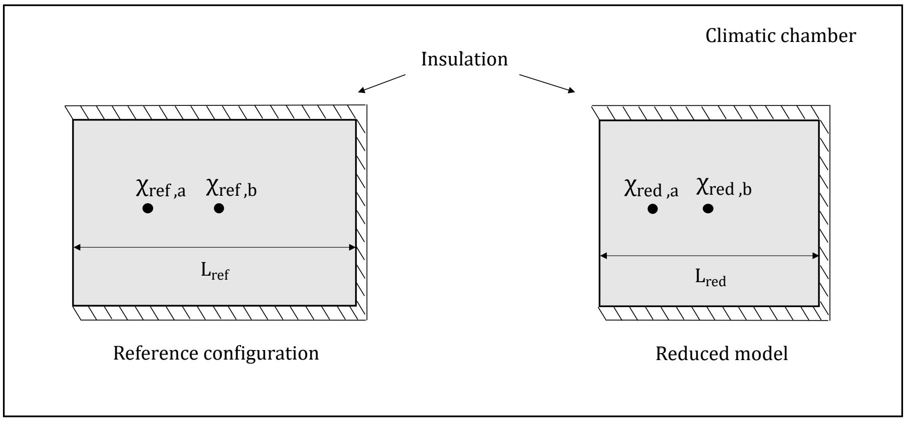

FIGURE 3.8 – The similar experimental configurations.

The chosen set of positions to carry a comparison is the quarter and middle of the sample. According to the Figure 3.8, an experimental confrontation is performed in temperature and relative humidity between $\chi_{ref,\,a}$ and $\chi_{red,\,a}$ as well as between $\chi_{ref,\,b}$ and $\chi_{red,\,b}$.

3.5 Definition of the study case

In order to apply similarities, a first configuration is considered and designated reference. It is based on a hemp concrete sample where $L_{ref} = 10\,[\mathsf{cm}]$. First, temperature and relative humidity were set at $T_0 = 23\,[°\mathsf{C}]$ and $\phi_0 = 50\,[\%]$. Afterwards, boundary conditions are defined by an air relative humidity which varies as shown in Figure 3.7 where temperature remains constant and equals $T^{\infty} = 23\,[°\mathsf{C}]$. Moreover, the experiment duration is set to $t_{ref} = 11.5\,[\mathsf{d}]$. In order to compare temperature and relative humidity between configurations, two sensors were positioned at the positions whose coordinates are : $\chi_{ref\,a} = 2.5\,[\mathsf{cm}]$ and $\chi_{ref\,b} = 5\,[\mathsf{cm}]$ along the x axis.

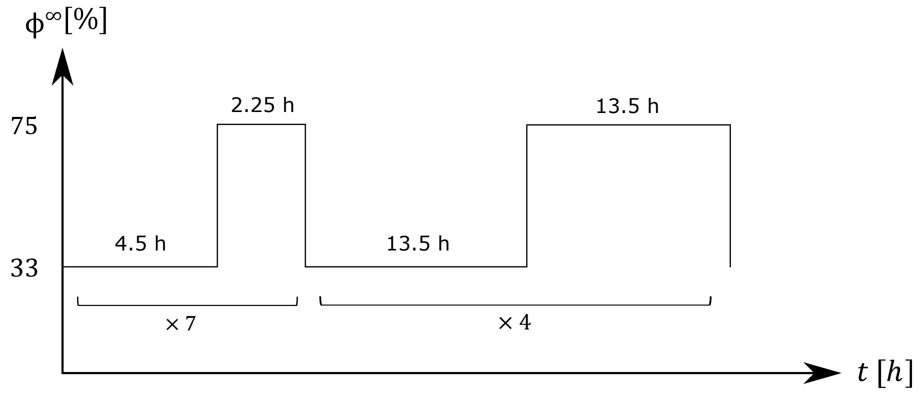

FIGURE 3.9 – Moisture stress applied in the reduced configuration.

Hereafter, the factor proportionality is set to $\Sigma = 0.75\,[-]$ to deduce the second equivalent configuration which is denoted reduced. Relying on this, the reference sample underwent a 25 % scale reduction along the x axis. Thus, the reduced thickness is obtained $L_{red} = \Sigma\, L_{ref} = 7.5\,[\mathsf{cm}]$. Additionally, similarity requires the same preconditioning for the reduced sample in temperature and relative humidity. As for the boundary conditions, the duration is reduced in the equivalent configuration. According to Eq. (3.24), the periodicity of the experiment is decreased by 43.75 %. Indeed, the reduced sample should undergo a stress which lasts $t_{red} = \Sigma^2\, t_{ref} = 6.47\,[\mathsf{d}]$. The reduced stress scenario is shown in Figure 3.9. Finally, the equivalent positions inside the reduced sample are obtained by applying the proportionality factor on $\chi_{ref,\,a}$ and $\chi_{ref,\,b}$. Therefore, $\chi_{red,\,a} = \Sigma\,\chi_{ref,\,a} = 1.875\,[\mathsf{cm}]$ and $\chi_{red,\,b} = \Sigma\,\chi_{ref,\,b} = 3.75\,[\mathsf{cm}]$. Remind that this four positions have the same coordinates along y and z axis.

In section 4, the notion of uncertainties is discussed. In the first place, a definition and the utility of this quantity are given. Then, in the framework of our study, the global uncertainty is formulated. With further details, different sub-uncertainties are identified by defining and expressing them analytically.

4 Evaluation of uncertainties related to heat and moisture diffusion experiment

During any experiment, there are certain sources of error that are unavoidable and that influence a result. These can include the calibration, environmental conditions during the experiment, manipulator behavior or even the response time of a used device. Thus, it is important for the experimenter to be able to define the margin of error related to his measurements. As similarity experiments are exposed to sources of errors, both tests are associated to two global uncertainties σ_T and σ_ϕ [°C]. According to Taylor [134, 169], uncertainties on temperature and relative humidity are expressed as follows :

$$\sigma_T^2 = \sigma_{T,\,\mathrm{Sys}}^2 + \sigma_{T,\,x}^2 + \sigma_{T,\,t}^2 + \sigma_{T,\,\mathrm{Rdm}}^2 + \sigma_{T,\,\mathrm{H2}}^2 \,. \tag{3.32a}$$

$$\sigma_\phi^2 = \sigma_{\phi,\,\mathrm{Sys}}^2 + \sigma_{\phi,\,x}^2 + \sigma_{\phi,\,t}^2 + \sigma_{\phi,\,\mathrm{Rdm}}^2 + \sigma_{\phi,\,\mathrm{H2}}^2 \,. \tag{3.32b}$$

σ_T and σ_ϕ are the global uncertainties associated to temperature and relative humidity fields respectively. According to Equations (3.32a) and (3.32b), it was chosen to limit at five the number of sub-uncertainties. The assessment of a global uncertainty helps defining the confidence interval related to an experimental result. Mathematically, confidence intervals related to temperature or relative humidity and denoted I_T and I_ϕ, respectively, are defined as follows :

$$I_T(\chi, t) = \left\{ m \in \mathbb{R}^+ ; \quad T(\chi, t) - \sigma_T(\chi, t) \leq m \leq T(\chi, t) + \sigma_T(\chi, t) \right\}, \tag{3.33a}$$

$$I_\phi(\chi, t) = \left\{ m \in \mathbb{R}^+ ; \quad \phi(\chi, t) - \sigma_\phi(\chi, t) \leq m \leq \phi(\chi, t) + \sigma_\phi(\chi, t) \right\}. \tag{3.33b}$$

Where χ and t define the measurement position and the instant of the experiment, respectively.

4.1 Systematic uncertainty

Starting with $\sigma_{T,\mathrm{Sys}}$ and $\sigma_{\phi,\mathrm{Sys}}$ [°C], which are the systematic uncertainties on both fields and related to the sensors used for the measurements. They arise from the sensor calibration defects and are provided by the manufacturer [170]. Moreover, they depend on the temperature and relative humidity ranges that a sensor measures. In this study, it is assumed that this uncertainty is constant during carried experiments. Their values are given in Section 3.2.

4.2 Uncertainty related to sensor position

Another source of error could result from the sensor position accuracy. It is taken into account since the experimenter runs the risk of being inaccurate, and also because of the diameter of used sensors. In this purpose, the uncertainties $\sigma_{T,x}$ and $\sigma_{\phi,x}$ [°C] regarding the sensor position are expressed as follows :

$$\sigma_{T,x}(x, t) = \frac{\partial T}{\partial x}\,\delta_x + o(\delta_x), \tag{3.34a}$$

$$\sigma_{\phi,x}(x, t) = \frac{\partial \phi}{\partial x}\,\delta_x + o(\delta_x). \tag{3.34b}$$

Where :

$$\frac{\partial \phi}{\partial x} = \frac{1}{P_{sat}}\frac{\partial P_v}{\partial x} - \frac{P_v}{P_{sat}^2}\frac{\partial P_{sat}}{\partial T}\frac{\partial T}{\partial x}. \tag{3.35}$$

The saturation pressure derivative according to temperature is given by the relation of Clapeyron in Eq. (3.36) :

$$\frac{\partial P_{sat}}{\partial T} = \frac{M\,L_v}{RT^2}\,P_{sat}. \tag{3.36}$$

As for this uncertainty, it depends on time and space. It is based on the infinitesimal development of temperature and relative humidity around the sensor position. Particularly, this development is limited to the first order. The partial derivatives are evaluated, at the desired location and instant, by solving Eqs. (3.1) and (3.2). For that, finite elements method is used. In addition, δ_x [m] designates the distance that represents the error committed on the position of the sensor. This error is mainly due to the drilling of a material and introducing the sensors. The order of magnitude of δ_x is assumed equivalent to the diameter of the sensor.

4.3 Uncertainty related to sensor response time

The response time of a sensor can also impact an experimental result. It describes the reaction of a sensor following a change in temperature or relative humidity. The less time a sensor takes to display the correct value, the more accurate it is. Thus, the sensor time response uncertainty is defined by :

$$\sigma_{T,t}(x,t) = \frac{\partial T}{\partial t}\,\delta_t + o(\delta_t)\,. \tag{3.37a}$$

$$\sigma_{\phi,t}(x,t) = \frac{\partial \phi}{\partial t}\,\delta_t + o(\delta_t)\,. \tag{3.37b}$$

Where :

$$\frac{\partial \phi}{\partial t} = \frac{1}{P_{sat}}\frac{\partial P_v}{\partial t} - \frac{P_v}{P_{sat}^2}\frac{\partial P_{sat}}{\partial T}\frac{\partial T}{\partial t}\,. \tag{3.38}$$

$\sigma_{T,t}$ and $\sigma_{\phi,t}$ [°C] vary also according to time and space. The temporal partial derivatives are determined, in the same way, based on the solution computation of Eqs. (3.1) and (3.2). δ_t [s] represents the response time of the sensor. Its value for Ahlborn sensors is given in Section 3.2.

4.4 Random uncertainty

Equations (3.32a) and (3.32b) introduce each a fourth term which is $\sigma_{T,\mathrm{Rdm}}$ or $\sigma_{\phi,\mathrm{Rdm}}$ [°C]. This uncertainty characterizes the random aspect of a given experiment. Generally, it constitutes the parameter which is used to evaluate the reproducibility of a test. Particularly, it informs on the variability of the micro-structure from one sample to another. Consider N samples undergoing the same experiment. And let T_i and ϕ_i be the temperature and relative humidity measured in the sample i at the instant t where $i \in \{1, N\}$. $\bar{T}$ and $\bar{\phi}$ are the arithmetic means of both fields respectively for N samples. The random uncertainty is given by the formula below :

$$\sigma_{T,\mathrm{Rdm}}(x,t) = \frac{1}{N^{1/2}}\left(\frac{1}{N-1}\sum_{i=1}^{N}(T_i - \bar{T})^2\right)^{1/2}, \qquad \bar{T} = \frac{1}{N}\sum_{i=1}^{N} T_i\,. \tag{3.39a}$$

$$\sigma_{\phi,\mathrm{Rdm}}(x,t) = \frac{1}{N^{1/2}}\left(\frac{1}{N-1}\sum_{i=1}^{N}(\phi_i - \bar{\phi})^2\right)^{1/2}, \qquad \bar{\phi} = \frac{1}{N}\sum_{i=1}^{N} \phi_i\,. \tag{3.39b}$$

Note that the random uncertainty is a time function because temperature and relative humidity and their averages are as well. Moreover, these parameters are evaluated at positions where the study is carried.

4.5 Assumption 2 uncertainty

Finally, this uncertainty involves the evaluation of the error related to the modeling of the Dirichlet type boundary condition. On the one hand, it is based on the study of the sensitivity on temperature and relative humidity within the material in regard to those at the interaction surface. On the other hand, it depends on the discrepancy in a field between the interaction surface and air. $\sigma_{T,\mathrm{H2}}$ and $\sigma_{\phi,\mathrm{H2}}$ are expressed via the Eqs. (3.40a) and (3.40b) :

$$\sigma_{T,\mathrm{H2}}(x,t) = \frac{\partial T}{\partial T_s}\,\delta_{T_s} + o(\delta_{T_s}), \tag{3.40a}$$

$$\sigma_{\phi,\mathrm{H2}}(x,t) = \frac{\partial \phi}{\partial \phi_s}\,\delta_{\phi_s} + o(\delta_{T_s}). \tag{3.40b}$$

Where T_s and ϕ_s are the temperature and relative humidity at the interaction surface respectively. Furthermore, $\delta_{T\,s}$ and $\delta_{\phi\,s}$ represent the discrepancy in temperature and relative humidity between air and the material surface. These two quantities are evaluated experimentally thanks to the used sensors. Concerning the partial derivatives, they are calculated numerically by carrying out a study of sensitivity according to surface temperature and relative humidity. Furthermore, these derivatives are denoted θ_1 and θ_2 such that :

$$\theta_1 = \frac{\partial T}{\partial T_s}, \qquad \theta_3 = \frac{\partial \phi}{\partial \phi_s}. \tag{3.41}$$

In the Section 1 of the appendix, the governing equation related to both quantities θ_1 and θ_2 are detailed.

5 Results and discussion

5.1 Experimental evaluation of the assumption : Dirichlet condition modeling

The objective is to evaluate temperature and relative humidity discrepancies δ_{T_s} and δ_{ϕ_s}, introduced in Eq. (3.31), between the material surface and the air inside the chamber.

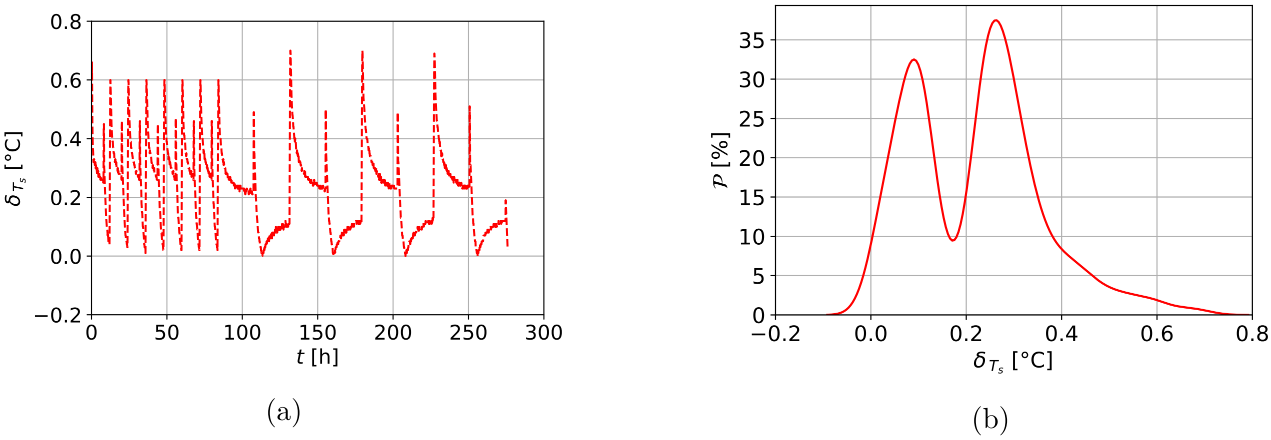

(a)

(b)

FIGURE 3.10 – (a) Temperature discrepancy between air and the sample surface, (b) Probability density related to the discrepancy on temperature.

Despite maintaining a constant temperature, periodic fluctuations are noticed Figure 3.10a. This can be explained by the impact of moisture diffusion on the temperature variation. In addition, this latter follows the periodicity of the moisture stress. Furthermore, the variation in δ_{T_s} follows two different periodicity which are the same as the ones defining the experiment cycles. During the first 7 cycles, δ_{T_s} varies from 0 to 0.6 °C. As for the following cycles, the curve remains almost in the same shape but has larger periodicity. In this case, δ_{T_s} reaches maximum values slightly higher 0.7 °C than those during the first cycles. Moreover, Figure 3.10b highlights the variation of a new function which will be used frequently in next Sections. It is the probability density and denoted $\mathcal{P}$ [171, 172]. It calculates δ_{T_s} values distribution. In this work, the Kernel distribution is adopted as a probability density. It is based on the Parzen – Rosenblatt method. The latter helps to estimate the density at each point of an interval. Contrary to other methods, namely the one introduced by Rudemo or Bowman, it is more accurate. This method generalizes the histogram estimation method which is not continuous. For this, the bar centered at a given value and considering a smoothing parameter, is replaced by a Gaussian centered at this same value. By analyzing the curve in Figure 3.10b, $\mathcal{P}$ represent two local maximums. First one around 0.1 °C with a probability of 32 %. Then, we reach another maximum of 37 % around 0.25 °C.

In terms of relative humidity, δ_{ϕ_s} is plotted in Figure 3.11a. Similarly to temperature, the discrepancy on relative humidity varies in accordance with two periodicity. During short cycles, δ_{ϕ_s} varies between 0 and 0.062. As for long cycles, the discrepancy is relatively smaller. Indeed, it ranges this time between 0 and 0.054. Moreover, large discrepancies are due to transitions from 0.33 to 0.75 and vice versa. Notice also that discrepancy reaches 0 many times during the second phase. The reason behind is the cycle duration in the experiment second part, which is longer.

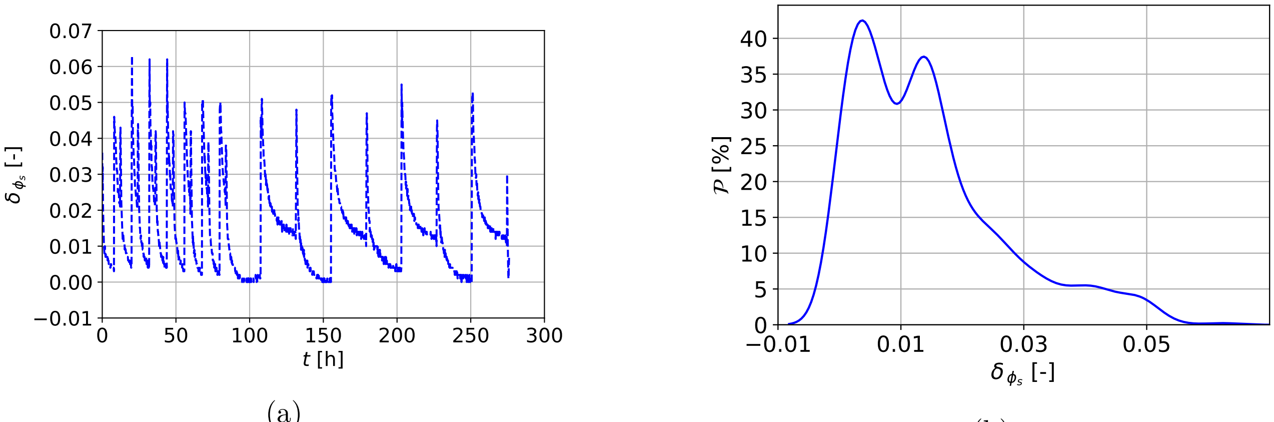

(a)

(b)

FIGURE 3.11 – (a) Discrepancy on relative humidity between air and the sample surface, (b) Probability density representing this discrepancy.

Indeed, maintaining a constant air relative humidity for longer helps decreasing the discrepancy between ϕ^{∞} and ϕ_s. Focusing on the distribution of values taken by δ_{ϕ_s}, it is assessed and illustrated according to Figure 3.11b. Based on that, probability density takes maximum values ranging from 30 % to 40 % for discrepancies between 0 and 0.02 approximately. In addition, notice that zero discrepancy is reached with about 27 % of probability. Hence, based on the results of temperature and relative humidity errors, it is deduced that the assumption 2 is not quite ensured. To conclude, the discrepancy in temperature is different from 0 in 90 %

of the experiment instants. However, the order of magnitude is not very significant. On the other hand, δ_{ϕ_s} turns to 0 in 27 % of the cases, thus a small improvement is observed when comparing the results of these two discrepancies. Nevertheless, the values reached by δ_{ϕ_s} are more meaningful, going up to 0.06. In this case, this would have a consequent effect on the similarities study especially in terms of relative humidity. Regarding this fact, it is decided to include these data in the uncertainty investigation.

In the next Sub-section, the necessary conditions are first recalled to create a similarity between two different configurations. Subsequently, these latter are introduced with their physical dimensions and boundary conditions.

5.2 Assessment of heat and moisture diffusion similarity

This Section deals with the evaluation of uncertainties on temperature and relative humidity in both configurations. It includes a first part where numerical schemes and an experimental methodology are presented. Subsequently, the variation of each sub-uncertainty is analyzed and compared between both configurations. To facilitate comparison, the colors blue and red are used to represent the reference and reduced configurations, respectively. Finally, temperature and relative similarity is assessed and discussed.

5.2.1 Assessment of the uncertainty in reference and reduced configuration

The calculation of uncertainties is based on the deterministic approach. In our case, this approach helps estimating the deviation in temperature or relative humidity at a given instant and position that is caused by the largest variation of each uncertain parameter (sensor response time, surface temperature ...). This variation is expressed using the terms δ, for example in Eq. (3.37a) and (3.40b). Beginning with the sensor systematic uncertainty, its value for temperature and relative humidity is already mentioned in Section 3.2. During experiments, it is assumed that the systematic accuracy do not depend on either the location or the instant of a measurement. Unlike $\sigma_{T,\,\mathsf{Sys}}$ and $\sigma_{\phi,\,\mathsf{Sys}}$, following sub-uncertainties $\sigma_{T,x}$, $\sigma_{T,t}$, $\sigma_{T,\,\mathsf{H2}}$, $\sigma_{\phi,x}$, $\sigma_{\phi,t}$ and $\sigma_{\phi,\,\mathsf{H2}}$ depend on that and are assessed numerically. To do so, the solver *Comsol Multiphysics*, which is based on finite elements method [173, 174], is used. The number of space nodes is set for both configurations to 500. As for the time step, it is set to $\Delta t_{ref} = 1\,[\mathsf{min}]$ for the reference configuration. Hence, the one related to the reduced configuration is obtained by applying similarity which leads to $\Delta t_{red} = \Delta t_{ref}\,\Sigma^2 = 0.56\,[\mathsf{min}]$. Additionally, the resolution of $\sigma_{T,\,\mathsf{H2}}$ and $\sigma_{\phi,\,\mathsf{H2}}$ requires complementary data which are surface temperature and relative humidity. These are recorded each five minutes by a sensor (Section 3.2) and included in the simulation (Section 4.5) using spline interpolations. Finally, $\sigma_{T,\,\mathsf{Rdm}}$ and $\sigma_{\phi,\,\mathsf{Rdm}}$ were approximated by using $N = 3\,[-]$ samples in each configuration (assumption 8). Ideally, the calculation of the random uncertainty is more accurate if the number N is larger. In this case, the consideration of this uncertainty requires to perform the experiments related to both configurations on a large number of samples. Three samples are experimented per configuration on the basis of the six samples, that were manufactured for the study. Thus, $\sigma_{T,\,\mathsf{Rdm}}$ and $\sigma_{\phi,\,\mathsf{Rdm}}$ are evaluated in order to obtain an approximate order of magnitude with regard to other uncertainties.

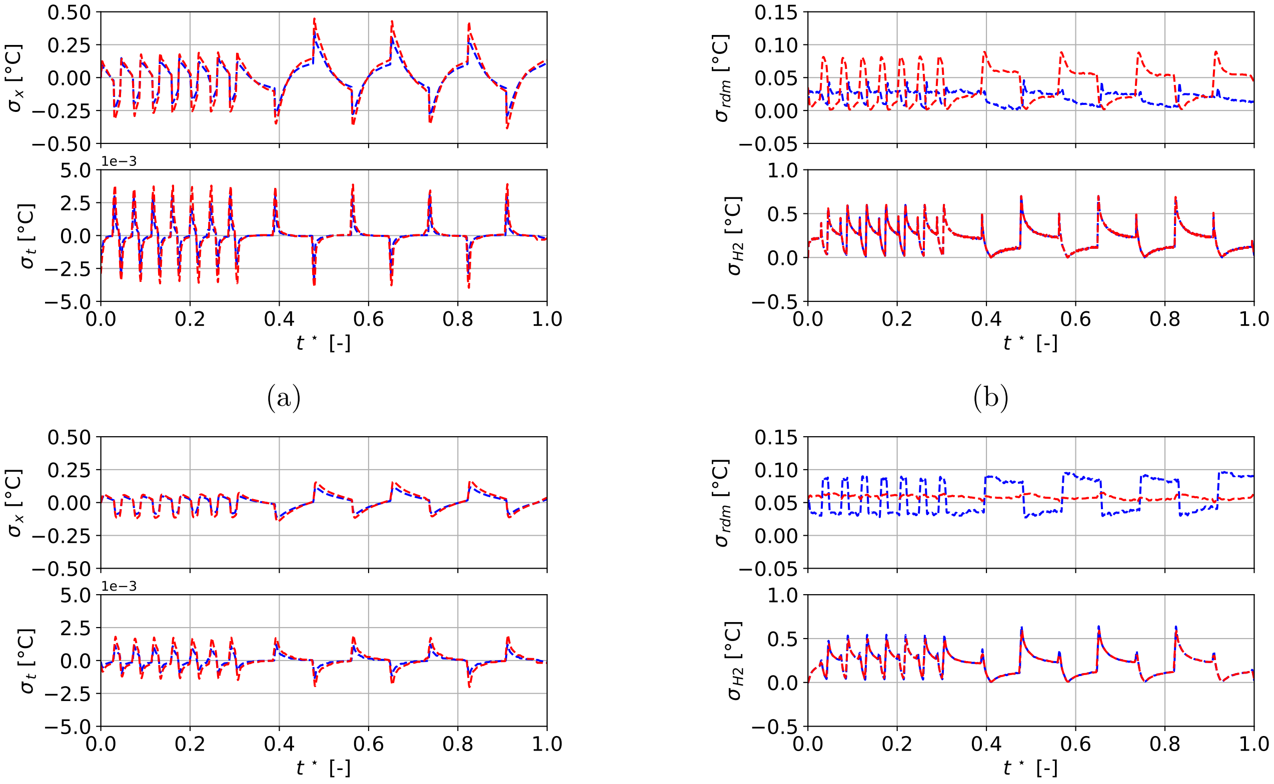

(a)

(b)

(c)

(d)

FIGURE 3.12 – Variation of different uncertainties on temperature at (a,b) the quarter given by χ_1 (Reference) and χ_3 (Reduced), (c,d) the middle given by χ_2 (Reference) and χ_4 (Reduced).

Figure 3.12 plots the variation in uncertainties on temperature $\sigma_{T,x}$, $\sigma_{T,t}$, $\sigma_{T,\mathsf{Rdm}}$ and $\sigma_{T,\mathsf{H2}}$ at the quarter and the middle in both configurations. Firstly, two phases of variations are noticed. The first one, with high frequency, corresponds to the stress cycles that have a small time period. While the second, with a low frequency, refers to the moisture stress phase with a large period. Focusing on the uncertainty related to sensor position and the one due to sensor time response, it is worth noting that at the quarter, they are greater in reduced configuration with values ranging from 0 to 0.43 °C for $\sigma_{T,x}$ and from 0 to 0.004 °C for $\sigma_{T,t}$. This is due to the fact that the uncertainty on a sensor position regarding the reference thickness is smaller than the one with regard to the reduced thickness. Otherwise, the following relation is verified :

$$\frac{\delta_{x,ref}}{L_{ref}} < \frac{\delta_{x,red}}{L_{red}} . \tag{3.42}$$

Same logic is adopted for $\sigma_{T,t}$ when addressing the response time of a sensor and the duration of both experiments, t_{ref} and t_{red}, instead of the uncertainty on a sensor position and thicknesses. Afterwards, it is also observed that $\sigma_{T,\mathsf{Rdm}}$ is greater at the quarter in reduced configuration with maximal values reaching 0.09 °C. However, the interpretation of this finding is not related to both sample thickness or experiment duration. It is rather due to the reproductibility of both tests. Indeed, the order of magnitude of $\sigma_{T,\mathsf{Rdm}}$ depends only on the variability of thermal properties around positions of measurement considering three samples in each configuration. The fact that this sub-uncertainty, at the quarter, is more significant in reduced configuration means that the standard deviation of thermal properties is larger around χ_3 than χ_1. Finally, $\sigma_{T,\mathsf{H2}}$ is also estimated, it is the largest sub-uncertainty which reached 0.7 °C. Additionally, negligible discrepancies are obtained regarding both configurations. Indeed, air temperature related to the reference and reduced configuration coincide closely in the dimensionless domain which is due to similarities.

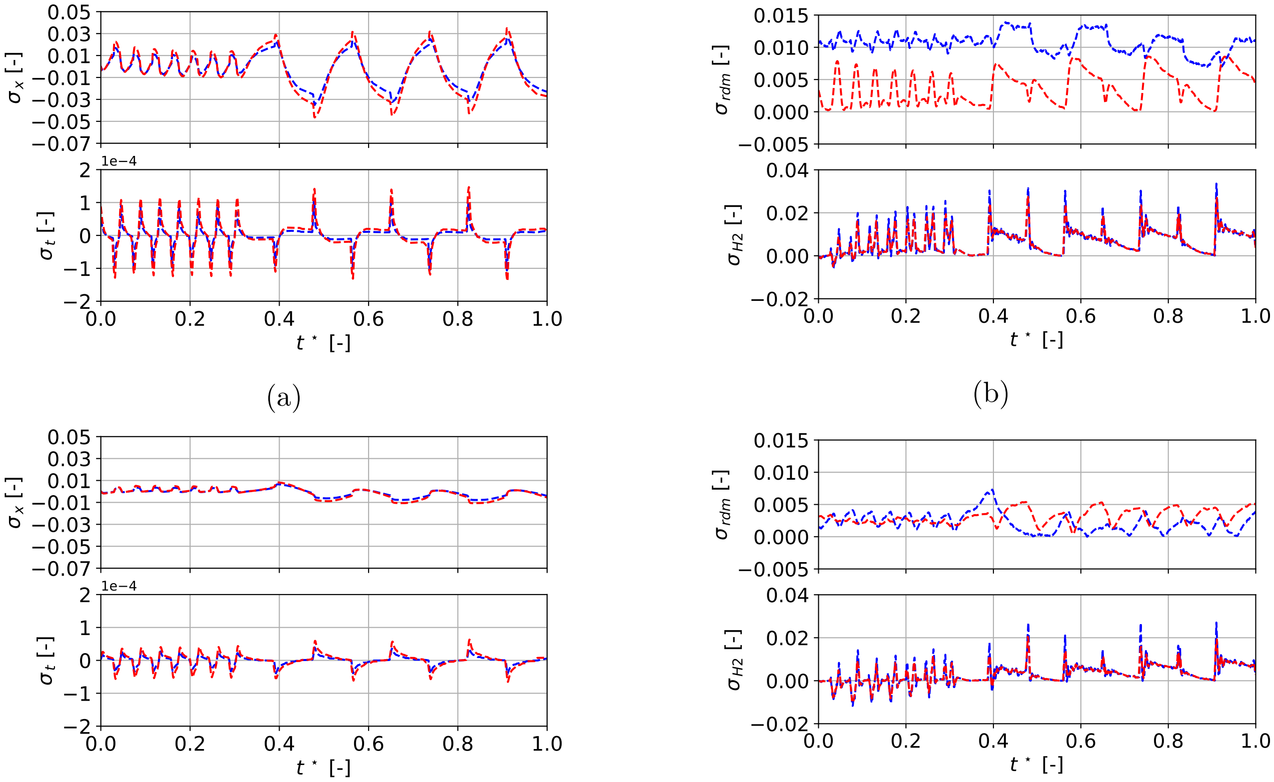

(a)

(b)

(c)

(d)

FIGURE 3.13 – Variation of different uncertainties on relative humidity at (a,b) the quarter given by χ_1 (Reference) and χ_3 (Reduced), (c,d) the middle given by χ_2 (Reference) and χ_4 (Reduced).

On the other hand, quite same results are noticed at the middle for both configurations. $\sigma_{T,x}$ and $\sigma_{T,t}$ are still higher in the reduced configuration. They reach peaks of about 0.16 °C and 0.002 °C, respectively. Secondly, the variation in $\sigma_{T,\mathsf{H2}}$ for both configurations is almost identical following the same reason as for $\chi_{ref,a}$ and $\chi_{red,a}$. Contrary to the result regarding $\sigma_{T,\mathsf{Rdm}}$ at the quarter, it reaches larger values in the reference configuration when focusing on the middle. This means that the variability of thermal properties around $\chi_{ref,b}$ is large. This is due to the random aspect related to a material micro-structure and pore distribution. Last, note that $\sigma_{T,x}$, $\sigma_{T,t}$ and $\sigma_{T,\mathsf{H2}}$ are smaller when getting away from the surface $x = 0$, i.e. the variation magnitude in temperature is smaller when approaching the surface bottom, where an adiabatic condition is set. Thus, the magnitude of temperature derivatives according to space, time and surface temperature is smaller when approaching the surface bottom.

In parallel, a study of uncertainties on relative humidity is also performed. Figure 3.13 represents the variation in uncertainties on relative humidity[1]. At the quarter, $\sigma_{\phi,x}$ and $\sigma_{\phi,t}$ vary more significantly in the reduced configuration with peaks around 0.05 and $1.4\,10^{-4}$ respectively. In addition, $\sigma_{\phi,\mathrm{Rdm}}$ informs about the variability of moisture properties around a position of measurement for a given number of samples. Considering three samples for each configuration, the variability is larger around $\chi_{ref,a}$ where a maximum of 0.014 is remarked. Finally, the variation range of $\sigma_{\phi,\mathrm{H2}}$ at a given position does not depend on a configuration since it involves air temperature. It is about 0.03 as maximum at the quarter. Indicatively, the most dominant sub-uncertainty regarding relative humidity is the one related to sensor position.

As for the middle, it is shown that the uncertainties $\sigma_{\phi,x}$ and $\sigma_{\phi,t}$ were more important in the reduced configuration. Likewise, the uncertainty related to the modeling of boundary conditions varies little when comparing both configurations. As for $\sigma_{\phi,\mathrm{Rdm}}$, it is relatively larger in reduced configuration, which means that the variability of moisture properties is larger around $\chi_{red,b}$ than around $\chi_{ref,b}$. The influence of a position on a calculated uncertainty can also be relevant. Indeed, when considering the material in reduced configuration, notice that the magnitude of the sub-uncertainties $\sigma_{\phi,x}$, $\sigma_{\phi,t}$ and $\sigma_{\phi,\mathrm{H2}}$ is smaller at $\chi_{red,b}$ with peaks around 0.01, $5\,10^{-5}$ and 0.0275 respectively. This is due to the fact that $\chi_{red,b}$ is more distant than $\chi_{red,a}$ from areas with high temperature gradients.

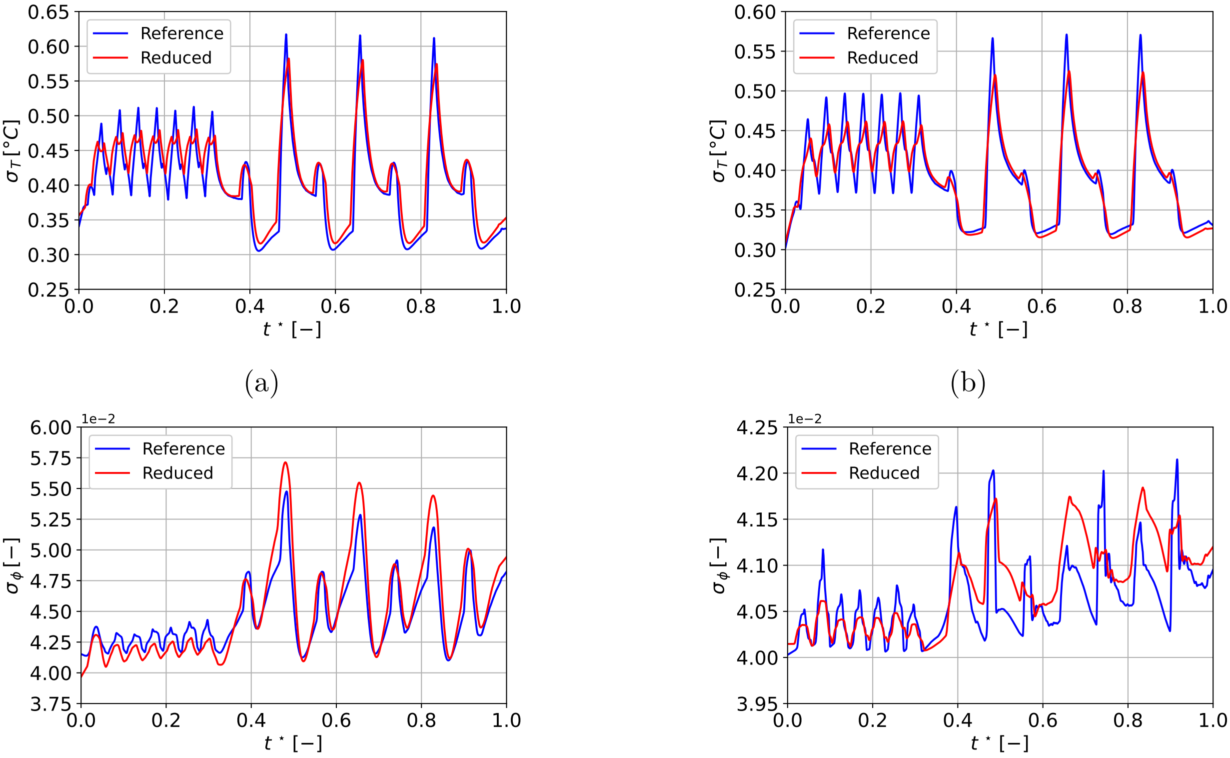

(a) (b)

(c) (d)

FIGURE 3.14 – Uncertainty on temperature and relative humidity for both configurations at $\chi_{ref,a}$ and $\chi_{red,a}$ (a,c), $\chi_{ref,b}$ and $\chi_{red,b}$ (b,d).

---

[1] To avoid any confusion, the results are presented in absolute value and not percentage (of vapor pressure according to saturation one) since the latter could be confusing with relative uncertainties.

Figure 3.14 shows the variation in the entire uncertainty on temperature and relative humidity at the quarter comparing $\chi_{ref,a}$ and $\chi_{red,a}$ and the middle considering $\chi_{ref,b}$ and $\chi_{red,b}$. Remark that σ_T, at the quarter of the material in both configurations, is slightly larger than the one at the middle with maximums of 0.62 °C and 0.53 °C respectively. The same comment can be made in regard to σ_ϕ where a maximum of about 0.0575 is observed for the material quarter against 0.042 for the middle. Based on these results, two major results can be deduced. The entire uncertainty in temperature or relative humidity is more significant in the reduced configuration. This is mainly due to the fact that the relative uncertainty on the position of the sensor and the one related to its time of response (with a lower contribution) are larger in this configuration as shown in Eq. (3.42) for example. Moreover, a second result is to mention. The uncertainty on relative humidity is larger at the quarter of the material than at its middle. Indeed, the position at the quarter is closer to areas with significant moisture gradients, while the middle is more distant.

Thereafter, entire uncertainties (Figure 3.14) are then used to calculate the confidence intervals in temperature and relative humidity as defined in Eqs. (3.33a) and (3.33b). Additionally, the magnitude of each sub-uncertainty is important in order to discuss the validity of similarity on heat and moisture diffusion. In other words, the upcoming comparison, carried out on temperature and relative humidity between both configurations, is based on the results of uncertainty. Next Section discusses the experimental results of heat and moisture similarity.

5.2.2 Discussion of the validity of heat and moisture diffusion similarity

Figure 3.15 illustrates the variation in temperature and relative humidity at the quarter and the middle of the material in both configurations. The variation is periodic where two temporal sequences are distinguished. The first part with a high frequency and the second with a low one. This observation is related to the nature of the stress scenario as explained in the previous Section. Regarding temperature at $\chi_{ref,a}$ and $\chi_{red,a}$, it varies in the same way, ranging between 22.6 and 23.75 °C approximately. In addition, slight discrepancies are observed around the peaks of curves. However, they are relatively higher when comparing temperature at the middle between both configurations ($\chi_{ref,b}$ and $\chi_{red,b}$). It reaches maximums around curve peaks of about 0.25 °C. Generally, results in temperature highlight an acceptable agreement.

Same figure shows the variation in relative humidity at the quarter and middle of the material in the reference and reduced configuration. The curves vary following two sequences while showing a good agreement especially the ones associated to $\chi_{ref,a}$ and $\chi_{red,a}$. Considering the mentioned positions, a considerable variation is observed during the second sequence where values range from 0.38 up to 0.66. Contrary to temperature, discrepancies on relative humidity between reference and reduced configuration are more significant, particularly when air relative humidity changes from 0.33 to 0.75 and vice versa. At the middle, the variation is less significant where relative humidity at $\chi_{ref,b}$ and $\chi_{red,b}$ ranges from 0.43 to 0.6. Moreover, a remarkable dephasing is illustrated when comparing relative humidity at middles. It could be caused by a difference in micro-structure between areas around χ_2 and χ_4. In order to evaluate discrepancies in relative humidity and its distribution, the Kernel density of probability is plotted in Fig 3.16.

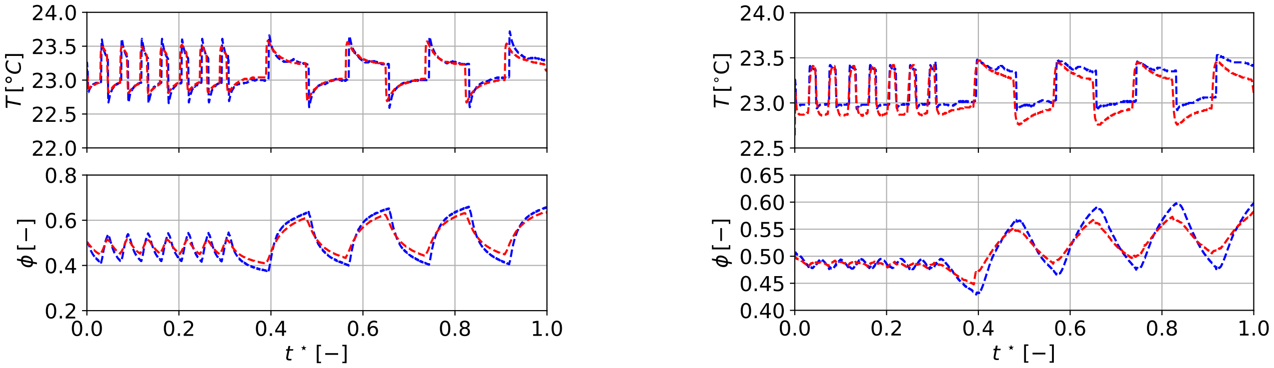

(a) (b)

FIGURE 3.15 – Variation in temperature and relative humidity for both configurations at (a) $\chi_{ref,\,a}$ and $\chi_{red,\,a}$, (b) $\chi_{ref,\,b}$ and $\chi_{red,\,b}$.

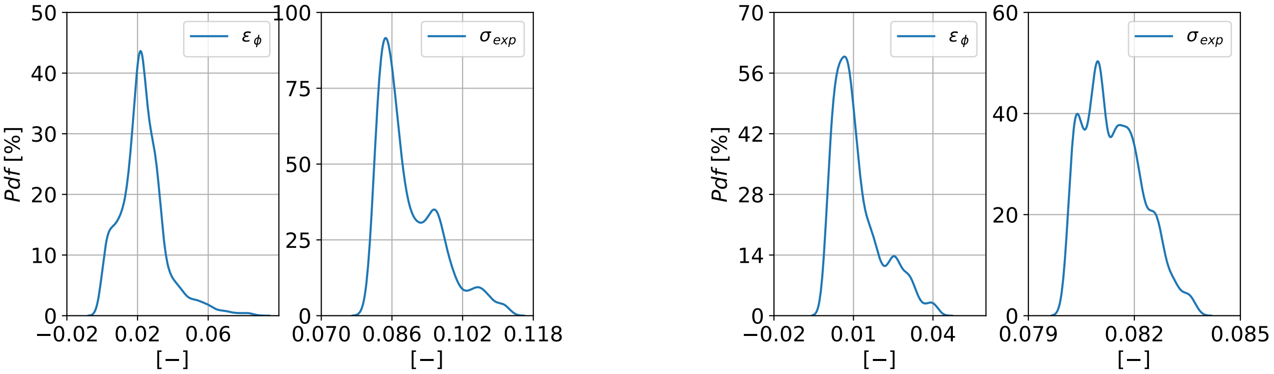

(a) (b)

FIGURE 3.16 – Distribution of the discrepancy on relative humidity for both configurations and the sum of the corresponding uncertainties at (a) $\chi_{ref,\,a}$ and $\chi_{red,\,a}$, (b) $\chi_{ref,\,b}$ and $\chi_{red,\,b}$.

It highlights the distribution of discrepancies on relative humidity between configurations. It is worth noting that it reaches higher values when it is evaluated at the quarter. According to Figure 3.16, the discrepancy can go up to 0.05 with a probability less than 5 %. In addition, the probability reaches its maximum for values around 0.02. Furthermore, the discrepancy on relative humidity is relatively smaller at the middle. It reaches a maximum of 0.035 for a probability of about 5 % and is largely around 0.007 for a probability of 60 %. Based on this comparison, it is deduced that the discrepancy between both configurations is larger if positions of measurement are close to areas with high stress gradients. This is evidenced via Figure 3.16, the discrepancy at the quarter is two times larger than the one at the middle. However, there is less discrepancy if the positions of measurement are more distant from areas under intense stress, as relative humidity varies slower when increasing distance.

Obtained discrepancies on temperature and relative humidity have to be discussed by considering the uncertainties at $\chi_{ref,\,a}$, $\chi_{ref,\,b}$, $\chi_{red,\,a}$ and $\chi_{red,\,b}$ as shown in Figure 3.14. Otherwise, confidence intervals [175, 176], as given in Eqs. (3.33a) and (3.33b), must be evaluated during the entire experiment.

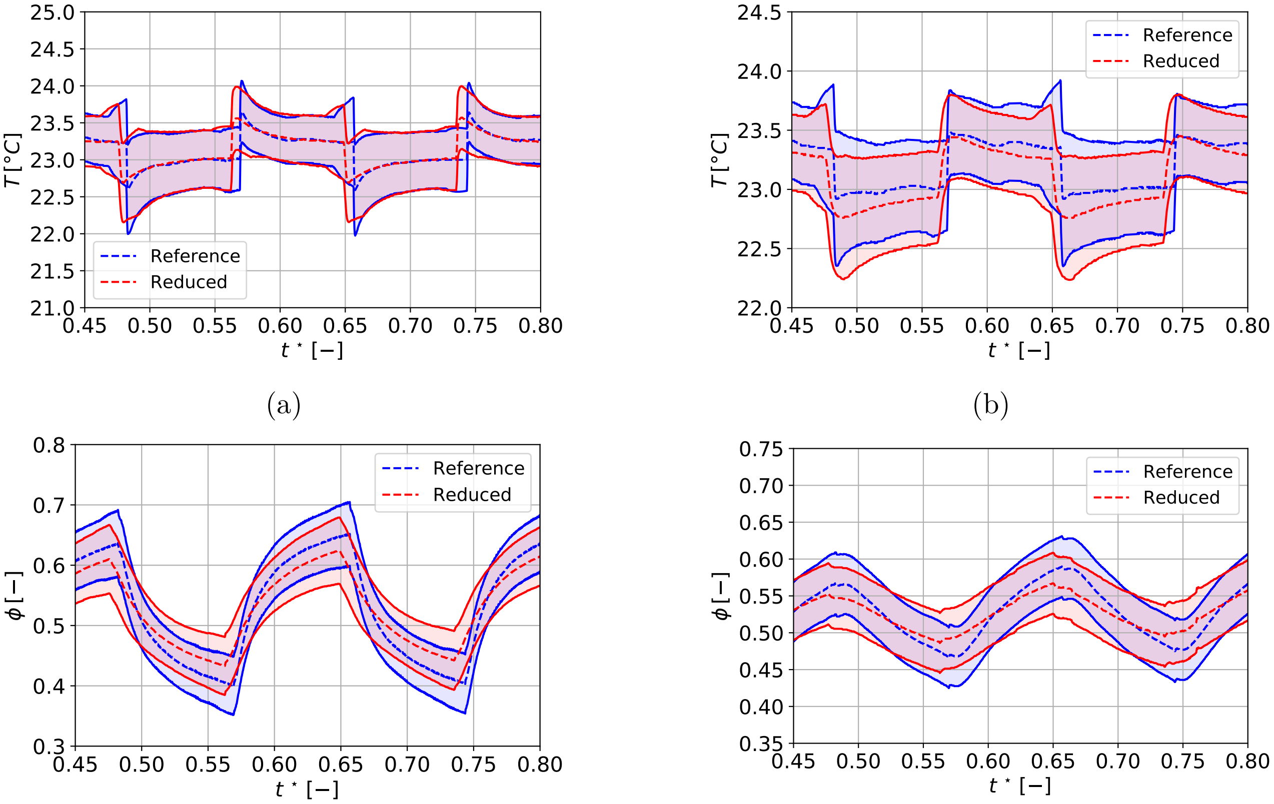

(a) (b)

(c) (d)

FIGURE 3.17 – Temperature and relative humidity variation at $\chi_{ref,a}$, $\chi_{red,a}$ (a,c) and $\chi_{ref,b}$, $\chi_{red,b}$ (b,d) with the associated confidence intervals.

Figure 3.17 illustrates the confidence intervals associated to temperature and relative humidity at $\chi_{ref,a}$, $\chi_{ref,b}$, $\chi_{red,a}$ and $\chi_{red,b}$ during a given sequence. The dotted lines represent the measured data, also considered as averages. Additionally, colored areas, which are delimited by two continuous lines, indicate a confidence interval, using blue for the reference positions and red for the reduced configuration. It is important noting that for two equivalent positions, significant areas are noticeable where the confidence intervals coincide. In particular, when comparing temperatures at the quarter and relative humidity at the middle. In this respect, measurements are quite comparable between the configurations with the occurrence of considerable discrepancies, mainly in relative humidity.

Figure 3.18 helps to evaluate the magnitude of discrepancies and hence, verify entirely the conditions expressed in Eqs. (3.27a) and (3.27b). At the quarter, the discrepancy on temperature is almost 0 with oscillations up to 0.5 °C. As for relative humidity, it is larger with a maximum of about 0.075. Despite its magnitude, the discrepancy remains smaller than the uncertainty which reaches 1.2 °C and 0.11 on temperature and relative humidity respectively. Focusing on the middle, the discrepancy in temperature reaches as well 0.5 °C as a maximum, while it is less significant in relative humidity than at the quarter with 0.04 as maximum. In this case, uncertainties are also larger than discrepancies, with peaks of 1 °C and 0.08 on temperature and relative humidity respectively. After this supplementary investigation, the conditions in Eqs. (3.27a) and (3.27b) are confirmed considering χ_1 and χ_2 and the entire duration of both configurations. Therefore, based on the results in Figure 3.18, similarity of heat and moisture diffusion investigations are verified experimentally considering the two configurations defined in the study. This can also be evidenced by comparing the distribution of discrepancies with the sum of uncertainties, as shown in Figure 3.16. The resulting discrepancies are justified by carrying out a parallel investigation that takes into account five different sources of uncertainties.

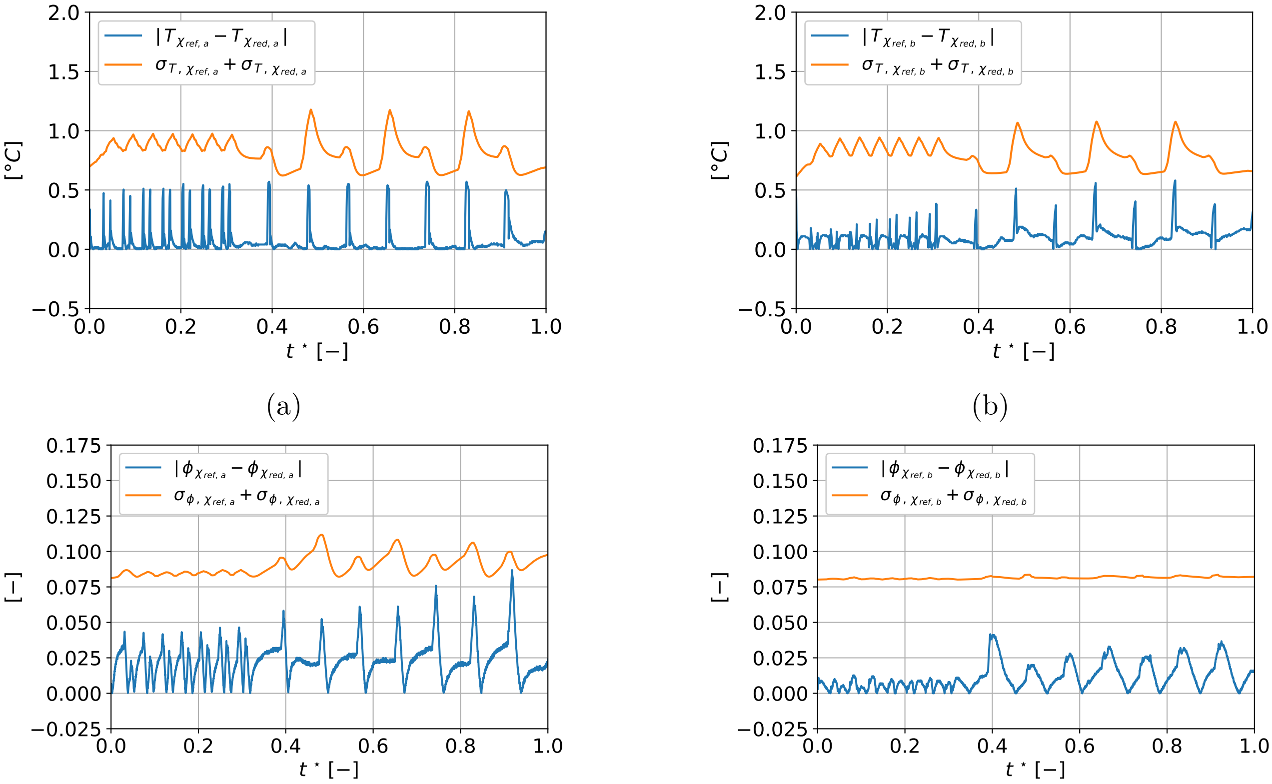

(a)

(b)

(c)

(d)

FIGURE 3.18 – Discrepancies on temperature and relative humidity between the reference and reduced configurations compared to the sum of the corresponding uncertainties at the quarter (a,c) and the middle (b,d).

5.3 Discussion and further remarks

Based on the results of the previous section, the discrepancies reached significant thresholds during several sequences. Indeed, several source errors are difficult to reduce because of certain experimental constraints. The inaccuracy of used equipment for the two similarity experiments is a first source of error. Indeed, the ambient conditions in the climate chamber are not perfectly regulated especially relative humidity because of the size of this facility and its high inertia. As a result, air temperature and relative humidity are exposed to a margin of error. Moreover, the preconditioning of the material in relative humidity may not be completely ensured, which is caused by the high heterogeneity of its micro-structure and the presence of closed pore networks. Nevertheless, the causes previously identified, which reflect the relativity of this type of experiment, can be improved.

The results related to both configurations can also be improved. This requires a better control of the experimental conditions, i.e. an accurate verification of the assumptions set in the physical model. Considering the assumption 1, which implies that the flux is along a single direction, namely the x axis. This statement is theoretical and was verified experimentally within an acceptable error [155]. Indeed, the flux is one-dimensional if the thermal conductivity of the insulator is very high compared to the one of the used material or if the latter is a semi-infinite medium along y and z axes. Thus, two additional sub-uncertainties $\sigma_{T,1D}$ and $\sigma_{\phi,1D}$ could have been added to address the relativity of this assumption during both similarity experiments. Ideally, its evaluation at a given coordinate $x = \chi$ is based on the measurement of temperature T and relative humidity ϕ at all positions which have the same x coordinate. This uncertainty in temperature and relative humidity is formulated as follows :

$$\sigma_{T,\,\mathsf{1D}}(\chi\,,\,t) = \lim_{N\to+\infty}\left(\frac{1}{N\,(N-1)}\sum_{i=1}^{N}(T_i-\bar{T})^2\right)^{0.5}, \tag{3.43a}$$

$$\sigma_{\phi,\,\mathsf{1D}}(\chi\,,\,t) = \lim_{N\to+\infty}\left(\frac{1}{N\,(N-1)}\sum_{i=1}^{N}(\phi_i-\bar{\phi})^2\right)^{0.5}. \tag{3.43b}$$

N represents the number of sensors inside the material along the y-axis while fixing the x coordinate. As remarked, the assessment of this uncertainty is definitely accurate if N is infinite. However, given experimental constraints, it is quite challenging to set up a high number of sensors along a single direction. $\bar{T}$ and $\bar{\phi}$ represent the mean values at a position χ, while considering variations along y and z axes, they are given in Eqs. (3.44a) and (3.44b) respectively :

$$\bar{T}(\chi\,,\,t) = \lim_{N\to+\infty}\frac{1}{N}\sum_{i=1}^{N}T_i\,, \tag{3.44a}$$

$$\bar{\phi}(\chi\,,\,t) = \lim_{N\to+\infty}\frac{1}{N}\sum_{i=1}^{N}\phi_i\,. \tag{3.44b}$$

In [155], authors tried to estimate this uncertainty in the framework of a heat diffusion experiment. The determination of this quantity was limited to some positions on the same plane that is defined by x and y axes. Values ranging from 0 to 0.1 °C were obtained for the middle of a hemp concrete sample, while applying a stress ranging from 11 to 39 °C. Thus, the uncertainty on the one-dimensional diffusion would probably be considered negligible in our study.

Otherwise, the application of similarity can be extended to three-dimensional heat and moisture diffusion. Assume that the material is used without insulation, moisture and heat flux propagate in all directions. In this respect, the physical model and its dimensionless formulation are written while introducing two additional dimensions L_y and L_z. Consequently, besides the coefficients δ, γ and η, four additional Fourier numbers $\mathrm{Fo}_{\mathrm{q,y}}$, $\mathrm{Fo}_{\mathrm{q,z}}$, $\mathrm{Fo}_{\mathrm{m,y}}$ and $\mathrm{Fo}_{\mathrm{m,z}}$ would be obtained. These are expressed according to Eqs. (3.45a) and (3.45b). In this case, the same factor of proportionality Σ is used for L_y and L_z to obtain an equivalent configuration.

$$\mathrm{Fo}_{q,\,y} = \frac{\lambda_0\,t_f}{\rho_{s0}\,C_{p0}\,L_y^2} \quad , \quad \mathrm{Fo}_{q,\,z} = \frac{\lambda_0\,t_f}{\rho_{s0}\,C_{p0}\,L_z^2}\,, \tag{3.45a}$$

$$\mathrm{Fo}_{m\,y} = \frac{k_{m0}\,t_f}{\rho_{s0}\,C_{m0}\,L_y^2} \quad , \quad \mathrm{Fo}_{m\,z} = \frac{k_{m0}\,t_f}{\rho_{s0}\,C_{m0}\,L_z^2}\,. \tag{3.45b}$$

A second assumption was considered in the diffusion model which is the modeling of the boundary conditions at the exposed surface using Dirichlet. This implies that air has no heat or moisture resistance, hence air temperature and relative humidity and the ones at $x = 0$ are equal. In reality, convective fluxes exist at the interacting surface which are due to the heat and water vapor coefficients h_c and h_m. In this respect, Robin boundary conditions are the most adequate. Considering these two coefficients in the model would lead to the introduction of the Biot numbers as defined in Eq. (3.30). As a result, the equivalence between configurations requires an additional condition on h_c and h_m expressed as follows :

$$h_{c1}\,L_1 = h_{c2}\,L_2 \quad , \quad h_{m1}\,L_1 = h_{m2}\,L_{21}\,. \tag{3.46}$$

In order to ensure a similarity, it is necessary to estimate the convective coefficients associated to both configuration. However, the assessment of these coefficients relies on the knowledge of certain parameters, i.e. air physical properties, the geometry of the problem and especially air flow velocity. In the literature, empirical models were developed in fluid dynamics to estimate these coefficients, although they are limited. The reason is the experimental conditions that are different from one study to another. Consequently, the estimation of h_c and h_m could be possible if a correlation, proper to our experimental design, exists between these coefficients and air velocity. In this regard, the adjustment of air velocity during a configuration would help control heat and moisture convective coefficients. This might represent an experimental constraint if the climatic chamber operates at a constant air flow rate. Indeed, varying these coefficients to study the reduced configuration would not be possible, even-though their values are assumed known for the reference configuration. As a result, the verification of similarity, while using the Robin type, would rely on the realization of an experimental bench which monitors the temperature, relative humidity and air velocity.

The latter requires that properties and their laws of variation are identical between configurations. This implies that the sample micro-structure in the reduced model is similar to the one in the reference configuration.

6 Conclusion

Similarity laws may constitute an efficient approach to reduce the duration of a heat and moisture diffusion experiment. In this work, similarity on these coupled phenomena is experimentally assessed. In this respect, two major limitations are considered during experiments. It is assumed that heat and moisture transfer are one-dimensional. Moreover, Dirichlet boundary conditions are taken into account at the exposed material surface. A first configuration denoted reference is proposed and defined by a 10 cm thick hemp concrete sample that is exposed to a constant temperature and a variable moisture stress during 11.5 d. As for boundary conditions, material-air interactions occur by means of a single surface. Other surfaces are considered adiabatic against heat and water vapor fluxes. To obtain the reduced configuration, a factor of proportionality 0.75 is considered. Hence, the deduced configuration involves a reduced material thickness 7.5 cm and a shorter test duration 6.47 d. To discuss similarity, temperature and relative humidity are compared at the quarter and middle of the material during both experiments. Regarding temperature, the discrepancies at the quarter and middle have the same of magnitude. As for relative humidity, the curves show a good agreement. Meanwhile, discrepancies are more relevant at the quarter than at the middle. Afterwards, the validity of similarity is tested by proposing a detailed investigation which aims, on the one hand, at evaluating the uncertainties associated to both configurations and on the other, to compare the magnitude of discrepancy with uncertainty on temperature and relative humidity.

In addition, five sub-uncertainties are proposed and defined using the deterministic approach. Results showed that for the quarter of the material, the uncertainty on temperature related to the assumption on Dirichlet boundary conditions is the dominant. As for relative humidity, the uncertainty at the quarter and related to the sensor position is the most prevalent. It is worth noting that the entire uncertainty is more significant in the reduced configuration. Finally, the validity of similarities is rigorously investigated by comparing the combined entire uncertainties of both configurations with the calculated discrepancies. Based on the latter, it is agreed that similarity on heat and moisture diffusion can be correctly applied for building materials. The verification of these laws on hemp concrete can help in future works to address scientific issues such as the investigations of material aging. It is a slow kinetic phenomenon which induces variation in material properties with time. Similarities would be employed to approach phenomena in the framework of a reduced duration experiment.

Acknowledgments

The Region and the European Union support the project <CPER-FEDER Bâtiment durable Axis 2 MADUR Project : High-performance building materials with low environmental impact, sustainable and resilient> within the framework of the « Operational Program FEDER/FSE 2015-2020 and Energy saving certificate program of the Ministry of Ecological and Solidarity Transition "SmartReno support" 2019-2021.

Chapitre 4

On the development of an accelerated aging design : assessment of its effects on a bio-based material

Abstract

Recently, bio-based materials are tested often in construction. Contrary to conventional materials, the properties of a bio-based material varies significantly in time due to heat and moisture stresses. This phenomenon is widely known as "aging". The latter is investigated within this research on hemp concrete. This study proposes a new methodology to develop an accelerated and realistic aging protocol. The real scale design is established by means of annual meteorological data. Then, it is accelerated by using the laws of similarity where the time horizon decreases from one year to roughly 40 days. Second part is experimental, where measurements of thermal conductivity, intrinsic permeability, porosity and pH index are conducted gradually on different samples and at 9 time instants. These instants correspond to each 1.5 months in the real scale aging test. Consequently, the time variation of these properties is obtained to assess the material aging. Two correlations are deduced, these reveal variation laws of thermal conductivity and intrinsic permeability with respect to porosity. Afterwards, these correlations are compared to empirical models from the literature. Besides, no risk of mold growth is observed according to the pH index variation. Finally, the study concludes on the importance of considering the effect of aging on porosity and thus on depending properties in further heat and mass transfer investigations.

Highlights

1. A methodology to develop a realistic and representative aging protocol.
2. A long protocol is proposed on the basis of a one-year climate data and down-scaled using the similarity laws.
3. Measurements of thermal conductivity, intrinsic permeability, porosity and pH index are carried on hemp concrete at each 1.5 months during one year.
4. Correlations relating thermal conductivity and intrinsic permeability to porosity are deduced.
5. Concordances are noticed between the experimental results and existing empirical models.
6. No mold growth risks are observed for hemp concrete according to the pH index results.

Keywords

Climate data, aging protocol, similarity laws, material properties, uncertainty, mold growth, heat and mass transfer.

1 Introduction

The choice of construction materials is based on thermal, environmental and sustainability requirements [177, 178]. To attain these objectives, standards have risen over the final two decades, such as the BREEAM, LEED and Green Globes certifications. Recently, it has become more important to take into account the impacts of selected materials on various sustainability indicators [179]. In this context, the use of conventional construction materials, such as concrete and mortar, ensures a good building sustainability level. However, it contributes to almost half of carbon dioxide emissions [180], making it one of the main contributors to global warming [181].

To overcome this double issue, research is being conducted on a new generation of materials. Partially based on cement or lime, bio-based materials [182, 183] would be a valuable contribution to a better energy and environmental performance. Apart from its benefits [184, 185], the sustainability indicators of a bio-based material are difficult to predict when it undergoes heat and moisture stresses. This statement is mainly due to the degree of complexity of a bio-based material micro-structure [186, 187]. Additionally, a complementary solid phase is present in a bio-based material, namely the plant fibers. These are sensitive to the presence of liquid water and high temperatures. Both stress forms modify regularly the micro-structural properties [188] and more particularly porosity. Affected properties can be mechanical, thermal, acoustic [74]. This phenomenon is known as aging or weathering according to the scientific community. Furthermore, the exposure of bio-based materials to such stresses may lead to microbial and fungi growth risks [189] when suitable conditions occur.

Broadly stated, the aging of a material is merely a variation of its structure at the micro-scale and the macroscopic properties related to its micro-structure. According to the literature, the exposure of materials to high temperatures can induce aging. For example, This investigation

[190] highlights the effect of age hardening on the mechanical properties of graphite-reinforced aluminum composites fabricated by stir-casting routing. The fabricated specimens were subjected to an accelerated aging at the temperatures 170 °C, 270 °C and 500 °C. Based on an electron microscope, fractured surfaces were analyzed to understand the failure mechanism.

Within This paper, conducted investigations focus more on aging due to heat and water mass transfer. In the literature, numerous researches were interested in reproducing the effects of natural aging of a material by proposing accelerated cycles of heat and humidity stresses that are occasionally aggressive. Indeed, aging is a phenomenon that occurs withing a long duration whose magnitude varies from several months to years. Therefore, this time issue arises when applying a natural aging test in the laboratory. For this reason, evaluating the effects of this long phenomenon requires the definition of accelerated experimental designs. According to [191], authors aimed to recreate in laboratory the pathologies [192] observed on building stones of ancient monuments in Sardinia. For this, samples underwent accelerated cycles of thermo-hygrometric conditions and solar radiation based on a Mediterranean climate sequence. Monitoring of some physical and mechanical properties before and after aging indicates the appearance of decay patinas and a slight worsening of mechanical resistances. Moreover, an accelerated hygrothermal aging was observed by means of wet-dry and freeze-thaw cycles. In [193], an experimental test is carried out on a cement based composite with Silica Fume and recycled textile waste. By considering wet-dry cycles, mechanical and durability properties of the composite were assessed. It was shown that wet dry accelerated aging cycles affected negatively the post-cracking properties of the reinforced composites as compared to the initial samples. Similarly to the previous study, the durability of different external thermal insulation composite systems [194] was assessed. First, samples were subjected to heat, cold and rain cycles at 70 °C, −20 °C and $1\,\mathsf{L.m}^{-2}.\mathsf{min}^{-1}$, respectively. Then, these were exposed to cycles with 25 ppm of SO_2 pollutant. The experimental results showed that both surface hardness and surface gloss decreased, whereas traces of biological growth were detected. Furthermore, immersion and drying cycles were also adopted to approach aging. According to [72], the influence of an accelerated aging is examined through a succession of entire immersion and drying cycles at 50 °C during 40 days. Microscopic observations highlighted morphology changes of hemp concrete and porosity variations caused by swelling and shrinkage phenomena. A significant decrease in compression strength was noted for the weathered samples. In addition, thermal conductivity and water vapor permeability were affected following the porosity variation.

Last mentioned studies contribute significantly to the evaluation of aging effects due to heat and water mass transfers. However, proposed experimental designs are not entirely realistic and lacks representativeness. First, defined stresses can either vary widely or be time constant while lying on extreme weather conditions. In reality, the latter are not reached frequently. In this perspective, the application of extreme weather condition based designs could overestimate the aging effects. Moreover, to our best knowledge, the duration of these designs as well as the size of used samples are not clearly related. Besides that, no equivalences between carried tests and real scale configurations are defined. In this case, aging is only evaluated throughout downscaled, accelerated designs. Its effects at a real-scale configuration remains unknown. In this regard, this paper provides two scientific contributions. First, the authors propose a methodology to develop a realistic, accelerated and a representative aging protocol. The latter is carried out in the laboratory by proposing a suitable experimental approach. Secondly, the effect of this protocol is evaluated by studying the variation of properties of hemp concrete.

This paper will be organized respecting six sections. The first one highlights the methodology for the development of a long protocol based on three climate variables. Then, the laws of similarity are defined and applied on a three-dimensional heat and mass transfer problem in order to reduce the duration of the long configuration. Moreover, the third part exposes the experimental campaign where the material manufacture, the studied properties, the measurement procedure and the used equipment are described. In the results part, the introduced methodology is applied by using climate data of a french city. In addition, the time variation of properties is evidenced while performing the resulting protocol. Afterwards, the important observations are interpreted and compared to empirical correlations. Finally, the conclusion suggests to conduct similar protocols in order to enrich the aging database and integrate this phenomenon in the prediction of hygrothermal behavior of bio-based construction materials.

2 Methodology for the development of an annual aging design

2.1 Creating a representative aging design

A realistic long-term aging protocol is developed in a laboratory in this section. First, air temperature T_{ext} $[\mathsf{°C}]$, rainfall flux j_m $[\mathsf{g.m^{-2}.s^{-1}}]$ and short wave solar radiation j_q $[\mathsf{W.m^{-2}}]$ are the climate variables used to elaborate this protocol. This represents the first assumption where these variables are hold with a one-hour time step. Such data could be gathered thanks to weather station measurements [195, 196]. Afterwards, a typical week that represents a season is in the framework of a second assumption. Several approaches to create such typical week [197] exist based for instance on the averaging method.

Moreover, the assumption 3 is based on the consideration of the measurement uncertainty on the rainfall flux sensor. It aims at neglecting the value of this quantity as long as it remains smaller than the measurement uncertainty :

$$\hat{j}_m(t_i) = \begin{cases} \bar{j}_m(t_i) \quad , & \text{if} \quad \bar{j}_m(t_i) \geq j_{m,lim}\,, \\ \\ \quad 0 \qquad , & \text{else}\,. \end{cases} \tag{4.1}$$

The transition from Figure 4.1a to 4.1c illustrates the equation (4.1). Furthermore, it is possible to observe simultaneously solar radiation and rainfall during a natural climate scenario. However, it is difficult to reproduce, during a laboratory test, both events at the same time. In order to overcome this experimental difficulty, assumption 4 is required : thermal and water stresses are time-separated. In particular, the presence of rain overrides that of solar radiation. In parallel to this assumption, the rain sequences are regarded in the protocol as complete water immersions. Consequently, an immersion indicator Γ_m $[-]$ is introduced :

$$\Gamma_m(t_i) = \begin{cases} 1\,, & \text{if} \quad \hat{j}_m(t_i) > 0\,, \\ \\ 0\,, & \text{else}\,. \end{cases} \tag{4.2}$$

It represents an index that equals 0 if there is no rain and equals 1 when there is rain and the material should be submitted to immersion (Figure 4.1e). Then, it is possible to introduce the indicator related to heat stress as shown in Figure 4.1d. It is noted $\Gamma_q\,[-]$ and depends on Γ_m via the following expression :

$$\Gamma_q\,(\,t_i\,) = 1 - \Gamma_m\,(\,t_i\,)\,. \tag{4.3}$$

Finally, an additional experimental limitation lies on the difficulty to control an incident heat flux on the material in contrast to a temperature. A proposal consists in combining convection and radiation effects during the protocol in order to model thermal stress [198, 199]. It represents the assumption 5. For this purpose, an equivalent temperature is defined when $\Gamma_m = 0$ as illustrated in Figure 4.1f. It combines both air temperature and heat flux to express an equivalent air temperature :

$$T_{eq}\,(\,t_i\,) = \bar{T}_{ext}\,(\,t_i\,) + \frac{b\,\bar{j}_q\,(\,t_i\,)}{h_c}\,, \tag{4.4}$$

where $h_c\,[\mathsf{W.m^{-2}.K^{-1}}]$ is the heat convection coefficient and $b\,[-]$ is the material surface absorptivity. Note that the blank in Figure 4.1f means that the sample is submitted to an immersion during these periods. In the end, Figure 4.2 resumes the aging protocol methodology that is developed in this section. Accordingly, a typical week aging test is performed as shown in the Figure 4.1g. During a week, the test consists in setting a temperature in the range 15 to 37 °C over 12 hours. Following this, a 36-hour immersion period is performed. Subsequently, a 60-hour temperature cycle ranging from 5 to 40 °C is applied. The material is then subjected to an immersion for 46 h. Finally, a variable temperature is applied during the last 12 h. In the end, this sequence represent the aging design of one typical week for one season. Thus, it is repeated sequentially 13 times to produce the aging design of the whole season. Last, this procedure can be extended to a whole year by repeating sequentially aging design of each of the four seasons.

As the aim is to assess the effect of a long-term aging (1 year) on a material, a regular sample collecting is scheduled along the test. This is essential to characterize the material at different instants of a year.

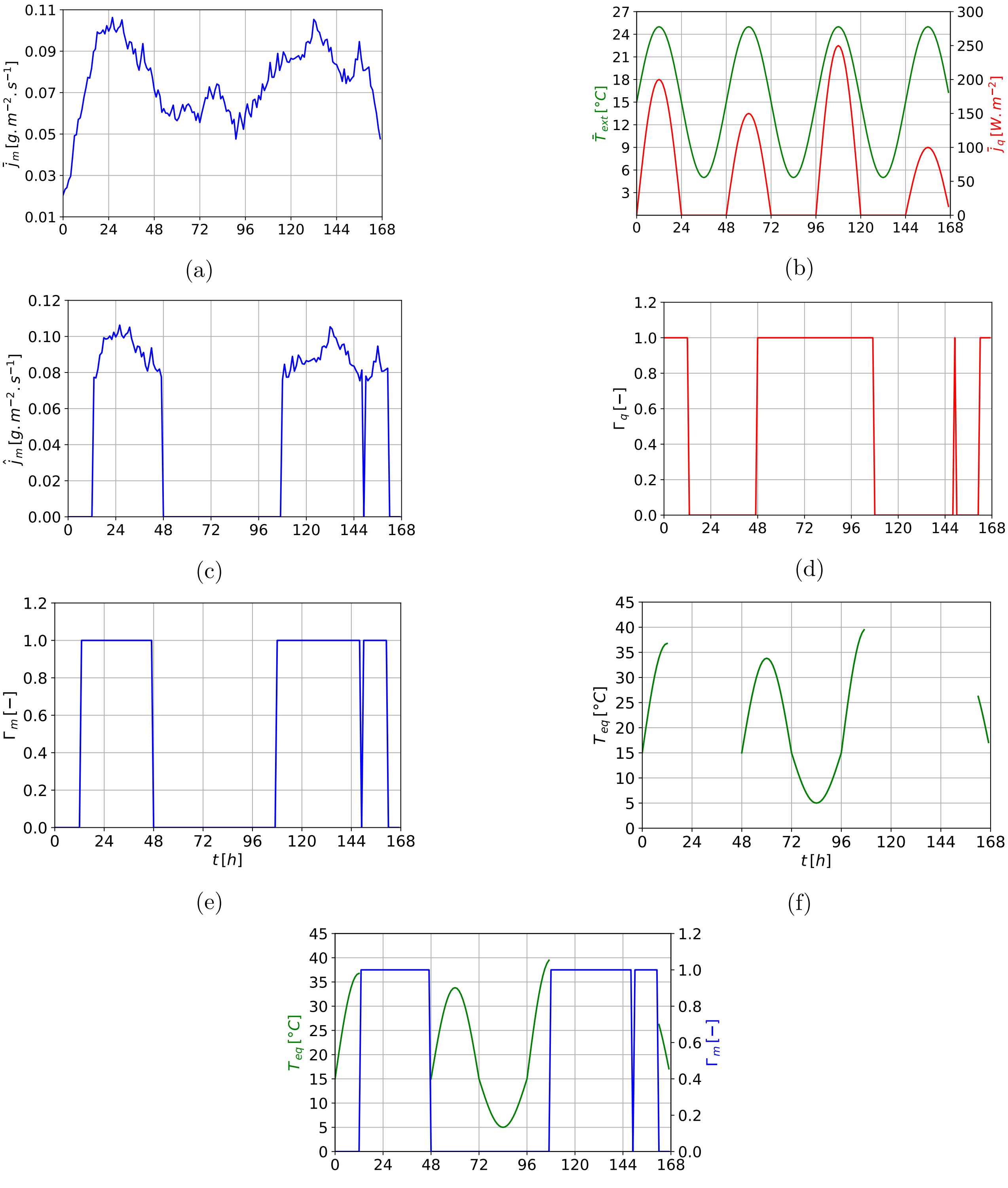

(a) (b) (c) (d) (e) (f) (g)

FIGURE 4.1 – The approach of developing an aging design applied to an illustrative thermal and water stress scenario. The variation during a typical week of precipitation (a), temperature and solar radiation (b). Rain flux after considering the sensor uncertainty. (c) Heat stress indicator (d). Immersion indicator (e) and equivalent temperature (f). The resulting aging design during a typical week (g).

2.2 The study assumptions

In this part, the assumptions that are set to obtain this experimental design are synthesized.

- Available climate data including air temperature, rainfall flux and solar radiation with an hour time step measurement.
- Each year season is represented by a typical week which is hold and obtained via the arithmetic mean method.
- Rainfall flux values that are smaller than the uncertainty of measurement, are neglected.
- Solar radiation sequences are not considered when coinciding with rainfall scenarios.
- An equivalent temperature is defined in order to represent the thermal stress.
- the aging protocol is repeated sequentially 13 times to produce a season aging protocol. Then with similar procedure it is extended to one year.

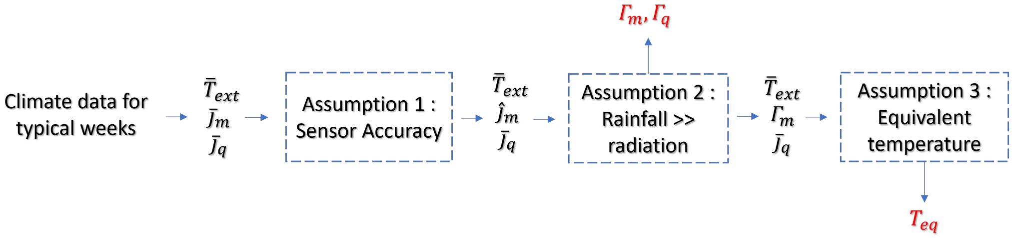

FIGURE 4.2 – Synthesis illustration of the steps for the development of an aging protocol.

The next section describes the approach used to accelerate a long-term aging protocol. It consists of three essential steps. First, a suitable heat and moisture transfer model is defined. Secondly, this model is formulated in the dimensionless domain. Lastly, similarity laws are deduced in order to propose a short duration experiment, that is equivalent to the long aging test.

3 The accelerated aging protocol

3.1 Aging driving potentials

Due to immersion sequences and temperature variation, coupled heat and mass transfer occur within porous materials. Due to immersion phases, the material is submitted to capillary imbibition. Thus, the model of Philip and DeVries [200, 90, 201] is chosen here. The problem is written according to a physical Cartesian basis using the coordinates x, y and z. Where $x \in \Omega_x$, $y \in \Omega_y$, $z \in \Omega_z$ and noting that $\Omega_x = [0, L_x]$, $\Omega_y = [0, L_y]$ and $\Omega_z = [0, L_z]$ are the space domains. L_x, L_y, L_z [m] are the material dimensions along x, y, z axes, respectively. Let Γ refer to the material boundaries. Moreover, $t \in \Omega_t$ is time where $\Omega_t = [0, t_f]$ is the corresponding domain. t_f [s] designates the final instant. Considering the three space dimensions, the model is written as follows :

$$\frac{\partial \theta}{\partial t} = \nabla \cdot \Big(D_\theta \nabla \theta + D_T \nabla T \Big), \tag{4.5a}$$

$$\rho \, C_p \, \frac{\partial T}{\partial t} = \nabla \cdot \Big(\lambda \, \nabla T \Big) + L_v \, \rho_l \, \nabla \cdot \Big(D_{TV} \, \nabla T + D_{\theta V} \, \nabla \theta \Big) \,. \tag{4.5b}$$

Equations (4.5a) and (4.5b) introduce $\theta \, [-]$ and $T \, [\mathsf{K}]$ which represent the material moisture content and temperature, respectively. $D_T \, [\mathsf{m^2.s^{-1}.K^{-1}}]$ is the mass transport coefficient associated to a temperature gradient, $D_\theta \, [\mathsf{m^2.s^{-1}}]$ mass transfer coefficient associated to a moisture content gradient, $\rho \, [\mathsf{kg.m^{-3}}]$ material density, $C_p \, [\mathsf{J.kg^{-1}.K^{-1}}]$ specific heat, $\lambda \, [\mathsf{W.m^{-1}.K^{-1}}]$ thermal conductivity, $L_v \, [\mathsf{J.kg^{-1}}]$ heat of vaporization, $\rho_l \, [\mathsf{kg.m^{-3}}]$ water density, $D_{TV} \, [\mathsf{m^2.s^{-1}.K^{-1}}]$ vapor phase transport coefficient associated to a temperature gradient, $D_{\theta V} \, [\mathsf{m^2.s^{-1}}]$ vapor phase transport coefficient associated to a moisture content gradient. Additionally, The diffusion coefficients mentioned above are related according to Eq. (4.6) :

$$D_T = D_{TL} + D_{TV} \quad , \quad D_\theta = D_{\theta L} + D_{\theta V} \,, \tag{4.6}$$

where $D_{TL} \, [\mathsf{m^2.s^{-1}.K^{-1}}]$ and $D_{\theta L} \, [\mathsf{m^2.s^{-1}}]$ are the liquid phase transport coefficients associated to a temperature and moisture content gradients, respectively. Besides D_θ, water vapor permeability $K_v \, [\mathsf{s}]$ represents the most measured property for the evaluation of the hydric behavior of a porous material. It is given by Equation (4.7) :

$$K_v = k_s \, \frac{\rho_v}{\mu_v} \,, \tag{4.7}$$

where $\mu_v \, [\mathsf{kg.m^{-1}.s^{-1}}]$ and $\rho_v \, [\mathsf{kg.m^{-3}}]$ are the dynamic viscosity and density of water vapor, respectively. In addition, $k_s \, [\mathsf{m^2}]$ designates the intrinsic permeability, it depends only on the structure and pores interconnections and not on the fluid which flows inside a material. Performing a total immersion requires the use of a Dirichlet boundary condition which is given in Eq. (4.8) :

$$\theta = \theta_{sat} \,, \quad (\, x, \, y, \, z \,) \, \in \, \Gamma \,, \, t \, \in \, \Omega_t \,, \tag{4.8}$$

where $\theta_{sat} \, [-]$ defines the material moisture content at the saturation state. Furthermore, heat stress is represented on the basis of the equivalent temperature. In this context, the heat boundary condition at Γ is assumed of the Dirichlet type while using the mentioned temperature. This condition is expressed in the following :

$$T = \tilde{T}_{eq} \,, \quad (\, x, \, y, \, z \,) \, \in \, \Gamma \,, \, t \, \in \, \Omega_t \,. \tag{4.9}$$

At the initial state, material temperature and moisture content are known and assumed constants. The initial condition of the material is expressed via Eq. (4.10) :

$$\theta = \theta_0 \,, \quad T = T_0 \,, \quad x \, \in \, \Omega_x \,, \, y \, \in \, \Omega_y \,, \, z \, \in \, \Omega_z \,, \, t = 0 \,. \tag{4.10}$$

3.2 Dimensionless formulation

In order to scale the physical model, each variable would be associated to a constant. In the dimensionless domain, space coordinates and time are as follows :

$$x^\star = \frac{x}{L_0} \,, \quad y^\star = \frac{y}{L_0} \,, \quad z^\star = \frac{z}{L_0} \,, \quad t^\star = \frac{t}{t_f} \,. \tag{4.11}$$

$L_0 \, [\mathsf{m}]$ is a length which is defined as $L_0 = \max \{ L_x \,, \, L_y \,, \, L_z \}$. Subsequently, dimensionless temperature and water content are defined :

$$T^{\star} = \frac{T}{T_0}\,, \quad \theta^{\star} = \frac{\theta}{\theta_0}\,. \tag{4.12}$$

Moreover, the dimensionless material properties are given as follows :

$$D_{\theta}^{\star} = \frac{D_{\theta}}{D_{\theta 0}}\,, \quad D_{T}^{\star} = \frac{D_{T}}{D_{T 0}}\,, \quad \rho^{\star} = \frac{\rho}{\rho_0}\,, \quad C_p^{\star} = \frac{C_p}{C_{p0}}\,, \tag{4.13a}$$

$$\lambda^{\star} = \frac{\lambda}{\lambda_0}\,, \quad L_v^{\star} = \frac{L_v}{L_{v0}}\,, \quad D_{TV}^{\star} = \frac{D_{TV}}{D_{TV0}}\,, \quad D_{\theta V}^{\star} = \frac{D_{\theta V}}{D_{\theta V 0}}\,. \tag{4.13b}$$

In this study, the scaling constants, that are associated to the material properties, are those evaluated at the dry state. Characteristic vaporization heat is provided at $T = T_0$. Finally, the boundary conditions are :

$$\theta_{sat}^{\star} = \frac{\theta_{sat}}{\theta_0}\,, \quad T_{eq}^{\star} = \frac{\tilde{T}_{eq}}{T_0}\,. \tag{4.14}$$

The next step is to replace the variables in the physical model by the dimensionless quantities. Thus, Eqs. (4.5a) and (4.5b) are transformed into :

$$\frac{\partial \theta^{\star}}{\partial t^{\star}} = \mathrm{Fo}_m\, \nabla^{\star} \cdot \Big(D_{\theta}^{\star}\, \nabla^{\star} \theta^{\star} + D_T^{\star}\, \delta\, \nabla^{\star} T^{\star} \Big)\,, \tag{4.15a}$$

$$\rho^{\star}\, C_p^{\star}\, \frac{\partial T^{\star}}{\partial t^{\star}} = \mathrm{Fo}_q\, \nabla^{\star} \cdot \Big(\lambda^{\star}\, \nabla^{\star} T^{\star} \Big) + \alpha\, \mathrm{Fo}_q\, L_v^{\star}\, \nabla^{\star} \cdot \Big(D_{TV}^{\star}\, \nabla^{\star} T^{\star} + D_{\theta V}^{\star}\, \gamma\, \nabla^{\star} \theta^{\star} \Big)\,. \tag{4.15b}$$

Accordingly, certain dimensionless numbers are obtained. In particular, The Fourier number which is related on one hand to heat transfer via the constant Fo_q, and on the other to mass transfer thanks to Fo_m. These are expressed according to :

$$\mathrm{Fo}_m = \frac{D_{\theta 0}\, t_f}{L_0^2}\,, \quad \mathrm{Fo}_q = \frac{\lambda_0\, t_f}{\rho_0\, C_{p0}\, L_0^2}\,. \tag{4.16}$$

Thereafter, δ, α and γ represent dimensionless numbers as well and are defined as follows :

$$\delta = \frac{D_{T0}\, T_0}{D_{\theta 0}\, \theta_0}\,, \quad \alpha = \frac{L_{v0}\, \rho_l\, D_{TV0}}{\lambda_0}\,, \quad \gamma = \frac{\theta_0\, D_{\theta V 0}}{T_0\, D_{TV0}}\,. \tag{4.17}$$

As an example, the dimensionless formulation of mass and heat boundary conditions is :

$$\theta^{\star} = \theta_{sat}^{\star}\,, \quad x^{\star} = 0\,,\, t^{\star} \in [\,0\,,\,1\,]\,, \tag{4.18a}$$

$$T^{\star} = T_{eq}^{\star}\,, \quad x^{\star} = 0\,,\, t^{\star} \in [\,0\,,\,1\,]\,, \tag{4.18b}$$

The same boundary conditions are applied for the surfaces given by the Equations $x^{\star} = 1$, $y^{\star} = 0$, $y^{\star} = 1$, $z^{\star} = 0$ and $z^{\star} = 1$. Lastly, dimensionless water content and temperature at the initial state are written as follows :

$$\theta^{\star} = 1\,, \quad T^{\star} = 1\,, \quad x^{\star} \in [\,0\,,\,1\,]\,,\, y^{\star} \in [\,0\,,\,1\,]\,,\, z^{\star} \in [\,0\,,\,1\,]\,,\, t^{\star} = 0\,. \tag{4.19}$$

3.3 Similarity laws

Similarity represents a mathematical law that aims to set links of equivalence between different configurations. The latter can be different in terms of space dimensions, time scale and magnitude of physical properties. The use of these laws is widespread in many scientific fields, especially in fluid dynamics and aerodynamics [202, 203, 144, 86]. Through similarities, these real scales are reduced into small experimental designs to facilitate the investigations. Similarity of heat and mass transfer has also been investigated and verified experimentally in [155, 204, 94, 95].

In the ongoing study, similarity laws are used to reduce the duration that is required to conduct the aging design experiment. For this purpose, assume that a physical quantity is noted X for a reference configuration 1 and **X** for a reduced configuration 2. Thus, both configurations are similar if the obtained dimensionless numbers remain the same when going from the long to the short configuration :

$$\mathrm{Fo}_m = \boldsymbol{\mathrm{Fo}_m}\,, \quad \delta = \boldsymbol{\delta}\,, \quad \alpha = \boldsymbol{\alpha}\,, \quad \mathrm{Fo}_q = \boldsymbol{\mathrm{Fo}_q}\,, \quad \gamma = \boldsymbol{\gamma}\,. \tag{4.20}$$

Since the material is assumed equal from a macroscopic point of view between configurations, heat and moisture properties at the dry state and their variation laws are identical. Moreover, assume $\theta_0 = \boldsymbol{\theta_0}$ and $T_0 = \boldsymbol{T_0}$. Consequently, the equality in Fourier numbers leads to the following equivalence :

$$\frac{t_f}{\boldsymbol{t_f}} = \frac{L_x^2}{\boldsymbol{L_x}^2} = \frac{L_y^2}{\boldsymbol{L_y}^2} = \frac{L_z^2}{\boldsymbol{L_z}^2}\,. \tag{4.21}$$

At this level, the coefficient Σ is introduced which designates the scaling parameter between the two configurations. It is defined as follows :

$$\Sigma = \frac{\boldsymbol{L_x}}{L_x} = \frac{\boldsymbol{L_y}}{L_y} = \frac{\boldsymbol{L_z}}{L_z}\,. \tag{4.22}$$

It represents the ratio of a material dimension in configuration 2 to the one in configuration 1. In this respect, the duration of an experiment in configuration 2 is obtained :

$$\boldsymbol{t_f} = \Sigma^2\, t_f\,. \tag{4.23}$$

If $\Sigma < 1$, then the reference configuration 1 undergoes a reduction and the reduced configuration 2 is obtained. In this case, the dimensions of the material in the second configuration are necessarily smaller than the ones in the first configuration. Further on, sections 5.1 and 5.2 expose the configurations 1 and 2, which are also called "reference" and "reduced", respectively.

4 Experimental facility

This section focuses on the experimental part of the study. First, the material is presented while specifying the adopted formulation. Then, material properties are defined for the measurement. Finally, the devices dedicated to the experimental characterization are described.

4.1 Material

The study is carried on hemp concrete which is a bio-based material and used increasingly to reinforce wall thermal insulation. The manufacturing phase is carried according to the standards NF EN 459, NFP 15−314 and NF EN 197−1. These recommend the following mass proportions in the case of a wall design : 16 % of hemp shives, 34 % of lime and 50 % of water. The lime is provided from the Tradical^{R} PF 70 product. It is a formulated lime of class FL A 3.5 in accordance with the standard NF EN 459.

(a) (b)

Figure 4.3 – Hemp concrete samples during immersions (a) and heat stress (b).

Generally, it is meant, once mixed with aggregates and water, to make laying mortars, hollow or full bricks. In the raw state, its thermal conductivity is less than 0.2 $\mathsf{W.m^{-1}.K^{-1}}$ and its density is around 620 $\mathsf{kg.m^{-3}}$. Furthermore, the used hemp is issued from the Biofibat mark. It is a granulate made exclusively of calibrated and dust-free hemp straw, whose transformation process requires neither water nor solvent. Its density is estimated at 110 $\mathsf{kg.m^{-3}}$ and its thermal conductivity is about 0.05 $\mathsf{W.m^{-1}.K^{-1}}$. The manufacturing phase [72, 205] includes the mold preparation, the mixing of the different components, the curing and finally the storage of samples. Finally, 18 cubes and 18 cylinder samples are prepared for the aging protocol and the experimental characterization. In effect, 36 samples undergo the aging design. During the latter, it is agreed to define 9 measurement instants including the initial instant and the final one. At each defined instant, 2 cube and 2 cylinder samples are removed to conduct measurements.

4.2 Measured properties to evaluate material aging

A mixing step was carried out during the material manufacture in order to ensure a mixture homogenization. It is nearly certain that one mold does not contain necessarily the same binder and hemp amounts as others. In addition, time variation in a property will be obtained based on measurements on different samples at different instants of the design. To do so, it must be ensured that a time variation in a property is only due to aging, and not induced by differences between samples. As for measured properties, the impact of aging is investigated on porosity, thermal conductivity, vapor permeability and pH. For this purpose, cylinder samples are used to determine water vapor permeability, while other properties are measured on cube samples.

Hereafter, the quantity p is introduced, it represents typically each of the above mentioned properties except of pH. At each design instant, $N_p\,[-]$ property measurements are performed in order to take into account a random uncertainty. Table 4.1 resumes the measurement number N_p for each property. The difference in N_p between properties is due to the sample size considered in each case.

Table 4.1 – Measurement number N_p at each instant according to the aging design to determine thermal conductivity, porosity, vapor permeability and pH indicator.

Property	Thermal conductivity	Porosity	Vapor permeability	pH
N_p	4	6	2	4

Since all measurements are carried at the dry state, it is stated that a property varies according to density and aging effect (excluding the pH indicator which does not depend on density). In this respect, a corrected time variation in a property p is deduced by carrying out a Taylor development of first order :

$$p\,(\,t_i\,) = \bar{p}\,(\,t_0\,) + \frac{\partial p}{\partial \rho}\,\Big(\,\bar{\rho}\,(\,t_i\,) - \bar{\rho}\,(\,t_0\,)\,\Big)\,. \tag{4.24}$$

where $i \in \{\,0\,,\,2\,,\ldots,\,m-1\,\}$ and $m = 9$ is the instant number when measurements are performed. Furthermore, $\bar{p}\,(\,t_0\,)$ and $\bar{\rho}\,(\,t_0\,)$ are the values of a property and density that are measured at $t = t_0$ (before the aging protocol). According to (4.24), a corrected variation in p is assessed by considering the carried measurement on one hand. On the other hand, the property derivative with respect to density is required as well. Throughout the remaining sections, the notation $\bar{p}$ is dedicated to an experimental result.

The uncertainty propagation formula [134] is applied on the Equation (4.24) in order to determine the entire uncertainty on a corrected property p. Remark that this equation includes $\bar{p}$ and $\bar{\rho}$ which vary likewise within corresponding confidence intervals. In this respect, the entire uncertainty σ_p is given as follows :

$$\sigma_p\,(\,t_i\,) = \Big(\,\sigma^2_{\bar{p}_0} + \frac{\partial p}{\partial \rho}^{2}\,\Big(\,\sigma^2_{\bar{\rho}}\,(\,t_i\,) + \sigma^2_{\bar{\rho}_0}\,\Big)\,\Big)^{\frac{1}{2}}\,. \tag{4.25}$$

$\sigma_{\bar{p}_0}$, $\sigma_{\bar{\rho}}$ and $\sigma_{\bar{\rho}_0}$ are the entire uncertainties on $\bar{p}\,(\,t_0\,)$, $\bar{\rho}\,(\,t_i\,)$ and on $\bar{\rho}\,(\,t_0\,)$. Thus, only $\sigma_{\bar{\rho}}$ is time-dependent, other quantities are constants.

4.3 Experimental equipment

This part describes the different experimental equipment that are used for the measurement of the properties introduced in Section 4.2. This part emphasizes also the conformity of these tests to international standards as well as the systematic uncertainty related to each equipment.

4.3.1 Climate chamber

Before initiating the aging protocol, it is necessary to ensure that all samples are set at the initial temperature required by this test. This temperature value depends on the climate that is chosen to develop an aging protocol. For this reason, the samples are placed in a thermal chamber that controls air temperature. This equipment is issued from the mark memmert and the generation UN75 plus. Furthermore, temperature variations are programmed thanks to the AtmoCONTROL software, which can be processed by the thermal chamber.

4.3.2 Thermal conductivity

It represents the first measured property. The test is carried out using the $\lambda -$ Meter EP500e. It is a device based on an embedded PC for performing absolute value measurements following the single plate method in accordance with ISO 8302, DIN EN 1946-2, DIN EN 12667, DIN EN 12664, ASTM C177, DIN 52612. The measuring zone is located in the center of the plate and has a different size depending on the device version (e.g. $200 \times 200\,\mathsf{mm}^2$ or $150 \times 150\,\mathsf{mm}^2$). According to the technical data of the manufacturer, the device is accurate within a relative systematic uncertainty of $\sigma_{\bar{\lambda},\,sys} = 1\,\%$.

4.3.3 Porosity

The porosity that is accessible to water informs about the amount of voids contained in a material. The experimental evaluation of this quantity is based on the protocol proposed according to the NF P18-459 standard. This method requires the use of a desiccator, a pump and a balance. The desiccator is connected on one side to the pump and on the other to a water reservoir. First, $5 \times 5 \times 5\,\mathsf{cm}^3$ samples are placed in an empty desiccator. The test is initiated by a degassing step for 4 hours using the pump. Afterwards, the desiccator is filled with a sufficient quantity of water to ensure the saturation of samples. This operation is carried under a vacuum for two days. Then, saturation continues for one week while the pump is off. By means of a balance, a saturated sample is weighed twice. Its mass in open air M_a is evaluated first. Then, a second mass M_w is obtained by performing a hydrostatic weighing which is based on the principle of Archimedes buoyancy. Finally, the mass at the dry state M_d is also measured. For this purpose, it is placed in the thermal chamber at a temperature $T = 105\,^\circ\mathsf{C}$ while performing weighting each 24 hours and considering an equilibrium criterion of $0.05\,\%$ between two successive values. Based on the values of M_a, M_w, $M_d\,[\mathsf{g}]$, a porosity $\bar{n}$ is calculated according to the Equation (4.26).

$$\bar{n} = \frac{M_a - M_d}{M_a - M_w}\,. \tag{4.26}$$

4.3.4 Vapor permeability

The experimental characterization includes also the measurement of vapor permeability. As discussed previously, the latter describes the capacity of a material to let a water vapor diffusion throughout its thickness under a vapor pressure gradient in the steady state. The measurement of this property is conducted using the Gravitest device which is based on the cup method with respect to the ISO 12572 standard. The main feature of this device is the automated mass monitoring thanks to an accurate balance with an uncertainty of $\sigma_m = 10^{-4}\,\mathsf{g}$. The test consists in exposing the two sample facets to two different relative humidity, by using a saturated saline solution on one side and a climate cell on the other.

The relative humidity gradient generates a vapor flux going from high to low pressures. Thereafter, this flux is evaluated through a regular weighing in order to assess the water vapor transmission rate at the equilibrium. The test is performed on dry cups where the relative humidity inside is set at 3 % using silica gel and 50 % outside. Temperature and air velocity are set at 25 °C and 2 m.s^{-1} respectively. The manufactured cylinder samples of 8 cm diameter and 5 cm height are used to conduct this test. Finally, the systematic uncertainty on vapor permeability is not stated explicitly in the technical data of this equipment. It can be assessed by considering the accuracy of the balance σ_m as well as the uncertainty on relative humidity $\sigma_\phi = 1.5\,\%$, which is given within the technical data. In this respect, the systematic uncertainty on vapor permeability $\sigma_{\bar{K}_v, sys}$ [s] is deduced according to the uncertainty propagation formula :

$$\sigma_{\bar{K}_v, sys} = \bar{K}_v \left(\left(\frac{\sigma_m}{m} \right)^2 + \left(\frac{\sigma_\phi}{\Delta \phi} \right)^2 \right)^{\frac{1}{2}}, \tag{4.27}$$

$\bar{K}_v$ [s] is a measured vapor permeability and $\Delta \phi$ [%] the relative humidity discrepancy between the inside and the outside of a cup. m [kg] is the mass of vapor diffused through a sample in the steady state.

4.3.5 The pH index

The mold growth is one of the aspects that reflect the degradation of green or bio-based materials such as wood or hemp concrete. In this regard, the pH indicator represents a chemical property which informs on the possibility of getting a fungal growth along the aging process. Its measurement is based on the use of the pH-meter 780 from Metrohm and the preparation of aqueous solutions. Firstly, the equipment is calibrated by means of two buffer solutions with the following pH values 4 and 7. Following the last operation, the systematic uncertainty is constant and is estimated at $\sigma_{pH, sys} = 0.003$. Thereafter, aqueous solutions are made by diluting sample powder in distilled water according to the liquid-solid ratio 9 ml.g^{-1}.

Next section highlights first the reference configuration that is considered for the application of similarity. Afterwards, based on a scaling parameter value, the reduced configuration is deduced. Moreover, Section 5.3 highlights the effective aging protocol with regard to the theoretical one. Both are compared and discrepancies are quantified during each season. Subsequently, time variation in properties, i.e. thermal conductivity, porosity, vapor permeability and pH index, is illustrated with the consideration of corresponding uncertainties (Equation (4.25)).

5 Results

5.1 Reference configuration

The reference configuration is defined by hemp concrete cube samples with the dimensions $L_x = 15$ cm, $L_y = 45$ cm and $L_z = 45$ cm. In addition, cylinders are also considered, where the diameter and the height equal $d = 24$ cm and $h = 15$ cm, respectively. Note that in the appendix part, Section 1 establishes these laws for a cylindrical coordinate system.

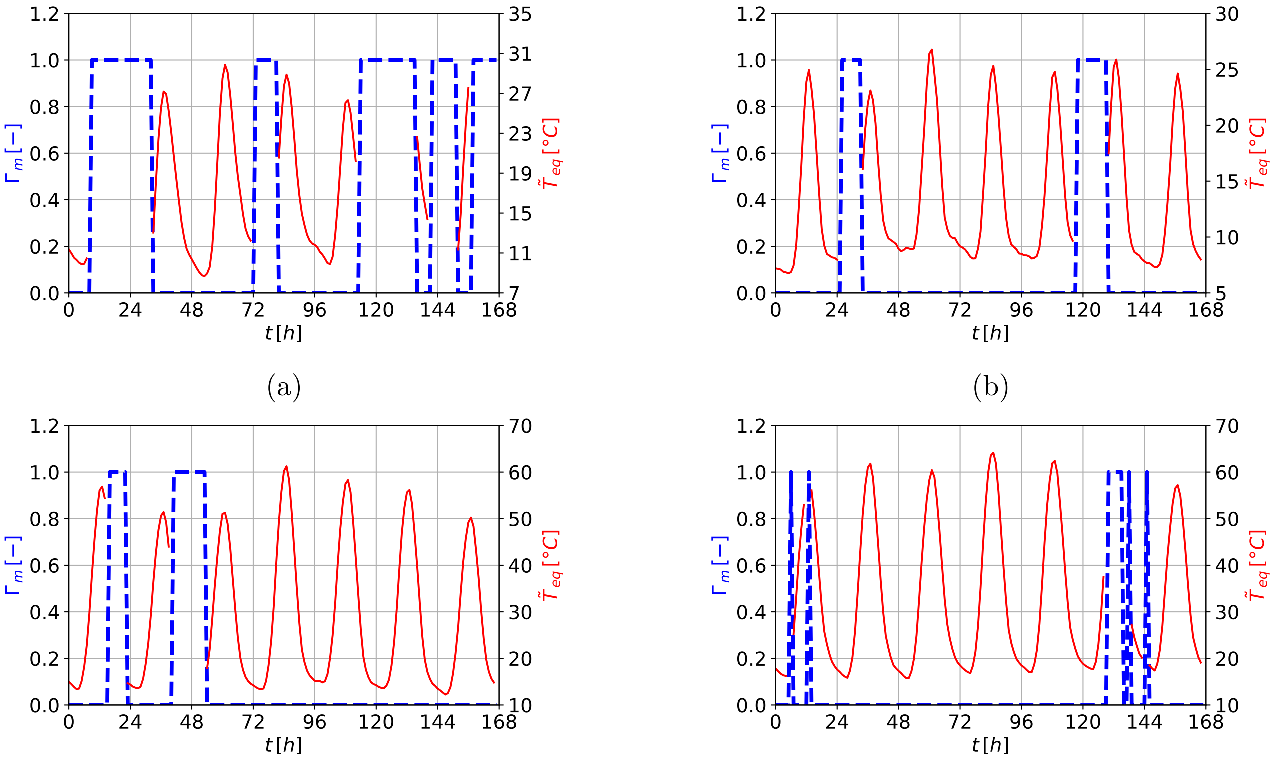

(a) (b)

(c) (d)

FIGURE 4.4 – The immersion indicator and the equivalent temperature variations during the reference configuration. Sub-figures (a),(b),(c) and (d) refer to typical weeks representing Autumn, Winter, Spring and Summer, respectively.

The sample is exposed to immersion and heat stress cycles. For this, the climate in La Rochelle (France) for the year 2020 is chosen [206]. Remind that 2020 is a leap year which includes the 29th of February. The cycles are obtained for each season by following the methodology in Section 2. The sensors used to measure rainfall, radiation and outdoor temperature are accurate to the order $0.05\,\mathsf{g.m^{-2}.s^{-1}}$, $1\,\mathsf{W.m^{-2}}$ and $0.3\,\mathsf{°C}$ respectively. Thermal and water stress are shown for each season in Figure 4.4. It illustrates the succession of immersions and thermal stresses during the four typical weeks thereby $t = 168\,\mathsf{h}$. These sequences are repeated $N_w = 13$ times while following the season order.

5.2 Reduced configuration

The equivalent protocol carried in the laboratory, which represents the reduced configuration, correspond to hemp concrete cube samples with the following dimensions $\boldsymbol{L_x} = 5\,\mathsf{cm}$, $\boldsymbol{L_y} = 15\,\mathsf{cm}$ and $\boldsymbol{L_z} = 15\,\mathsf{cm}$. As for the cylindrical samples, $\boldsymbol{d} = 8\,\mathsf{cm}$ and $\boldsymbol{h} = 5\,\mathsf{cm}$. Hence, the scaling parameter is obtained $\Sigma = \dfrac{1}{3}$. Indeed, by writing the model under the cylindrical coordinates, the scaling parameter links both configurations by means of the radius and the diameter.

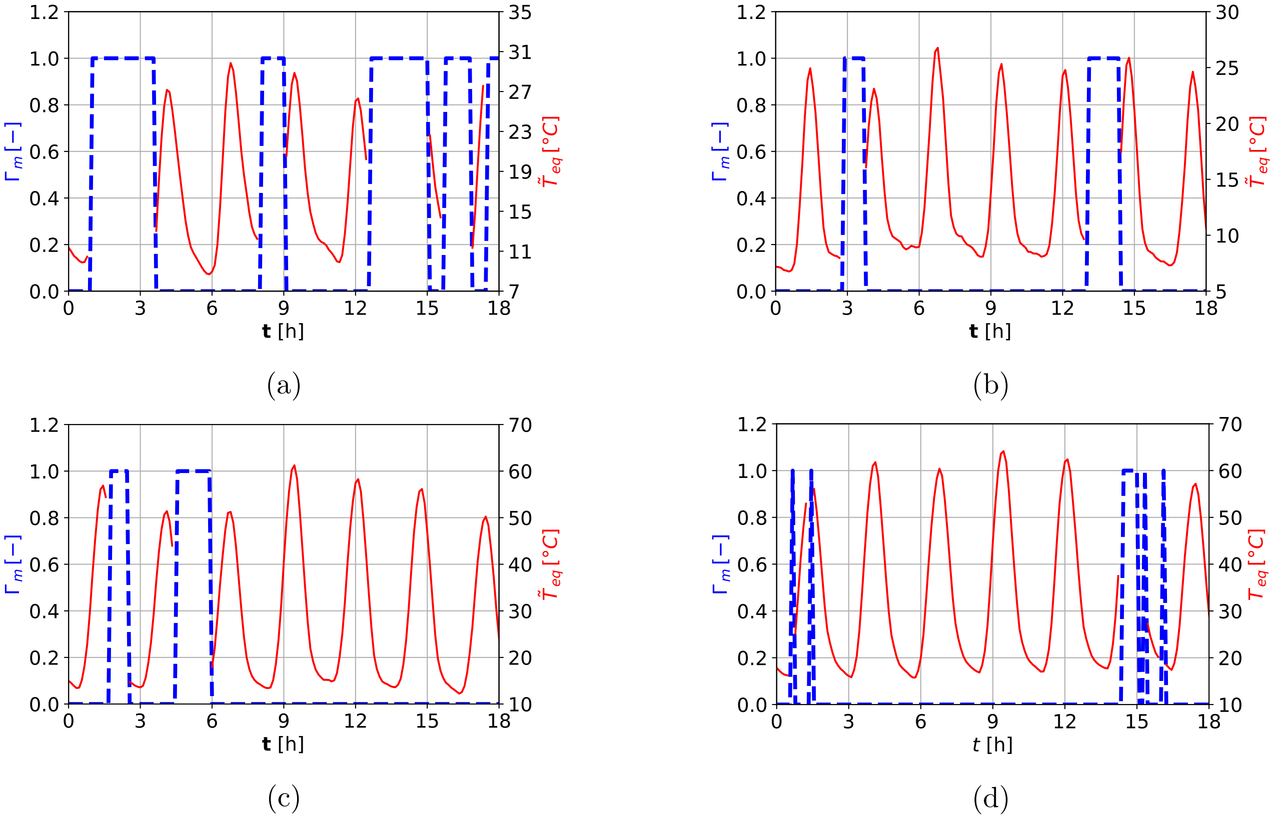

FIGURE 4.5 – The immersion indicator and the equivalent temperature variations during the reduced configuration. Sub-figures (a),(b),(c) and (d) refer to typical weeks representing Autumn, Winter, Spring and Summer, respectively.

As for the duration of a reduced typical week, $\boldsymbol{t} = \Sigma^2 \, t \simeq 18.66\,\mathsf{h}$. Figure 4.5 illustrates the aging protocol in the reduced configuration during the four season sequences. Notice that similarities maintain the same magnitude of the climate stress when comparing this protocol to the one introduced in the previous Section. However, the duration of typical weeks is reduced by Σ^2. Last, it is worth noting that each sequence is iterated also 13 times starting with Autumn in order to reproduce the climate scenarios that occur during a year.

TABLE 4.2 – Cube and cylinder sample dimensions in the reduced and reference configuration.

	parallelepiped samples			Cylinder samples	
	Length [cm]	Depth [cm]	Height [cm]	Diameter [cm]	Height [cm]
Reduced configuration	5	15	15	8	5
Reference configuration	15	45	45	24	15

5.3 Effective experimental design

As a reminder, the reduced aging design is initiated with 36 samples. In addition, the transition from an imbibition to a thermal stress and vice versa is carried out manually. Consequently, the duration of each seasonal sequence is relatively longer than the theoretical duration. In this respect, Table 4.3 shows the theoretical cycles duration in each seasonal sequence. The purpose of this part is the estimation of time deviations between the theoretical and effective duration in each sequence. For this reason, the quantity t_{ef} [h] is introduced and refers to the effective duration of a season sequence.

Table 4.3 – Theoretical duration of immersion (IM) and heat stress (HS) in the reduced configuration for each season sequence.

Autumn		Winter		Spring		Summer	
Stress	Duration [h]	Stress	Duration [h]	Stress	Duration [h]	Stress	Duration [h]
HS	1.66	HS	2.88	HS	1.78	HS	0.66
IM	2.66	IM	0.86	IM	0.78	IM	0.11
HS	4.45	HS	9.33	HS	2	HS	0.66
IM	1.55	IM	1.33	IM	1.45	IM	0.11
HS	3.55	HS	4.23	HS	12.66	HS	12.88
IM	2.45	-	-	-	-	IM	0.66
HS	0.66	-	-	-	-	HS	0.23
IM	1.11	-	-	-	-	IM	0.11
HS	0.66	-	-	-	-	HS	0.66
IM	1.11	-	-	-	-	IM	0.11
-	-	-	-	-	-	HS	2.45

Figure 4.6 highlights the variation in the mean effective duration for each season sequence according to the theoretical. These mean values are obtained on the basis of the sequence iterations. As illustrated particularly during the Autumn sequence, a transition corresponds to instants where the t_{ef} slope becomes larger. In this context, remind that the duration of a seasonal sequence in the reduced configuration is $\boldsymbol{t} = 18.66\,\mathsf{h}$. In Autumn, the sequence duration is estimated at 20.87 h. It represents the longest one with a delay of 2.31 h. Obviously, this observation is due to the frequent operations and the large sample number at the beginning of this test. In parallel, Winter and Spring overall delays are about 0.79 and 0.37 h, respectively. Note that this decrease between both sequences is related only to the remaining samples which are more numerous in winter. Indeed, both sequences are equal in terms of operation number (three drying and two immersions). Lastly, Summer sequence is relatively longer than Spring with a delay of about 0.47 h. Indeed, there are fewer samples that remain during Summer, whereas more operations are performed during this sequence (Table 4.3). As shown in Table B.1, all delays are listed where the statistical information, related to each duration, is estimated using the mean and the standard deviation.

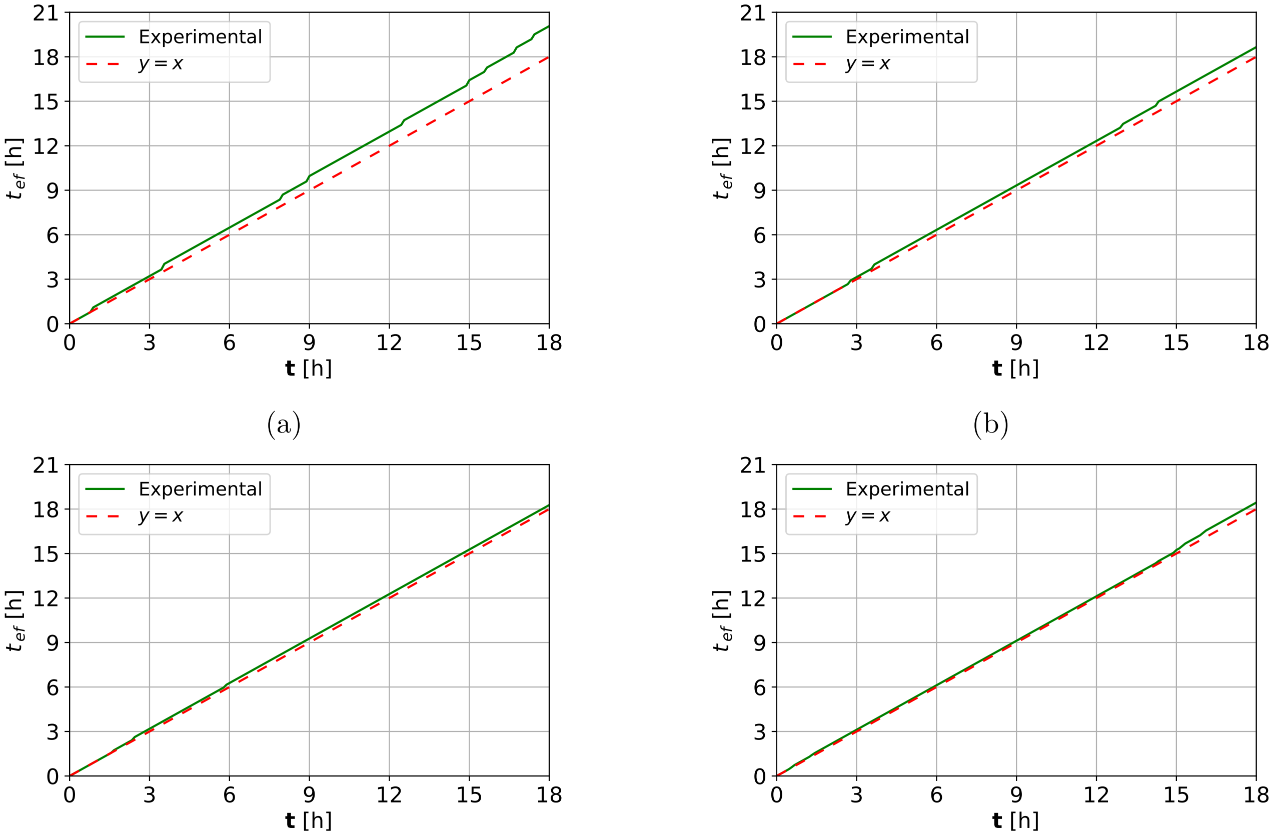

(a)

(b)

(c)

(d)

FIGURE 4.6 – Theoretical (red) and effective mean (green) duration of the Autumn (a), Winter (b), Spring (c) and Summer (d) sequences.

In the next part, time variation in thermal conductivity, porosity and vapor permeability is obtained after considering the correction defined by Equation (4.24). Results in terms of pH are also highlighted. The objective is to show the effect of the developed protocol on the variation of the properties set by this study.

5.4 Time variation of properties

In the study, the entire uncertainty on each property is evaluated using the propagation formula [134]. It combines, in this case, the random aspect of an experiment and the systematic precision of a device [207]. Corrected results are given directly for thermal conductivity, porosity and vapor permeability. These data are introduced in Table 4.4. $\bar{\rho}_{cub}$ represents the density of cube-sized samples that are used to measure thermal conductivity and porosity. While $\bar{\rho}_{cyl}$ is the density of cylindrical samples that are considered for vapor permeability measurements. Therefore, the correction of thermal conductivity and porosity measurements is assessed according to $\bar{\rho}_{cub}$. As for a corrected vapor permeability measurement, it is calculated respecting $\bar{\rho}_{cyl}$. Note that the same formulation of hemp concrete yields a variability for each property. In this context, the density of a sample can vary between 483 and 553 $\mathsf{kg.m^{-3}}$. In terms of thermal conductivity, it can reach 82 and 98 $\mathsf{mW.m^{-1}.K^{-1}}$ as minimum and maximum, respectively. For porosity, the obtained values range between 0.744 and 0.786 in this case. Finally, the magnitude of vapor permeability varies between 10^{-12} and 10^{-11} [s]. When comparing these values with those of the literature, it is noticed that they are of the same order of magnitude with previous studies for similar hemp concrete formulations [208, 209].

Table 4.4 – Mean and corrected measurements of thermal conductivity, porosity and vapor permeability at the different protocol instants with the corresponding densities.

t [h]	$\bar{\rho}_{cub}$ [kg.m^{-3}]	λ [mW.m^{-1}.K^{-1}]	n [-]	$\bar{\rho}_{cyl}$ [kg.m^{-3}]	K_v [10^{-11} s]
0	545.57	91.29	0.778	534.41	1.581
122	532.95	96.16	0.761	526.1	0.874
244	533.65	89.92	0.785	523.51	1.584
366	509.47	98.57	0.748	521.3	0.505
488	483.02	95.27	0.764	553.85	0.969
610	507.74	97.49	0.754	505.88	0.814
732	518.2	95.23	0.77	495.18	1.09
854	526	92.09	0.774	534.32	1.31
976	505.1	103.18	0.74	528.79	4.63
Std	17.82	3.85	0.014	15.96	1.162

According to Equation (4.24), the correction of a property variation requires the determination of the derivative with respect to density. In [41], the authors studied different formulations of hemp concrete. In each case, properties were measured including density, thermal conductivity and porosity. Based on the latter, thermal conductivity and porosity variations, with respect to density, are approximated in this study as linear functions. Furthermore, due to the lack of data regarding vapor permeability, an assumption is made for this purpose. This hypothesis states that the variation in K_v according to ρ is obtained, supposing that the minimum and maximum measured values of vapor permeability correspond to those of porosity in the correlation. These correlations are given in the Appendix part according to Figures B.1 and B.2. As a result, Equation (4.28) highlights the approximated values of λ, n and K_v derivatives according to ρ :

$$\frac{\partial \lambda}{\partial \rho} \approx 1.22\,.10^{-4}\,\mathsf{m^4.s^{-3}.K^{-1}}\,,\ \frac{\partial n}{\partial \rho} \approx -1.13\,.10^{-4}\,\mathsf{kg^{-1}.m^3}\,,\ \frac{\partial K_v}{\partial \rho} = -3.65\,.10^{-14}\,\mathsf{kg^{-1}.m^3.s} \quad (4.28)$$

Having these derivative values, time variation in a property can be calculated in the downscaled configuration and deduced for the reference configuration. Firstly, porosity time variation is illustrated in Figure 4.7a. According to the latter, porosity drops then increases during Autumn, Winter and Spring with different variation rates. In Summer, it is different where a slight increase followed by a drop are observed. As for uncertainty, it is minimal at $t = 10.5$ months with a value of $4.47\,10^{-3}$ $[-]$ and maximal at $t = 3$ months where a value of $1.09\,10^{-2}$ $[-]$ is noticed. With regard to thermal conductivity, it varies depending on time as shown in Figure 4.7b. It varies from a minimum to a maximum equal to 89.92 and 103.19 mW.m^{-1}.K^{-1}, respectively. In terms of uncertainty, its variation is random and can reach 1.36 and 4.15 mW.m^{-1}.K^{-1} as extremes. Remind that these are entire uncertainty values. They are induced on the one hand by the random variation in density and studied properties between samples at each instant (random uncertainty). On the other, they are also due to systematic uncertainties throughout the aging protocol. Furthermore, thermal conductivity decreases during Autumn, increases slightly in winter, goes up during Spring and Summer. It is noteworthy that porosity variation is the opposite to that of thermal conductivity. Indeed, a decrease in porosity according to time is followed with an increase in thermal conductivity and vice versa. When examining time variation in porosity, thermal conductivity over a year, the discrepancies $3.8\,10^{-2}\,[-]$ and $11.89\,[\mathsf{mW.m^{-1}.K^{-1}}]$ are found, respectively. In this case, the aging design has a real effect on the material since variation on both properties is larger than twice obtained uncertainties. Indeed, the maximal uncertainty is $1.09\,10^{-2}\,[-]$ for porosity and $4.15\,[\mathsf{mW.m^{-1}.K^{-1}}]$ for thermal conductivity.

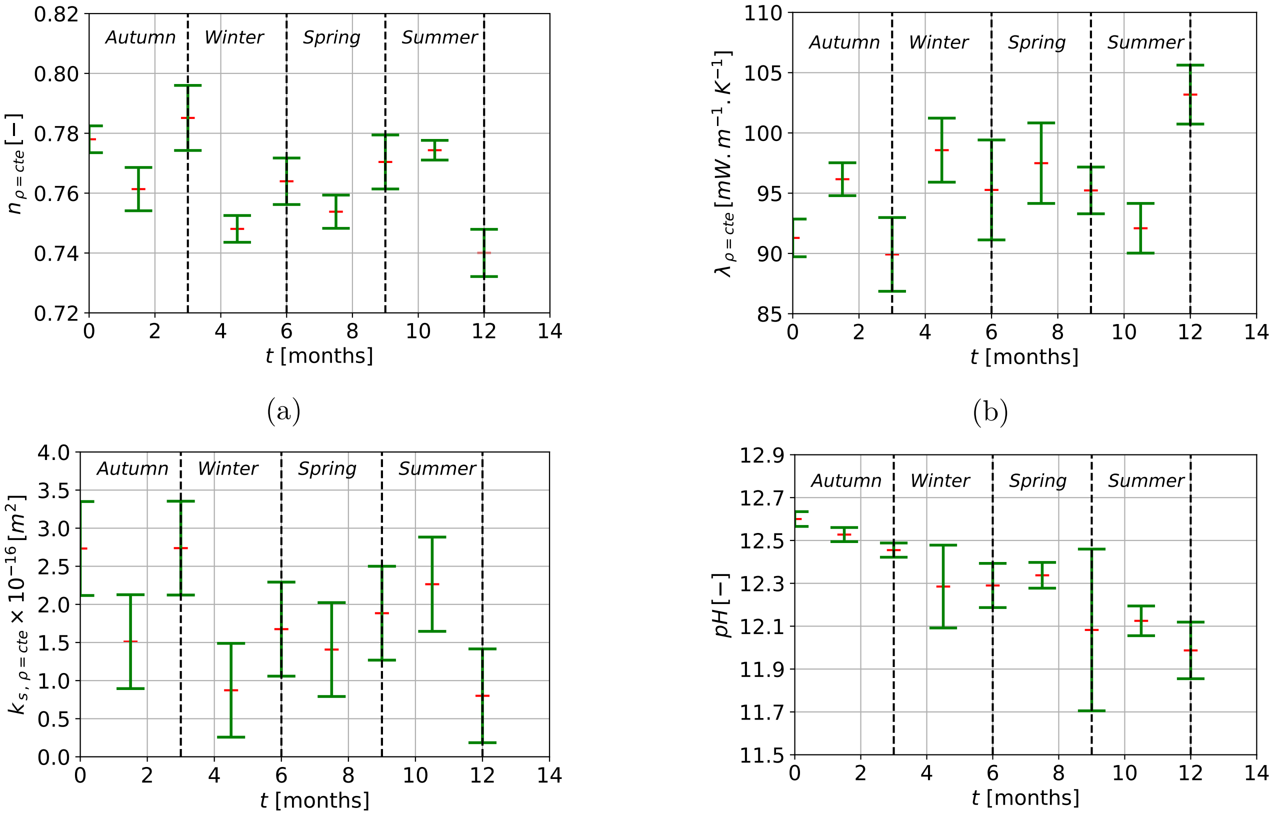

(a)

(b)

(c)

(d)

FIGURE 4.7 – Time variation in porosity (a), thermal conductivity (b), intrinsic permeability (c) and pH indicator (d) while considering the reference time scale.

In addition, it is chosen to study the influence of the aging protocol on the intrinsic permeability introduced in Equation (4.7). Indeed, this property is linked directly to the microstructure of a porous material, contrary to the vapor permeability which depends also on the characteristics of the fluid "vapor". The variation in intrinsic permeability is deduced and highlighted in Figure 4.7c. Intrinsic permeability varies within an interval delimited by $8\,10^{-17}$ and $2.74\,10^{-16}\,\mathsf{m}^2$ as lower and upper bounds, respectively. In terms of uncertainties, it is almost constant and its values range around $6.16\,10^{-17}\,\mathsf{m}^2$. As for the impact of each season sequence, the same scenario of porosity is observed for this property.

Table 4.5 – Sample powder quantities used for pH measurements.

t [months]	0	1.5	3	4.5	6	7.5	9	10.5	12
m_{powder} [g]	27.91	26.76	25.78	23.29	25.75	29.6	29.17	23.78	25.96
Std	2.93	3.18	1.7	0.71	2.23	2.17	2.35	1.94	1.16

Afterwards, the last test is destructive and aims to measure pH values at each instant. This property is chemical and does not depend on density when performing measurements on a same material. Consequently, the variation in this property does not require any correction and is directly due to climate stress. Figure 4.7d illustrates time variation in pH with respect to the reference time scale. The values are measured on the basis of powder masses that are given in Table 4.5. pH mean values are calculated each instant based on $N_{pH} = 4$. pH indicator is relatively decreasing from 12.6 to 11.98. In addition, it is noticed that the most uncertain value is the one measured after 9 months with a dispersion estimated at 0.38. This uncertainty is significantly higher than the ones at all other instants. This means that selected sample powders represent a high chemical variability. Moreover, the effect of aging is confirmed through the variations in intrinsic permeability and pH indicator over a year. The sum of calculated uncertainties at the initial and final instants is smaller than the corresponding discrepancy for both properties.

6 Discussion

In this section, the uncertainties evaluated on the different properties are addressed with respect to the number of samples that have been considered for measurements. Next, the risk of mold growth is evaluated based on the pH indicator data. Furthermore, the results related to thermal conductivity, intrinsic permeability are exploited in order to deduce their variation according to porosity. Finally, the last part focuses on the effect of climatic loads on porosity.

6.1 Uncertainty

In this study, properties measurements are given every 1.5 months considering the reference time scale. The experimental data are provided after conducting the effective design which is defined by the theoretical one plus the additional time deviations (Section 5.3). These time lags are induced during the practical application of the experimental design. Based on that, it is assumed that the data in Table 4.4 are not influenced by this uncertainty. In reality, a change in the duration of an immersion or a thermal stress could change the micro-structure of hemp concrete and thereby, vary λ and k_s. Indeed, a delay in an operation induces a duration decrease of the next one. For this reason, this assumption could be consequent.

Furthermore, the estimation of a random uncertainty that is related to a measurement is relevant in this study. Remind that porosity is the property with the largest number of measurements, which is 6 at each design instant. In general, the estimation of random uncertainty with a good accuracy relies on the consideration of a large number of samples [134]. The disposition of few samples would lead to an inaccurate standard deviation. In this study, measuring less properties would have increased the estimation accuracy of random uncertainties by disposing of more samples. An analysis of magnitude revealed that the random uncertainty represents from 50 to 97 % of the entire uncertainty for the case of thermal conductivity. A consideration of more samples would have decreased this large range of magnitude.

6.2 pH indicator and mold growth risk

Based on Figure 4.7d, weathering may have an effect on the pH variation, although the noticed decrease remains minor. According to [210], bio-based material formulations were resistant to fungal growth after an accelerated aging, based on microscopic observations. After pH measurements, the corresponding values were greater than or equal to 10. In addition, the same work highlighted that other hemp concrete formulations have a significant fungal development for pH values less than or equal to 6. Relying on these investigations, it is deduced that a sample of hemp concrete, having the dimensions indicated in Section 5.1, is not susceptible to mold growth over a one-year period in La Rochelle. However, a potential risk could be imagined after a long time by adopting the same climate. For example, pH might reach a value of 6 after about 10.64 years when considering an annual and linear decrease of 0.62.

6.3 Variation in thermal conductivity and intrinsic permeability depending on porosity

Based on the results in Figures 4.7a and 4.7b, variation in thermal conductivity according to porosity is deduced as shown in Figure 4.8a. At the dry state, an increase in pore volume induces more accessible air space. As a result, the insulating property of hemp concrete is improved according to a decrease in thermal conductivity. This variation is linked to an increase in porosity. In parallel, mass transfer properties are also affected by a micro-structure evolution. This statement is confirmed thanks to Figure 4.8b. An increase in porosity is followed by an increase in k_s. This finding can be justified by water vapor flux that become larger as a result of a pore size increase.

Relating thermal conductivity and intrinsic permeability to porosity is useful. Indeed, measuring only porosity throughout another aging design could be sufficient to deduce thermal conductivity and intrinsic permeability. Furthermore, it is interesting to compare the experimental results in this study to empirical models which were provided in the literature. As for thermal conductivity, it is defined for a porous medium considering the solid matrix, water in liquid and gas form and dry air [18] as follows :

$$\lambda = n\, S_l\, \lambda_l + n\,(\,1 - S_l\,)\,\lambda_{air} + (\,1 - n\,)\,\lambda_s, . \tag{4.29}$$

In this formula, porosity, saturation degree in water S_l, water thermal conductivity λ_l, the one of solid phase λ_s and that of dry air λ_{air} are highlighted. Given that measurements were carried at the dry state, the saturation degree in water is neglected $S_l \simeq 0$. Considering that $\lambda_{air} = 0.025\,\mathsf{W.m^{-1}.K^{-1}}$. It is assumed that this quantity is very negligible compared to solid phase thermal conductivity, i.e. $\lambda_{air} \ll \lambda_s$. Thus, thermal conductivity is expressed under theses hypotheses according to the following model :

$$\lambda \simeq (\,1 - n\,)\,\lambda_s\,. \tag{4.30}$$

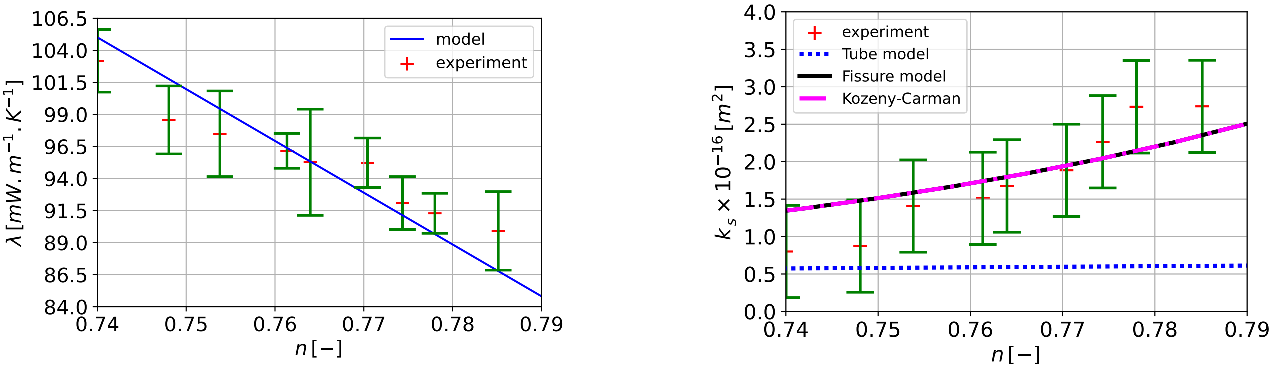

(a) (b)

FIGURE 4.8 – Thermal conductivity variation according to porosity (a) and its confrontation to an empirical model (b).

Based on Equation (4.30), thermal conductivity is a linear function of porosity where the slope is negative $-\lambda_s$ [211] and the ordinate at $n = 0$ is λ_s. Lying on Figure 4.8a, the model is relatively in accordance with the experimental result. The curve covers mostly all values and their associated confidence intervals. In this case, the parameter λ_s is estimated at 403.88 $\mathsf{mW.m^{-1}.K^{-1}}$. Moreover, by considering the used amounts of water, lime and hemp fibers during the formulation, a value of 375 $\mathsf{mW.m^{-1}.K^{-1}}$ is calculated. This value is assessed on the basis of the law of mixture. Note that it is close to the value obtained theoretically by the model.

Further, three empirical models linking the intrinsic permeability to porosity, are introduced based on [18]. The tube model represents the simplest case where the pore network of a material is modeled by tubes that are parallel to the direction of water flow :

$$k_s = n\,\frac{d^2}{32}\,, \tag{4.31}$$

where $d\,[\mathsf{m}]$ represents the diameter of tubes. The second approach consists in considering a pore path as a narrow capillary fissure. The fissure model is expressed as follows :

$$k_s = \frac{n^3}{(1-n)^2}\,\frac{a^2}{12}\,, \tag{4.32}$$

where $a\,[\mathsf{m}]$ denotes the mean grain size. The last model uses the notion of the hydraulic radius in the context of an interconnected channel network. The development of the model is based on a relation that links the hydraulic radius to porosity and specific area. According to this model, the intrinsic permeability is expressed by Kozeny − Carman :

$$k_s = c_0\,\frac{n^3}{(1-n)^2}\,\frac{1}{M_s^2}\,, \tag{4.33}$$

where $M_s\,[\mathsf{m^{-1}}]$ represents specific area which is referred to a volume unit of the material solid phase, and $c_0\,[-]$ is a fitting constant that was introduced by Carman.

As shown in Figure 4.8b, the intrinsic permeability empirical laws are plotted. Regarding the tube model, it shows that except for the first two values, the remaining are not in agreement with the experimental result. This confirms the complexity of the micro-structure of hemp concrete [212], i.e. there are no privileged directions inside the pore network and the pore size distribution is large. In addition, the fissure model is in a good concordance with the experimental values. The corresponding curve crosses the confidence interval of each experimental value. According to calculations, the law of variation in intrinsic permeability is relatively similar to the one of clay-stone. Indeed, a grain size of $a = 0.164$ µm is obtained theoretically. This value is literally close to 2 µm which represents the mean grain size of clay [213]. Finally, the curve corresponding to the second and last model are overlapped. Indeed, the term that depends on porosity is identical in Equations (4.32) and (4.33). The difference lies on the parameters of each model. Specific area could be measured using the BET theory [214] (Brunauer, Emmett and Teller). Hence, by disposing of such data, c_0 can be deduced for this formulated hemp concrete in further investigations.

6.4 Variation in porosity due to climate loads

Before addressing the evolution of porosity, it is important to recall the micro-structural behavior of a bio-sourced material due to heat and moisture stress. In particular, the absorption of a water quantity leads to the swelling of hemp fibers [72]. Meanwhile, the increase of humidity causes the expansion of pores which are accessible to water. In addition, the coalescence of micro-pores occurs, which are adjacent to each other, in order to form larger ones [215]. As a result, the open porosity increases after an immersion operation. The other case, which is the shrinkage of these fibers, is induced by the exposure to high heat radiation (drying). After the absorption of a large heat amount, pore volume decreases while bulk volume remains the same, which leads to the drop in porosity. Based on this analysis, porosity evolution in this study could be interpreted by considering the climate loads during each season. Mainly, immersion frequency and thermal stress intensity could be the parameters that affect porosity. This is consistent with the variation in porosity that goes up and down each three months. However, the variation rates are different as shown in Figure 4.7a. For example, during Summer, the increase remains negligible. Meanwhile, Autumn is a reverse example, where a significant increase in porosity is noticed between the instants 1.5 and 3 months. This difference in rate variation might be related to the duration of immersion periods. The latter are short in Summer and long during Autumn as recalled in Table 4.3.

7 Conclusion

The aging of building materials due to heat and mass stresses is a phenomenon that has to be investigated since its effect on bio-based materials is significant. Accordingly, the material micro-structure evolves under heat and moisture stresses, leading to the variation of its properties. On the one hand, this work highlights a methodology to elaborate an accelerated and realistic aging design. On the other hand, the effect of this design is evaluated on hemp concrete by using 1-year climate data. In this paper, the methodology is based on the similarity laws. These ensure an equivalence between a reference and a reduced configuration. By disposing of a configuration and assuming a proportionality factor of 3, the duration decreases by 89 % approximately. As a result, the effect of a one year aging design is similar to that during 40.43 d by choosing samples three times smaller in the reduced configuration.

Concerning the experimental part, the accelerated aging design is carried out on 36 samples of hemp concrete. During this experiment, measurements of thermal conductivity, intrinsic permeability, porosity and pH index are made at 9 different instants. Afterwards, time variation in those properties is assessed after a correction with respect to density differences between samples. In terms of results, the pH index decreases slightly and remains around 12. This would indicate the absence of mold growth risk in this material for one year. Furthermore, considerable variations in porosity, thermal conductivity and intrinsic permeability are noticed. In particular, maximum and minimum values are reached during the sequences representing winter and summer, respectively for porosity and intrinsic permeability. As for thermal conductivity, the opposite is shown. These experimental findings yield the law of variation in thermal conductivity and intrinsic permeability depending on porosity. Subsequently, these are compared to empirical models from the literature, one for thermal conductivity and three for intrinsic permeability. The comparison shows that thermal conductivity variation is consistent with the mixing law, while intrinsic permeability more with the fissure and Kozeny-Carman models.

In order to extend the database on aging of bio-based materials, further investigations could be carried out. In this paper, the developed methodology can be adopted further to study the effect of aging on other materials using other climate types. This would improve the numerical prediction of heat and mass transfer into bio-based materials. Besides that, porosity defines one of the principal material properties that evolves under the exposure to thermal and water stresses. However, its variation is determined only by means of experimental observations. In this respect, the development of theoretical model based on climate loads might be useful to predict the variation of porosity. Such behavior law can be integrated into the models of heat and mass transfer through porous materials. This would constitute a wide step towards the aging modeling.

Acknowledgments

The Region and the European Union support the project <CPER-FEDER Bâtiment durable Axis 2 MADUR Project : High-performance building materials with low environmental impact, sustainable and resilient> within the framework of the « Operational Program FEDER/FSE 2015-2020 and Energy saving certificate program of the Ministry of Ecological and Solidarity Transition "SmartReno support" 2019-2021.

Competing interests

The authors have no relevant financial or non-financial interests to disclose.

Author contributions

Achraf Charaka : conceptualization, methodology, experimentation, software, investigation, writing-original draft. Julien Berger : conceptualization, methodology, validation, writing-review and editing, supervision. Ferhat Benmahiddine : methodology, investigation, experimentation, resources. Rafik Belarbi : conceptualization, methodology, resources, validation, writing-review and editing resources, supervision.

Data availability

The data-sets generated during and/or analyzed during the current study are available from the corresponding author on reasonable request.

Chapitre 5

Critical assessment of an aging phenomenological model for building materials

Abstract

The description of aging of construction materials represents a significant issue. This phenomenon arises due to the exposure of building walls to varying climate stresses. According to previous studies, aging is addressed by using experimental approaches which consist in submitting materials to accelerated aging designs in the laboratory. These are based, mostly, on series of drying and liquid water imbibition cycles. The effect of the phenomenon is, then, highlighted by performing measurements at different stages of material aging. These discrete configurations are considered to evaluate the impact of aging at the building scale. Hence, aging is integrated into building energy simulations only on the basis of a discrete approach. The latter lies on the experimental data that define each discrete configuration. Within this context, this research proposes a phenomenological model that describes the aging of a material in time. It assesses the variation in porosity depending on drying and imbibition loads, each expressed by means of an indicator. Also, a cumulative and a moving approach are used to express each load. Afterwards, the model unknown parameters are estimated by solving an inverse problem. The results of the estimation are obtained based on experimental observations of an aging experimental design on hemp concrete. For each load approach, it is shown that the model fits good most of porosity measurements. In particular, the moving approach is better adapted to study the aging of materials. Further, the model of porosity is integrated into equations of heat and mass transfer within porous media. The objective consists in evaluating the impact of aging, with a continuous approach, on the energy efficiency of the material at the wall scale. Based on a case study, the impact is evaluated by assessing the energy efficiency for a first configuration without aging and a second with it. Computations of sensible and latent heat fluxes reveal that thermal losses through the wall are underestimated by about 30 % when aging effects are neglected. This finding highlights the significance of this phenomenon and encourages its consideration of in future building energy simulations.

1 Introduction

In light of the current energy context, various standards encourage the design of new buildings using materials with good energy performance and a low carbon footprint [216, 217]. They also recommend extending their use to the retrofitting of existing buildings. For this reason, research has been increasingly targeting the development of an innovative generation of materials [218]. In particular, different studies have highlighted the beneficial heat and moisture properties of bio-sourced materials [219, 220]. However, these materials stand out from conventional concretes through the high sensitivity to weather conditions. This phenomenon drives the evolution of the material micro-structure throughout the building life cycle. In the literature, studies name this phenomenon aging and evaluate its effects at various scales, by proposing different weathering cycles [221, 222]. Typically, temperature, ultraviolet radiation, water are the common parameters to represent climate stresses.

Based on previous findings, the impact of aging is modeled by measuring a set of properties at different instants over aging experimental designs. A first study addresses an aging protocol and its effect on hemp mortars [74]. It consists in heat, rain and cold cycles. Micro-structural observations and heat and moisture transfer properties are evaluated. According the experimental set-up, an evolution is noticed by performing an initial and a final stage measurement to the aging protocol. The variation in properties is, thus, stated by referring only to two values, before and after aging. This approach is fairly adopted in other investigations [72]. For example, two plant-based concretes are submitted to two aging tests in order to examine their durability [223]. Observations are obtained by means of two measurements per material and aging test. Furthermore, durability properties of corn and stalk based concrete are studied according to [179]. The materials are exposed to immersion and freeze-thaw cycles. A decay is noticed in properties such as weight, area and compressive strength. This finding lies on measurements before and after weathering. Unlike mentioned investigations, other research studies such as [71] consider intermediate measurement instants other than the initial and the final instants. According to [224], authors investigate the durability of a high performance bio-composite through an 8-week weathering test. The test induces a damage which is modeled on the basis of measurements each two weeks. Moreover, another study reports an experimental investigation of the durability of normal and reinforced hemp concrete samples [225]. The impact of the proposed test is highlighted by testing properties initially and after 15, 25 and 50 cycles. The same methodology is adopted in [226], which aims at quantifying the effect of humidification and drying cycles on mechanical properties of flax-epoxy composite. Clear decrease in tensile modulus is measured by fixing six instants going from the scale of weeks to months. At this level, the effect of aging is evidenced only through experimental approaches. Performing few measurements on properties is not sufficient to understand the material behavior under heat and moisture stresses.

According to some investigations in the last paragraph, performing aging experimental designs on materials drives variations in heat and moisture properties. Building energy simulations can be impacted under the aging of materials. In this context, literature features some works that take into account wall aging in the prediction of building heat and cooling demands. It is the case in [227] where an insulation deterioration of roof and walls is assumed to predict its effect on the energy efficiency of a building. For this, a high and a low degradation scenarios over 50 years are proposed. Aging is taken into account by setting in each scenario an increase rate per decade in thermal conductivity. Further, [228] aims at assessing the impact of the degradation of some components on heating energy consumption of two building categories. Focusing on thermal insulation, the study defines an aging scenario which assumes a 12.5 % increase in thermal conductivity over 25 years. In this case, results show that heating energy consumption increases by 8.1 % and 13.48 % for detached houses and apartment buildings, respectively. Furthermore, other studies are more interested in the effect of wall weathering at the building scale. For instance, a novel aerogel-based render is developed and submitted to a large-scale weathering test [229]. Before and after the experiment, heat transmission coefficient is measured to assess the weather impact on the render performance. It is found that this coefficient increases. During heating periods, a building energy simulation highlights a 7 % demand increase due to the negative impact of weathering. Finally, an experimental and numerical investigation [76] are conducted to evaluate the aging effects on hemp concrete at the material and the building scale, respectively. Observations before and after the experiment show an increase in porosity and a decrease in thermal conductivity. At the building scale, the material behavior is marked by less heat losses when considering the aged properties. This finding is related to the decrease in thermal conductivity under the weathering test.

The review of the literature reveals the non-existence of continuous models that simulate aging under heat and moisture loads. In particular, a physical model, that describes the intrinsic behavior at the macroscopic scale under climate loads, is still not developed. Indeed, the effect of this phenomenon is evidenced by experimental investigations. Except for instants where measurements are performed, the evolution of material properties remains unknown. Further on, the aging effect at the building scale is assessed mostly by comparing discrete configurations corresponding to the stages before and after aging. Also, properties are assumed constant throughout each configuration. Since aging reflects a continuous evolution, previous studies do not investigate accurately the effect of this phenomenon. To address these issues, this paper deals first with the development of a phenomenological aging model. It simulates the variation in porosity with respect to drying and imbibition loads. Subsequently, this model is integrated in heat and moisture transfer within porous media. This step helps assessing the material behavior under the variation of porosity over time. The paper is divided into five parts. The first part is devoted to the definition of a phenomenological aging model under two load approaches. Thereafter, the model parameters are estimated through the resolution of an inverse problem. The third part shows the results of the estimation for each load approach. Further on, a case study is defined, investigating the effect of aging on the energy performance at the building scale. At the end, paper results are addressed through a discussion part.

2 Porosity variation under climate loads

This part aims at developing a model to simulate the variation of porosity of a material. For this purpose, drying and imbibition loads are considered as the driven potentials of this variation. First, the physical model is introduced where two involved parameters are involved. The model is designed on the basis of population growth theory. The expression of drying and imbibition loads lies on temperature and rain flux data, respectively. Two approaches are used to define these loads.

2.1 Physical model

The size of the material is assumed larger than the representative elementary volume. The material is regarded as an homogeneous medium. Under this assumption, porosity $n\,[-]$ is a quantity that varies over time and discounts the material space variability. The model of porosity is defined according to :

$$\forall t \in [\,0\,,\,t_{\,f}\,]\,, \qquad \frac{\partial n}{\partial t} = \alpha_{\,q}\, n\,\Big(n_{\,q}^{\,\infty} - n\Big) + \alpha_{\,m}\, n\,\left(n_{\,m}^{\,\infty} - n\,\right)\,, \tag{5.1}$$

where $t_{\,f}$ [s] represents the final instant. In addition, $n_{\,q}^{\,\infty}\,[-]$ and $n_{\,m}^{\,\infty}\,[-]$ are the limits that define the bounds of porosity variation. These threshold values depend on the material. Moreover, $\alpha_{\,q}\,[\mathsf{s}^{-1}]$ and $\alpha_{\,m}\,[\mathsf{s}^{-1}]$ are expressed as follows :

$$\alpha_{\,q}\,(\,t\,) = \alpha_{\,q,\,0}\, Q_{\,q}\,(\,t\,)\,, \tag{5.2}$$

$$\alpha_{\,m}\,(\,t\,) = \alpha_{\,m,\,0}\, Q_{\,m}\,(\,t\,)\,. \tag{5.3}$$

$\alpha_{\,q,\,0}\,[\mathsf{s}^{-2}]$ and $\alpha_{\,m,\,0}\,[\mathsf{s}^{-2}]$ are positive attracting coefficients. Drying and imbibition loads are defined by $Q_{\,q}$ [s] and $Q_{\,m}$ [s], respectively. Temperature is used to express $Q_{\,q}$. As for imbibition loads, they are assessed using water flux data during rainfall. At this level, we assume that the model neglects the effect of water vapor on material porosity. Based on experimental observations, porosity decreases when submitting a material to drying periods and increases under imbibition exposures. Furthermore, the magnitude of $\alpha_{\,q,\,0}$ and $\alpha_{\,m,\,0}$ affects the variation in porosity between the thresholds $n_{\,q}^{\,\infty}$ and $n_{\,m}^{\,\infty}$. Porosity attains slowly $n_{\,q}^{\,\infty}$ for small values of $\alpha_{\,q,\,0}$. Similarly, porosity reaches rapidly $n_{\,m}^{\,\infty}$ for large values of $\alpha_{\,m,\,0}$. The initial condition on porosity is given in :

$$t = 0\,, \qquad n = n_{\,0}\,, \tag{5.4}$$

where $n_{\,0}\,[-]$ is constant and refers to initial porosity. In the following, $Q_{\,q}$ and $Q_{\,m}$ are expressed regarding two different approaches.

2.2 Heat and imbibition loads

2.2.1 Heat and imbibition indicators

The imbibition indicator is denoted $\Gamma_{\,m}\,[-]$. It represents a Boolean function which takes the value 1 during water imbibition and 0 during drying. The number of imbibition sequences during the entire time horizon is referred to as $N_{m}\,[-]$. To express drying loads, the following indicator is adopted :

$$\forall t \in [\,0\,,\,t_{\,f}\,]\,, \qquad \Gamma_{\,q}\,(\,t\,) = \frac{T_{eq}\,(\,t\,) - T_{min}}{T_{max} - T_{min}}\,. \tag{5.5}$$

It involves the three temperatures T_{eq} [°C], T_{min} [°C] and T_{max} [°C]. First one reflects the equivalent outdoor temperature which combines air convection and radiation effects :

$$T_{eq} = T_{ext} + \frac{b\,E}{h_{\,c}}\,. \tag{5.6}$$

Where T_{ext} [°C] is outdoor air temperature, b [−] the material surface absorptivity, E [W.m^{-2}] the incident short wave solar radiation and h_c [W.m^{-2}.K^{-1}] the heat convection coefficient. T_{min} [°C] and T_{max} [°C] are the minimal and maximal value of the equivalent temperature over the time period, respectively. We consider that drying cycles are considered when imbibition is not occurring, i.e. $\Gamma_m = 0$.

2.2.2 Cumulative loads

In this approach, a climate load is defined according to a cumulative integral. Given stress sequences over a period, loads at an instant are assessed by applying a stress integral which considers the entire interval before this instant. Accordingly, moisture and heat loads are expressed as follows :

$$\forall t \in [\,0\,,\,t_f\,]\,, \qquad Q_m(\,t\,) = \int_0^t \Gamma_m(\,\tau\,)\,\mathrm{d}\tau\,. \tag{5.7}$$

$$\forall t \in [\,0\,,\,t_f\,]\,, \qquad Q_q(\,t\,) = \int_0^t \Gamma_q(\,\tau\,)\,\mathrm{d}\tau\,. \tag{5.8}$$

2.2.3 Moving loads

Unlike the first approach, a variation in porosity is only induced by current imbibition and drying loads. In this case, the latter are expressed according to :

$$Q_m(\,t\,) = \begin{cases} \displaystyle\int_{t_k}^{t_k+\Delta t_k} \Gamma_m(\,\tau\,)\,\mathrm{d}\tau\,, & \tau \in [\,t_k\,,\,t_k+\Delta t_k\,]\,, \quad k \in \{\,1\,,\,2\,,\dots,\,N_m\,\}\,, \\ 0\,, & \text{else}\,. \end{cases} \tag{5.9}$$

$$Q_q(\,t\,) = \begin{cases} \displaystyle\int_{t_l}^{t_l+\Delta t_l} \frac{T_{ext}(\,\tau\,) - T_{min}}{T_{max} - T_{min}}\,\mathrm{d}\tau\,, & \tau \in [\,t_l\,,\,t_l+\Delta t_l\,]\,, \quad \Gamma_m(\,\tau\,) = 0\,, \\ 0\,, & \text{else}\,. \end{cases} \tag{5.10}$$

t_k [s] is the start instant of the k-imbibition sequence and $k \in \{\,1\,,\,2\,,\dots,\,N_m\,\}$ defines the index of imbibition sequences. The symbol l refers to the index of drying sequences. Drying loads are considered when imbibition is not occurring, i.e. $\Gamma_m = 0$ and thus $Q_m = 0$. When imbibition occurs, Q_q equals zero. It is also noteworthy that a load is reset to zero at the beginning of a corresponding sequence. After defining the climate loads, next part proposes a numerical method to approximate the solution of the porosity model

2.3 Numerical method

The temporal grid is discretized using a constant time mesh Δt. Thus, $n(\,t\,)$ is approximated by $n(\,t^j\,) \approx n^j$ where j is the time node index. For $j \in \{\,1\,,\,\dots\,,\,N_t\,\}$, with N_t the number of time nodes, the numerical model is written according to :

$$\frac{n^{j+1} - n^{j}}{\Delta t} = \alpha_{q}^{j+1} n^{j+1} \left(n_{q}^{\infty} - n^{j+1} \right) + \alpha_{m}^{j+1} n^{j+1} \left(n_{m}^{\infty} - n^{j+1} \right) . \tag{5.11}$$

As a result, knowing porosity at t_{j}, its value at t_{j+1} is computed by solving the Equation :

$$\Delta t \left(\alpha_{q}^{j+1} + \alpha_{m}^{j+1} \right) \left(n^{j+1} \right)^{2} + \left[1 - \Delta t \left(\alpha_{q}^{j+1} n_{q}^{\infty} + \alpha_{m}^{j+1} n_{m}^{\infty} \right) \right] n^{j+1} - n^{j} = 0 . \tag{5.12}$$

The discriminant is time-dependent and strictly positive. It is denoted δ and expressed with respect to :

$$\delta^{j} = \left[1 - \Delta t \left(\alpha_{q}^{j+1} n_{q}^{\infty} + \alpha_{m}^{j+1} n_{m}^{\infty} \right) \right]^{2} + 4 \, \Delta t \left(\alpha_{q}^{j+1} + \alpha_{m}^{j+1} \right) n^{j} . \tag{5.13}$$

For $j \in \{ 1 , \ldots , N_{t} \}$, the solution is as follows :

$$n^{j+1} = \frac{\Delta t \left(\alpha_{q}^{j+1} n_{q}^{\infty} + \alpha_{m}^{j+1} n_{m}^{\infty} \right) - 1 + \left(\delta^{j} \right)^{0.5}}{2 \, \Delta t \left(\alpha_{q}^{j+1} + \alpha_{m}^{j+1} \right)} . \tag{5.14}$$

$\alpha_{q,0}$ and $\alpha_{m,0}$ represents the model input parameters. However, these are unknown and need to be estimated. The next section defines the parameter estimation problem related to the model of porosity.

3 Parameter estimation problem

This section aims at describing the procedure to estimate the unknown parameters of the porosity model $\alpha_{q,0}$ and $\alpha_{m,0}$. The sensitivity of the model is investigated with respect to its parameters $\alpha_{m,0}$ and $\alpha_{q,0}$. Through the sensitivity analysis, the effect of a parameter variation on porosity is assessed. Sensitivity lies on the calculation of the following derivatives :

$$\forall t \in [0 , t_{f}] , \quad \chi (t) = \frac{\partial n}{\partial \alpha_{q,0}} , \quad \xi (t) = \frac{\partial n}{\partial \alpha_{m,0}} \tag{5.15}$$

$\chi \, [\mathsf{s}^{2}]$ and $\xi \, [\mathsf{s}^{2}]$ represent the sensitive coefficients with respect to $\alpha_{q,0}$ and $\alpha_{m,0}$, respectively. In the appendix, Section 1 provides the equations of sensitivity and the assessment method. In the case of small variations in χ, the sensitivity of porosity to $\alpha_{q,0}$ could be neglected. Inversely, large variations in ξ means that porosity is more sensitive to $\alpha_{m,0}$. The analysis of sensitivity is required to study the identifiability of model parameters before their estimation [230]. They are identifiable if sensitive coefficients are linearly independent. For the estimation of the unknown parameters $\alpha_{m,0}$ and $\alpha_{q,0}$, we define the least square estimator [231, 232] between experimental data $\hat{n}$ and the model prediction :

$$J (\boldsymbol{p}) = \sum_{i=1}^{N} \left[n (\boldsymbol{p} , t_{i}) - \hat{n} (t_{i}) \right]^{2} . \tag{5.16}$$

$\boldsymbol{p} = (\alpha_{m,0} , \alpha_{q,0})$ represents the unknown parameter vector. $\hat{n} \, [-]$ refers to porosity measurements and $N \, [-]$ is the number of these measurements. The estimated parameters are defined by :

$$\boldsymbol{p}^{\star} = \arg\min \left[J (\boldsymbol{p}) \right] . \tag{5.17}$$

$\boldsymbol{p}^{\star}$ is assessed following a process of iterations and a convergence criterion. The $\mathsf{Gauss - Newton}$ algorithm [233, 234] is adopted to solve this nonlinear least-square problem.

4 Parameter estimation results

This part highlights the results of the parameter estimation problem. First, it exposes the experimental observations that are related to a weathering experiment. Over this test, the variation in porosity was obtained through some measurements. These data are adopted to solve the estimation problem for each load approach.

4.1 Materials and experiments

The experiment was carried out to study the aging of hemp concrete. The effect of aging was highlighted by measuring porosity throughout this design. According to this one, samples of hemp concrete were subjected sequentially to four different scenarios including water imbibition and drying. Each sequence lasts one week and was repeated 13 times to complete a year season before proceeding to the next one. Figure 5.1 illustrates the four weathering test sequences.

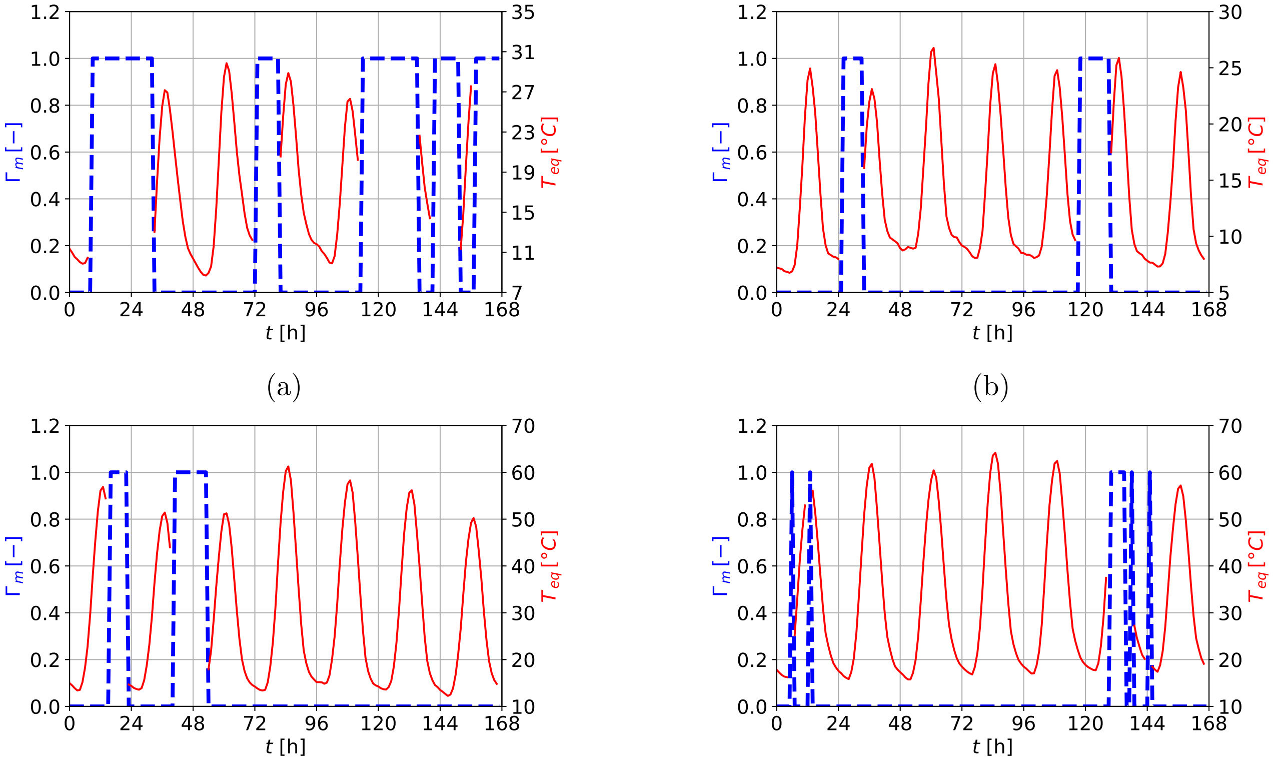

(a) (b)

(c) (d)

FIGURE 5.1 – Variations in the imbibition indicator and equivalent temperature according to each typical week for : Autumn (a), Winter (b), Spring (c) and Summer (d) [235].

It shows the instants when imbibition occurs using the defined indicator. Otherwise, variations in temperature are presented. Notice that temperature reaches 60 °C during Spring and Summer typical weeks. This magnitude exceeds the one of outdoor air temperature. Indeed, the aging design is developed while considering also the radiation effects to define the drying cycles. These data are then used to assess the variables Q_m and Q_q according to both climate load approaches. For the sake of calculations, the values $n_m^{\infty} = 0.8$ and $n_q^{\infty} = 0.73$ are taken into account. Note that n_m^∞ should be superior to n_q^∞ because of the material behavior under heat and moisture stresses. Also, these values are fixed with respect to the considered material. Indeed, porosity measurements on hemp concrete are provided in Figure 5.2. Accordingly, obtained values range between 0.74 and 0.785.

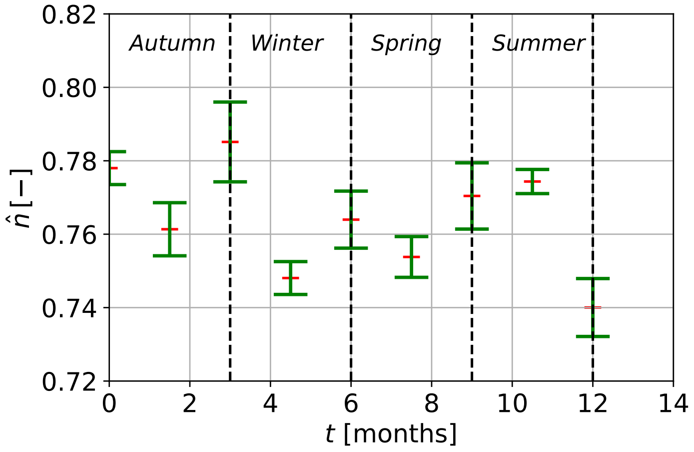

FIGURE 5.2 – The experimental porosity observations over the aging design [235].

4.2 Results for the cumulative load approach

4.2.1 Identifiability

The sensitive coefficients are assessed considering the a priori parameters $\alpha_{m,0} = 0.1\,\mathrm{s}^{-2}$ and $\alpha_{q,0} = 0.05\,\mathrm{s}^{-2}$. According to Figure 5.3, the effect of $\alpha_{q,0}$ on porosity is quite twice as large as that of $\alpha_{m,0}$.

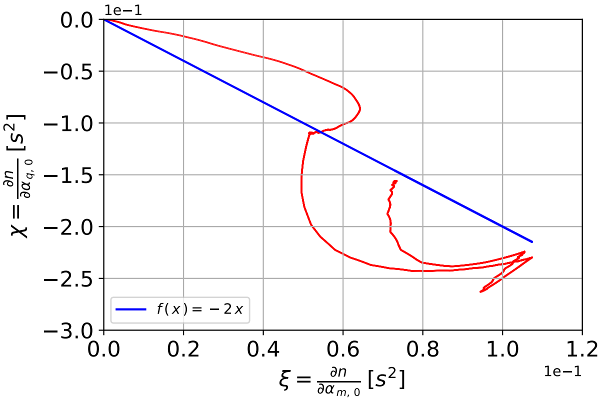

FIGURE 5.3 – Variation in the variable χ according to ξ under the cumulative load approach.

It shows also that the variation of χ according to ξ is not linearly dependent. Thus, the model parameters are considered linearly independent. The choice of the a priori parameters $\boldsymbol{p}^\circ$ is important in the minimization procedure since it can leads to local minimums of the least square residual.

4.2.2 Estimation results

The inverse problem is solved using the five porosity measurements as reported in Table 5.1. The cost function is evaluated for four initial parameter choices. Figure 5.4a shows the variation in the cost function according to algorithm iterations. A progressive decrease is noticed regardless of the prior candidate choice. The lower the cost function, the closer the parameters converge to the optimal candidate. The magnitude of the cost function is initially around 10^{-3}, then decreases until reaching 10^{-4}. Note also that the end values are almost identical regardless of the a priori parameter choice. These are given in Table 5.2, in addition to the a priori and end values of parameters. Accordingly, the optimal parameters are $\boldsymbol{p}^{\star} = (\,0.16\,,\,0.074\,)$.

Table 5.1 – Used porosity measurements in the estimation of parameters for the cumulative load approach [235].

t [months]	0	3	6	9	12
$\hat{n}$	0.778	0.785	0.764	0.77	0.74

Further, the optimal values are used to compute the prediction of the porosity model. Figure 5.4b plots the variation of porosity considering $\boldsymbol{p}^{\star} = (\,0.16\,,\,0.074\,)$ and $\boldsymbol{p}^{\circ} = (\,1\,,\,10^{-2}\,)$. It reports also the measurements of porosity. By using the a priori parameters, the simulated porosity deviates largely from the measurements and reaches promptly the upper bound. This is due to the magnitude of $\alpha_{\,m,0}$ which is 100 times that of $\alpha_{\,q,0}$. Also, the large deviation is driven by the imbibition loads which are dominant during Autumn and Winter. During Spring and Summer, a slight decrease in porosity is observed. The cause is the imbibition periods that become shorter during these seasons. The prediction fits good the experimental observations, except for the porosity at $t = 9\,\mathsf{months}$. At this instant, the computed value of porosity lies beyond the uncertainty range of the underestimated measurement. According to the prediction, porosity increases up to 0.79 over Autumn, then follows a gradual decrease from 0.79 to 0.74.

Table 5.2 – The a priori parameters, their corresponding cost function end value and optimal parameters, under the cumulative load approach.

A priori parameter	Optimal parameter	Cost function final value
$\boldsymbol{p}^{\circ} = (\,\alpha^{\circ}_{\,m,0}\,,\,\alpha^{\circ}_{\,q,0}\,)$	$\boldsymbol{p}^{\star} = (\,\alpha^{\star}_{\,m,0}\,,\,\alpha^{\star}_{\,q,0}\,)$	$J\,(\,\boldsymbol{p}^{\star}\,)$
$(\,10^{-2}\,,\,1\,)$	$(\,9.88 \times 10^{-3}\,,\,8.29 \times 10^{-3}\,)$	2.71×10^{-4}
$(\,1\,,\,10^{-2}\,)$	$(\,0.16\,,\,0.074\,)$	2.54×10^{-4}
$(\,1\,,\,10\,)$	$(\,0.16\,,\,0.074\,)$	2.54×10^{-4}
$(\,10\,,\,1\,)$	$(\,0.16\,,\,0.074\,)$	2.54×10^{-4}

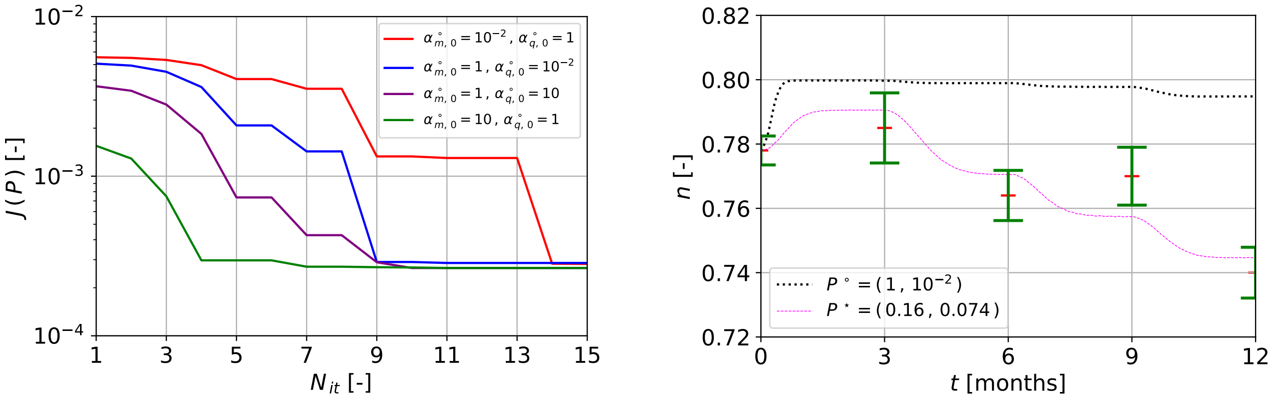

(a) (b)

FIGURE 5.4 – The cost function variation under the cumulative load approach and using four initial parameter (a). Variation in porosity according to time, under the cumulative load approach while considering a priori parameter and the optimal one (b).

4.3 Results for moving load approach

4.3.1 Identifiability

For this approach, the resolution of this inverse problem is carried out per season. Sensitive coefficients are assessed using the a priori parameters $\alpha_{m,0} = 1\,\mathsf{s}^{-2}$ and $\alpha_{q,0} = 1\,\mathsf{s}^{-2}$. Figure 5.5 highlights the variation of χ according to ξ per season. As noticed under the previous load approach, χ is negative in contrary to ξ. The sign of each coefficient is related to the effect of the corresponding climate load on porosity. It is consistent with the decrease and the increase of porosity with regard to drying and imbibition loads, respectively. By Autumn, the sensitive coefficients have relatively the same magnitude. It is the result of the existence of many imbibition as drying sequences. From Winter onward, porosity becomes more sensitive to drying loads. Based on plotted slope values, the ratio of χ to ξ increases significantly until reaching 150 approximately. This is due to the large drying loads during Spring and Summer. Moreover, the study reveals that $\alpha_{m,0}$ and $\alpha_{q,0}$ are linearly independent in the case of Autumn and Winter. Meanwhile, the scatter plots are more in the vicinity of straight lines in the case of Spring and Summer. The assessment of the correlation coefficient between χ and ξ gives the value -0.94 for Spring and -0.97 for Summer.

TABLE 5.3 – Used porosity measurements per season in the estimation of parameters for the moving load approach [235].

t [months]	0	1.5	3
Autumn	0.778	0.761	0.785
Winter	0.785	0.748	0.764
Spring	0.764	0.754	0.77
Summer	0.77	0.774	0.74

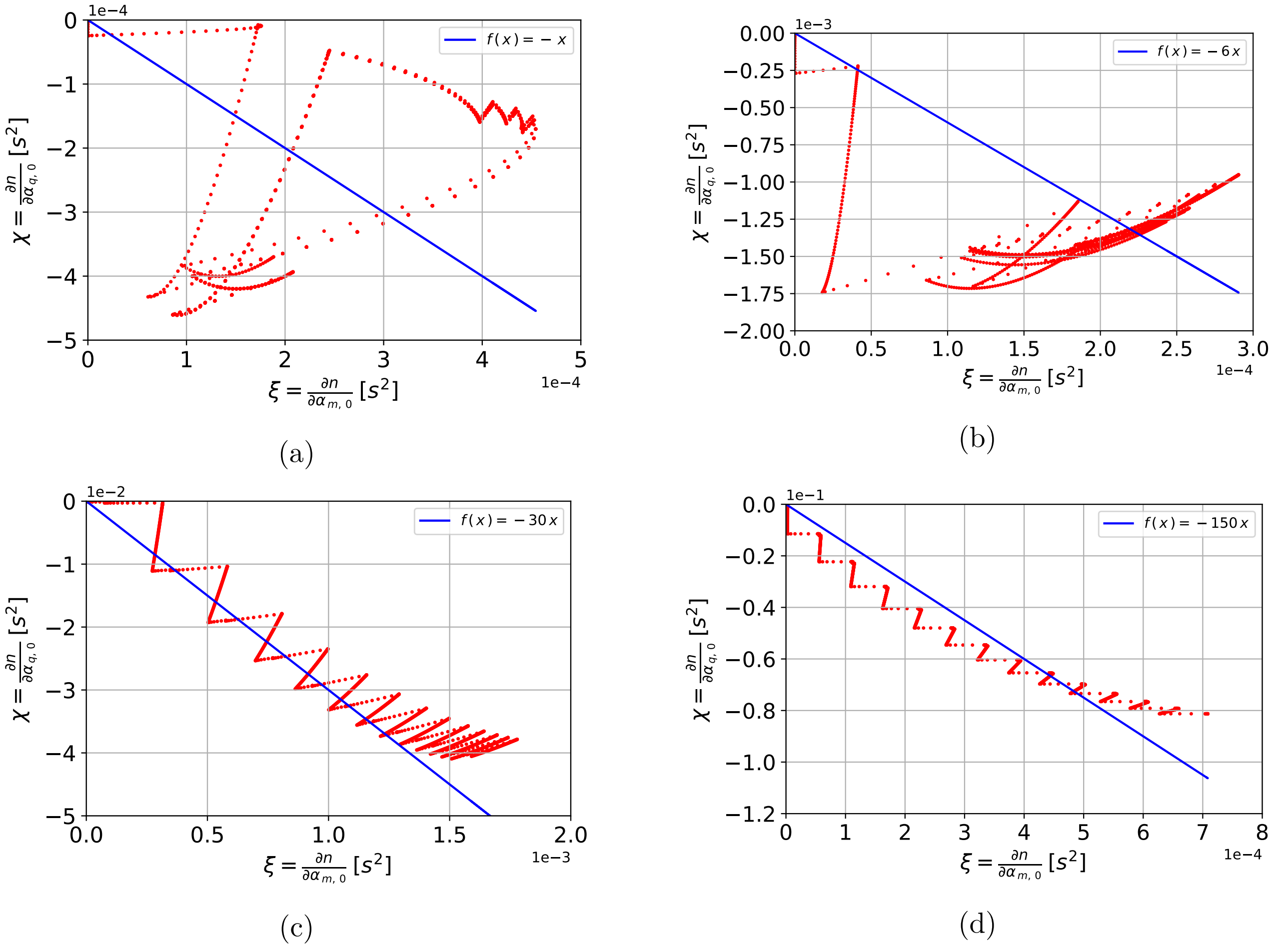

(a) (b)

(c) (d)

FIGURE 5.5 – Variation of χ according to ξ while considering the moving load approach in : Autumn (a), Winter (b), Spring (c) and Summer (d).

4.3.2 Estimation results

Per season, the resolution of the inverse problem is based on three measurements, as reported in Table 5.3. As previously, four a priori parameters are proposed. Figure 5.6 shows the variation, per season, in the cost function according to iterations number. In Autumn, the magnitude decreases progressively from 10^{-4} to 10^{-17}. The cost function lowest value is obtained after 74 iterations by considering the initial parameters $\alpha_{m,0} = 10$ and $\alpha_{q,0} = 3$. The corresponding optimal parameters are $\boldsymbol{p}^{\star} = (\,47.62\,,\,51.91\,)$. As for Winter, the minimization algorithm required fewer iterations to reach the optimal solution. The magnitude of the cost function decreases only by 10^{-2}. By choosing $\boldsymbol{p}^{\circ} = (\,20\,,\,27\,)$, the estimation leads to the optimal values $\boldsymbol{p}^{\star} = (\,73.66\,,\,11.74\,)$. In this case, the cost function reaches 5.15×10^{-5} after 23 iterations. Regarding Spring, the magnitude of the cost function decreases from 10^{-3} to 10^{-4}. In particular, the minimum 1.49×10^{-4} is reached after 30 iterations for the initial parameters $\alpha_{m,0} = 5$ and $\alpha_{q,0} = 3$. This configuration provides $\boldsymbol{p}^{\star} = (\,8.95\,,\,0.41\,)$. Finally, the cost function convergence is similar in Summer as in Spring. Indeed, it reaches The lowest value 3.42×10^{-4} considering $\boldsymbol{p}^{\circ} = (\,1\,,\,1\,)$. In Summer, the optimal parameters are $\boldsymbol{p}^{\star} = (\,0.025\,,\,0.17\,)$. To sum up, Table 5.4 provides the estimation results considering the moving load approach.

Table 5.4 – The a priori parameters, their corresponding cost function end value and optimal parameters, per season and under the moving load approach.

Season	A priori parameter	Optimal parameter	Cost function final value
	$\boldsymbol{p}^{\circ} = (\alpha^{\circ}_{m,0}, \alpha^{\circ}_{q,0})$	$\boldsymbol{p}^{\star} = (\alpha^{\star}_{m,0}, \alpha^{\star}_{q,0})$	$J(\boldsymbol{p}^{\star})$
Autumn	$(5, 1)$	$(47.62, 51.91)$	9.31×10^{-17}
	$(10, 3)$	$(47.62, 51.91)$	4.63×10^{-17}
	$(1, 1)$	$(47.62, 51.91)$	1.61×10^{-17}
	$(15, 20)$	$(47.62, 51.91)$	2.13×10^{-16}
Winter	$(2, 4)$	$(83.34, 10.9)$	7.06×10^{-5}
	$(10, 10)$	$(81.7, 11.69)$	5.44×10^{-5}
	$(20, 27)$	$(73.66, 11.74)$	5.15×10^{-5}
	$(30, 50)$	$(70.88, 11.63)$	5.35×10^{-5}
Spring	$(5, 3)$	$(8.95, 0.41)$	1.49×10^{-4}
	$(9, 2)$	$(6.04, 0.17)$	1.71×10^{-4}
	$(17, 20)$	$(4.81, 0.18)$	1.73×10^{-4}
	$(10, 7)$	$(1.18, 4 \times 10^{-3})$	1.58×10^{-4}
Summer	$(4, 4)$	$(2.71, 0.18)$	3.54×10^{-4}
	$(9, 13)$	$(0.46, 0.19)$	3.48×10^{-4}
	$(1, 1)$	$(0.025, 0.17)$	3.42×10^{-4}
	$(12, 10)$	$(3.94, 0.23)$	3.76×10^{-4}

As for the cumulative load approach, the variation in porosity is assessed considering an initial guess and the optimal parameters. That is shown for each season in Figure 5.7. In Autumn, considering $\boldsymbol{p}^{\circ} = (10, 3)$ leads to high values of porosity close to the upper bound. Indeed, Autumn is marked by long imbibition sequences. Also, coefficients such as $\alpha_{m,0} > \alpha_{q,0}$ are responsible for the increase in porosity. The predicted porosity is in the vicinity of measurements. During the estimation, the superiority order of $\alpha_{m,0}$ and $\alpha_{q,0}$ is reversed to adjust the effect of imbibition. In Winter, temperatures are relatively lower than in Autumn. However, drying loads predominate over imbibition. An initial choice such that $\alpha_{q,0} > \alpha_{m,0}$ tends porosity sharply towards the lower bound value. After the optimization process, the optimal parameters are such that $\alpha^{\star}_{q,0} < \alpha^{\star}_{m,0}$.

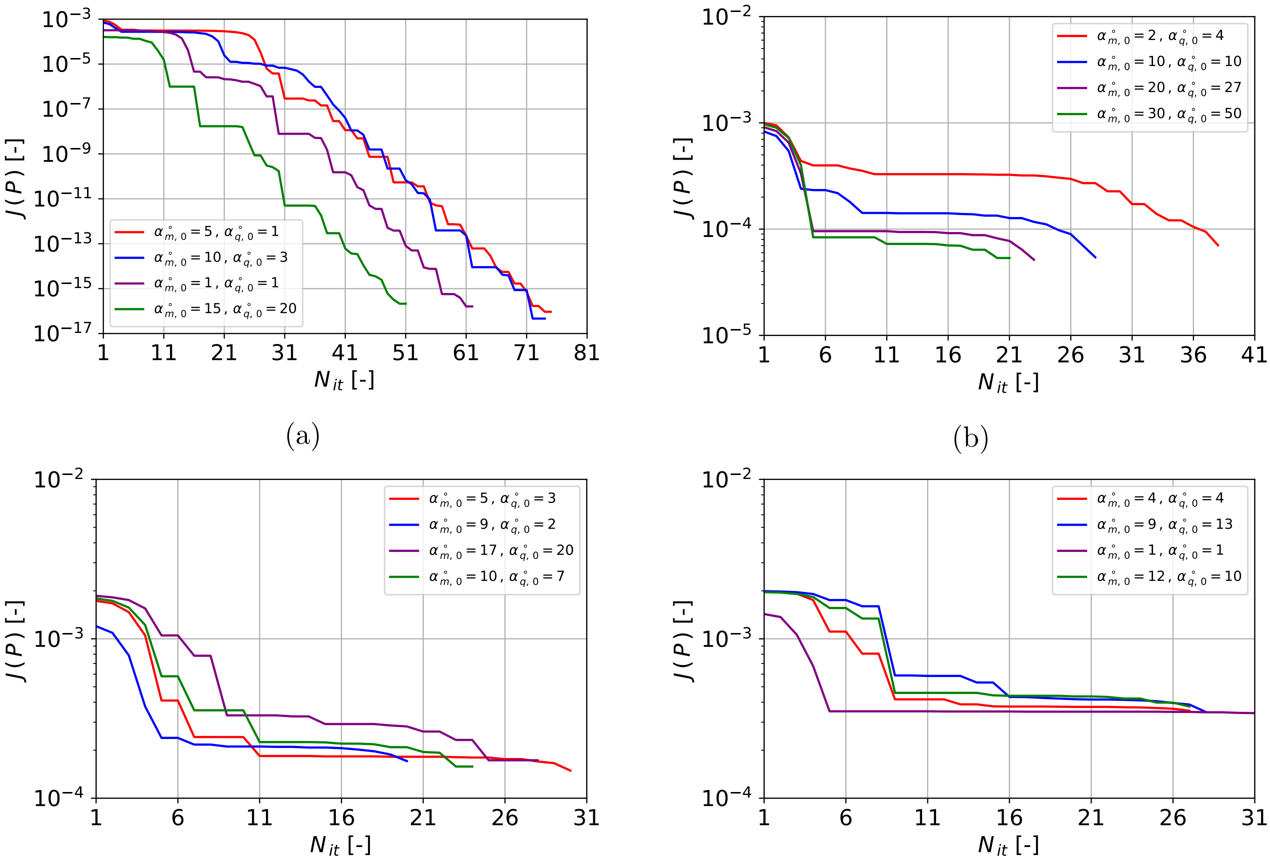

(a) (b)

(c) (d)

FIGURE 5.6 – Variation in the cost function depending on the iterations number under the moving load approach and considering the four a priori parameters. The results are given per season : Autumn (a), Winter (b), Spring (c) and Summer (d).

Further on, Spring is similar to Winter in terms of imbibition sequences. Differences lie on temperatures magnitude which is higher during Spring. This explains the prompt decrease in porosity, even though $\alpha^{\circ}_{m,0} > \alpha^{\circ}_{q,0}$. Considering the optimal parameters, porosity falls within the confidence interval of 2 out of 3 measurements. It is also seen that it varies even less than during Winter due to the small magnitude of the optimal parameters. Finally, imbibition sequences are the least during Summer. With $\boldsymbol{p}^{\circ} = (\,1\,,\,1\,)$, the decrease in porosity is obvious under intense drying loads. Still is the case when the optimal parameters are considered. In contrast to previous seasons, less agreement is shown between the model prediction and the experimental observations. The second measurement lies relatively off the assessed value. During the exposure to climate loads, the consideration of porosity evolution over time could improve the prediction of heat and moisture transfers at the material scale. In this regard, next section defines a heat and moisture transfer model that takes into account the evolution of porosity. Subsequently, the effect of porosity is highlighted through a case study at the building scale.

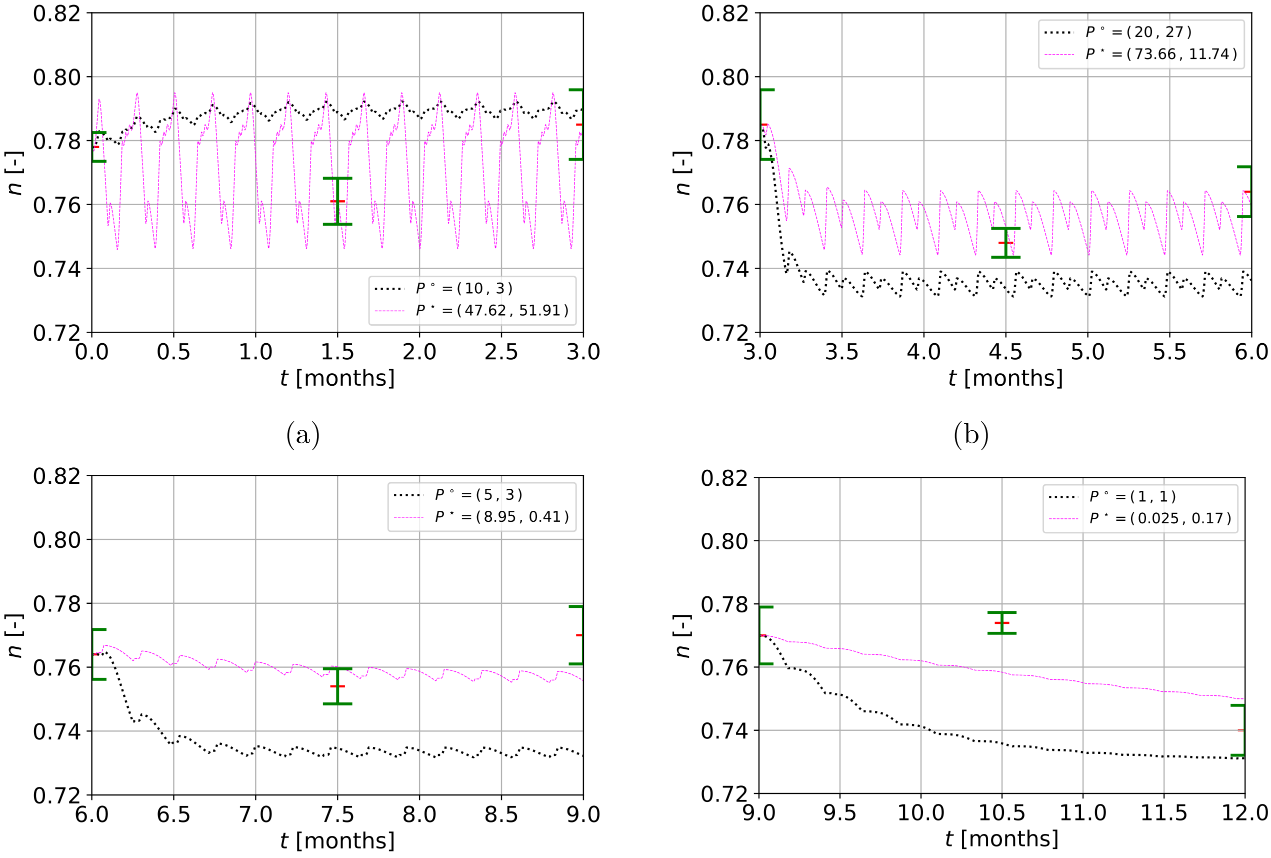

(a)

(b)

(c)

(d)

FIGURE 5.7 – Variation in porosity per season, under the moving load approach, considering an initial parameter guess and the corresponding optimal ones.

4.4 Result analysis

The model of porosity is addressed according to a cumulative and a moving load approaches. When regarding the first one, the assessment of porosity takes into account previous imbibition and drying stress sequences while considering the entire time period. In reality, the characteristic times of swelling and shrinkage of materials are shorter than an entire aging design duration. Thus, the moving load approach is more adapted to model the evolution of porosity. Note also that the competition between heat and imbibition stress is well highlighted under this approach. This is noticeable through the variation in porosity in Figure 5.7. For the next investigations in this work, the moving load approach is chosen. The following parameter values $(47.62, 51.91)$, $(73.66, 11.74)$, $(8.95, 0.41)$ and $(0.025, 0.17)$ are used during Autumn, Winter, Spring and Summer, respectively.

Moreover, the model of porosity is based on the mechanisms of swelling and shrinkage. Imbibition loads are the driving potential of swelling, leading to an increase in porosity. Also, the latter decreases under material shrinking. In the model, the decrease in porosity is driven by drying loads. The parameter estimation reveals that the model do not reproduce all experimental observations. There are some which are not reached : one considering the cumulative load approach and two in the other. As a common point, these measurements were performed during the periods of Spring and Summer. According to Figure 5.1, both season sequences feature few imbibition cycles against many drying ones. Within drying periods, temperatures exceed 60 °C. Hence, drying loads Q_q dominates over imbibition loads Q_m during the second half of the experiment. It is then seen that predicted porosity drops in general. In contrast to the prediction, a significant increase is necessary to reach all three experimental points. The model of porosity could be improved through an additional term. This one should induce a porosity increase under the effect of high temperatures, considering the magnitude of this climate variable at the building scale. Experimentally, this microscopic behavior is fully justified by the appearance of cracks during drying periods [236, 237]. The breakdown of bonds between the plant matter and the cement matrix is the main reason. In most cases, cracks contribute to additional microscopic voids. Finally, the involvement of an additional term in the model could lead to extra parameters.

5 Heat and moisture transfer under the variation of porosity

Note that the parameter of the phenomenological model have been determined, the latter is included in heat and mass transfer equations to assess the influence on the thermal and hydric behavior of porous materials.

5.1 Physical model

Heat and moisture transfer are based on the criteria of energy and mass conservation. Since water imbibition is used to define moisture loads in Sections 2.2 and 2.2.3, water content represents a suitable moisture driving potential to model the mass transfer. Based on the Philipp and De Vries model [238, 239], heat and moisture transfer equations are given as :

$$\frac{\partial \theta}{\partial t} = \frac{\partial}{\partial x} \left(D_{\theta} \frac{\partial \theta}{\partial x} + D_{T} \frac{\rho_{w}}{\rho} \frac{\partial T}{\partial x} \right) , \tag{5.18}$$

$$\rho C_{p} \frac{\partial T}{\partial t} = \frac{\partial}{\partial x} \left(\lambda \frac{\partial T}{\partial x} \right) + L_{v} \rho_{w} \frac{\partial}{\partial x} \left(D_{TV} \frac{\partial T}{\partial x} + D_{\theta V} \frac{\rho}{\rho_{w}} \frac{\partial \theta}{\partial x} \right) . \tag{5.19}$$

A first assumption states that the transfer is one-dimensional along the x-axis. $x\,[\mathsf{m}]$ defines the space coordinate and varies within $[\,0\,,\,L\,]$. Here, $L\,[\mathsf{m}]$ is the dimension along which the transfer occurs. The simulation interval is $[\,0\,,\,t_f\,]$ where $t_f\,[\mathsf{s}]$ is the final time. Water content is denoted $\theta\,[-]$ and refers to a mass ratio. Moreover, $D_{\theta}\,[\mathsf{m^2.s^{-1}}]$ and $D_T\,[\mathsf{m^2.s^{-1}.K^{-1}}]$ are the moisture transport coefficients due to moisture content and temperature gradients, respectively. $L_v\,[\mathsf{J.kg^{-1}}]$, $\rho_w\,[\mathsf{kg.m^{-3}}]$ and $\rho\,[\mathsf{kg.m^{-3}}]$ are the heat of vaporization, water density and material density, respectively. As for heat transfer properties, $\lambda\,[\mathsf{W.m^{-1}.K^{-1}}]$ represents thermal conductivity. Also, $D_{TV}\,[\mathsf{m^2.s^{-1}.K^{-1}}]$ and $D_{\theta V}\,[\mathsf{m^2.s^{-1}}]$ are the vapor phase transport coefficient due to a temperature and water content gradient, respectively. Heat and moisture transfer properties are expressed as :

$$D_{\theta} = \frac{k_m}{\rho C_m} , \quad D_T = \frac{k_T}{\rho_w} , \quad D_{TV} = \frac{h_l k_T}{L_v \rho_w} , \quad D_{\theta V} = \frac{\beta}{L_v \rho C_m} . \tag{5.20}$$

k_m [s] is the moisture permeability. It combines both water liquid conductivity and water vapor permeability. C_m [Pa^{-1}] represents the moisture storage capacity. k_T [kg.m^{-1}.s^{-1}.K^{-1}] and β [W.kg^{-1}.s^2] are also introduced, these are expressed according to [204]. Additionally, h_l [J.kg^{-1}] designates the water enthalpy. The initial condition on temperature and water content is given :

$$x \in [\,0\,,\,L\,]\,,\, t = 0 \qquad T = T_0\,(\,x\,)\,, \quad \theta = \theta_0\,(\,x\,)\,, \tag{5.21}$$

where T_0 [°C] and θ_0 [−] are space-dependent functions that describe its initial state. θ_0 [−] can be assessed using relative humidity and the material adsorption curve. A second assumption consists in considering the type of Dirichlet. Hence, temperature and water content at the outdoor material surface are given :

$$x = 0\,,\, t \in [\,0\,,\,t_f\,] \qquad T = T_{eq}\,(\,t\,)\,, \quad \theta = \theta_{ext}\,(\,t\,)\,. \tag{5.22}$$

Additionally to T_{eq} which has been defined, θ_{ext} [−] is the water content at the material external surface. In this respect, a third assumption considers that the effect of rain on porosity is equal to that of water imbibition. During rain periods, θ_{ext} is assumed equal to the material water content at the saturation state θ_{sat}. During periods without rain, θ_{ext} is assessed using outdoor air relative humidity and the material adsorption isotherm. At the inner side, the boundary condition is written as :

$$x = L\,,\, t \in [\,0\,,\,t_f\,] \qquad T = T_{int}\,(\,t\,)\,, \quad \theta = \theta_{int}\,(\,t\,)\,. \tag{5.23}$$

T_{int} [°C] refers to the indoor air temperature. θ_{int} [−] is indoor air water content and is assessed lying on internal air relative humidity and the adsorption curve.

5.2 Effect of porosity on transfer properties

This part outlines the consideration of porosity through the transfer properties. Apart from porosity, these properties depend also on temperature and water content. Firstly, D_θ is defined as follows :

$$D_\theta\,(\,\theta\,,\,T\,,\,n\,) = \frac{k_m\,(\,n\,)}{\rho\, C_m\,(\,\theta\,,\,T\,)}\,, \tag{5.24}$$

where :

$$C_m\,(\,\theta\,,\,T\,) = \frac{1}{P_{sat}\,(\,T\,)}\,\frac{\partial\theta}{\partial\phi}\,, \quad k_m\,(\,n\,) = \frac{\rho_w}{\mu_w}\,k_s\,(\,n\,)\,, \quad k_s\,(\,n\,) = \frac{a^2}{12}\,\frac{n^3}{(\,1-n\,)^2}\,. \tag{5.25}$$

P_{sat} [Pa] is the saturation pressure. According to the law of Antoine [240], this pressure is given as follows :

$$P_{sat}\,(\,T\,) = P^{\circ}_{sat}\,\left(\frac{T - T_c}{T_d}\right)^p\,, \qquad T \geq T_c\,. \tag{5.26}$$

$P^{\circ}_{sat} = 997.3\,\mathrm{Pa}$, $T_c = 159.5\,\mathrm{K}$, $T_d = 120.6\,\mathrm{K}$ and $p = 8.275$. C_m involves the derivative of water content according to relative humidity ϕ [−]. It can be assessed by means of the isotherm of adsorption. Furthermore, the dynamic viscosity of water vapor μ_w [kg.m^{-1}.s^{-1}] and the intrinsic permeability k_s [m^2] are used to assess k_m. In this respect, the coefficient k_s is a property that is specific to the material and depends only on the micro-structure. We express intrinsic permeability on the basis of [18]. Additionally, $a\,[-]$ is a correlation constant and equals $1.64 \times 10^{-7}\,\mathsf{m}$ for hemp concrete [235]. Moreover, D_T is expressed as follows :

$$D_T(\theta, T, n) = \frac{k_T(\theta, T, n)}{\rho_w}, \tag{5.27}$$

where :

$$k_T(\theta, T, n) = \frac{k_m(n)\,\phi(\theta)}{\rho}\,\frac{\partial P_{sat}}{\partial T}(T). \tag{5.28}$$

Relative humidity is evaluated at a water content value θ thanks to the inverse of the adsorption curve. According to [18], thermal conductivity is expressed in the following :

$$\lambda(\theta, n) = \theta\,\frac{\rho}{\rho_w}\,(\lambda_w - \lambda_{air}) + n\,\lambda_{air} + (1-n)\,\lambda_s, \tag{5.29}$$

where $\lambda_{air}\,[\mathsf{W.m^{-1}.K^{-1}}]$ and $\lambda_s\,[\mathsf{W.m^{-1}.K^{-1}}]$ are the thermal conductivity of air and the material solid matrix. Finally, D_{TV} and $D_{\theta V}$ are defined as :

$$D_{TV}(\theta, T, n) = \frac{h_l}{L_v\,\rho_w}\,k_T(\theta, T, n). \tag{5.30}$$

$$D_{\theta V}(\theta, T, n) = \frac{\beta(n)}{L_v\,\rho\,C_m(\theta, T)}, \tag{5.31}$$

where :

$$\beta(n) = (h_l + L_v)\,k_m(n). \tag{5.32}$$

5.3 Case study

The definition of this case study is inspired from a numerical investigation in [76]. A single-layer building wall is subjected to indoor and outdoor conditions (Figure 5.8). The wall is made from hemp concrete and is $L = 10\,\mathsf{cm}$ thick. Initially, temperature and water content inside the wall are assumed uniform and equal $T_0 = 20\,°\mathsf{C}$ and $\theta_0 = 0.046$, respectively.

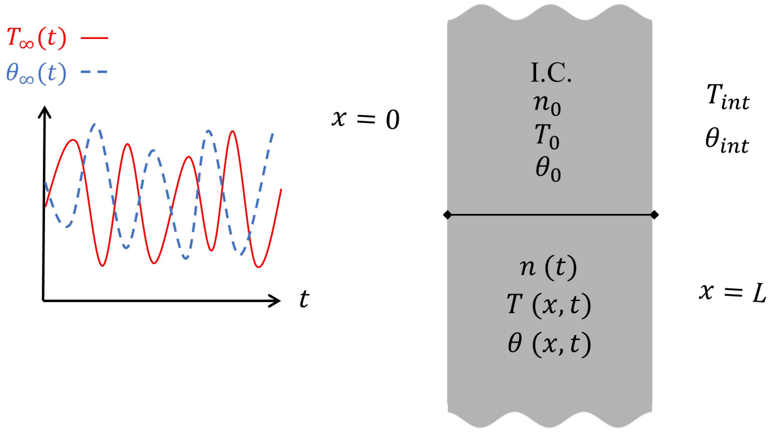

FIGURE 5.8 – Illustration of the case study.

This water content value is that corresponding to 50 % relative humidity. In this regard, adsorption curve data are provided from [72]. To assess vapor permeability and thermal conductivity, we consider the following values : $a = 1.64 \times 10^{-7}\,\mathsf{m}$ and $\lambda_s = 403.88\,\mathsf{W.m^{-1}.K^{-1}}$. The latter are given based on a previous study on hemp concrete [235]. Indoor and outdoor conditions depend on time according to Figure 5.9. At the external side, air temperature and relative humidity data originates from a meteorological station in the city of La Rochelle (France). This choice is related to the aging investigation which was conducted using the climate data of that city. outdoor air temperature can range from $-5\,^{\circ}\mathsf{C}$ and $32\,^{\circ}\mathsf{C}$. Whereas relative humidity varies between 0.48 and 1. In addition, normal short wave solar radiation and rainfall data from the same station are considered. To assess the equivalent temperature, it is assumed that the wall is exposed to these normal radiations (see Figure 5.10), i.e. $b = 1$. Also, we consider that $h_c = 17\,\mathsf{W.m^{-2}.K^{-1}}$. Accordingly, the variation in climate loads is highlighted in Figure 5.11. As for indoor conditions, assume that temperature is maintained at $19\,^{\circ}\mathsf{C}$ during heating periods. Then, it increases until $25\,^{\circ}\mathsf{C}$ over cooling ones. Also, indoor relative humidity varies between 0.45 and 0.6 as seen in Figure 5.9b.

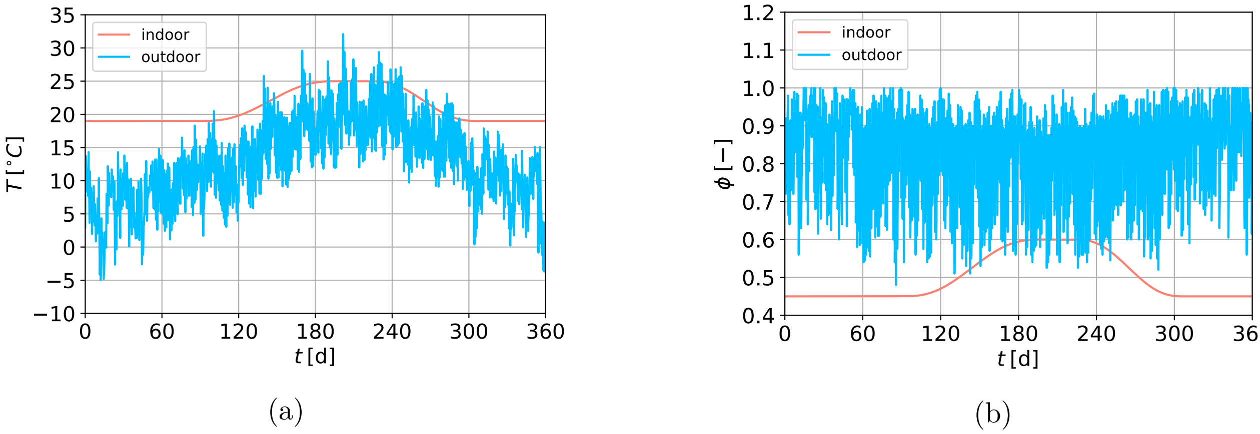

FIGURE 5.9 – Variation in air temperature (a) and relative humidity (b) at the indoor and outdoor environments.

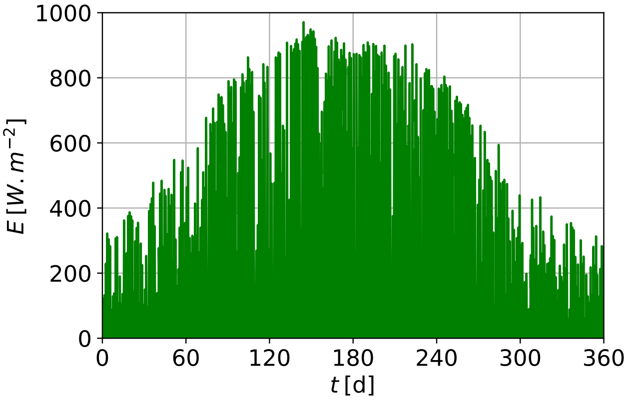

FIGURE 5.10 – Variation in short wave solar radiation.

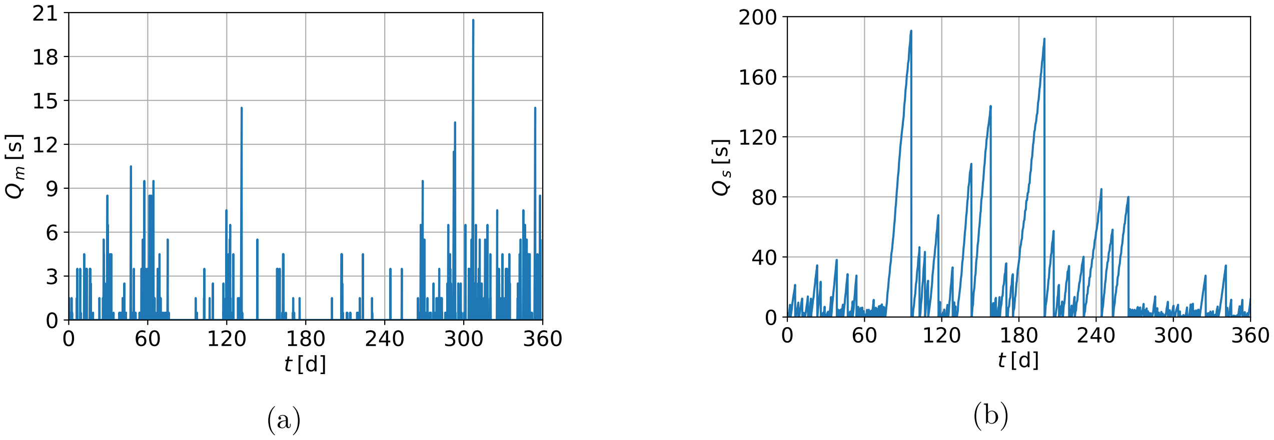

(a)

(b)

FIGURE 5.11 – Variation in imbibition (a) and drying (b) moving loads based on equivalent air temperature and rainfall data of La Rochelle, respectively.

Furthermore, the heat and mass transfer model is computed according to two different configurations. First one considers a constant porosity $n_0 = 0.778$, which reflects the initial state of the material. Note that this value represents the first porosity measurement in Figure 5.4b, which corresponds to a new material that was not submitted to aging. As for the second configuration, porosity varies due to outdoor stresses. At this level, the notations n_0 and $n(t)$ are used to distinguish the configurations with a constant porosity (without aging) and a variable one. To model imbibition and drying loads, the moving integral approach is taken into account. Remind that porosity is assessed using the parameters mentioned in Section 4.4. The purpose consists in confronting the results of both configurations. In particular, moisture j_m $[\mathsf{kg.m^{-2}.s^{-1}}]$ and heat fluxes j_q $[\mathsf{W.m^{-2}}]$ at the inner wall surface are calculated. The discrepancies on both quantities are assessed lying on the density of probability.

5.4 Results

PYTHON is used to compute the numerical model of heat and mass transfer. 5000 space nodes and a 1 hour time step were considered. Figure 5.12 illustrates the annual variation in moisture at the wall indoor surface for both porosity configurations. Moisture flux is always positive. It implies that the wall releases continuously vapor quantities which arises from the studied configuration. Throughout a year, clear discrepancies in moisture flux are observed. Higher fluxes are noticed for the constant porosity configuration. The maximum is around $11\,\mathsf{g.m^{-2}.h^{-1}}$ and is reached near the end of the year. Moreover, heat flux varies sharply in both configurations. This is due to the rapid kinetics of heat transfer in contrary to the moisture diffusion/transport. Thermal fluxes are negative during heating periods and turn positive over cooling period sequences. The lowest heat flux value is about $-25\,\mathsf{W.m^{-2}}$ which is noticed during the first month of Autumn (see Figure 5.13a). The highest is around $55\,\mathsf{W.m^{-2}}$ and is obtained during the first month of Spring (see Figure 5.13b). High positive values are justified with regard to the consideration of solar radiations. To ease the comparison, heat and moisture flux discrepancies are highlighted using the Kernel density function.

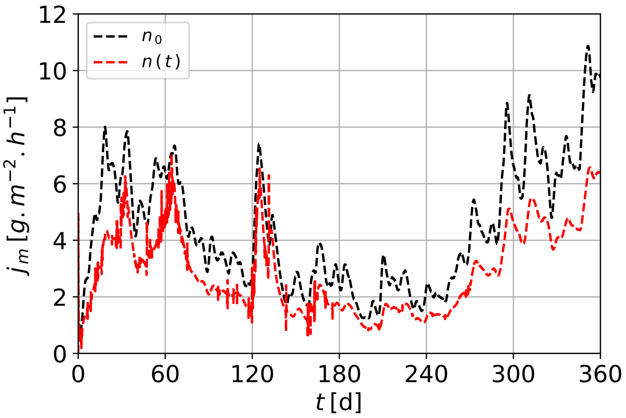

FIGURE 5.12 – Yearly variation in moisture flux at the wall indoor surface for the configurations : constant and variable porosity.

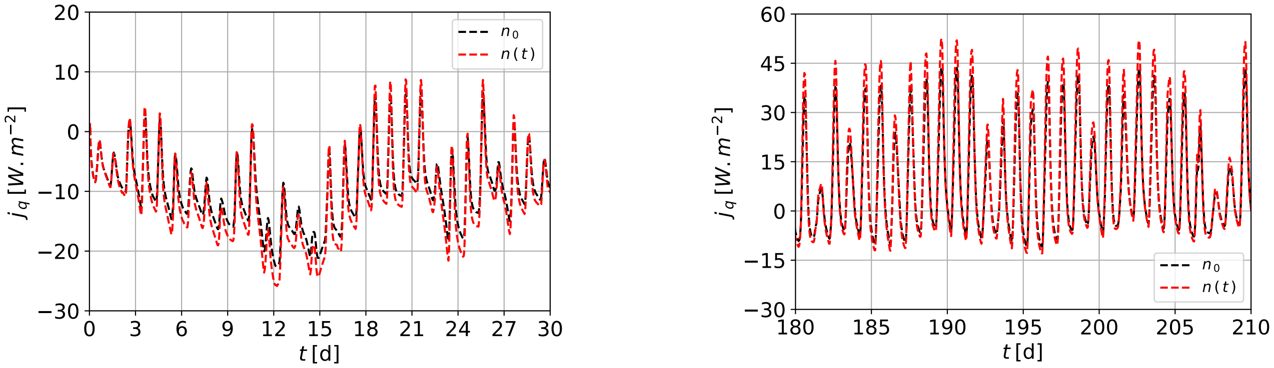

(a)

(b)

FIGURE 5.13 – Variation in heat flux at the wall indoor surface, during a month sequence of Autumn (a) and Spring (b), for the configurations : constant and variable porosity.

Figure 5.14a highlights the probability density related to the heat flux discrepancies. The quantity $|\,j_q(n_0)\,| - |\,j_q(n_t)\,|$ is generally negative and can reach $-9\,\mathsf{W.m^{-2}}$. However, this value is rarely reached. According to the density of probability, the mean discrepancy is around $-1\,\mathsf{W.m^{-2}}$. These results show that heat flux losses are higher when porosity is variable. Further on, the distribution of moisture flux discrepancies is shown in Figure 5.14b. Notice that $|\,j_m(n_0)\,| - |\,j_m(n_t)\,|$ is mainly positive. This result is confirmed by Figure 5.12, where the flux is greater in the constant porosity case. Discrepancies range from -0.5 to $4\,\mathsf{g.m^{-2}.h^{-1}}$. The most recorded values are located between 1 and $1.5\,\mathsf{g.m^{-2}.h^{-1}}$.

In the discussion part, the results of the case study are analyzed with respect to the microstructure evolution. Indeed, porosity is the only regarded parameter that yields discrepancies in the material behavior. Lastly, both configurations flux results are used to comment the wall energy and moisture contributions. Through these elements, the effect of aging can be outlined at the building scale.

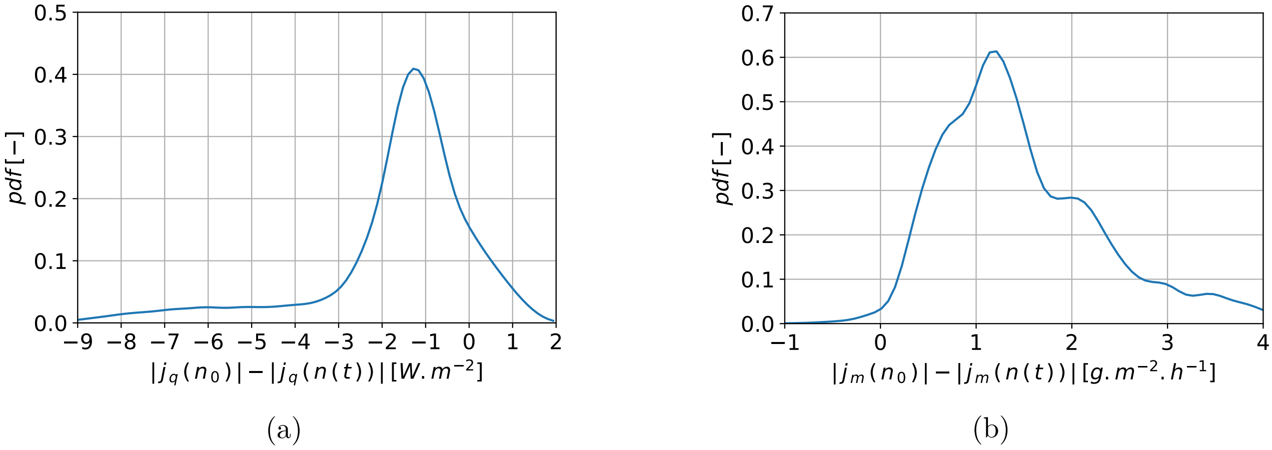

(a) (b)

FIGURE 5.14 – Probability density function on the discrepancies in heat (a) and moisture (b) flux between the configurations : a constant and a variable porosity.

5.5 Discussion and further remarks

5.5.1 Porosity and heat and moisture transfer

As highlighted in Section 5.4, hemp concrete behaves differently when porosity varies over time. The material porosity remains close to the final value particularly during Spring and Summer. This is confirmed by Figure 5.15. The porosity evolution is consistent with the presence of long drying cycles. In Autumn and Winter, porosity exceeds the final value during with the occurrence of imbibitions. Further on, discrepancies in moisture and heat fluxes can be justified. Initial porosity is set large. This value is hardly reached again due to the effect of frequent drying sequences. As a result, moisture flux is mainly larger in the constant porosity configuration whereas the opposite is noticed for heat flux. Finally, the effect of porosity on heat and moisture flux is similar to that on thermal conductivity and moisture permeability, respectively. Indeed, thermal conductivity decreases with porosity unlike moisture permeability according to Equations 5.29 and 5.25, respectively.

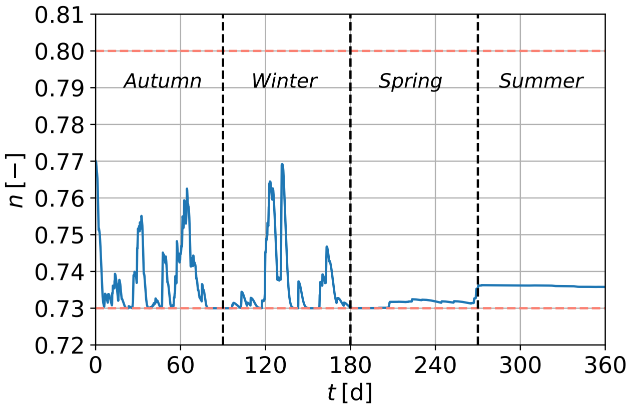

FIGURE 5.15 – Variation in hemp concrete porosity due to outdoor air temperature and rainfall fluxes.

5.5.2 Energy efficiency under aging

Inside a building, several entities contribute to the energy efficiency. These include external walls which are responsible for heating losses. They can affect moisture indoor moisture balance as well. This section highlights the contribution of hemp concrete wall to the energy balance, considering both porosity cases. For this, sensible and latent heat fluxes are assessed separately. Table 5.5 reports the annual sensible flux $E_{q,s}$ [MJ.m^{-2}], latent flux gains $E_{q,l}$ [MJ.m^{-2}] and the total loss in energy E_q [MJ.m^{-2}] in both cases. In this case, $E_q = E_{q,s} + E_{q,l}$. The losses in sensible heat are underestimated without taking the porosity variation into account, whereas the opposite is noticed for latent heat gains. By combining the sensible and latent flux, the assessment of total energy losses, considering a constant porosity, results in an underestimate of $-45.3\,\%$ with respect to the correct value. Indeed, they drop from 115.41 to 63.09 MJ.m^{-2}.

Table 5.5 – Annual heat loss and moisture gain through a 1 m^2 hemp concrete wall, considering a constant and a variable porosity.

	Constant porosity (no aging)	Variable porosity
$E_{q,s}$ [MJ.m^{-2}]	−146.54	−170.48
$E_{q,l}$ [MJ.m^{-2}]	83.45	55.07
E_q [MJ.m^{-2}]	−63.09	−115.41

In order to situate these results with regard to the literature, a numerical investigation [76], which is similar to the case study of this work, is reviewed. The difference lies in the experimental approach adopted by this investigation. In particular, two discrete configurations were considered to assess the impact of aging. The first represents the initial state of the material and the other its state at the end of the considered aging design. Porosity increased by measuring its value after aging, which induced a decrease in thermal conductivity. Results show that aging improves the energy efficiency of the wall through a reduction in thermal losses. This finding is completely opposite to the results of this work. This gap is due to a difference in the approaches of integrating aging into building simulations. Previous studies lie on experimental approaches to address aging while this one proposes a phenomenological model.

6 Conclusion

Throughout a building life time, the transfer properties of materials vary continuously. This is the phenomenon of aging, it is caused by ongoing changes in external climate conditions. Existing researches investigate the effects of this phenomenon using experimental approaches. It consists in measuring material properties at different stages during accelerated aging designs. These are mostly defined by drying and imbibition cycles. According to this approach, the effect of the studied phenomenon is described through discrete experimental observations. To our best knowledge, no continuous models were proposed to represent the phenomenon of aging at the macroscopic scale.

This work develops a methodology to address this issue. Within this framework, a phenomenological model of aging is developed. It assesses, at the macroscopic scale, the variation in porosity under the effect of drying and imbibition loads. The model expresses the climate loads by means of drying and imbibition indicators. In addition, these loads are defined according to a cumulative and a moving approach. Next, the model parameters are estimated using experimental observations related to the aging of hemp concrete. The results show that the moving load approach is better suited to modeling the phenomenon. Moreover, the model prediction, under this approach, is satisfactory with regard to most of experimental observations. Further on, aging is integrated into a model of heat and mass transfer within porous media. This step aims at assessing the effect of aging on heat and moisture behavior of materials. Within a case study, the contribution of a single-layer wall of hemp concrete to the indoor energy balance is assessed. Two configurations, without and with aging, are considered. Heat and moisture fluxes at the indoor surface are obtained in both configurations. When aging is taken into account, sensible heat losses are larger whereas latent heat gains are smaller. According to the simulations, neglecting this phenomenon results in an underestimate up to 30 % of heat loss through the wall. This shows that building energy efficiency is sensitive to the aging of materials. Finally, the developed methodology can be extended to other materials to enrich current aging data. Also, the development of new experimental aging designs could enhance the reliability of the model of porosity.

Conclusion générale

Dans le cadre de l'enjeu énergétique actuel, l'effet du vieillissement sur les matériaux de construction est fréquemment étudié. Particulièrement, le comportement des matériaux biosourcés a freiné leur application dans le secteur du bâtiment. En effet, le gonflement et le rétrécissement de la matière végétale, dus aux conditions climatiques extérieures, favorise l'évolution de la microstructure. Ces sollicitations se résument aux variations de température d'air, des radiations solaires et des flux pluviaux. Au cours du temps, la succession de ces sollicitations se traduit par des charges d'imbibition et de séchage. Ces dernières affectent les propriétés intrinsèques d'un matériau biosourcé. La littérature fait état d'approches expérimentales pour étudier ce phénomène. Il s'agit d'exposer des matériaux à des cycles thermiques et hydriques accélérés. Ceux-ci reflètent des sollicitations extrêmes qui ne représentent que des configurations climatiques défavorables. Le vieillissement est un processus lent contrairement à l'aspect accéléré des essais proposés. A ce propos, les études existantes n'établissent aucun lien entre les essais réalisés au laboratoire et un cas d'étude réel. Finalement, les mesures réalisées durant ces essais ne sont pas exploitées pour la prédiction du comportement du matériau en fonction du temps. Ce travail propose une méthodologie afin de mieux aborder, modéliser et évaluer les effets du vieillissement thermique et hydrique. Pour répondre aux problématiques discutées, le manuscrit de thèse est scindé en cinq chapitres complémentaires.

Le premier chapitre constitue un état bibliographique. Dans un premier temps, il aborde des généralités concernant le milieu poreux. Avec la présence des réseaux poreux ouverts, les phénomènes de transfert sont entraînés au sein de ces milieux. Ces phénomènes dépendent de la microstructure. A ce propos, le chapitre liste et définit les propriétés intrinsèques d'un milieu poreux à savoir la porosité, la surface spécifique, la connectivité, la tortuosité, la perméabilité intrinsèque. La connaissance de ces dernières aide à l'évaluation des caractéristiques thermiques et hydriques du milieu. A cet effet, la conductivité thermique, la chaleur spécifique, la perméabilité à la vapeur d'eau et les isothermes d'adsorption et de désorption sont présentés. Cette partie cite également les méthodes de mesure de ces propriétés, les normes auxquelles ces essais sont conformes, et les dispositifs courants de mesure. La troisième partie est consacrée aux matériaux biosourcés de construction et leurs performances en cas d'applications dans le bâtiment. En effet, le béton de chanvre est un milieu poreux et représente notre choix d'application dans le cadre de cette thèse. Le comportement hygroscopique et les performances énergétiques d'un matériau biosourcé sont investigués à travers des exemples d'études. Outre ses avantages dans la construction, la microstructure d'un matériau biosourcé évolue sous l'effet des charges thermiques et hydriques extérieurs. Ce phénomène, dit vieillissement, engendre la variation des propriétés de transfert du matériau. A ce propos, la quatrième partie définit ce phénomène et distingue ses différents types. Afin d'évaluer ses effets, des études ont développé des essais en laboratoire pour représenter chaque type. Les résultats sont présentés sur la base des vieillissements les plus investigués dans la littérature. En particulier, l'impact du vieillissement thermique et hydrique sur les matériaux biosourcés est mis en évidence. Les résultats montrent que le vieillissement modifie les propriétés thermiques, hydriques, mécaniques et chimiques des matériaux biosourcés. Toutefois, la définition de tels essais repose sur la considération de configurations climatiques extrêmes. De plus, ces travaux sont marqués par l'absence d'une méthodologie qui permet d'établir une équivalence entre l'essai réalisé et une configuration réelle où le vieillissement est lent et naturel. Dans ce contexte, la dernière partie s'adresse aux lois de similitude. Ces dernières représentent le moyen pour définir une équivalence entre des configurations aux échelles caractéristiques différentes. Dans le cadre de la thèse, ils sont appliqués pour générer un essai accéléré et représentatif d'une configuration réelle de vieillissement. Nous distinguons dans cette partie les types de similitudes ainsi que quelques domaines d'application, notamment les transferts de chaleur et de masse. Pour quelques domaines, ces lois sont utilisées pour parvenir à des modèles plus simples à étudier en regard d'une configuration réelle. D'autres les emploient pour comparer des configurations équivalentes. Cependant, aucun des deux ne vérifient la fiabilité de leur application expérimentale. Ceci consiste l'objectif du deuxième et du troisième chapitre.

Le deuxième chapitre est dédié à vérifier la robustesse de l'application expérimentale des lois de similitude sur le phénomène de transfert de chaleur au sein des matériaux poreux. Pour la définition du modèle physique, quelques hypothèses sont considérées dont une conduction thermique unidirectionnelle et des conditions aux limites du type Dirichlet. Ensuite, ce modèle est formulé dans le domaine adimensionnel. Pour cela, chaque variable du problème est attribué à une grandeur caractéristique, notamment les dimensions spatiales, le temps de l'expérience et les propriétés du matériau. A l'issue de cette formulation, le nouveau modèle fait apparaître le nombre sans dimension Fourier. Ce paramètre est adimensionnel et traduit l'invariant du phénomène étudié. En s'appuyant sur ce nombre, deux configurations expérimentales, une dite de référence et l'autre réduite, sont définies en considérant les mêmes conditions aux limites. L'égalité des nombres de Fourier des deux configurations permet de relier leurs échelles spatiales et temporelles. Pour cela, le même matériau est utilisé tout en supposant que les deux échantillons représentent les mêmes propriétés. Pour la comparaison, deux positions de mesure équivalentes sont définies. A l'issue des deux expériences, les écarts de température entre les deux positions sont obtenues pour des instants temporels équivalents. Ensuite, la fiabilité de l'application de ces lois est vérifiée au regard des incertitudes totales de mesures. Dans ce cadre, l'approche déterministe est adoptée pour investiguer la propagation de huit incertitudes sur les mesures de température. Certaines incertitudes sont dues aux défauts des capteurs alors que d'autres sont liées aux hypothèses du modèle physique. En particulier, le transfert unidirectionnel, les conditions aux limites considérées et la négligence des transferts de masse d'eau en font partie. Les résultats montrent que l'incertitude globale liée aux deux expériences est supérieure aux écarts mesurés. Ces constats concluent sur la validité de l'application expérimentale de ces lois sur les transferts de chaleur.

Le troisième chapitre généralise les propos du précédent en s'intéressant aux transferts de chaleur et de masse au sein des milieux poreux. En effet, la présence d'eau dans un matériau biosourcé entraîne une modification importante de sa microstructure. Le modèle physique étudié fait intervenir des équations fortement couplées aux dérivées partielles. La pression de vapeur constitue le moteur des transferts de masse. Pour la modélisation des conditions aux limites en température et en pression de vapeur, les transferts sont supposés unidirectionnels et le type Dirichlet est considéré. Similairement au chapitre précédent, nous définissons pour chaque variable du modèle une grandeur caractéristique. S'ensuit la formulation adimensionnelle des équations du modèle et l'obtention des invariants. Ces derniers incluent deux nombres de Fourier, le premier lié au transfert de chaleur et le deuxième au transfert de masse. Plus loin, nous définissons deux maquettes expérimentales équivalentes en s'inspirant de la même démarche utilisée dans le chapitre précédent. Les champs de température et d'humidité relative sont comparés en définissant deux couples de positions équivalentes. Cette fois-ci, le calcul des incertitudes considère cinq sources d'erreur. Celles-ci sont liées à la calibration du capteur, sa position, son temps de réponse, l'aspect aléatoire de l'expérience ainsi que l'hypothèse sur les conditions aux limites. Moyennant cette investigation, les intervalles de confiance associés aux mesures de température et d'humidité relative sont obtenus. Ainsi, nous montrons que les écarts observés restent inférieurs aux incertitudes combinées des deux expériences. Ce résultat permet de généraliser l'utilisation des lois de similitudes dans les problèmes de transfert de chaleur et de masse. En l'occurrence, ces lois sont appliquées pour proposer un essai de vieillissement naturel accéléré.

L'effet du vieillissement sur les propriétés des matériaux biosourcés constitue l'objectif du quatrième chapitre. Dans un premier lieu, nous proposons une méthodologie pour le développement d'un protocole expérimental annuel. Ce protocole permet de représenter la configuration d'un vieillissement naturel. Son élaboration nécessite des données météorologiques de température, de précipitations et de radiations solaires incidentes normales. A l'issue de la démarche, un indicateur d'imbibition et une température équivalente sont obtenues. Le premier paramètre indique la présence ou l'absence de pluie. Quant à la température équivalente, elle tient compte de l'effet combiné de la température d'air et des radiations solaires. Ainsi, les deux grandeurs représentent les variables du protocole du vieillissement et varient suivant quatre semaines type pour chaque saison. Ainsi, le protocole est achevé en itérant treize fois chaque semaine type, tout en respectant l'ordre des saisons. La réalisation de ce protocole nécessite un an. Cette durée représente un vrai obstacle expérimental. A cette occasion, les lois de similitude aident à lever ce verrous en générant une maquette expérimentale réduite. Ainsi, le protocole expérimental annuel est équivalent à une maquette réduite réalisable sur quelques dizaines de jours. A différents moments de l'essai, l'effet du vieillissement est évalué en mesurant des propriétés du béton de chanvre. La porosité, la conductivité thermique, la perméabilité à la vapeur et le pH sont considérés. Les observations expérimentales montrent que la variation des trois premières propriétés est notable. Quant au degré pH, il diminue légèrement tout en restant supérieur à la limite du risque de développement de moisissures. Ces résultats montrent que le vieillissement entraîne la modification du caractère intrinsèque du matériau étudié. En parallèle, les propriétés de transfert subissent des variations notables. De plus, il est conclu sur l'absence du risque de croissance fongique sous un vieillissement d'une année. Par ailleurs, les données expérimentales ont contribué à l'obtention des lois de variation de la conductivité thermique et de la perméabilité à la vapeur en fonction de la porosité. Ces lois sont comparés à des corrélations empiriques issues de la littérature. Finalement, les mesures de porosité, étant une propriété intrinsèque, sont exploitées dans le dernier chapitre.

Ce dernier chapitre porte sur le développement d'un modèle phénoménologique du vieillissement des matériaux. Le modèle est défini en s'inspirant de la dynamique de croissance des populations. Cette modélisation consiste à calculer la variation de la porosité en fonction des charges de séchage et d'imbibition. Ces dernières sont définies respectivement à partir de la température équivalente et l'indicateur d'imbibition. Ces deux grandeurs représentent les variables du protocole de vieillissement obtenu dans le chapitre précédent. D'après le modèle, l'évolution de la porosité vis-à-vis des charges est consistante avec des observations expérimentales dans la littérature. En effet, le gonflement du matériau pendant l'imbibition se traduit par une augmentation de porosité. L'inverse est observé pendant le rétrécissement dû au séchage. Plus loin, deux approches différentes sont adoptés pour le calcul des charges climatiques. D'après l'approche glissante, une variation de porosité est due aux sollicitations de séchage et d'imbibition actuelles. Pour l'approche des charges cumulées, les sollicitations précédentes sont également considérés pour le calcul de porosité. Ensuite, les paramètres inconnus du modèle sont estimés en s'appuyant sur les mesures de porosité obtenues durant la réalisation de la maquette réduite du vieillissement. La prédiction du modèle montre que l'approche glissante est mieux adaptée pour définir les charges climatiques. Sous cette approche, la compétitivité des charges climatiques est mise mieux en évidence. Subséquemment, le modèle de porosité est intégré dans les transferts de chaleur et de masse au sein des milieux poreux. Cette démarche permet de tenir compte de l'impact du vieillissement sur le comportement thermique et hydrique des parois du bâtiment. En guise d'application, un cas d'étude d'une paroi de béton de chanvre est défini sur une année. Deux configurations sont comparées où la première suppose que la porosité est constante (pas de vieillissement) alors que la deuxième tient compte de la variation de porosité. Les flux de vapeur d'eau ainsi que ceux thermiques sensibles et latents sont calculés pour chaque configuration. Des écarts notables sont obtenus entre les deux configurations. D'après ces résultats, la non prise en compte du vieillissement induit une sous-estimation significative des déperditions thermiques à travers la paroi.

Perspectives

Cette thèse répond à la problématique liée à l'étude du vieillissement naturel des matériaux de construction. Elle propose une méthodologie pour le développement d'un essai de vieillissement naturel accéléré. Ce dernier est obtenu en utilisant des données climatiques réalistes et les lois de similitude. En considérant les résultats obtenus au cours de cette thèse, quelques perspectives de recherche émergent pour des travaux futurs.

Hypothèses pour l'application des lois de similitudes

Le deuxième et le troisième chapitre proposent d'investiguer la fiabilité de l'application expérimentale des lois de similitude pour les phénomènes de transfert. L'étude de ces modèles physiques est basée sur un certain nombre d'hypothèses. Ces dernières visent à simplifier les configurations expérimentales. Par exemple, le transfert unidirectionnel est considéré afin de mener la comparaison des configurations équivalentes suivant une seule direction. Sur le plan expérimental, cette hypothèse est approximée en utilisant des couches d'isolants afin de limiter les flux dans les autres directions. D'après l'estimation de ces flux, le transfert n'est pas entièrement unidirectionnel. Pour cela, Le flux suivant la direction privilégiée et ceux suivant les directions isolées sont comparés. Les écarts mesurés, lors de la vérification expérimentale des similitudes, sont dû en partie au manque de robustesse de cette hypothèse. Cette source d'incertitudes peut être minimisée en optimisant les configurations étudiées. L'hypothèse du transfert unidirectionnel serait mieux vérifiée en renforçant l'isolation extérieure. Une autre démarche serait de définir la taille du matériau tel que la dimension du transfert soit plus petite par rapport aux autres. Ces deux alternatives peuvent contribuer à la réduction de cette source d'incertitudes.

Par ailleurs, les conditions aux limites associées aux modèles physiques sont supposées de type Dirichlet. D'après cette hypothèse, l'air ambiant et la surface du matériau sont supposés avoir instantanément la même température et humidité relative. En réalité, il existe des écarts qui sont dus au phénomène de convection d'air. Il se traduit par une résistance thermique et hydrique entre l'air et la surface du matériau. Ces écarts sont mesurés en développant un banc expérimental dédié à la vérification de cette hypothèse. Ces résultats montrent que les conditions aux limites liées aux deux configurations comparées ne sont pas parfaitement identiques. Ainsi, ces différences génèrent une source d'incertitude supplémentaire. Ce genre d'incertitudes peut être négligé en optant pour les conditions aux limites de type Robin. Les échanges thermiques et hydriques à l'interface air-matériau sont mieux représentées à travers ce type de conditions. Dans ce cas, la formulation adimensionnelle aurait donné le nombre sans dimension Biot. A travers ce dernier, une condition supplémentaire est obtenue en définissant les lois de similitude. Il s'agit d'une équivalence liant les longueurs caractéristiques et les coefficients d'échange convectif des deux configurations. Ainsi, une similitude est assurée en définissant ces coefficients via le contrôle des conditions d'écoulement d'air, notamment sa vitesse. Dans ce contexte, un banc expérimental permettant de contrôler cette grandeur pourrait contribuer à mieux vérifier l'application expérimentale des lois de similitude.

Plus loin, une autre source d'incertitudes est liée à la nature du matériau utilisé. Le béton de chanvre est un matériau composite à forte hétérogénéité. Il en résulte une variabilité spatiale importante de ses propriétés. Ainsi, les échantillons sélectionnés pour l'investigation expérimentale des similitudes traduisent des incertitudes sur les propriétés du matériau utilisé. Il s'ensuit que les lois de variation des propriétés du transfert ne sont pas parfaitement identique malgré le choix du même matériau. Dans le deuxième et le troisième chapitre, le non respect de cette hypothèse se traduit par l'intégration de l'incertitude aléatoire dans le calcul des intervalles de confiance. L'incertitude aléatoire pourrait être minimisée en faisant recours à des matériaux homogènes. En effet, la variabilité spatiale des propriétés de ces matériaux est négligeable pour des volumes supérieurs au VER. Également, les imprimantes 3D peuvent être utilisées pour contrôler les microstructures des échantillons. Grâce à cette démarche, la vérification de l'application des similitudes est menée sur la base d'échantillons avec des microstructures identiques. C'est une contribution qui pourrait renforcer le propos de ces lois.

Protocole expérimental du vieillissement

D'après le quatrième chapitre, une méthodologie est développée pour la proposition d'un protocole expérimental de vieillissement. Dans un premier temps, des données de flux pluviaux sont utilisés pour définir l'indicateur d'imbibition. Ce dernier indique les séquences d'imbibition totale du matériau. En réalité, les parois d'un bâtiment sont exposées du côté extérieur à des débits d'eau liquide plus ou moins uniformes. Ces débits varient en fonction de plusieurs paramètres, dont la vitesse du vent, son orientation ainsi que celle de la paroi. Ainsi, la méthodologie développée pourrait être améliorée en considérant les débits d'eau pluviaux au lieu des imbibitions. Il serait intéressant de tenir compte des paramètres introduits pour calculer ces débits.

Dans un deuxième temps, la température d'air et les radiations solaires sont considérés pour calculer la température équivalente. Cependant, les données de radiations sont issues d'une station météo en se basant sur une surface d'incidence horizontale. En réalité, des paramètres peuvent influencer l'intensité des radiations, notamment la situation géographique du bâtiment, la position verticale des parois et leurs orientations. Idéalement, il serait préférable de monter des capteurs de mesure d'ensoleillements sur la surface de la paroi.

Plus loin, le protocole expérimental est donné suivant quatre semaines types. Chacune est obtenue en moyennant les mesures sur les treize semaines de la saison correspondante. Cette procédure ne tient pas compte de la distribution des mesures au cours de la saison. Dans ce cadre, des méthodes autres que la moyenne arithmétique pourraient être développées afin d'améliorer la méthodologie. Pour résumer, l'utilisation d'un dispositif expérimental qui génère des variations de température, et surtout des jets d'eau à débit contrôlé, aiderait à automatiser l'essai du vieillissement.

Modélisation phénoménologique du vieillissement

Au final, cette thèse est achevée par la proposition d'un modèle phénoménologique qui décrit le vieillissement des matériaux. Selon le modèle, le vieillissement est représenté par la variation de la porosité en fonction du temps. Le développement de ce modèle s'inspire de la dynamique de croissance des populations. Il est important de souligner que les deux paramètres du modèle dépendent du matériau et de la formulation considérés. Dans cette perspective, la base des données du vieillissement pourrait s'enrichir en estimant ces paramètres pour d'autres matériaux. Ceci requiert le recours à des essais accélérés avec des cycles de séchage et d'imbibition afin d'obtenir des mesures de porosité. Cette démarche contribuerait, de plus, à fiabiliser le modèle développé. En effet, ce dernier peut être confronté à l'expérience en développant d'autres bancs expérimentaux. En outre, la considération du phénomène de fissuration sous hautes températures peut améliorer la prédiction. Ceci est justifié vis-à-vis de la sous-estimation de porosité par le modèle durant les saisons de printemps et d'été (voir Chapitre 5). Plus loin, l'effet du vieillissement des matériaux sur l'efficacité énergétique des enveloppes peut être calculé. Ceci est possible via l'intégration du modèle de porosité dans les codes de calcul thermique dynamique. Le modèle phénoménologique développé décrit le vieillissement d'un point de vue macroscopique. Il considère que la porosité est indépendante de l'espace. En réalité, la plupart des matériaux de construction sont hétérogènes, induisant une variabilité spatiale des propriétés intrinsèques. Pour cette raison, la considération des effets microscopiques aiderait à mieux prédire l'effet du vieillissement sur le comportement hygrothermique de ces matériaux.

Appendices

Appendix A

(Chapitre 3)

1 Sensitivity study in regard to surface temperature and relative humidity

This section focuses on the sensitivity study [241, 242, 243] of heat and mass transfer model to both surface temperature and relative humidity. This is necessary in order to evaluate the partial derivatives defined in Eqs. (3.41). Following this, we perform a derivation of Eqs. (3.1), (3.2) (3.13), (3.14) and (3.15) according to surface temperature and vapor pressure. The derivation of Eq. (3.2) induces the following :

$$C_p \rho_s \frac{\partial \theta_1}{\partial t} = \frac{\partial}{\partial x}\left(\lambda_{ef}\frac{\partial \theta_1}{\partial x} + \frac{\partial \lambda_{ef}}{\partial T_s}\frac{\partial T}{\partial x} + \alpha \frac{\partial \Psi_2}{\partial x} + \frac{\partial \alpha}{\partial T_s}\frac{\partial P_v}{\partial x}\right). \tag{A.1}$$

$$C_p \rho_s \frac{\partial \Psi_1}{\partial t} = \frac{\partial}{\partial x}\left(\lambda_{ef}\frac{\partial \Psi_1}{\partial x} + \frac{\partial \lambda_{ef}}{\partial P_{vs}}\frac{\partial T}{\partial x} + \alpha \frac{\partial \theta_2}{\partial x} + \frac{\partial \alpha}{\partial P_{vs}}\frac{\partial P_v}{\partial x}\right). \tag{A.2}$$

Where θ_1, θ_2, Ψ_1 and Ψ_2 are variables depending on space and time. Ψ_1 is defined as follows :

$$\Psi_1(x, t) = \frac{\partial T}{\partial P_{vs}}. \tag{A.3}$$

They define the temperature sensitivity variables within the material regarding surface temperature and vapor pressure respectively. Additionally, θ_2 and Ψ_2 are also sensitivity variables in this case. They represent the derivatives of the vapour pressure regarding the surface vapor pressure and temperature respectively. The are given by Eq. (A.4) :

$$\theta_2(x, t) = \frac{\partial P_v}{\partial P_{vs}}, \qquad \Psi_2(x, t) = \frac{\partial P_v}{\partial T_s}. \tag{A.4}$$

This time, we derive the second equation of the physical model according to the vapor pressure and surface temperature respectively. This operation allows us to obtain the Equations (A.5) and (A.6) :

$$\begin{gathered} C_m \rho_s \frac{\partial \theta_2}{\partial t} + \rho_s \frac{\partial C_m}{\partial P_{vs}}\frac{\partial P_v}{\partial t} = \frac{\partial}{\partial x}\left(k_m \frac{\partial \theta_2}{\partial x} + \frac{\partial k_m}{\partial P_{vs}}\frac{\partial P_v}{\partial x} + k_T \frac{\partial \Psi_1}{\partial x} + \frac{\partial k_T}{\partial P_{vs}}\frac{\partial T}{\partial x}\right) + \\ \beta \frac{\partial \Psi_1}{\partial t} + \frac{\partial \beta}{\partial P_{vs}}\frac{\partial T}{\partial t}. \end{gathered} \tag{A.5}$$

$$\begin{aligned} C_m \rho_s \frac{\partial \Psi_2}{\partial t} + \rho_s \frac{\partial C_m}{\partial T_s}\frac{\partial P_v}{\partial t} = \frac{\partial}{\partial x}\Big(k_m \frac{\partial \Psi_2}{\partial x} + \frac{\partial k_m}{\partial T_s}\frac{\partial P_v}{\partial x} + k_T \frac{\partial \theta_1}{\partial x} + \frac{\partial k_T}{\partial T_s}\frac{\partial T}{\partial x}\Big) + \\ \beta \frac{\partial \theta_1}{\partial t} + \frac{\partial \beta}{\partial T_s}\,. \end{aligned} \tag{A.6}$$

Equations (A.1), (A.2), (A.5) and (A.6) include terms related to the influence of a surface temperature or vapor pressure variation on material thermal and moisture properties. These terms are non-zero because model parameters depend on both material thermal and hydric states. Starting with moisture storage capacity C_m , its derivatives according to surface temperature and vapor pressure are given by Eqs. (A.7) and (A.8) :

$$\frac{\partial C_m}{\partial T_s} = -\frac{1}{P_{sat}^2}\frac{\partial P_{sat}}{\partial T}\,\theta_1\Big(\frac{\partial \omega}{\partial \phi} + \phi\,\frac{\partial^2 \omega}{\partial \phi^2}\Big) + \frac{\Psi_2}{P_{sat}^2}\frac{\partial^2 \omega}{\partial \phi^2}\,, \tag{A.7}$$

$$\frac{\partial C_m}{\partial P_{vs}} = -\frac{1}{P_{sat}^2}\frac{\partial P_{sat}}{\partial T}\,\Psi_1\Big(\frac{\partial \omega}{\partial \phi} + \phi\,\frac{\partial^2 \omega}{\partial \phi^2}\Big) + \frac{\theta_2}{P_{sat}^2}\frac{\partial^2 \omega}{\partial \phi^2}\,. \tag{A.8}$$

Secondly, the derivative of the total mass permeability k_m according to T_s and P_{vs} are given as follows :

$$\frac{\partial k_m}{\partial T_s} = \frac{\partial k_m}{\partial \phi}\frac{\partial \phi}{\partial T}\,\theta_1, \qquad \frac{\partial k_m}{\partial P_{vs}} = \frac{1}{P_{sat}}\frac{\partial k_m}{\partial \phi}\,\theta_2\,. \tag{A.9}$$

The derivative of the total mass permeability according to relative humidity in Eq. (A.9) is estimated based on experimental data. Precisely, this data describe the evolution of k_m according to ϕ inside the material. Subsequently, the coefficient k_T depend also on temperature and vapor pressure as demonstrated in Eq. (3.8). Thus, its derivatives are obtained according to Eqs. (A.10) and (A.11) :

$$\begin{aligned} \frac{\partial k_T}{\partial T_s} = \frac{R\rho_l}{M}\Big[\frac{k_l R\rho_l}{M P_v}\,\theta_1\Big(T\frac{\partial \ln\phi}{\partial T} + \ln\phi\Big) + k_l\Big(\theta_1\frac{\partial \ln\phi}{\partial T} + T\frac{\partial}{\partial T}\Big(\frac{\Psi_2}{P_v} - \frac{\theta_1}{P_{sat}}\frac{\partial P_{sat}}{\partial T}\Big) + \\ \frac{\Psi_2}{P_v} - \frac{\theta_1}{P_{sat}}\frac{\partial P_{sat}}{\partial T}\Big)\Big]\,. \end{aligned} \tag{A.10}$$

$$\begin{aligned} \frac{\partial k_T}{\partial P_{vs}} = \frac{R\rho_l}{M}\Big[\frac{k_l R\rho_l}{M P_v}\,\Psi_1\Big(T\frac{\partial \ln\phi}{\partial T} + \ln\phi\Big) + k_l\Big(\Psi_1\frac{\partial \ln\phi}{\partial T} + T\frac{\partial}{\partial T}\Big(\frac{\theta_2}{P_v} - \frac{\Psi_1}{P_{sat}}\frac{\partial P_{sat}}{\partial T}\Big) + \\ \frac{\theta_2}{P_v} - \frac{\Psi_1}{P_{sat}}\frac{\partial P_{sat}}{\partial T}\Big)\Big]\,. \end{aligned} \tag{A.11}$$

Moreover, the coefficient β is the last one in mass conservation Eq. (3.1) that varies according to temperature and vapor pressure. Its derivatives regarding these two variables are expressed following Eqs. (A.12) and (A.13) :

$$\frac{\partial \beta}{\partial T_s} = \Big(\frac{\rho_s C_m}{P_{sat}}\frac{\partial P_{sat}}{\partial T} + \frac{\rho_s P_v}{P_{sat}^3}\frac{\partial^2 \omega}{\partial \phi^2}\frac{\partial P_{sat}}{\partial T}\Big)\,\Psi_2\,. \tag{A.12}$$

$$\frac{\partial \beta}{\partial P_{vs}} = \Big(\frac{\rho_s C_m}{P_{sat}}\frac{\partial P_{sat}}{\partial T} + \frac{\rho_s P_v}{P_{sat}^3}\frac{\partial^2 \omega}{\partial \phi^2}\frac{\partial P_{sat}}{\partial T}\Big)\,\theta_2\,. \tag{A.13}$$

Finally, effective thermal conductivity and the coefficient α are the two varying properties considered in Eq. (3.2). Thus, their derivatives are obtained as follows :

$$\frac{\partial \lambda_{ef}}{\partial T_s} = \lambda_{ef}\, C_m\, \rho_l\, \rho_s\, \ln(\lambda_l)\, \Psi_2\,, \qquad \frac{\partial \lambda_{ef}}{\partial T_s} = \lambda_{ef}\, C_m\, \rho_l\, \rho_s\, \ln(\lambda_l)\, \theta_2\,. \tag{A.14}$$

$$\frac{\partial \alpha}{\partial T_s} = (h_l + L_v)\, \frac{\partial k_m}{\partial \phi}\, \frac{\partial \phi}{\partial T}\, \theta_1\,, \qquad \frac{\partial \alpha}{\partial P_{vs}} = \frac{1}{P_{sat}}\, (h_l + L_v)\, \frac{\partial k_m}{\partial \phi}\, \theta_2\,. \tag{A.15}$$

Regarding the boundary conditions, Equations expressing them given in Section 2.2 are derived according to P_{vs} and T_s. First, we begin with Dirichlet condition given in Eq. (3.14). We obtain therefore $\forall\, t \in [\,0\,,\, t_f\,]\,,\; x = 0$:

$$\theta_1 = 1\,, \quad \Psi_2 = 0\,. \tag{A.16}$$

$$\theta_2 = 1\,, \quad \Psi_1 = 0\,. \tag{A.17}$$

On the other hand, the boundary conditions in the Eq. (3.15) regarding thermal and mass flux undergo the same derivation resulting in the following where $t \in [\,0\,,\, t_f\,]$ and $x = L$:

$$\frac{\partial \theta_1}{\partial x} = 0\,, \quad \frac{\partial \Psi_2}{\partial x} = 0\,. \tag{A.18}$$

$$\frac{\partial \theta_2}{\partial x} = 0\,, \quad \frac{\partial \Psi_1}{\partial x} = 0\,. \tag{A.19}$$

Finally, we derive Eq. (3.13) in order to express initial conditions regarding the variables θ_1, θ_2, ϕ_1 and ϕ_2. Therefore, we obtain :

$$\forall\, x \in [\,0\,,\, L\,]\,,\; t = 0 \qquad \theta_1 = 0\,,\, \theta_2 = 0\,,\, \Psi_1 = 0\,,\, \Psi_2 = 0\,. \tag{A.20}$$

To conclude, the study of the temperature and relative humidity sensitivity with regard to that at the material surface $x = 0$, allows us to evaluate the coefficients θ_1, θ_2, Ψ_1 and Ψ_3 by solving Eqs. (A.1), (A.2), (A.5) and (A.6). The boundary conditions corresponding to the study of sensitivity are given by Eq. (A.16), (A.17), (A.18) and (A.19). At the end, the initial conditions are represented in Eq. (A.20). Once the results are obtained, we deduce $\sigma_{T,\,\mathrm{H2}}$ and $\sigma_{\phi,\,\mathrm{H2}}$ considering that :

$$\begin{aligned} \theta_3 = & \Big(\frac{\theta_2}{P_{sat}} - \frac{P_v}{P_{sat}^2}\, \frac{\partial P_{sat}}{\partial T}\, \Psi_1 \Big)\, P_{sat}\,(T_s) - \\ & \Big(\frac{\Psi_2}{P_{sat}} - \frac{P_v}{P_{sat}^2}\, \frac{\partial P_{sat}}{\partial T}\, \theta_1 \Big) \Big(\frac{\phi_s}{P_{sat}\,(T_s)}\, \frac{\partial P_{sat}\,(T_s)}{\partial T_s} \Big)^{-1}\,. \end{aligned} \tag{A.21}$$

Appendix B

(Chapitre 4)

1 The Dimensionless formulation of a heat and mass transfer model using a cylindrical coordinate system

Remind that coupled heat and mass transfer are based in this part on Equations (4.5a) and (4.5b). Considering a cylindrical coordinate system, r defines the radial distance where $r \in \Omega_x = [\,0\,,\,R\,]$. The azimuth is denoted φ where $\varphi \in \Omega_\varphi = [\,0\,,\,2\pi\,]$. In addition, z represents the axial coordinate and $z \in \Omega_z = [\,0\,,\,L\,]$. $R\,[\mathsf{m}]$ and $L\,[\mathsf{m}]$ are the radius and the height, respectively. In the dimensionless domain, space coordinates and time are as follows :

$$r^\star = \frac{r}{L_0}\,, \quad \varphi^\star = \varphi\,, \quad z^\star = \frac{z}{L_0}\,, \quad t^\star = \frac{t}{t_f}\,. \tag{B.1}$$

$L_0\,[\mathsf{m}]$ is a given length. Subsequently, dimensionless temperature and water content are defined in Equation :

$$T^\star = \frac{T}{T_0}\,, \quad \theta^\star = \frac{\theta}{\theta_0}\,. \tag{B.2}$$

Moreover, the dimensionless material properties are given as follows :

$$D_\theta^\star = \frac{D_\theta}{D_{\theta\,0}}\,, \quad D_T^\star = \frac{D_T}{D_{T\,0}}\,, \quad \rho^\star = \frac{\rho}{\rho_0}\,, \quad C_p^\star = \frac{C_p}{C_{p\,0}}\,, \tag{B.3a}$$

$$\lambda^\star = \frac{\lambda}{\lambda_0}\,, \quad L_v^\star = \frac{L_v}{L_{v\,0}}\,, \quad D_{TV}^\star = \frac{D_{TV}}{D_{TV\,0}}\,, \quad D_{\theta V}^\star = \frac{D_{\theta V}}{D_{\theta V\,0}}\,. \tag{B.3b}$$

First, the temperature gradient operator is expressed in the dimensionless domain as follows :

$$\begin{aligned}\nabla T &= \left(\frac{\partial T}{\partial r}\,\vec{u}_r + \frac{1}{r}\,\frac{\partial T}{\partial \varphi}\,\vec{u}_\varphi + \frac{\partial T}{\partial z}\,\vec{u}_z\right) \\ &= \frac{1}{L_0}\,\left(\frac{\partial T}{\partial r^\star}\,\vec{u}_r + \frac{1}{r^\star}\,\frac{\partial T}{\partial \varphi^\star}\,\vec{u}_\varphi + \frac{\partial T}{\partial z^\star}\,\vec{u}_z\right) \\ &= \frac{1}{L_0}\,\nabla^\star T\end{aligned}$$

Similarly to temperature, water content gradient is given in the following :

$$\nabla\,\theta = \frac{\theta_{\,0}}{L_{\,0}}\,\nabla^{\star}\,\theta^{\star}\,.$$

Moreover, by adopting the same approach for divergence, this operator is expressed for the vector field $\nabla\,\theta$ as given :

$$\begin{aligned}
\nabla\cdot(\,\nabla\,\theta\,) &= \frac{1}{r}\,\frac{\partial}{\partial\,r}\,\left(r\,\frac{\partial\theta}{\partial r}\right) + \frac{1}{r}\,\frac{\partial}{\partial\varphi}\,\left(\frac{1}{r}\,\frac{\partial\theta}{\partial\varphi}\right) + \frac{\partial}{\partial z}\,\left(\frac{\partial\theta}{\partial z}\right)\\
&= \frac{1}{L_{\,0}}\,\left[\frac{1}{r^{\star}}\,\frac{\partial}{\partial\,r^{\star}}\,\left(r^{\star}\,\frac{\partial\theta}{\partial r}\right) + \frac{1}{r^{\star}}\,\frac{\partial}{\partial\varphi^{\star}}\,\left(\frac{1}{r}\,\frac{\partial\theta}{\partial\varphi}\right) + \frac{\partial}{\partial z^{\star}}\,\left(\frac{\partial\theta}{\partial z}\right)\right]\\
&= \frac{1}{L_{\,0}}\,\nabla^{\star}\cdot(\,\nabla\,\theta\,)
\end{aligned}$$

Similarly, the divergence of a temperature gradient is deduced in Equation (B.4).

$$\nabla\cdot(\,\nabla\,T\,) = \frac{1}{L_{\,0}}\,\nabla^{\star}\cdot(\,\nabla\,T\,)\;. \tag{B.4}$$

Thus, the substitution of variables and dimensionless operators in the equations of the model gives :

$$\frac{\partial\theta^{\,\star}}{\partial t^{\,\star}} = \mathrm{Fo}_{\,m}\,\nabla^{\star}\cdot\,\Big(\,D_{\theta}^{\star}\,\nabla^{\star}\,\theta^{\,\star} + D_{T}^{\star}\,\delta\,\nabla^{\star}\,T^{\,\star}\,\Big)\,, \tag{B.5a}$$

$$\rho^{\,\star}\,C_{\,p}^{\,\star}\,\frac{\partial T^{\,\star}}{\partial t^{\,\star}} = \mathrm{Fo}_{\,q}\,\nabla^{\star}\cdot\,\Big(\,\lambda^{\star}\,\nabla^{\star}\,T^{\,\star}\,\Big) + \alpha\,\mathrm{Fo}_{\,q}\,L_{\,v}^{\,\star}\,\nabla^{\star}\cdot\,\Big(\,D_{TV}^{\star}\,\nabla^{\star}\,T^{\,\star} + D_{\theta V}^{\star}\,\gamma\,\nabla^{\star}\,\theta^{\,\star}\,\Big)\,. \tag{B.5b}$$

Where :

$$\mathrm{Fo}_{\,m} = \frac{D_{\,\theta\,0}\,t_{\,f}}{L_{\,0}^{\,2}}\,,\quad \mathrm{Fo}_{\,q} = \frac{\lambda_{\,0}\,t_{\,f}}{\rho_{\,0}\,C_{\,p\,0}\,L_{\,0}^{\,2}}\,. \tag{B.6}$$

$$\delta = \frac{D_{\,T\,0}\,T_{\,0}}{D_{\,\theta\,0}\,\theta_{\,0}}\,,\quad \alpha = \frac{L_{\,v\,0}\,\rho_{\,l}\,D_{\,TV\,0}}{\lambda_{\,0}}\,,\quad \gamma = \frac{\theta_{\,0}\,D_{\,\theta V\,0}}{T_{\,0}\,D_{\,TV\,0}}\,. \tag{B.7}$$

2 Behavior law of thermal conductivity, porosity and vapor permeability according to density

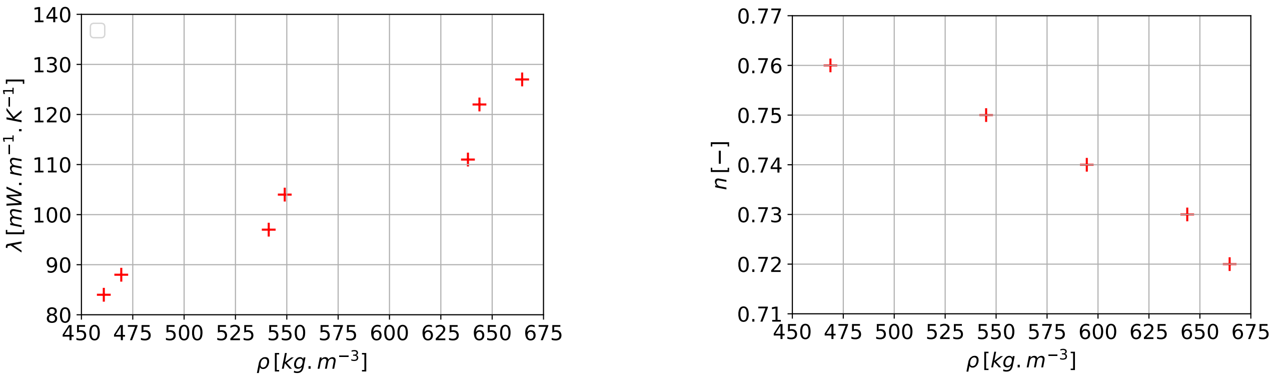

(a) (b)

FIGURE B.1 – Variation in thermal conductivity (a) and porosity (b) depending on density for hemp concrete.

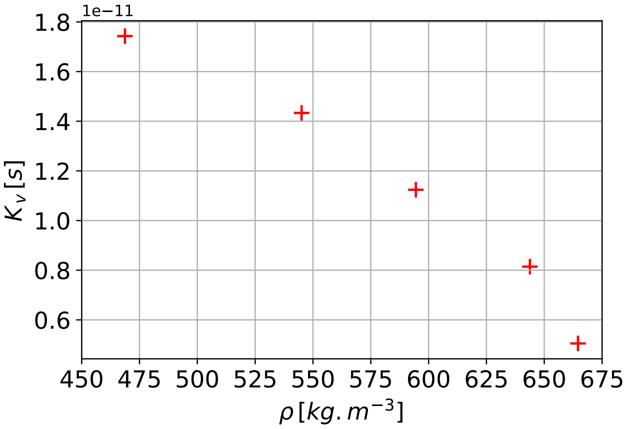

FIGURE B.2 – Variation in vapor permeability depending on density for hemp concrete.

3 Time lag throughout the effective aging design

Table B.1 – Time lag delay and standard deviation in minutes in the reduced configuration during the four season sequences

Autumn		Winter		Spring		Summer	
Duration	Std	Duration	Std	Duration	Std	Duration	Std
12.65	2.69	8.61	2.04	4.43	3.74	1.58	1.10
16.14	2.76	11.06	2.99	6.56	1.47	2.51	1.57
13.37	1.99	8.83	3.45	4.51	3.70	1.98	1.06
15.37	3.04	10.80	3.24	5.13	2.77	1.07	0.41
12.55	2.91	–	–	–	–	2.51	2.08
15.14	2.63	–	–	–	–	4.66	3.45
11.38	3.38	–	–	–	–	3.45	1.48
14.62	3.13	–	–	–	–	2.67	1.8
12.88	2.59	–	–	–	–	3.34	2.03
15.03	2.96	–	–	–	–	2.58	2.15

Appendix C

(Chapitre 5)

1 Sensitivity equations of the model of porosity

Porosity varies due to climate loads according to :

$$\frac{\partial n}{\partial t} = \alpha_{q,0}\, Q_q\, n \left(n_q^{\infty} - n \right) + \alpha_{m,0}\, Q_m\, n \left(n_m^{\infty} - n \right) . \tag{C.1}$$

By deriving Equation (C.1) according to $\alpha_{q,0}$, we obtain the following :

$$\begin{aligned} \frac{\partial \chi}{\partial t} = Q_q \Big[n \left(n_q^{\infty} - n \right) + \alpha_{q,0}\, \chi \left(n_q^{\infty} - n \right) - \alpha_{q,0}\, n\, \chi \Big] + \\ Q_m\, \alpha_{m,0} \Big[\chi \left(n_m^{\infty} - n \right) - \chi\, n \Big] , \end{aligned} \tag{C.2}$$

where :

$$\chi(t) = \frac{\partial n}{\partial \alpha_{q,0}} . \tag{C.3}$$

χ defines the first sensitive coefficient which evaluates the variation of porosity according to the parameter $\alpha_{q,0}$. The time variation in χ is provided by :

$$\frac{\partial \chi}{\partial t} = Q_q \left[n \left(n_q^{\infty} - n \right) + \alpha_{q,0}\, \chi \left(n_q^{\infty} - 2\, n \right) \right] + Q_m\, \alpha_{m,0}\, \chi \left(n_m^{\infty} - 2\, n \right) . \tag{C.4}$$

Discretizing the last equation induces the following :

$$\begin{aligned} \frac{\chi^{j+1} - \chi^{j}}{\Delta t} = Q_q^{j+1} \left[n^{j+1} \left(n_q^{\infty} - n^{j+1} \right) + \alpha_{q,0}\, \chi^{j+1} \left(n_q^{\infty} - 2\, n^{j+1} \right) \right] + \\ Q_m^{j+1}\, \alpha_{m,0}\, \chi^{j+1} \left(n_m^{\infty} - 2\, n^{j+1} \right) . \end{aligned} \tag{C.5}$$

At the end, the coefficient χ is assessed numerically according to :

$$\chi^{j+1} = \left[\chi^{j} + \Delta t \, n^{j+1} \, Q_{q}^{j+1} \left(n_{q}^{\infty} - n^{j+1} \right) \right] \Big[1 - \Delta t \left(n_{q}^{\infty} - 2 \, n^{j+1} \right) \alpha_{q,0} \, Q_{q}^{j+1} - \Delta t \left(n_{m}^{\infty} - 2 \, n^{j+1} \right) \alpha_{m,0} \, Q_{m}^{j+1} \Big]^{-1} . \tag{C.6}$$

The second sensitive coefficient ξ is likewise addressed, it is defined as follows :

$$\xi \, (\, t \,) = \frac{\partial n}{\partial \alpha_{m,0}} \, . \tag{C.7}$$

It reflects the variation of porosity with respect to $\alpha_{m,0}$. The variation in time of ξ is obtained by deriving the equation (C.1) according to $\alpha_{m,0}$. This leads to :

$$\frac{\partial \xi}{\partial t} = Q_{m} \Big[n \left(n_{m}^{\infty} - n \right) + \alpha_{m,0} \, \xi \left(n_{m}^{\infty} - n \right) - \alpha_{m,0} \, n \, \xi \Big] + Q_{q} \, \alpha_{q,0} \Big[\xi \left(n_{q}^{\infty} - n \right) - \xi \, n \Big] . \tag{C.8}$$

By considering the same methodology as for χ, computing ξ lies on the following expression :

$$\xi^{j+1} = \left[\xi^{j} + \Delta t \, n^{j+1} \, Q_{m}^{j+1} \left(n_{m}^{\infty} - n^{j+1} \right) \right] \Big[1 - \Delta t \left(n_{m}^{\infty} - 2 \, n^{j+1} \right) \alpha_{m,0} \, Q_{m}^{j+1} - \Delta t \left(n_{q}^{\infty} - 2 \, n^{j+1} \right) \alpha_{q,0} \, Q_{q}^{j+1} \Big]^{-1} . \tag{C.9}$$

Moreover, initial porosity is assumed constant. Thus, the initial condition on χ and ξ is as given :

$$t = 0 \, , \qquad \chi = 0 \, , \quad \xi = 0 \, . \tag{C.10}$$

2 Numerical heat and moisture transfer model

The development of a numerical model lies on Equations (5.18) and (5.19). First, these are expressed according to the dimensionless domain. Indeed, the numerical solution is more efficient if computed variables have a small magnitude. L and t_{f} are the characteristic quantities for space and time coordinates, respectively. As for water content and temperature, we use θ_{0} and T_{0}. Moreover, heat and moisture coefficients are scaled with regard to their values at the initial state. In this case, their characteristic quantities are denoted according to the form X_{0}, where X refers to a given coefficient. In the dimensionless domain, Equation (5.18) becomes :

$$\frac{\partial \theta^{\star}}{\partial t^{\star}} = \mathrm{Fo}_{\mathrm{m}} \, \frac{\partial}{\partial x^{\star}} \left(D_{\theta}^{\star} \, \frac{\partial \theta^{\star}}{\partial x^{\star}} + \delta \, D_{T}^{\star} \, \frac{\partial T^{\star}}{\partial x^{\star}} \right) \, . \tag{C.11}$$

$\mathrm{Fo}_{\mathrm{m}} \, [-]$ and $\delta \, [-]$ are dimensionless numbers. Their expressions are :

$$\mathrm{Fo}_{m} = \frac{D_{\theta\,0}\,t_{f}}{L^{2}}\,, \qquad \delta = \frac{D_{T\,0}\,T_{0}}{D_{\theta\,0}\,\theta_{0}}\,. \tag{C.12}$$

The initial conditions on temperature and water content are scaled :

$$\forall x^{\star} \in [\,0\,,\,1\,]\,,\, t^{\star} = 0 \qquad \theta^{\star} = 1\,, \quad T^{\star} = 1\,, \tag{C.13}$$

Boundary conditions are expressed in the dimensionless domain at $x^{\star} = 0$ and $x^{\star} = 1$ according to Equations (C.14) and (C.15), respectively.

$$x^{\star} = 0\,,\, \forall t^{\star} \in [\,0\,,\,1\,] \qquad T^{\star} = T^{\star}_{\infty}\,(\,t\,)\,, \quad \theta^{\star} = \theta^{\star}_{\infty}\,(\,t\,)\,. \tag{C.14}$$

$$x^{\star} = 1\,,\, \forall t^{\star} \in [\,0\,,\,1\,] \qquad T^{\star} = T^{\star}_{int}\,(\,t\,)\,, \quad \theta^{\star} = \theta^{\star}_{int}\,(\,t\,)\,. \tag{C.15}$$

$T^{\star}_{\infty}$, $T^{\star}_{int}$, $\theta^{\star}_{\infty}$ and $\theta^{\star}_{int}$ are time dependent functions. In order to alleviate the notations while developing the numerical model, dimensionless quantities are expressed without the exponent *. For the numerical discretization, space and time nodes are represented by $x_{\,i}$ and $t^{\,j}$ where $i \in \{\,1\,,\,\ldots\,,\,N_{x}\,\}$ and $j \in \{\,1\,,\,\ldots\,,\,N_{t}\,\}$. Based in the implicit scheme method, Equation (C.11) becomes for $i \in \{\,2\,,\,\ldots\,,\,N_{x} - 1\,\}$:

$$\begin{aligned} \theta_{i}^{j+1} - \theta_{i}^{j} = \frac{\mathrm{Fo}_{\mathrm{m}}\,\Delta t}{\Delta x^{2}} \Big[& D_{\theta\,i+\frac{1}{2}}^{j+1}\,\theta_{i+1}^{j+1} - \Big(D_{\theta\,i+\frac{1}{2}}^{j+1} + D_{\theta\,i-\frac{1}{2}}^{j+1} \Big)\,\theta_{i}^{j+1} + D_{\theta\,i-\frac{1}{2}}^{j+1}\,\theta_{i-1}^{j+1} + \\ & \delta\,D_{T\,i+\frac{1}{2}}^{j+1}\,T_{i+1}^{j+1} - \delta\,\Big(D_{T\,i+\frac{1}{2}}^{j+1} + D_{T\,i-\frac{1}{2}}^{j+1} \Big)\,T_{i}^{j+1} + \delta\,D_{T\,i-\frac{1}{2}}^{j+1}\,T_{i-1}^{j+1} \Big]\,. \end{aligned} \tag{C.16}$$

Where D_{θ} is assessed at $x = x_{\,i-\frac{1}{2}}$ and $x = x_{\,i+\frac{1}{2}}$ $\forall j \in \{\,1\,,\,\ldots\,,\,N_{\,t} - 1\,\}$ as given :

$$D_{\theta\,i-\frac{1}{2}}^{j} = D_{\theta}\,\left(\frac{\theta_{i}^{j} + \theta_{i-1}^{j}}{2}\,,\, \frac{T_{i}^{j} + T_{i-1}^{j}}{2}\,,\, n^{\,j} \right)\,, \tag{C.17}$$

$$D_{\theta\,i+\frac{1}{2}}^{j} = D_{\theta}\,\left(\frac{\theta_{i}^{j} + \theta_{i+1}^{j}}{2}\,,\, \frac{T_{i}^{j} + T_{i+1}^{j}}{2}\,,\, n^{\,j} \right)\,. \tag{C.18}$$

As for the coefficient D_{T}, it is discretized similarly as in Equations (C.17) and (C.18). $\Delta x\,[-]$ and $\Delta t\,[-]$ are the space and time steps, respectively. Therefore, by moving the terms at the instant $t^{\,j+1}$ to one side and the one at $t^{\,j}$ to the other, the following equality is deduced :

$$a_{i+\frac{1}{2}}^{j+1}\,\theta_{i+1}^{j+1} + b_{i}^{j+1}\,\theta_{i}^{j+1} + a_{i-\frac{1}{2}}^{j+1}\,\theta_{i-1}^{j+1} + c_{i+\frac{1}{2}}^{j+1}\,T_{i+1}^{j+1} + d_{i}^{j+1}\,T_{i}^{j+1} + c_{i-\frac{1}{2}}^{j+1}\,T_{i-1}^{j+1} = \theta_{i}^{j}\,, \tag{C.19}$$

where the coefficients a, and c are expressed $\forall i \in \{\,1\,,\,\ldots\,,\,N_{\,x}\,\}$ and $\forall j \in \{\,1\,,\,\ldots\,,\,N_{\,t}\,\}$ as follows :

$$a_{i}^{j} = -D_{\theta\,i}^{j}\,\frac{\mathrm{Fo}_{\mathrm{m}}\,\Delta t}{\Delta x^{2}}\,, \quad c_{i}^{j} = -D_{T\,i}^{j}\,\frac{\mathrm{Fo}_{\mathrm{m}}\,\delta\,\Delta t}{\Delta x^{2}}\,. \tag{C.20}$$

As for b and d, they are given $\forall i \in \{\,2\,,\,...\,,\,N_x\,\}$ and $\forall j \in \{\,1\,,\,...\,,\,N_t\,\}$ in the following :

$$b_i^j = 1 + a_{i+\frac{1}{2}}^j + a_{i-\frac{1}{2}}^j\,, \quad d_i^j = c_{i-\frac{1}{2}}^j + c_{i+\frac{1}{2}}^j\,. \tag{C.21}$$

Writing the equation for $i \in \{\,2\,,\,...\,,\,N_x - 1\,\}$ leads to the following matrix system :

$$\forall j \in \{\,1\,,\,...\,,\,N_t - 1\,\}\,, \quad M^{\,j+1}\,\Theta^{\,j+1} + N^{\,j+1}\,\mathcal{T}^{\,j+1} = \Theta^{\,j} + Q^{\,j+1} + R^{\,j+1}\,. \tag{C.22}$$

M and N are $(\,N_x - 2\,)^2$ sized matrices. In addition, Θ and $\mathcal{T}$ are $N_x - 2$ sized vectors which represent the water content and temperature fields inside the material, respectively. Furthermore, Q and R are $N_x - 2$ sized vectors. First one defines the boundary conditions in water content and the second one in temperature. These matrices and vectors are time-dependent and are expressed as follows :

$$\forall j \in \{\,1\,,\,...\,,\,N_t\,\}\,, \quad M^{\,j} = \begin{pmatrix} b_2^j & a_{\frac{5}{2}}^j & 0 & 0 & 0 & \cdots & 0 \\ a_{\frac{5}{2}}^j & b_3^j & a_{\frac{7}{2}}^j & 0 & 0 & \cdots & 0 \\ 0 & a_{\frac{7}{2}}^j & b_4^j & a_{\frac{9}{2}}^j & 0 & \cdots & 0 \\ \vdots & \vdots & \ddots & \ddots & \ddots & \vdots & \vdots \\ 0 & 0 & \cdots & 0 & a_{N_x-\frac{5}{2}}^j & b_{N_x-2}^j & a_{N_x-\frac{3}{2}}^j \\ 0 & 0 & \cdots & 0 & 0 & a_{N_x-\frac{3}{2}}^j & b_{N_x-1}^j \end{pmatrix}, \Theta^{\,j} = \begin{pmatrix} \theta_2^j \\ \theta_3^j \\ \vdots \\ \theta_{N_x-2}^j \\ \theta_{N_x-1}^j \end{pmatrix},$$

$$N^{\,j} = \begin{pmatrix} d_2^j & c_{\frac{5}{2}}^j & 0 & 0 & 0 & \cdots & 0 \\ c_{\frac{5}{2}}^j & d_3^j & c_{\frac{7}{2}}^j & 0 & 0 & \cdots & 0 \\ 0 & c_{\frac{7}{2}}^j & d_4^j & c_{\frac{9}{2}}^j & 0 & \cdots & 0 \\ \vdots & \vdots & \ddots & \ddots & \ddots & \vdots & \vdots \\ 0 & 0 & \cdots & 0 & c_{N_x-\frac{5}{2}}^j & d_{N_x-2}^j & c_{N_x-\frac{3}{2}}^j \\ 0 & 0 & \cdots & 0 & 0 & c_{N_x-\frac{3}{2}}^j & d_{N_x-1}^j \end{pmatrix}, \mathcal{T}^{\,j} = \begin{pmatrix} T_2^j \\ T_3^j \\ \vdots \\ T_{N_x-2}^j \\ T_{N_x-1}^j \end{pmatrix},$$

$$Q^{\,j} = \begin{pmatrix} -a_{\frac{3}{2}}^j\,\theta_1^j \\ 0 \\ \vdots \\ 0 \\ -a_{N_x-\frac{1}{2}}^j\,\theta_{N_x}^j \end{pmatrix}, R^{\,j} = \begin{pmatrix} -c_{\frac{3}{2}}^j\,T_1^j \\ 0 \\ \vdots \\ 0 \\ -c_{N_x-\frac{1}{2}}^j\,T_{N_x}^j \end{pmatrix},$$

Furthermore, Equation (5.19) is written according to the dimensionless domain as :

$$\frac{\partial T}{\partial t} = \mathrm{Fo}_{\,\mathrm{q}}\,\frac{\partial}{\partial x}\left(\lambda^{\star}\,\frac{\partial T}{\partial x}\right) + \eta\,\mathrm{Fo}_{\,\mathrm{q}}\,\frac{\partial}{\partial x}\left(D_{TV}^{\star}\,\frac{\partial T}{\partial x} + \gamma\,D_{\theta V}^{\star}\,\frac{\partial \theta}{\partial x}\right)\,. \tag{C.23}$$

$\mathrm{Fo}_{q}\,[-]$, $\eta\,[-]$ and $\gamma\,[-]$ are dimensionless numbers which are defined as :

$$\mathrm{Fo}_{q} = \frac{\lambda_{0}\, t_{f}}{\rho\, C_{p0}\, L^{2}}\,, \quad \eta = \frac{L_{v0}\, \rho_{w}\, D_{TV0}}{\lambda_{0}}\,, \quad \gamma = \frac{\theta_{0}\, D_{\theta V0}}{T_{0}\, D_{TV0}}\,. \tag{C.24}$$

By following the same discretization method, Equation (C.23) yields :

$$\forall j \in \{\, 1\,,\, ...\,,\, N_{t} - 1 \,\}\ , \quad S^{\,j+1}\, \mathcal{T}^{\,j+1} + U^{\,j+1}\, \Theta^{\,j+1} = \mathcal{T}^{\,j} + V^{\,j+1} + W^{\,j+1}\,. \tag{C.25}$$

S and U are $(\, N_{x} - 2\,)^{2}$ sized matrices. In addition, V and W are $N_{x} - 2$ sized vectors which define the temperature and water content boundary conditions, respectively. These matrices and vectors are time-dependent :

$$\forall j \in \{\, 1\,,\, ...\,,\, N_{t} \,\}\ , \quad S^{\,j} = \begin{pmatrix} f_{2}^{\,j} & e_{\frac{5}{2}}^{\,j} & 0 & 0 & 0 & \cdots & 0 \\ e_{\frac{5}{2}}^{\,j} & f_{3}^{\,j} & e_{\frac{7}{2}}^{\,j} & 0 & 0 & \cdots & 0 \\ 0 & e_{\frac{7}{2}}^{\,j} & f_{4}^{\,j} & e_{\frac{9}{2}}^{\,j} & 0 & \cdots & 0 \\ \vdots & \vdots & \ddots & \ddots & \ddots & \vdots & \vdots \\ 0 & 0 & \cdots & 0 & e_{N_{x}-\frac{5}{2}}^{\,j} & f_{N_{x}-2}^{\,j} & e_{N_{x}-\frac{3}{2}}^{\,j} \\ 0 & 0 & \cdots & 0 & 0 & e_{N_{x}-\frac{3}{2}}^{\,j} & f_{N_{x}-1}^{\,j} \end{pmatrix}, V^{\,j} = \begin{pmatrix} -e_{\frac{3}{2}}^{\,j}\, T_{1}^{\,j} \\ 0 \\ \vdots \\ 0 \\ -e_{N_{x}-\frac{1}{2}}^{\,j} T_{N_{x}}^{\,j} \end{pmatrix},$$

$$U^{\,j} = \begin{pmatrix} h_{2}^{\,j} & g_{\frac{5}{2}}^{\,j} & 0 & 0 & 0 & \cdots & 0 \\ g_{\frac{5}{2}}^{\,j} & h_{3}^{\,j} & g_{\frac{7}{2}}^{\,j} & 0 & 0 & \cdots & 0 \\ 0 & c_{\frac{7}{2}}^{\,j} & d_{4}^{\,j} & c_{\frac{9}{2}}^{\,j} & 0 & \cdots & 0 \\ \vdots & \vdots & \ddots & \ddots & \ddots & \vdots & \vdots \\ 0 & 0 & \cdots & 0 & g_{N_{x}-\frac{5}{2}}^{\,j} & h_{N_{x}-2}^{\,j} & g_{N_{x}-\frac{3}{2}}^{\,j} \\ 0 & 0 & \cdots & 0 & 0 & g_{N_{x}-\frac{3}{2}}^{\,j} & h_{N_{x}-1}^{\,j} \end{pmatrix}, W^{\,j} = \begin{pmatrix} -g_{\frac{3}{2}}^{\,j}\, \theta_{1}^{\,j} \\ 0 \\ \vdots \\ 0 \\ -g_{N_{x}-\frac{1}{2}}^{\,j}\, \theta_{N_{x}}^{\,j} \end{pmatrix}.$$

e and g are time-variant coefficients. They are expressed $\forall i \in \{\, 1\,,\, ...\,,\, N_{x} \,\}$ and $\forall j \in \{\, 1\,,\, ...\,,\, N_{t} \,\}$ with respect to :

$$e_{i}^{\,j} = -\frac{\mathrm{Fo_{q}}\, \Delta t}{\Delta x^{2}} \left(\lambda_{i}^{\,j} + \eta\, D_{TV\,i}^{\,j} \right)\,, \quad g_{i}^{\,j} = -\frac{\eta\, \gamma\, \mathrm{Fo_{q}}\, \Delta t}{\Delta x^{2}}\, D_{\theta V\,i}^{\,j}\,. \tag{C.26}$$

As for f and h, they are given $\forall i \in \{\, 2\,,\, ...\,,\, N_{x} \,\}$ and $\forall j \in \{\, 1\,,\, ...\,,\, N_{t} \,\}$ in the following :

$$f_{i}^{\,j} = 1 + e_{i+\frac{1}{2}}^{\,j} + e_{i-\frac{1}{2}}^{\,j}\,, \quad h_{i}^{\,j} = g_{i-\frac{1}{2}}^{\,j} + g_{i+\frac{1}{2}}^{\,j}\,. \tag{C.27}$$

Similarly to Equations (C.17) and (C.18), the coefficients $D_{\theta V}$ and D_{TV} are estimated at $x = x_{i+\frac{1}{2}}$ and $x = x_{i-\frac{1}{2}}$. Finally, the solution in temperature and water content is assessed based on (C.22) and (C.25).

References

[1] M. Santamouris and K. Vasilakopoulou, “Present and future energy consumption of buildings : Challenges and opportunities towards decarbonisation,” *e-Prime-Advances in Electrical Engineering, Electronics and Energy*, vol. 1, p. 100002, 2021.

[2] P. Nejat, F. Jomehzadeh, M. M. Taheri, M. Gohari, and M. Z. A. Majid, “A global review of energy consumption, co2 emissions and policy in the residential sector (with an overview of the top ten co2 emitting countries),” *Renewable and sustainable energy reviews*, vol. 43, pp. 843–862, 2015.

[3] P. Huovila, “Buildings and climate change : status, challenges, and opportunities,” 2007.

[4] H. Sozer, “Improving energy efficiency through the design of the building envelope,” *Building and environment*, vol. 45, no. 12, pp. 2581–2593, 2010.

[5] M. Sawadogo, F. Benmahiddine, A. E. A. Hamami, R. Belarbi, A. Godin, and M. Duquesne, “Investigation of a novel bio-based phase change material hemp concrete for passive energy storage in buildings,” *Applied Thermal Engineering*, vol. 212, p. 118620, 2022.

[6] F. Pittau, F. Krause, G. Lumia, and G. Habert, “Fast-growing bio-based materials as an opportunity for storing carbon in exterior walls,” *Building and Environment*, vol. 129, pp. 117–129, 2018.

[7] J. J. Andrew and H. Dhakal, “Sustainable biobased composites for advanced applications : recent trends and future opportunities–a critical review,” *Composites Part C : Open Access*, vol. 7, p. 100220, 2022.

[8] M. Cyr, M. Trinh, B. Husson, and G. Casaux-Ginestet, “Effect of cement type on metakaolin efficiency,” *Cement and Concrete Research*, vol. 64, pp. 63–72, 2014.

[9] P. Hakala, O. Orell, E. Sarlin, E. Pääkkönen, L. Jutila, and M. Kanerva, “Durability of sandwich structures with a maximized natural raw material basis : comparison of expanded polystyrene, cellulose foam and polylactic acid subjected to uv-rain aging,” *Rakenteiden mekaniikka*, vol. 56, no. 1, pp. 24–40, 2023.

[10] E. G. Assis, J. C. dos Santos, R. J. da Silva, L. Á. de Oliveira, G. G. del Pino, F. Scarpa, and T. H. Panzera, “Water aging effects on the flexural properties of fully biobased coir fiber composites,” *Polymer Engineering & Science.*

[11] H. Cochard, C. Bodet, T. Améglio, and P. Cruiziat, “Cryo-scanning electron microscopy observations of vessel content during transpiration in walnut petioles. facts or artifacts ?” *Plant physiology*, vol. 124, pp. 1191–202, 12 2000.

[12] C. G. Jacquin and P. Adler, “Fractal porous media ii : geometry of porous geological structures,” *Transport in Porous Media*, vol. 2, pp. 571–596, 1987.

[13] F. Bennai, C. El Hachem, K. Abahri, and R. Belarbi, "Microscopic hydric characterization of hemp concrete by x-ray microtomography and digital volume correlation," *Construction and Building Materials*, vol. 188, pp. 983–994, 11 2018.

[14] A. E. Scheidegger, *The physics of flow through porous media.* University of Toronto press, 1957.

[15] R. N. Wenzel, "Resistance of solid surfaces to wetting by water," *Industrial & Engineering Chemistry*, vol. 28, no. 8, pp. 988–994, 1936.

[16] C. Brooks and W. Purcell, "Surface area measurements on sedimentary rocks," in *Fall Meeting of the Petroleum Branch of AIME.* OnePetro, 1952.

[17] F. A. Dullien, *Porous media : fluid transport and pore structure.* Academic press, 2012.

[18] J. Bear, "Dynamics of fluids in porous media," *Soil Science*, vol. 120, pp. 162–163, 1972.

[19] G. M. Fair, L. P. Hatch, and H. E. Hudson, "Fundamental factors governing the streamline flow of water through sand [with discussion]," *Journal American Water Works Association*, 1933.

[20] P. C. Carman, "Fluid flow through a granular bed," *Trans. Inst. Chem. Eng. London*, vol. 15, pp. 150–156, 1937.

[21] C. S. Slichter, *U.S. Geological Survey,* 19*th* *annual report, Part* 2, vol. 301, 1899.

[22] J. M. DallaValle, "Micromeritics : The technology of fine particles," *Pitman, New York*, vol. 269, 1899.

[23] D. Tareste, "Liaisons par chélation et liaisons hydrogène : une mesure directe," Ph.D. dissertation, Université Pierre et Marie Curie-Paris VI, 2002.

[24] J. Xamán, L. Lira, and J. Arce, "Analysis of the temperature distribution in a guarded hot plate apparatus for measuring thermal conductivity," *Applied Thermal Engineering*, vol. 29, no. 4, pp. 617–623, 2009.

[25] H. Watanabe, "Further examination of the transient hot-wire method for the simultaneous measurement of thermal conductivity and thermal diffusivity," *Metrologia*, vol. 39, no. 1, p. 65, 2002.

[26] P. Gabbott, "A practical introduction to differential scanning calorimetry," *Principles and applications of thermal analysis*, pp. 1–50, 2008.

[27] F. Benmahiddine, "Études des transferts couplés de chaleur, d'air et d'humidité par des techniques de changement d'échelle (microscopique-macroscopique) : Application à l'évaluation de la performance énergétique et la durabilité des matériaux de construction," Ph.D. dissertation, Université de La Rochelle ; Université Abderrahmane Mira-Bejaïa (Bejaïa, Algérie), 2020.

[28] N. Issaadi, "Effets de la variabilité des propriétés de matériaux cimentaires sur les transferts hygrothermiques : développement d'une approche probabiliste," Ph.D. dissertation, Université de La Rochelle ; École Royale Militaire (Bruxelles), 2015.

[29] N. Issaadi, A. Nouviaire, R. Belarbi, and A. Aït-Mokhtar, "Moisture characterization of cementitious material properties : assessment of water vapor sorption isotherm and permeability variation with ages," *Construction and Building Materials*, vol. 83, pp. 237–247, 2015.

[30] D. Lelievre, T. Colinart, and P. Glouannec, “Hygrothermal behavior of bio-based building materials including hysteresis effects : Experimental and numerical analyses,” *Energy and Buildings*, vol. 84, pp. 617–627, 2014.

[31] C. Rode, R. H. Peuhkuri, K. K. Hansen, B. Time, K. Svennberg, J. Arfvidsson, and T. Ojanen, “Nordtest project on moisture buffer value of materials,” in *AIVC Conference ‘Energy performance regulation’ : Ventilation in relation to the energy performance of buildings.* INIVE eeig, 2005, pp. 47–52.

[32] T. Abbasi and S. Abbasi, “Biomass energy and the environmental impacts associated with its production and utilization,” *Renewable and sustainable energy reviews*, vol. 14, no. 3, pp. 919–937, 2010.

[33] S. McMahon and J. Parnell, “The deep history of earth’s biomass,” *Journal of the Geological Society*, vol. 175, no. 5, pp. 716–720, 2018.

[34] M. Lagouin, C. Magniont, P. Sénéchal, P. Moonen, J.-E. Aubert, and A. Laborel-Préneron, “Influence of types of binder and plant aggregates on hygrothermal and mechanical properties of vegetal concretes,” *Construction and Building Materials*, vol. 222, pp. 852–871, 2019.

[35] M. Palumbo, A. Lacasta, N. Holcroft, A. Shea, and P. Walker, “Determination of hygrothermal parameters of experimental and commercial bio-based insulation materials,” *Construction and Building Materials*, vol. 124, pp. 269–275, 2016.

[36] J. Johansson, “Collaborative governance for sustainable forestry in the emerging bio-based economy in europe,” *Current opinion in environmental sustainability*, vol. 32, pp. 9–16, 2018.

[37] A. FALK, P. VEGH, and J. CHILTON, “Bio-based material hybrids seeking new applications in construction,” *Proceedings of the IASS WORKING GROUPS*, vol. 12, no. 18, 2015.

[38] C. Martínez-García, B. González-Fonteboa, F. Martínez-Abella, and D. Carro-López, “Performance of mussel shell as aggregate in plain concrete,” *Construction and building materials*, vol. 139, pp. 570–583, 2017.

[39] M. L. Santarelli, F. Sbardella, M. Zuena, J. Tirillò, and F. Sarasini, “Basalt fiber reinforced natural hydraulic lime mortars : A potential bio-based material for restoration,” *Materials & Design*, vol. 63, pp. 398–406, 2014.

[40] D. Liu, J. Song, D. P. Anderson, P. R. Chang, and Y. Hua, “Bamboo fiber and its reinforced composites : structure and properties,” *Cellulose*, vol. 19, pp. 1449–1480, 2012.

[41] F. Benmahiddine, R. Cherif, F. Bennai, R. Belarbi, A. Tahakourt, and K. Abahri, “Effect of flax shives content and size on the hygrothermal and mechanical properties of flax concrete,” *Construction and Building Materials*, vol. 262, p. 120077, 2020.

[42] P. Brzyski, M. Gładecki, M. Rumińska, K. Pietrak, M. Kubiś, and P. Łapka, “Influence of hemp shives size on hygro-thermal and mechanical properties of a hemp-lime composite,” *Materials*, vol. 13, no. 23, p. 5383, 2020.

[43] K. Bysheim, A. Nyrud, and K. Strobel, “Building materials and well-being in indoor environments,” *A Focus Group Study, Norsk Treteknisk Institutt*, vol. 88, 2016.

[44] R. F. Beims, R. Arredondo, D. J. S. Carrero, Z. Yuan, H. Li, H. Shui, Y. Zhang, M. Leitch, and C. C. Xu, "Functionalized wood as bio-based advanced materials : Properties, applications, and challenges," *Renewable and Sustainable Energy Reviews*, vol. 157, p. 112074, 2022.

[45] O. Vololonirina, M. Coutand, and B. Perrin, "Characterization of hygrothermal properties of wood-based products–impact of moisture content and temperature," *Construction and Building Materials*, vol. 63, pp. 223–233, 2014.

[46] P. Navi and F. Heger, *Comportement thermo-hydromécanique du bois : Applications technologiques et dans les structures.* PPUR presses polytechniques, 2005.

[47] V. Baroghel-Bouny, "Water vapour sorption experiments on hardened cementitious materials : Part i : Essential tool for analysis of hygral behaviour and its relation to pore structure," *Cement and Concrete Research*, vol. 37, no. 3, pp. 414–437, 2007.

[48] B. EN, "12524," *Building Materials and Products. Hygrothermal Properties. Tabulated Design Values*, 2000.

[49] S. Cascone, F. Catania, A. Gagliano, and G. Sciuto, "Energy performance and environmental and economic assessment of the platform frame system with compressed straw," *Energy and Buildings*, vol. 166, pp. 83–92, 2018.

[50] N. Oudhof, M. Labat, C. Magniont, and P. Nicot, "Measurement of the hygrothermal properties of straw-clay mixtures," *Academic Journal of Civil Engineering*, vol. 33, no. 2, pp. 474–479, 2015.

[51] S. Liuzzi, C. Rubino, F. Martellotta, P. Stefanizzi, C. Casavola, and G. Pappalettera, "Characterization of biomass-based materials for building applications : The case of straw and olive tree waste," *Industrial Crops and Products*, vol. 147, p. 112229, 2020.

[52] E. A. Guggenheim, "Applications of statistical mechanics," *(No Title)*, 1966.

[53] R. Walker, S. Pavia, and R. Mitchell, "Mechanical properties and durability of hemp-lime concretes," *Construction and Building Materials*, vol. 61, pp. 340–348, 2014.

[54] R. Fernea, D. L. Manea, D. R. Tămaș-Gavrea, and I. C. Roșca, "Hemp-clay building materials-an investigation on acoustic, thermal and mechanical properties," *Procedia Manufacturing*, vol. 32, pp. 216–223, 2019.

[55] A. Hussain, J. Calabria-Holley, M. Lawrence, and Y. Jiang, "Hygrothermal and mechanical characterisation of novel hemp shiv based thermal insulation composites," *Construction and Building Materials*, vol. 212, pp. 561–568, 2019.

[56] S. A. Grammatikos, R. G. Jones, M. Evernden, and J. R. Correia, "Thermal cycling effects on the durability of a pultruded gfrp material for off-shore civil engineering structures," *Composite Structures*, vol. 153, pp. 297–310, 2016.

[57] D. M. Freire-Lista, R. Fort, and M. J. Varas-Muriel, "Thermal stress-induced microcracking in building granite," *Engineering geology*, vol. 206, pp. 83–93, 2016.

[58] M. An, H. Huang, Y. Wang, and G. Zhao, "Effect of thermal cycling on the properties of high-performance concrete : Microstructure and mechanism," *Construction and Building Materials*, vol. 243, p. 118310, 2020.

[59] J. Castro, D. Bentz, and J. Weiss, "Effect of sample conditioning on the water absorption of concrete," *Cement and Concrete Composites*, vol. 33, no. 8, pp. 805–813, 2011.

[60] J. Watt, J. Tidblad, V. Kucera, and R. Hamilton, *The effects of air pollution on cultural heritage.* Springer, 2009, vol. 6.

[61] C. Sabbioni, "Mechanisms of air pollution damage to stone," *The effects of air pollution on the built environment*, vol. 2, pp. 63–88, 2003.

[62] H.-W. Song, S.-J. Kwon, K.-J. Byun, and C.-K. Park, "Predicting carbonation in early-aged cracked concrete," *Cement and Concrete Research*, vol. 36, no. 5, pp. 979–989, 2006.

[63] R. Webster and L. E. Kukacka, "Effects of acid deposition on portland cement concrete." ACS Publications, 1985.

[64] M. Wayman, A. Tallevi, and B. Winsborrow, "Hydrolysis of biomass by sulphur dioxide," *Biomass*, vol. 6, no. 1-2, pp. 183–191, 1984.

[65] S. Gibeaux, C. Thomachot-Schneider, S. Eyssautier-Chuine, B. Marin, and P. Vazquez, "Simulation of acid weathering on natural and artificial building stones according to the current atmospheric so 2/no x rate," *Environmental Earth Sciences*, vol. 77, pp. 1–19, 2018.

[66] A. Moudood, W. Hall, A. Öchsner, H. Li, A. Rahman, and G. Francucci, "Effect of moisture in flax fibres on the quality of their composites," *Journal of Natural Fibers*, vol. 16, no. 2, pp. 209–224, 2019.

[67] C. Achour, S. Remond, and N. Belayachi, "Swelling and shrinkage of plant aggregates : Experimental and treatment effect," *Industrial Crops and Products*, vol. 203, p. 117173, 2023.

[68] T. Lundin, S. M. Cramer, R. H. Falk, and C. Felton, "Accelerated weathering of natural fiber-filled polyethylene composites," *Journal of Materials in Civil Engineering*, vol. 16, no. 6, pp. 547–555, 2004.

[69] H.-C. Hsueh, J. H. Kim, S. Orski, A. Fairbrother, D. Jacobs, L. Perry, D. Hunston, C. White, and L. Sung, "Micro and macroscopic mechanical behaviors of high-density polyethylene under uv irradiation and temperature," *Polymer degradation and stability*, vol. 174, p. 109098, 2020.

[70] D. Viljoen, J. Labuschagné, and I. Kuehnert, "The weathering resistance of quaternary high-density polyethylene (hdpe) composites : Effects of weld lines, formulation and degradation on tensile properties," *Journal of Polymer Science*, 2023.

[71] G. Delannoy, S. Marceau, P. Gle, E. Gourlay, M. Guéguen-Minerbe, S. Amziane, and F. Farcas, "Durability of hemp concretes exposed to accelerated environmental aging," *Construction and Building Materials*, vol. 252, p. 119043, 2020.

[72] F. Benmahiddine, F. Bennai, R. Cherif, R. Belarbi, A. Tahakourt, and K. Abahri, "Experimental investigation on the influence of immersion/drying cycles on the hygrothermal and mechanical properties of hemp concrete," *Journal of Building Engineering*, vol. 32, p. 101758, 2020.

[73] F. Bennai, N. Issaadi, K. Abahri, R. Belarbi, and A. Tahakourt, "Experimental characterization of thermal and hygric properties of hemp concrete with consideration of the material age evolution," *Heat and Mass Transfer*, vol. 54, pp. 1189–1197, 2018.

[74] D. Kosiachevskyi, K. Abahri, A. Daubresse, E. Prat, and M. Chaouche, "Assessment of the hygrothermal, microstructural and chemical evolution of a hemp-based cementitious mortar under etics total weathering aging protocol," *Construction and Building Materials*, vol. 314, p. 125471, 2022.

[75] S. Marceau, P. Glé, M. Guéguen-Minerbe, E. Gourlay, S. Moscardelli, I. Nour, and S. Amziane, "Influence of accelerated aging on the properties of hemp concretes," *Construction and Building Materials*, vol. 139, pp. 524–530, 2017.

[76] F. Benmahiddine, R. Belarbi, J. Berger, F. Bennai, and A. Tahakourt, "Accelerated aging effects on the hygrothermal behaviour of hemp concrete : Experimental and numerical investigations," *Energies*, vol. 14, no. 21, p. 7005, 2021.

[77] E. Buckingham, "On physically similar systems ; illustrations of the use of dimensional equations," *Physical review*, vol. 4, no. 4, p. 345, 1914.

[78] D. Lacanette, S. Vincent, A. Sarthou, P. Malaurent, and J.-P. Caltagirone, "An eulerian/lagrangian method for the numerical simulation of incompressible convection flows interacting with complex obstacles : Application to the natural convection in the lascaux cave," *International Journal of Heat and Mass Transfer*, vol. 52, no. 11-12, pp. 2528–2542, 2009.

[79] J. Rezaeepazhand and G. Simitses, "Design of scaled down models for predicting shell vibration repsonse," *Journal of Sound and Vibration*, vol. 195, no. 2, pp. 301–311, 1996.

[80] A. Berry, O. Robin, F. Franco, S. De Rosa, and G. Petrone, "Similitude laws for the sound radiation of flat orthotropic flexural panels," *Journal of Sound and Vibration*, vol. 489, p. 115636, 2020.

[81] P. Singhatanadgid and A. N. Songkhla, "An experimental investigation into the use of scaling laws for predicting vibration responses of rectangular thin plates," *Journal of Sound and Vibration*, vol. 311, no. 1-2, pp. 314–327, 2008.

[82] S. Wang, F. Xu, X. Zhang, Z. Dai, X. Liu, and C. Bai, "A directional framework of similarity laws for geometrically distorted structures subjected to impact loads," *International Journal of Impact Engineering*, vol. 161, p. 104092, 2022.

[83] B. Roschning and N. Huber, "Scaling laws of nanoporous gold under uniaxial compression : Effects of structural disorder on the solid fraction, elastic poisson's ratio, young's modulus and yield strength," *Journal of the Mechanics and Physics of Solids*, vol. 92, pp. 55–71, 2016.

[84] P. H. Chan, K. Y. Tshai, M. Johnson, and S. Li, "The flexural properties of composite repaired pipeline : Numerical simulation and experimental validation," *Composite Structures*, vol. 133, pp. 312–321, 2015.

[85] S. Bogos and I. STROE, "Similarity criteria for "full" and "scale" aircraft on the lateral stabilty analysis," *UPB Sci. Bull., Series D*, vol. 74, no. 4, 2012.

[86] S. Delbecq, M. Budinger, A. Ochotorena, A. Reysset, and F. Defaÿ, "Efficient sizing and optimization of multirotor drones based on scaling laws and similarity models," *Aerospace Science and Technology*, vol. 102, p. 105873, 2020.

[87] G. Łukaszewicz and P. Kalita, *Navier–Stokes Equations : An Introduction with Applications.* Springer, 2016.

[88] D. Yamaguchi and G. Ishigami, "Experimental analysis on landing dynamics of martian moon spacecraft based on similarity law," 2018.

[89] *Martian Moons eXploration.* [Online]. Available : www.mmx.isas.jaxa.jp/en/

[90] N. Mendes, P. C. Philippi, and R. Lamberts, "A new mathematical method to solve highly coupled equations of heat and mass transfer in porous media," *International Journal of Heat and Mass Transfer*, vol. 45, no. 3, pp. 509–518, 2002.

[91] A. V. Luikov, “Heat and mass transfer in capillary-porous bodies,” in *Advances in heat transfer.* Elsevier, 1964, vol. 1, pp. 123–184.

[92] H. M. Künzel and K. Kiessl, “Calculation of heat and moisture transfer in exposed building components,” *International Journal of heat and mass transfer*, vol. 40, no. 1, pp. 159–167, 1996.

[93] J. Berger, T. Busser, S. Reddy, and G. S. Dulikravich, “Evaluation of the reliability of a heat and mass transfer model in hygroscopic material,” *International Journal of Heat and Mass Transfer*, vol. 142, p. 118258, 2019.

[94] J. Berger, C. Legros, and M. Abdykarim, “Dimensionless formulation and similarity to assess the main phenomena of heat and mass transfer in building porous material,” *Journal of Building Engineering*, vol. 35, p. 101849, 2021.

[95] J. Berger and C. Legros, “Experimental assessment of the similarity laws for two-dimensional nonlinear heat transfer in building material,” *Journal of Porous Media*, vol. 25, no. 10, 2022.

[96] M. Matsumoto and S. Fujiwara, “A study of annual moisture variation in an internally insulated building wall under a mild climate using a small-scale model and the similarity laws,” *Energy and Buildings*, vol. 16, no. 3-4, pp. 933–945, 1991.

[97] M. Santamouris, *Energy Consumption and Environmental Quality of the Building Sector.* Elsevier Ltd, 2019.

[98] S. B. Basturk, C. E. Dancer, and T. McNally, “Jo ur na l P re,” *Pharmacological Research*, p. 104743, 2020. [Online]. Available : https://doi.org/10.1016/j.phrs.2020.104743

[99] N. Mostefai, R. Hamzaoui, S. Guessasma, A. Aw, and H. Nouri, “Microstructure and mechanical performance of modified hemp fibre and shiv mortars : Discovering the optimal formulation,” *Materials and Design*, vol. 84, pp. 359–371, 2015.

[100] M. Rao, M. Li, H. Yang, X. Li, and Y. Dong, “Effects of carbonation and freeze-thaw cycles on microstructure of concrete,” *Journal Wuhan University of Technology, Materials Science Edition*, vol. 31, no. 5, pp. 1018–1025, 2016.

[101] B. Remki, K. Abahri, M. Tahlaiti, and R. Belarbi, “Hygrothermal transfer in wood drying under the atmospheric pressure gradient,” *International Journal of Thermal Sciences*, vol. 57, pp. 135–141, 2012. [Online]. Available : http://dx.doi.org/10.1016/j.ijthermalsci.2012.02.005

[102] A. Trabelsi, A. Belarbi, P. Turcry, K. Ait-Mokhtar, “Water vapour desorption variability in situ concrete effects on drying,” pp. 333–342, 2011. [Online]. Available : https://doi.org/10.1680/macr.9.00161

[103] N. Issaadi, A. A. Hamami, R. Belarbi, and A. Aït-Mokhtar, “Experimental assessment of the spatial variability of porosity, permeability and sorption isotherms in an ordinary building concrete,” *Heat and Mass Transfer/Waerme- und Stoffuebertragung*, vol. 53, no. 10, pp. 3037–3048, 2017.

[104] A. Trabelsi, Z. Slimani, and J. Virgone, “Response surface analysis of the dimensionless heat and mass transfer parameters of Medium Density Fiberboard,” *International Journal of Heat and Mass Transfer*, vol. 127, pp. 623–630, 2018. [Online]. Available : https://doi.org/10.1016/j.ijheatmasstransfer.2018.05.145

[105] R. M. Abumandour, I. M. Eldesoky, M. H. Kamel, M. M. Ahmed, and S. I. Abdelsalam, "Peristaltic thrusting of a thermal-viscosity nanofluid through a resilient vertical pipe," *Zeitschrift für Naturforschung A*, vol. 75, no. 8, pp. 727–738, 2020. [Online]. Available : https://doi.org/10.1515/zna-2020-0054

[106] S. R. Koumy, E. S. I. Barakat, and S. I. Abdelsalam, "Hall and Porous Boundaries Effects on Peristaltic Transport Through Porous Medium of a Maxwell Model," *Transport in Porous Media*, vol. 94, no. 3, pp. 643–658, 2012.

[107] S. I. Abdelsalam and A. Z. Zaher, "Leveraging elasticity to uncover the role of rabinowitsch suspension through a wavelike conduit : Consolidated blood suspension application," *Mathematics*, vol. 9, no. 16, 2021. [Online]. Available : https://www.mdpi.com/2227-7390/9/16/2008

[108] W. Neise, "Application of Similarity Laws To the Blade Passage Sound of Centrifugal Fans." *Journal of Sound and Vibration*, vol. 43, p. 1975, 1975. [Online]. Available : https://doi.org/10.1016/0022-460X(75)90205-9

[109] C. Codegone, "A law of similarity for temperatures in enclosed turbulent flames," *Combustion and Flame*, vol. 1, no. 2, pp. 194–198, 1957.

[110] L. M. Mazzariol and M. Alves, "Experimental verification of similarity laws for impacted structures made of different materials," *International Journal of Impact Engineering*, vol. 133, no. April, p. 103364, 2019. [Online]. Available : https://doi.org/10.1016/j.ijimpeng.2019.103364

[111] S. I. Abdelsalam, J. X. Velasco-Hernández, and A. Z. Zaher, "Electro-magnetically modulated self-propulsion of swimming sperms via cervical canal," *Biomechanics and Modeling in Mechanobiology*, vol. 20, no. 3, pp. 861–878, 2021. [Online]. Available : https://doi.org/10.1007/s10237-020-01407-3

[112] M. M. Bhatti and S. I. Abdelsalam, "Bio-inspired peristaltic propulsion of hybrid nanofluid flow with tantalum (ta) and gold (au) nanoparticles under magnetic effects," *Waves in Random and Complex Media*, vol. 0, no. 0, pp. 1–26, 2021. [Online]. Available : https://doi.org/10.1080/17455030.2021.1998728

[113] K. Mekheimer, R. Abo-Elkhair, S. Abdelsalam, K. K. Ali, and A. Moawad, "Biomedical simulations of nanoparticles drug delivery to blood hemodynamics in diseased organs : Synovitis problem," *International Communications in Heat and Mass Transfer*, vol. 130, p. 105756, 2022. [Online]. Available : https://www.sciencedirect.com/science/article/pii/S0735193321006497

[114] S. Samanta and A. Guha, "A similarity theory for natural convection from a horizontal plate for prescribed heat flux or wall temperature," *International Journal of Heat and Mass Transfer*, vol. 55, no. 13-14, pp. 3857–3868, 2012. [Online]. Available : http://dx.doi.org/10.1016/j.ijheatmasstransfer.2012.02.031

[115] I. M. Eldesoky, S. I. Abdelsalam, W. A. El-Askary, and M. M. Ahmed, "The integrated thermal effect in conjunction with slip conditions on peristaltically induced particle-fluid transport in a catheterized pipe," *Journal of Porous Media*, vol. 23, no. 7, pp. 695–713, 2020.

[116] Y. A. Elmaboud and S. I. Abdelsalam, "DC/AC magnetohydrodynamic-micropump of a generalized burger's fluid in an annulus," *Physica Scripta*, vol. 94, no. 11, p. 115209, aug 2019. [Online]. Available : https://doi.org/10.1088/1402-4896/ab206d

[117] M. M. Bhatti, S. Z. Alamri, R. Ellahi, and S. I. Abdelsalam, “Intra-uterine particle–fluid motion through a compliant asymmetric tapered channel with heat transfer,” *Journal of Thermal Analysis and Calorimetry*, vol. 144, no. 6, pp. 2259–2267, 2021. [Online]. Available : https://doi.org/10.1007/s10973-020-10233-9

[118] R. Raza, F. Mabood, R. Naz, and S. I. Abdelsalam, “Thermal transport of radiative Williamson fluid over stretchable curved surface,” *Thermal Science and Engineering Progress*, vol. 23, no. February, p. 100887, 2021. [Online]. Available : https://doi.org/10.1016/j.tsep.2021.100887

[119] M. Qin, R. Belarbi, A. Aït-Mokhtar, and A. Seigneurin, “An analytical method to calculate the coupled heat and moisture transfer in building materials,” *International Communications in Heat and Mass Transfer*, vol. 33, no. 1, pp. 39–48, 2006.

[120] J. M. Owen, P. J. Newton, and G. D. Lock, “Transient heat transfer measurements using thermochromic liquid crystal. Part 2 : Experimental uncertainties,” *International Journal of Heat and Fluid Flow*, vol. 24, no. 1, pp. 23–28, 2003.

[121] C. Wang and H. G. Matthies, “Non-probabilistic interval process model and method for uncertainty analysis of transient heat transfer problem,” *International Journal of Thermal Sciences*, vol. 144, no. April, pp. 147–157, 2019. [Online]. Available : https://doi.org/10.1016/j.ijthermalsci.2019.06.002

[122] M. A. Mendes, S. Ray, J. M. Pereira, J. C. Pereira, and D. Trimis, “Quantification of uncertainty propagation due to input parameters for simple heat transfer problems,” *International Journal of Thermal Sciences*, vol. 60, pp. 94–105, 2012. [Online]. Available : http://dx.doi.org/10.1016/j.ijthermalsci.2012.04.020

[123] C. Wang, Z. Qiu, and Y. Yang, “Uncertainty propagation of heat conduction problem with multiple random inputs,” *International Journal of Heat and Mass Transfer*, vol. 99, pp. 95–101, 2016. [Online]. Available : http://dx.doi.org/10.1016/j.ijheatmasstransfer.2016.03.094

[124] M. Fan, Y. Chen, and K. Wan, “Representative elementary volume analysis of hardened cement paste during hydration using X-ray Computed Tomography,” *Construction and Building Materials*, vol. 277, p. 122268, 2021. [Online]. Available : https://doi.org/10.1016/j.conbuildmat.2021.122268

[125] I. M. Gitman, H. Askes, and L. J. Sluys, “Representative volume : Existence and size determination,” *Engineering Fracture Mechanics*, vol. 74, no. 16, pp. 2518–2534, 2007.

[126] B. A. Schrefler and Z. Xiaoyong, “A fully coupled model for water flow and airflow in deformable porous media,” *Water Resources Research*, vol. 29, no. 1, pp. 155–167, 1993.

[127] F. Goia, G. Chaudhary, and S. Fantucci, “Modelling and experimental validation of an algorithm for simulation of hysteresis effects in phase change materials for building components,” *Energy and Buildings*, vol. 174, pp. 54–67, 2018.

[128] F. Liu, B. Jia, B. Chen, and W. Geng, “Moisture transfer in building envelope and influence on heat transfer,” *Procedia Engineering*, vol. 205, pp. 3654–3661, 2017. [Online]. Available : https://doi.org/10.1016/j.proeng.2017.10.229

[129] G. Gimenez, M. Errera, D. Baillis, Y. Smith, and F. Pardo, “A coupling numerical methodology for weakly transient conjugate heat transfer problems,” *International Journal of Heat and Mass Transfer*, vol. 97, pp. 975–989, 2016. [Online]. Available : http://dx.doi.org/10.1016/j.ijheatmasstransfer.2016.02.037

[130] S. Hamidi, T. Heinze, B. Galvan, and S. Miller, "Critical review of the local thermal equilibrium assumption in heterogeneous porous media : Dependence on permeability and porosity contrasts," *Applied Thermal Engineering*, vol. 147, no. October 2018, pp. 962–971, 2019. [Online]. Available : https://doi.org/10.1016/j.applthermaleng.2018.10.130

[131] J. Lévêque and A. Rezzoug, "Dimensionless and analytical studies of the thermal stability of a high temperature superconducting tube," *International Journal of Heat and Mass Transfer*, vol. 48, no. 14, pp. 2815–2821, 2005.

[132] L. M. Biberman, S. Y. Bronin, and A. N. Lagar'kov, "Radiative and convective heat transfer in hypersonic flow around a blunt body," *Fluid Dynamics*, vol. 7, no. 5, pp. 800–809, 1972.

[133] H. J. Kaeppeler and N. Ruhs, "Similarity laws in turbulent focus plasma with beam-beam neutron production," *Physics Letters A*, vol. 49, no. 5, pp. 383–385, 1974.

[134] J. R. Taylor, "[John_R._Taylor]_An_Introduction_to_Error_Analysis(BookZZ.org).pdf," 1997.

[135] M. Simo-Tagne, R. Rémond, Y. Rogaume, A. Zoulalian, and B. Bonoma, "Modeling of coupled heat and mass transfer during drying of tropical woods," *International Journal of Thermal Sciences*, vol. 109, pp. 299–308, 2016. [Online]. Available : http://dx.doi.org/10.1016/j.ijthermalsci.2016.06.012

[136] M. Y. Ferroukhi, R. Belarbi, K. Limam, and W. Bosschaerts, "Impact of Coupled Heat and Moisture Transfer," *Thermal Science*, vol. 21, no. 3, pp. 1359–1368, 2017.

[137] S. Gasparin, J. Berger, D. Dutykh, and N. Mendes, "An adaptive simulation of nonlinear heat and moisture transfer as a boundary value problem," *International Journal of Thermal Sciences*, vol. 133, no. July, pp. 120–139, 2018. [Online]. Available : https://doi.org/10.1016/j.ijthermalsci.2018.07.013

[138] T. Busser, J. Berger, A. Piot, M. Pailha, and M. Woloszyn, "Comparison of model numerical predictions of heat and moisture transfer in porous media with experimental observations at material and wall scales : An analysis of recent trends," *Drying Technology*, vol. 37, no. 11, pp. 1363–1395, 2019. [Online]. Available : https://doi.org/10.1080/07373937.2018.1502195

[139] H. Rafidiarison, R. Rémond, and E. Mougel, "Dataset for validating 1-d heat and mass transfer models within building walls with hygroscopic materials," *Building and Environment*, vol. 89, pp. 356–368, 2015. [Online]. Available : https://www.sciencedirect.com/science/article/pii/S0360132315001158

[140] T. Colinart, D. Lelievre, and P. Glouannec, "Experimental and numerical analysis of the transient hygrothermal behavior of multilayered hemp concrete wall," *Energy and Buildings*, vol. 112, pp. 1–11, 2016. [Online]. Available : https://www.sciencedirect.com/science/article/pii/S0378778815303960

[141] M. Maaroufi, R. Belarbi, K. Abahri, and F. Benmahiddine, "Full characterization of hygrothermal, mechanical and morphological properties of a recycled expanded polystyrene-based mortar," *Construction and Building Materials*, vol. 301, p. 124310, 2021. [Online]. Available : https://www.sciencedirect.com/science/article/pii/S0950061821020699

[142] R. L. Thompson and E. J. Soares, "Viscoplastic dimensionless numbers," *Journal of Non-Newtonian Fluid Mechanics*, vol. 238, pp. 57–64, 2016, viscoplastic Fluids From

Theory to Application 2015 (VPF6). [Online]. Available : https://www.sciencedirect.com/science/article/pii/S0377025716300465

[143] M. C. Ruzicka, “On dimensionless numbers,” *Chemical Engineering Research and Design*, vol. 86, no. 8, pp. 835–868, 2008.

[144] X. Qian, Z. Liu, and J. Xu, “A scaling law for designing a downscaled model to investigate submarine debris-flow impact on a pipeline in normal gravity,” *Ocean Engineering*, vol. 251, p. 111152, 2022. [Online]. Available : https://www.sciencedirect.com/science/article/pii/S0029801822005613

[145] A. Pucciarelli and W. Ambrosini, “A successful general fluid-to-fluid similarity theory for heat transfer at supercritical pressure,” *International Journal of Heat and Mass Transfer*, vol. 159, 2020.

[146] S. Kassem, A. Pucciarelli, and W. Ambrosini, “Insight into a fluid-to-fluid similarity theory for heat transfer at supercritical pressure : Results and perspectives,” *International Journal of Heat and Mass Transfer*, vol. 168, 2021.

[147] S. Sharma and S. K. Saha, “Development of scaling laws for prototyping and heat loss correlations for upward facing cylindrical helical coil and conical spiral coil receivers,” *International Journal of Heat and Mass Transfer*, vol. 190, p. 122773, 2022. [Online]. Available : https://www.sciencedirect.com/science/article/pii/S0017931022002551

[148] L. M. Mazzariol and M. Alves, “Similarity laws of structures under impact load : Geometric and material distortion,” *International Journal of Mechanical Sciences*, vol. 157-158, pp. 633–647, 2019. [Online]. Available : https://www.sciencedirect.com/science/article/pii/S0020740319304138

[149] B. Li, D. L. Zhou, Y. Wang, Y. Shuai, Q. Z. Liu, and W. H. Cai, “The design of a small lab-scale wind turbine model with high performance similarity to its utility-scale prototype,” *Renewable Energy*, vol. 149, pp. 435–444, 2020.

[150] K. Zhang, F. Lu, Y. Peng, and X. Li, “Study on dynamic response of gravity dam under air blast load based on similarity law,” *Engineering Failure Analysis*, vol. 138, p. 106225, 2022. [Online]. Available : https://www.sciencedirect.com/science/article/pii/S1350630722001996

[151] J. xi Chen, “Similarity law of flowrate for hot-gas ventilated supercavity flows,” *Journal of Hydrodynamics, Ser. B*, vol. 22, no. 5, Supplement 1, pp. 852–858, 2010. [Online]. Available : https://www.sciencedirect.com/science/article/pii/S1001605810600418

[152] Q. Ai, W. Wang, Y. Gong, X. Zhang, Y. Shuai, M. Xie, and H. Tan, “Study on similarity criteria for aerodynamic/thermal coupling analysis of the aircraft,” *International Communications in Heat and Mass Transfer*, vol. 129, no. October, p. 105705, 2021. [Online]. Available : https://doi.org/10.1016/j.icheatmasstransfer.2021.105705

[153] C. Zhang, J. Wei, S. Hou, and J. Zhang, “Scaling law of gear transmission system obtained from dynamic equation and finite element method,” *Mechanism and Machine Theory*, vol. 159, p. 104285, 2021. [Online]. Available : https://www.sciencedirect.com/science/article/pii/S0094114X21000434

[154] Y. Zhou, S. Feng, and J. Li, “Study on the failure mechanism of rock mass around a mined-out area above a highway tunnel – similarity model test and numerical analysis,” *Tunnelling and Underground Space Technology*, vol. 118, p. 104182, 2021. [Online]. Available : https://www.sciencedirect.com/science/article/pii/S0886779821003734

[155] A. Charaka, J. Berger, and R. Belarbi, "Experimental assessment of the similarity law for a heat conduction problem," *Thermal Science and Engineering Progress*, p. 101312, 2022. [Online]. Available : https://www.sciencedirect.com/science/article/pii/S2451904922001196

[156] F. Kong and M. Zheng, "Effects of combined heat and mass transfer on heating load in building drying period," *Energy and Buildings*, vol. 40, no. 8, pp. 1614–1622, 2008.

[157] M. Simo-Tagne, R. Remond, R. Kharchi, L. Bennamoun, M. C. Ndukwu, and Y. Rogaume, "Modeling, numerical simulation and validation of the hygrothermal transfer through a wooden building wall in Nancy, France," *Thermal Science and Engineering Progress*, vol. 22, no. December 2020, p. 100808, 2021. [Online]. Available : https://doi.org/10.1016/j.tsep.2020.100808

[158] S. Eraslan, I. M. Gitman, H. Askes, and R. de Borst, "Determination of representative volume element size for a magnetorheological elastomer," *Computational Materials Science*, vol. 203, p. 111070, 2022. [Online]. Available : https://www.sciencedirect.com/science/article/pii/S092702562100745X

[159] S. Whitaker, *Volume Averaging of Transport Equations*, 01 1997, pp. 1–60.

[160] L. Wang, L.-P. Wang, Z. Guo, and J. Mi, "Volume-averaged macroscopic equation for fluid flow in moving porous media," *International Journal of Heat and Mass Transfer*, vol. 82, pp. 357–368, 2015. [Online]. Available : https://www.sciencedirect.com/science/article/pii/S0017931014010448

[161] T. Colinart and P. Glouannec, "Temperature dependence of sorption isotherm of hygroscopic building materials. Part 1 : Experimental evidence and modeling," *Energy and Buildings*, vol. 139, pp. 360–370, 2017. [Online]. Available : http://dx.doi.org/10.1016/j.enbuild.2016.12.082

[162] F. Bennai, M. Y. Ferroukhi, F. Benmahiddine, R. Belarbi, and A. Nouviaire, "ff compared to conventional building materials at overall building scale," *Construction and Building Materials*, vol. 316, no. December 2021, p. 126007, 2022. [Online]. Available : https://doi.org/10.1016/j.conbuildmat.2021.126007

[163] M. Y. Ferroukhi, K. Abahri, R. Belarbi, and K. Limam, "Integration of a hygrothermal transfer model for envelope in a building energy simulation model : experimental validation of a HAM–BES co-simulation approach," *Heat and Mass Transfer/Waerme- und Stoffuebertragung*, vol. 53, no. 6, pp. 1851–1861, 2017.

[164] B. Jamal, M. Boukendil, A. Abdelbaki, and Z. Zrikem, "Numerical simulation of coupled heat transfer through double solid walls separated by an air layer," *International Journal of Thermal Sciences*, vol. 156, no. April 2018, p. 106461, 2020. [Online]. Available : https://doi.org/10.1016/j.ijthermalsci.2020.106461

[165] F. Collet, J. Chamoin, S. Pretot, and C. Lanos, "Comparison of the hygric behaviour of three hemp concretes," *Energy and Buildings*, vol. 62, pp. 294–303, 2013. [Online]. Available : http://dx.doi.org/10.1016/j.enbuild.2013.03.010

[166] M. I. H. Khan, Z. Welsh, Y. Gu, M. A. Karim, and B. Bhandari, "Modelling of simultaneous heat and mass transfer considering the spatial distribution of air velocity during intermittent microwave convective drying," *International Journal of Heat and Mass Transfer*, vol. 153, 2020.

[167] T. Defraeye, B. Blocken, and J. Carmeliet, "Convective heat transfer coefficients for exterior building surfaces : Existing correlations and CFD modelling," *Energy Conversion and Management*, vol. 52, no. 1, pp. 512–522, 2011. [Online]. Available : http://dx.doi.org/10.1016/j.enconman.2010.07.026

[168] W. Belazi, S. E. Ouldboukhitine, A. Chateauneuf, and A. Bouchair, "Uncertainty analysis of occupant behavior and building envelope materials in office building performance simulation," *Journal of Building Engineering*, vol. 19, no. May, pp. 434–448, 2018. [Online]. Available : https://doi.org/10.1016/j.jobe.2018.06.005

[169] H. Sari-Sarraf, E. Delp, T. Aach, M. S. Pattichis, and J. P. Havlicek, "Engineering analysis of experimental data," vol. 986, 2004.

[170] T. Lu and C. Chen, "Uncertainty evaluation of humidity sensors calibrated by saturated salt solutions," *Measurement : Journal of the International Measurement Confederation*, vol. 40, no. 6, pp. 591–599, 2007.

[171] S. Lee, "Monte Carlo simulation using support vector machine and kernel density for failure probability estimation," *Reliability Engineering and System Safety*, vol. 209, no. November 2020, p. 107481, 2021. [Online]. Available : https://doi.org/10.1016/j.ress.2021.107481

[172] T. P. Chang, "Estimation of wind energy potential using different probability density functions," *Applied Energy*, vol. 88, no. 5, pp. 1848–1856, 2011. [Online]. Available : http://dx.doi.org/10.1016/j.apenergy.2010.11.010

[173] J. Zhang and S. Chauhan, "Fast explicit dynamics finite element algorithm for transient heat transfer," *International Journal of Thermal Sciences*, vol. 139, no. October 2018, pp. 160–175, 2019. [Online]. Available : https://doi.org/10.1016/j.ijthermalsci.2019.01.030

[174] J. Xiao, Y. Liu, J. Wanga, P. Bénard, and R. Chahine, "Finite element simulation of heat and mass transfer in activated carbon hydrogen storage tank," *International Journal of Heat and Mass Transfer*, vol. 55, no. 23-24, pp. 6864–6872, 2012. [Online]. Available : http://dx.doi.org/10.1016/j.ijheatmasstransfer.2012.06.093

[175] R. Willink and I. Lira, "A united interpretation of different uncertainty intervals," *Measurement : Journal of the International Measurement Confederation*, vol. 38, no. 1, pp. 61–66, 2005.

[176] S. Rouchier, T. Busser, M. Pailha, A. Piot, and M. Woloszyn, "Hygric characterization of wood fiber insulation under uncertainty with dynamic measurements and Markov Chain Monte-Carlo algorithm," *Building and Environment*, vol. 114, pp. 129–139, 2017.

[177] L. Shi, X. Qi, Z. Yang, L. Tao, Y. Li, J. Qiu, and X. Jiang, "Comparative study of greenhouse gas emission calculations and the environmental impact in the life cycle assessment of buildings in china, finland, and the united states," *Journal of Building Engineering*, vol. 70, p. 106396, 2023. [Online]. Available : https://www.sciencedirect.com/science/article/pii/S2352710223005752

[178] M. K. Mattinen, J. Heljo, J. Vihola, A. Kurvinen, S. Lehtoranta, and A. Nissinen, "Modeling and visualization of residential sector energy consumption and greenhouse gas emissions," *Journal of Cleaner Production*, vol. 81, pp. 70–80, 2014. [Online]. Available : https://www.sciencedirect.com/science/article/pii/S0959652614005319

[179] M. R. Ahmad, Y. Pan, and B. Chen, "Physical and mechanical properties of sustainable vegetal concrete exposed to extreme weather conditions," *Construction*

and Building Materials, vol. 287, p. 123024, 2021. [Online]. Available : https://www.sciencedirect.com/science/article/pii/S0950061821007844

[180] A. Gaspard, L. Chateau, C. Laruelle, B. Lafitte, P. Léonardon, Q. Minier, K. Motamedi, L. Ougier, A. Pineau, and S. Thiriot, "Introducing sufficiency in the building sector in net-zero scenarios for france," *Energy and Buildings*, vol. 278, p. 112590, 2023. [Online]. Available : https://www.sciencedirect.com/science/article/pii/S0378778822007617

[181] C. J. Kibert, "Establishing principles and a model for sustainable construction," in *Proceedings of the first international conference on sustainable construction*, 1994, pp. 6–9.

[182] M. Yadav and M. Agarwal, "Biobased building materials for sustainable future : An overview," *Materials Today : Proceedings*, vol. 43, pp. 2895–2902, 2021, cRMSC-2021. [Online]. Available : https://www.sciencedirect.com/science/article/pii/S2214785321002492

[183] A. Vinod, M. Sanjay, S. Suchart, and P. Jyotishkumar, "Renewable and sustainable biobased materials : An assessment on biofibers, biofilms, biopolymers and biocomposites," *Journal of Cleaner Production*, vol. 258, p. 120978, 2020. [Online]. Available : https://www.sciencedirect.com/science/article/pii/S0959652620310258

[184] M.-M. Pang, M.-Y. Pun, W.-S. Chow, and Z. A. M. Ishak, "Carbon footprint calculation for thermoformed starch-filled polypropylene biobased materials," *Journal of Cleaner Production*, vol. 64, pp. 602–608, 2014. [Online]. Available : https://www.sciencedirect.com/science/article/pii/S0959652613004873

[185] R. Shogren, D. Wood, W. Orts, and G. Glenn, "Plant-based materials and transitioning to a circular economy," *Sustainable Production and Consumption*, vol. 19, pp. 194–215, 2019. [Online]. Available : https://www.sciencedirect.com/science/article/pii/S2352550919300715

[186] B. Mandili, M. Taqi, A. El Bouari, and M. Errouaiti, "Experimental study of a new ecological building material for a thermal insulation based on waste paper and lime," *Construction and Building Materials*, vol. 228, p. 117097, 2019. [Online]. Available : https://www.sciencedirect.com/science/article/pii/S0950061819325395

[187] M. Charai, A. Mezrhab, L. Moga, and M. Karkri, "Hygrothermal, mechanical and durability assessment of vegetable concrete mixes made with alfa fibers for structural and thermal insulating applications," *Construction and Building Materials*, vol. 335, p. 127518, 2022. [Online]. Available : https://www.sciencedirect.com/science/article/pii/S0950061822011953

[188] J. Martínez-Martínez, D. Benavente, M. Gomez-Heras, L. Marco-Castaño, and M. Á. García-del Cura, "Non-linear decay of building stones during freeze–thaw weathering processes," *Construction and Building Materials*, vol. 38, pp. 443–454, 2013.

[189] S. K. Lie, T. K. Thiis, G. I. Vestøl, O. Høibø, and L. R. Gobakken, "Can existing mould growth models be used to predict mould growth on wooden claddings exposed to transient wetting ?" *Building and Environment*, vol. 152, pp. 192–203, 2019.

[190] M. Ramesh, D. Kumar, and A. Kumar, "Investigation of the effect of age hardening on the mechanical properties of aluminium metal matrix composites reinforced with graphite particulate," *Materials Today : Proceedings*, 2023. [Online]. Available : https://www.sciencedirect.com/science/article/pii/S2214785323007034

[191] F. Sitzia, C. Lisci, and J. Mirão, “Accelerate ageing on building stone materials by simulating daily, seasonal thermo-hygrometric conditions and solar radiation of csa mediterranean climate,” *Construction and Building Materials*, vol. 266, p. 121009, 2021. [Online]. Available : https://www.sciencedirect.com/science/article/pii/S0950061820330130

[192] J. Berger, S. Guernouti, M. Woloszyn, and C. Buhe, “Factors governing the development of moisture disorders for integration into building performance simulation,” *Journal of Building Engineering*, vol. 3, pp. 1–15, 2015.

[193] P. Sadrolodabaee, J. Claramunt, M. Ardanuy, and A. de la Fuente, “Effect of accelerated aging and silica fume addition on the mechanical and microstructural properties of hybrid textile waste-flax fabric-reinforced cement composites,” *Cement and Concrete Composites*, vol. 135, p. 104829, 2023. [Online]. Available : https://www.sciencedirect.com/science/article/pii/S095894652200422X

[194] J. L. Parracha, G. Borsoi, R. Veiga, I. Flores-Colen, L. Nunes, A. R. Garcia, L. M. Ilharco, A. Dionísio, and P. Faria, “Effects of hygrothermal, uv and so2 accelerated ageing on the durability of etics in urban environments,” *Building and Environment*, vol. 204, p. 108151, 2021. [Online]. Available : https://www.sciencedirect.com/science/article/pii/S0360132321005527

[195] R. F. De Masi, A. Gigante, S. Ruggiero, and G. P. Vanoli, “Impact of weather data and climate change projections in the refurbishment design of residential buildings in cooling dominated climate,” *Applied Energy*, vol. 303, p. 117584, 2021. [Online]. Available : https://www.sciencedirect.com/science/article/pii/S0306261921009600

[196] D. Schwede and Y. Wang, “Reference weather datasets for building simulation in vietnam considering thermal and hygrothermal characteristics,” *Building and Environment*, vol. 220, p. 109022, 2022. [Online]. Available : https://www.sciencedirect.com/science/article/pii/S0360132322002645

[197] E. Huby, C. Thomachot-Schneider, P. Vázquez, G. Fronteau, and K. Beck, “Experimental thermo-hydric study to simulate natural weathering conditions,” *Journal of Cultural Heritage*, vol. 58, pp. 12–22, 2022. [Online]. Available : https://www.sciencedirect.com/science/article/pii/S1296207422001492

[198] O. Kaşka, R. Yumrutaş, and O. Arpa, “Theoretical and experimental investigation of total equivalent temperature difference (tetd) values for building walls and flat roofs in turkey,” *Applied Energy*, vol. 86, no. 5, pp. 737–747, 2009. [Online]. Available : https://www.sciencedirect.com/science/article/pii/S0306261908002225

[199] L. López-Pérez, J. Flores-Prieto, and C. Ríos-Rojas, “Comfort temperature prediction according to an adaptive approach for educational buildings in tropical climate using artificial neural networks,” *Energy and Buildings*, vol. 251, p. 111328, 2021. [Online]. Available : https://www.sciencedirect.com/science/article/pii/S0378778821006125

[200] J. R. Philip and D. A. D. Vries, “Moisture movement in porous materials under temperature gradients,” *Eos, Transactions American Geophysical Union*, vol. 38, pp. 222–232, 1957.

[201] M. Maaroufi, F. Bennai, R. Belarbi, and K. Abahri, “Experimental and numerical highlighting of water vapor sorption hysteresis in the coupled heat and moisture transfers,” *Journal of Building Engineering*, vol. 40, p. 102321, 2021. [Online]. Available : https://www.sciencedirect.com/science/article/pii/S2352710221001777

[202] W. Yossri, S. Ben Ayed, and A. Abdelkefi, "Airfoil type and blade size effects on the aerodynamic performance of small-scale wind turbines : Computational fluid dynamics investigation," *Energy*, vol. 229, p. 120739, 2021. [Online]. Available : https://www.sciencedirect.com/science/article/pii/S0360544221009877

[203] Y. Liu, "Dynamics and scale analysis of the transient convective flow induced by cooling a pr<1 fluid with linear thermal forcing," *International Journal of Heat and Mass Transfer*, vol. 154, p. 119767, 2020. [Online]. Available : https://www.sciencedirect.com/science/article/pii/S0017931020300077

[204] A. Charaka, J. Berger, F. Benmahiddine, and R. Belarbi, "Experimental assessment of the similarity law for a one-dimensional coupled heat and water vapor diffusion in hemp concrete," *International Journal of Heat and Mass Transfer*, vol. 209, p. 124122, 2023. [Online]. Available : https://www.sciencedirect.com/science/article/pii/S0017931023002752

[205] A. Rima, K. Abahri, F. Bennai, C. El Hachem, and M. Bonnet, "Microscopic estimation of swelling and shrinkage of hemp concrete in response to relative humidity variations," *Journal of Building Engineering*, vol. 43, p. 102929, 2021. [Online]. Available : https://www.sciencedirect.com/science/article/pii/S2352710221007877

[206] S. Martinez, A. Machard, A. Pellegrino, K. Touili, L. Servant, and E. Bozonnet, "A practical approach to the evaluation of local urban overheating– a coastal city case-study," *Energy and Buildings*, vol. 253, p. 111522, 2021. [Online]. Available : https://www.sciencedirect.com/science/article/pii/S0378778821008069

[207] R. Willink, "An improved procedure for combining type a and type b components of measurement uncertainty," *International Journal of Metrology and Quality Engineering*, vol. 4, pp. 55–62, 06 2013.

[208] D. Wu, M. Rahim, M. El Ganaoui, R. Bennacer, R. Djedjig, and B. Liu, "Dynamic hygrothermal behavior and energy performance analysis of a novel multilayer building envelope based on pcm and hemp concrete," *Construction and Building Materials*, vol. 341, p. 127739, 2022. [Online]. Available : https://www.sciencedirect.com/science/article/pii/S0950061822014143

[209] B. Seng, C. Magniont, S. Gallego, and S. Lorente, "Behavior of a hemp-based concrete wall under dynamic thermal and hygric solicitations," *Energy and Buildings*, vol. 232, p. 110669, 2021. [Online]. Available : https://www.sciencedirect.com/science/article/pii/S0378778820334551

[210] M. Viel, F. Collet, Y. Lecieux, M. L. M. François, V. Colson, C. Lanos, A. Hussain, and M. Lawrence, "Resistance to mold development assessment of bio-based building materials," *Composites Part B : Engineering*, vol. 158, pp. 406–418, 2019. [Online]. Available : https://www.sciencedirect.com/science/article/pii/S1359836818312873

[211] A. RAHMOUNI, Y. Géraud, A. Boulanouar, A. Mellouk, M. Boukalouch, A. Samaouali, I.-E. El Amrani El Hassani, and J. Sebbani, "Influence de la microstructure et de la saturation en fluide sur la conductivité thermique des milieux hétérogènes et poreux," 05 2010.

[212] R. Walker and S. Pavia, "Moisture transfer and thermal properties of hemp–lime concretes," *Construction and Building Materials*, vol. 64, pp. 270–276, 2014.

[213] K. Midttømme, E. Roaldset, and P. Aagaard, “Thermal conductivity of selected claystones and mudstones from england,” *Clay Minerals*, vol. 33, no. 1, pp. 131–145, 1998.

[214] S. Brunauer, P. H. Emmett, and E. Teller, “Adsorption of gases in multimolecular layers,” *Journal of the American Chemical Society*, vol. 60, pp. 309–319, 1938.

[215] J. Ha, J. Kim, Y. Jung, G. Yun, D.-N. Kim, and H.-Y. Kim, “Poro-elasto-capillary wicking of cellulose sponges,” *Science Advances*, vol. 4, no. 3, p. eaao7051, 2018. [Online]. Available : https://www.science.org/doi/abs/10.1126/sciadv.aao7051

[216] D. Kairies-Alvarado, C. Muñoz-Sanguinetti, and A. Martínez-Rocamora, “Contribution of energy efficiency standards to life-cycle carbon footprint reduction in public buildings in chile,” *Energy and Buildings*, vol. 236, p. 110797, 2021.

[217] C. J. Corbett and S. Muthulingam, “Adoption of voluntary environmental standards : The role of signaling and intrinsic benefits in the diffusion of the leed green building standards,” *Available at SSRN 1009294*, 2007.

[218] D. Jones and C. Brischke, *Performance of bio-based building materials.* Woodhead Publishing, 2017.

[219] F. Fedorik, J. Zach, M. Lehto, H. R. Kymäläinen, R. Kuisma, M. Jallinoja, K. Illikainen, and S. Alitalo, “Hygrothermal properties of advanced bio-based insulation materials,” *Energy and Buildings*, vol. 253, p. 111528, 2021. [Online]. Available : https://doi.org/10.1016/j.enbuild.2021.111528

[220] C. H. Koh, F. Gauvin, K. Schollbach, and H. Brouwers, “Investigation of material characteristics and hygrothermal performances of different bio-based insulation composites,” *Construction and Building Materials*, vol. 346, p. 128440, 2022.

[221] B. P. Chang, A. K. Mohanty, and M. Misra, “Studies on durability of sustainable biobased composites : a review,” *RSC advances*, vol. 10, no. 31, pp. 17 955–17 999, 2020.

[222] M. Ardanuy, J. Claramunt, H. Ventura, and A. M. Manich, “Effect of water treatment on the fiber–matrix bonding and durability of cellulose fiber cement composites,” *Journal of Biobased Materials and Bioenergy*, vol. 9, no. 5, pp. 486–492, 2015.

[223] J. Sheridan, M. Sonebi, S. Taylor, and S. Amziane, “The effect of long term weathering on hemp and rapeseed concrete,” *Cement and Concrete Research*, vol. 131, p. 106014, 2020.

[224] B. Zuccarello, C. Militello, and F. Bongiorno, “Environmental aging effects on high-performance biocomposites reinforced by sisal fibers,” *Polymer Degradation and Stability*, vol. 211, p. 110319, 2023.

[225] R. Zerrouki, A. Benazzouk, M. Courty, and H. B. Hamed, “Potential use of matakaolin as a partial replacement of preformulated lime binder to improve durability of hemp concrete under cyclic wetting/drying aging,” *Construction and Building Materials*, vol. 333, p. 127389, 2022.

[226] T. Cadu, L. Van Schoors, O. Sicot, S. Moscardelli, L. Divet, and S. Fontaine, “Cyclic hygrothermal ageing of flax fibers’ bundles and unidirectional flax/epoxy composite. are bio-based reinforced composites so sensitive ?” *Industrial Crops and Products*, vol. 141, p. 111730, 2019.

[227] D. A. Waddicor, E. Fuentes, L. Sisó, J. Salom, B. Favre, C. Jiménez, and M. Azar, “Climate change and building ageing impact on building energy performance and mitigation

measures application : A case study in turin, northern italy," *Building and Environment*, vol. 102, pp. 13–25, 2016.

[228] A. Taki and A. Zakharanka, "The effect of degradation on cold climate building energy performance : A comparison with hot climate buildings," *Sustainability*, vol. 15, no. 8, p. 6372, 2023.

[229] N. Sakiyama, J. Frick, M. Stipetic, T. Oertel, and H. Garrecht, "Hygrothermal performance of a new aerogel-based insulating render through weathering : Impact on building energy efficiency," *Building and Environment*, vol. 202, p. 108004, 2021.

[230] S. Mercier, B. Marcos, C. Moresoli, M. Mondor, and S. Villeneuve, "Effect of the water content measurements on the estimation and identifiability of water diffusion and convection mass transfer coefficients," *International Journal of Heat and Mass Transfer*, vol. 90, pp. 480–490, 2015.

[231] P. Huttunen and J. Vinha, "Dynamic water vapor sorption in wood-based fibrous materials and material parameter estimation," *Journal of Building Physics*, vol. 46, no. 4, pp. 399–424, 2023.

[232] L. Dantas, H. Orlande, and R. Cotta, "An inverse problem of parameter estimation for heat and mass transfer in capillary porous media," *International Journal of Heat and Mass Transfer*, vol. 46, no. 9, pp. 1587–1598, 2003.

[233] A. Jumabekova, J. Berger, and A. Foucquier, "An efficient sensitivity analysis for energy performance of building envelope : A continuous derivative based approach," in *Building Simulation*, vol. 14. Springer, 2021, pp. 909–930.

[234] M. Muhieddine, É. Canot, and R. March, "Heat transfer modeling in saturated porous media and identification of the thermophysical properties of the soil by inverse problem," *Applied Numerical Mathematics*, vol. 62, no. 9, pp. 1026–1040, 2012.

[235] A. Charaka, J. Berger, F. Benmahiddine, and B. Rafik, "On the development of an accelerated aging design : assessment of its effects on a biobased material," *International Journal of Civil Engineering*, vol. in the process of submission.

[236] X. Yang, J. Wang, C. Zhu, M. He, and Y. Gao, "Effect of wetting and drying cycles on microstructure of rock based on sem," *Environmental Earth Sciences*, vol. 78, pp. 1–10, 2019.

[237] I. Maruyama, H. Sasano, Y. Nishioka, and G. Igarashi, "Strength and young's modulus change in concrete due to long-term drying and heating up to 90 c," *Cement and Concrete Research*, vol. 66, pp. 48–63, 2014.

[238] G. H. dos Santos and N. Mendes, "Simultaneous heat and moisture transfer in soils combined with building simulation," *Energy and Buildings*, vol. 38, no. 4, pp. 303–314, 2006.

[239] N. Mendes and P. Philippi, "A method for predicting heat and moisture transfer through multilayered walls based on temperature and moisture content gradients," *International Journal of Heat and Mass Transfer*, vol. 48, no. 1, pp. 37–51, jan 2005. [Online]. Available : https://linkinghub.elsevier.com/retrieve/pii/S0017931004003680

[240] J. Clark, "Universal equations for saturation vapor pressure," in *40th AIAA/ASME/SAE/ASEE Joint Propulsion Conference and Exhibit*, 2004, p. 4088.

[241] A. Jumabekova, J. Berger, A. Foucquier, and G. S. Dulikravich, "Searching an optimal experiment observation sequence to estimate the thermal properties of a multilayer wall under real climate conditions," *International Journal of Heat and Mass Transfer*, vol. 155, p. 119810, 2020. [Online]. Available : https://doi.org/10.1016/j.ijheatmasstransfer.2020.119810

[242] E. S. P. B. V, E. Sidiropoulos, and C. Tzimopoulos, "Sensitivity analysis of a coupled heat and mass transfer model in unsaturated porous media," *Science*, vol. 64, pp. 281–298, 1983.

[243] A. Gelesz, E. Catto Lucchino, F. Goia, V. Serra, and A. Reith, "Characteristics that matter in a climate façade : A sensitivity analysis with building energy simulation tools," *Energy and Buildings*, vol. 229, p. 110467, 2020. [Online]. Available : https://doi.org/10.1016/j.enbuild.2020.110467